



Observation of a new boson with mass near 125 GeV in pp collisions at $\sqrt{s} = 7$ and 8 TeV

The CMS Collaboration*

Abstract

A detailed description is reported of the analysis used by the CMS Collaboration in the search for the standard model Higgs boson in pp collisions at the LHC, which led to the observation of a new boson. The data sample corresponds to integrated luminosities up to 5.1 fb^{-1} at $\sqrt{s} = 7 \text{ TeV}$, and up to 5.3 fb^{-1} at $\sqrt{s} = 8 \text{ TeV}$. The results for five Higgs boson decay modes $\gamma\gamma$, ZZ , WW , $\tau\tau$, and bb , which show a combined local significance of 5 standard deviations near 125 GeV, are reviewed. A fit to the invariant mass of the two high resolution channels, $\gamma\gamma$ and $ZZ \rightarrow 4\ell$, gives a mass estimate of $125.3 \pm 0.4 \text{ (stat.)} \pm 0.5 \text{ (syst.) GeV}$. The measurements are interpreted in the context of the standard model Lagrangian for the scalar Higgs field interacting with fermions and vector bosons. The measured values of the corresponding couplings are compared to the standard model predictions. The hypothesis of custodial symmetry is tested through the measurement of the ratio of the couplings to the W and Z bosons. All the results are consistent, within their uncertainties, with the expectations for a standard model Higgs boson.

Published in the Journal of High Energy Physics as doi:10.1007/JHEP06(2013)081.

1 Introduction

The standard model (SM) [1–3] of particle physics accurately describes many experimental results that probe elementary particles and their interactions up to an energy scale of a few hundred GeV [4]. In the SM, the building blocks of matter, the fermions, are comprised of quarks and leptons. The interactions are mediated through the exchange of force carriers: the photon for electromagnetic interactions, the W and Z bosons for weak interactions, and the gluons for strong interactions. All the elementary particles acquire mass through their interaction with the Higgs field [5–13]. This mechanism, called the “Higgs” or “BEH” mechanism [5–10], is the first coherent and the simplest solution for giving mass to W and Z bosons, while still preserving the symmetry of the Lagrangian. It is realized by introducing a new complex scalar field into the model. By construction, this field allows the W and Z bosons to acquire mass whilst the photon remains massless, and adds to the model one new scalar particle, the SM Higgs boson (H). The Higgs scalar field and its conjugate can also give mass to the fermions, through Yukawa interactions [11–13]. The SM does not directly predict the values of the masses of the elementary particles, and in the same context there is no prediction for the Higgs boson mass. The particle masses are considered parameters to be determined experimentally. Nevertheless, a number of very general arguments [14–17] have been used to narrow the range of possible values for the Higgs boson mass to below approximately 1 TeV. The wealth of electroweak precision data from the LEP and SLC colliders, the Tevatron, and other experiments predicted the Higgs boson mass to be at approximately 90 GeV, with an upper limit of 152 GeV at the 95% confidence level (CL) [4]. Direct searches at LEP excluded values lower than 114.4 GeV at 95% CL [18], and early Tevatron measurements excluded the mass range 162–166 GeV at 95% CL [19].

The discovery or exclusion of the SM Higgs boson is one of the primary scientific goals of the LHC. Previous direct searches at the LHC were based on data from proton-proton collisions corresponding to an integrated luminosity of 5.1 fb^{-1} collected at a centre-of-mass energy of 7 TeV. The CMS experiment excluded at 95% CL masses from 127 to 600 GeV [20]. The ATLAS experiment excluded at 95% CL the ranges 111.4–116.4, 119.4–122.1, and 129.2–541 GeV [21]. Within the remaining allowed mass region, an excess of events between 2 and 3 standard deviations (σ) near 125 GeV was reported by both experiments. In 2012, the proton-proton centre-of-mass energy was increased to 8 TeV, and by the end of June, an additional integrated luminosity of more than 5.3 fb^{-1} had been recorded by each of the two experiments, thereby enhancing significantly the sensitivity of the search for the Higgs boson. The result was the observation by the ATLAS and CMS Collaborations of a new heavy boson with a mass of approximately 125 GeV. The two experiments simultaneously published the observation in concise papers [22, 23]. The CMS publication [23] focused on the observation in the five main decay channels in the low-mass range from 110 to 145 GeV: $H \rightarrow \gamma\gamma$, $H \rightarrow ZZ \rightarrow 4\ell$, $H \rightarrow WW \rightarrow \ell\nu\ell\nu$, $H \rightarrow \tau\tau$, and $H \rightarrow bb$, where ℓ stands for electron or muon, and for simplicity our notation does not distinguish between particles and antiparticles. In the summer 2012 the analysis of the full data set by the CDF and D0 Collaborations resulted in an excess of events of about 3σ in the mass range $120 \leq m_H \leq 135 \text{ GeV}$, while searching for a SM Higgs boson decaying into b quarks [24].

The channels with the highest sensitivity for discovering the SM Higgs boson with a mass near 125 GeV are $H \rightarrow \gamma\gamma$ and $H \rightarrow ZZ \rightarrow 4\ell$. The other three final states have poorer mass resolution and, therefore, necessitate more data to achieve a similar sensitivity. Among them, the $H \rightarrow WW \rightarrow \ell\nu\ell\nu$ channel has the largest signal-to-background ratio. These five channels are complementary in the way they are measured in the detector, as is the information they can provide about the SM Higgs boson.

A light Higgs boson has a natural width of a few MeV [25], and therefore the precision of the mass measurement from fully reconstructed decays would be limited by the detector resolution. The first two channels, $H \rightarrow \gamma\gamma$ and $H \rightarrow ZZ \rightarrow 4\ell$, produce a narrow mass peak. These two high-resolution channels were used to measure the mass of the newly observed particle [22, 23].

In the SM, the properties of the Higgs boson are fully determined once its mass is known. All cross sections and decay fractions are predicted [25, 26], and thus the measured rates into each channel provide a test of the SM. The individual measurements can be combined, and from them the coupling constants of the Higgs boson with fermions and bosons can be extracted. The measured values can shed light on the nature of the newly observed particle because the Higgs boson couplings to fermions are qualitatively different from those to bosons.

The data described in this paper are identical to those reported in the observation publication [23]. The main focus of this paper is an in-depth description of the five main analyses and a more detailed comparison of the various channels with the SM predictions by evaluating the couplings to fermions and vector bosons, as well as various coupling ratios.

The paper is organized into several sections. Sections 2 and 3 contain a short description of the CMS detector and the event reconstruction of physics objects relevant for the Higgs boson search. Section 4 describes the data sample, the Monte Carlo (MC) event generators used for the signal and background simulation, and the evaluation of the signal sensitivity. Then the analyses of the five decay channels are described in detail in Sections 5 to 9. In the last section, the statistical method used to combine the five channels and the statistical treatment of the systematic uncertainties are explained. Finally, the results are combined and the first measurements of the couplings of the new particle to bosons and fermions are presented.

2 The CMS experiment

The discovery capability for the SM Higgs boson is one of the main benchmarks that went into optimizing the design of the CMS experiment [27–30].

The central feature of the detector [30] is a superconducting solenoid 13 m long, with an internal diameter of 6 m. The solenoid generates a uniform 3.8 T magnetic field along the axis of the LHC beams. Within the field volume are a silicon pixel and strip tracker, a lead tungstate crystal electromagnetic calorimeter (ECAL), and a brass/scintillator hadron calorimeter (HCAL). Muons are identified and measured in gas-ionization detectors embedded in the outer steel magnetic flux return yoke of the solenoid. The detector is subdivided into a cylindrical barrel and endcap disks on each side of the interaction point. Forward calorimeters complement the coverage provided by the barrel and endcap detectors.

The CMS experiment uses a right-handed coordinate system, with the origin at the nominal interaction point, the x axis pointing to the centre of the LHC, the y axis pointing up (perpendicular to the LHC plane), and the z axis along the anticlockwise-beam direction. The azimuthal angle ϕ is measured in the x - y plane. The pseudorapidity is defined as $\eta = -\ln[\tan(\theta/2)]$ where the polar angle θ is measured from the positive z axis. The centre-of-mass momentum of the colliding partons in a proton-proton collision is subject to Lorentz boosts along the beam direction relative to the laboratory frame. Because of this effect, the pseudorapidity, rather than the polar angle, is a more natural measure of the angular separation of particles in the rest frame of the detector.

Charged particles are tracked within the pseudorapidity range $|\eta| < 2.5$. The silicon pixel

tracker is composed of 66 million pixels of area $100 \times 150 \mu\text{m}^2$, arranged in three barrel layers and two endcap disks at each end. The silicon strip tracker, organized in ten barrel layers and twelve endcap disks at each end, is composed of 9.3 million strips with pitch between 80 and $205 \mu\text{m}$, with a total silicon surface area of 198m^2 . The performance of the tracker is essential to most analyses in CMS and has reached the design performance in transverse-momentum (p_T) resolution, efficiency, and primary- and secondary-vertex resolutions. The tracker has an efficiency larger than 99% for muons with $p_T > 1 \text{GeV}$, a p_T resolution between 2 and 3% for charged tracks of $p_T \approx 100 \text{GeV}$ in the central region ($|\eta| < 1.5$), and unprecedented capabilities for b-jet identification. Measurements of the impact parameters of charged tracks and secondary vertices are used to identify jets that are likely to contain the hadronization and decay products of b quarks (“b jets”). A b-jet tagging efficiency of more than 50% is achieved with a rejection factor for light-quark jets of ≈ 200 , as measured with $t\bar{t}$ events in data [31]. The dimuon mass resolution at the Y mass, dominated by instrumental effects, is measured to be 0.6% in the barrel region [32], consistent with the design goal. Due to the high spatial granularity of the pixel detector, the channel occupancy is less than 10^{-3} , allowing charged-particle trajectories to be measured in the high-rate environment of the LHC without loss of performance.

The ECAL is a fine-grained, homogeneous calorimeter consisting of more than 75 000 lead tungstate crystals, arranged in a quasi-projective geometry and distributed in a barrel region ($|\eta| < 1.48$) and two endcaps that extend up to $|\eta| = 3.0$. The front-face cross section of the crystals is approximately $22 \times 22 \text{mm}^2$ in the barrel region and $28.6 \times 28.6 \text{mm}^2$ in the endcaps. Preshower detectors consisting of two planes of silicon sensors interleaved with a total of three radiation lengths of lead absorber are located in front of the endcaps. Electromagnetic (EM) showers are narrowly distributed in the lead tungstate crystals (Molière radius of 21 mm), which have a transverse size comparable to the shower radius. The precise measurement of the transverse shower shape is the primary method used for EM particle identification, and measurements in the surrounding crystals are used for isolation criteria. The energy resolution of the ECAL is the single most important performance benchmark for the measurement of the Higgs boson decay into two photons and to a lesser extent for the decay to ZZ that subsequently decay to electrons. In the central barrel region, the energy resolution of electrons that interact minimally with the tracker material indicates that the resolution of unconverted photons is consistent with design goals. The energy resolution for photons with transverse energy of $\approx 60 \text{GeV}$ varies between 1.1% and 2.5% over the solid angle of the ECAL barrel, and from 2.2% to 5% in the endcaps. For ECAL barrel unconverted photons the diphoton mass resolution is estimated to be 1.1 GeV at a mass of 125 GeV.

The HCAL barrel and endcaps are sampling calorimeters composed of brass and plastic scintillator tiles, covering $|\eta| < 3.0$. The hadron calorimeter thickness varies from 7 to 11 interaction lengths within the solenoid, depending on $|\eta|$; a scintillator “tail catcher” placed outside the coil of the solenoid, just in front of the innermost muon detector, extends the instrumented thickness to more than 10 interaction lengths. Iron forward calorimeters with quartz fibres, read out by photomultipliers, extend the calorimeter coverage up to $|\eta| = 5.0$.

Muons are measured in the range $|\eta| < 2.4$, with detection planes based on three technologies: drift tubes ($|\eta| < 1.2$), cathode strip chambers ($0.9 < |\eta| < 2.4$), and resistive-plate chambers ($|\eta| < 1.6$). The first two technologies provide a precise position measurement and trigger, whilst the third one provides precise timing information, as well as a second independent trigger. The muon system consists of four stations in the barrel and endcaps, designed to ensure robust triggering and detection of muons over a large angular range. In the barrel region, each muon station consists of twelve drift-tube layers, except for the outermost station, which has

eight layers. In the endcaps, each muon station consists of six detection planes. The precision of the r - ϕ measurement is $100\ \mu\text{m}$ in the drift tubes and varies from 60 to $140\ \mu\text{m}$ in the cathode strip chambers, where r is the radial distance from the beamline and ϕ is the azimuthal angle.

The CMS trigger and data acquisition systems ensure that data samples with potentially interesting events are recorded with high efficiency. The first-level (L1) trigger, composed of the calorimeter, muon, and global-trigger processors, uses coarse-granularity information to select the most interesting events in less than $4\ \mu\text{s}$. The detector data are pipelined to ensure negligible deadtime up to a L1 rate of $100\ \text{kHz}$. After L1 triggering, data are transferred from the readout electronics of all subdetectors through the readout network to the high-level-trigger (HLT) processor farm, which assembles the full event and executes global reconstruction algorithms. The HLT filters the data, resulting in an event rate of $\approx 500\ \text{Hz}$ stored for offline processing.

All data recorded by the CMS experiment are accessible for offline analysis through the worldwide LHC computing grid. The CMS experiment employs a highly distributed computing infrastructure, with a primary Tier-0 centre at CERN, supplemented by seven Tier-1, more than 50 Tier-2, and over 100 Tier-3 centres at national laboratories and universities throughout the world. The CMS software running on this high-performance computing system executes a multitude of crucial tasks, including the reconstruction and analysis of the collected data, as well as the generation and detector modelling of MC simulation.

3 Event reconstruction

Figure 1 shows the distribution of the number of vertices reconstructed per event in the 2011 and 2012 data, and the display of a four-lepton event recorded in 2012. The large number of proton-proton interactions occurring per LHC bunch crossing (“pileup”), on average of 9 in 2011 and 19 in 2012, makes the identification of the vertex corresponding to the hard-scattering process nontrivial, and affects most of the physics objects: jets, lepton isolation, etc. The tracking system is able to separate collision vertices as close as $0.5\ \text{mm}$ along the beam direction [33]. For each vertex, the sum of the p_T^2 of all tracks associated with the vertex is computed. The vertex for which this quantity is the largest is assumed to correspond to the hard-scattering process, and is referred to as the primary vertex in the event reconstruction. In the $H \rightarrow \gamma\gamma$ final state, a large fraction of the transverse momentum produced in the collision is carried by the photons, and a dedicated algorithm, described in Section 5.2, is therefore used to assign the photons to a vertex.

A particle-flow (PF) algorithm [34, 35] combines the information from all CMS subdetectors to identify and reconstruct the individual particles emerging from all vertices: charged hadrons, neutral hadrons, photons, muons, and electrons. These particles are then used to reconstruct the missing transverse energy, jets, and hadronic τ -lepton decays, and to quantify the isolation of leptons and photons.

Electrons and photons can interact with the tracker material before reaching the ECAL to create additional electrons and photons through pair production and bremsstrahlung radiation. A calorimeter superclustering algorithm is therefore used to combine the ECAL energy deposits that could correspond to a photon or electron. In the barrel region, superclusters are formed from five-crystal-wide areas in η , centred on the locally most-energetic crystal and having a variable extension in ϕ . In the endcaps, where the crystals are arranged according to an x - y rather than η - ϕ geometry, matrices of 5×5 crystals around the most-energetic crystals are merged if they lie within a narrow road in η .

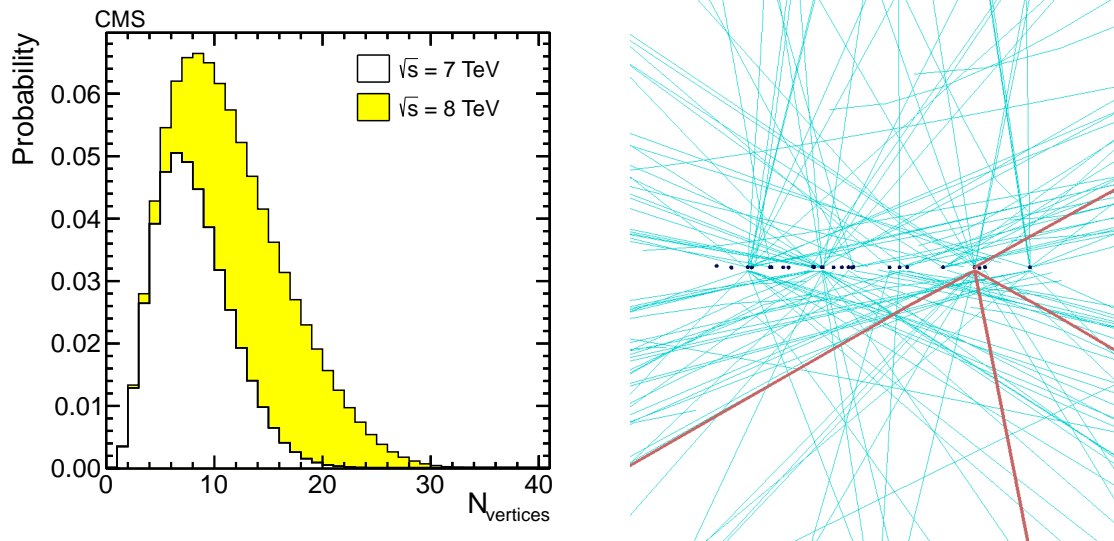


Figure 1: Left: probability distribution for the number of vertices N_{vertices} reconstructed per event in the 2011 and 2012 data. The $\sqrt{s} = 7$ and 8 TeV probability distributions are weighted by their equivalent integrated luminosity, and by the corresponding total cross section $\sigma(\text{pp} \rightarrow \text{H} + \text{X})$ for a SM Higgs boson of mass 125 GeV. Right: display of a four-lepton event recorded in 2012, with 24 reconstructed vertices. The four leptons are shown as thick lines and originate from the vertex chosen for the hard-scattering process.

The stability and uniformity of the ECAL response must be calibrated at a fraction of a percent to maintain the excellent intrinsic energy resolution of the ECAL [36]. A dedicated monitoring system, based on the injection of laser light into each crystal, is used to track and correct for channel response changes caused by radiation damage and subsequent recovery of the crystals [37]. Response variations are a few percent in the barrel region, and increase up to a few tens of percent in the most-forward endcap regions. The channel-to-channel response is equalized using several techniques that exploit reference signatures from collision events (mainly $\pi^0, \eta \rightarrow \gamma\gamma$) [38]. The residual miscalibration of the channel response varies between 0.5% in the central barrel to a few percent in the endcaps [39]. At the reconstruction level, additional correction factors to the photon energy are applied. These corrections are sizeable for photons that convert before entering the ECAL, for which the resolution is mainly limited by shower-loss fluctuations. Given the distribution of the tracker material in front of the ECAL, these effects are sizeable for $|\eta| > 1$ [39].

Candidate photons for the $\text{H} \rightarrow \gamma\gamma$ search are reconstructed from the superclusters, and their identification is discussed in Section 5.3. The photon energy is computed starting from the raw supercluster energy. In the region covered by the preshower detector ($|\eta| > 1.65$), the energy recorded in that detector is added. In order to obtain the best resolution, the raw energy is corrected for the containment of the shower in the clustered crystals and for the shower losses of photons that convert in the tracker material before reaching the calorimeter. These corrections are computed using a multivariate regression technique based on the boosted decision tree (BDT) implementation in TMVA [40]. The regression is trained on photons from a sample of simulated events using the ratio of the true photon energy to the raw energy as the target variable. The input variables are the η and ϕ coordinates of the supercluster, a collection of shower-shape variables, and a set of energy-deposit coordinates defined with respect to the supercluster. A second BDT, using the same input variables, is trained on a separate sample of

simulated photons to provide an estimate of the uncertainty in the energy value provided by the first BDT.

The width of the reconstructed Z resonance is used to quantify the ECAL performance, using decays to two electrons whose energies are measured using the ECAL alone, with their direction determined from the tracks. In the 7 TeV data set, the dielectron mass resolution at the Z boson mass, fitting for the measurement contribution separately from the natural width, is 1.56 GeV in the barrel and 2.57 GeV in the endcaps, while in the 8 TeV data sample, reconstructed with preliminary calibration constants, the corresponding values are 1.61 GeV and 3.75 GeV.

Electron reconstruction is based on two methods: the first where an ECAL supercluster is used to seed the reconstruction of a charged-particle trajectory in the tracker [41, 42], and the second where a candidate track is used to reconstruct an ECAL supercluster [43]. In the latter, the electron energy deposit is found by extrapolating the electron track to the ECAL, and the deposits from possible bremsstrahlung photons are collected by extrapolating a straight line tangent to the electron track from each tracker layer, around which most of the tracker material is concentrated. In both cases, the trajectory is fitted with a Gaussian sum filter [44] using a dedicated modelling of the electron energy loss in the tracker material. Merging the output of these two methods provides high electron reconstruction efficiency within $|\eta| < 2.5$ and $p_T > 2$ GeV. The electron identification relies on a TMVA BDT that combines observables sensitive to the amount of bremsstrahlung along the electron trajectory, the geometrical and momentum matching between the electron trajectory and the associated supercluster, as well as the shower-shape observables.

Muons are reconstructed within $|\eta| < 2.4$ and down to a p_T of 3 GeV. The reconstruction combines the information from both the silicon tracker and the muon spectrometer. The matching between the tracker and the muon system is initiated either “outside-in”, starting from a track in the muon system, or “inside-out”, starting from a track in the silicon tracker. Loosely identified muons, characterized by minimal requirements on the track components in the muon system and taking into account small energy deposits in the calorimeters that match to the muon track, are identified with an efficiency close to 100% by the PF algorithm. In some analyses, additional tight muon identification criteria are applied: a good global muon-track fit based on the tracker and muon chamber hits, muon track-segment reconstruction in at least two muon stations, and a transverse impact parameter with respect to the primary vertex smaller than 2 mm.

Jets are reconstructed from all the PF particles using the anti- k_T jet algorithm [45] implemented in FASTJET [46], with a distance parameter of 0.5. The jet energy is corrected for the contribution of particles created in pileup interactions and in the underlying event. This contribution is calculated as the product of the jet area and an event-by-event p_T density ρ , also obtained with FASTJET using all particles in the event. Charged hadrons, photons, electrons, and muons reconstructed by the PF algorithm have a calibrated momentum or energy scale. A residual calibration factor is applied to the jet energy to account for imperfections in the neutral-hadron calibration, the jet energy containment, and the estimation of the contributions from pileup and underlying-event particles. This factor, obtained from simulation, depends on the jet p_T and η , and is of the order of 5% across the whole detector acceptance. Finally, a percent-level correction factor is applied to match the jet energy response in the simulation to the one observed in data. This correction factor and the jet energy scale uncertainty are extracted from a comparison between the data and simulation of γ +jets, Z+jets, and dijet events [47]. Particles from different pileup vertices can be clustered into a pileup jet, or significantly overlap a jet

from the primary vertex below the p_T threshold applied in the analysis. Such jets are identified and removed using a TMVA BDT with the following input variables: momentum and spatial distribution of the jet particles, charged- and neutral-particle multiplicities, and consistency of charged hadrons within the jet with the primary vertex.

The missing transverse energy (E_T^{miss}) vector is calculated as the negative of the vectorial sum of the transverse momenta of all particles reconstructed by the PF algorithm. The resolution $\sigma(E_{x,y}^{\text{miss}})$ on either the x or y component of the E_T^{miss} vector is measured in $Z \rightarrow \mu\mu$ events and parametrized by $\sigma(E_{x,y}^{\text{miss}}) = 0.5 \times \sqrt{\Sigma E_T}$, where ΣE_T is the scalar sum of the transverse momenta of all particles, with σ and ΣE_T expressed in GeV. In 2012, with an average number of 19 pileup interactions, $\Sigma E_T \approx 600$ GeV for the analyses considered here.

Jets originating from b-quark hadronization are identified using different algorithms that exploit particular properties of such objects [31]. These properties, which result from the relatively large mass and long lifetime of b quarks, include the presence of tracks with large impact parameters, the presence of secondary decay vertices displaced from the primary vertex, and the presence of low- p_T leptons from semileptonic b-hadron decays embedded in the jets [31]. A combined secondary-vertex (CSV) b-tagging algorithm, used in the $H \rightarrow bb$ and $H \rightarrow \tau\tau$ searches, makes use of the information about track impact parameters and secondary vertices within jets in a likelihood discriminant to provide separation of b jets from jets originating from gluons, light quarks, and charm quarks. The efficiency to tag b jets and the rate of misidentification of non-b jets depends on the algorithm used and the operating point chosen. These are typically parameterized as a function of the transverse momentum and rapidity of the jets. The performance measurements are obtained directly from data in samples that can be enriched in b jets, such as $t\bar{t}$ and multijet events.

Hadronically decaying τ leptons (τ_h) are reconstructed and identified using an algorithm [48] which targets the main decay modes by selecting candidates with one charged hadron and up to two neutral pions, or with three charged hadrons. A photon from a neutral-pion decay can convert in the tracker material into an electron and a positron, which can then radiate bremsstrahlung photons. These particles give rise to several ECAL energy deposits at the same η value and separated in azimuthal angle, and are reconstructed as several photons by the PF algorithm. To increase the acceptance for such converted photons, the neutral pions are identified by clustering the reconstructed photons in narrow strips along the ϕ direction. The τ_h from W , Z , and Higgs boson decays are typically isolated from the other particles in the event, in contrast to misidentified τ_h from jets that are surrounded by the jet particles not used in the τ_h reconstruction. The τ_h isolation parameter R_{Iso}^τ is obtained from a multivariate discriminator, taking as input a set of transverse momentum sums $S_j = \sum_i p_{T,i,j}$, where $p_{T,i,j}$ is the transverse momentum of a particle i in a ring j centred on the τ_h candidate direction and defined in (η, ϕ) space. Five equal-width rings are used up to a distance $\Delta R = \sqrt{(\Delta\eta)^2 + (\Delta\phi)^2} = 0.5$ from the τ_h candidate, where $\Delta\eta$ and $\Delta\phi$ are the pseudorapidity and azimuthal angle differences (in radians), respectively, between the particle and the τ_h candidate direction. The effect of pileup on the isolation parameter is mainly reduced by discarding from the S_j calculation the charged hadrons with a track originating from a pileup vertex. The contribution of pileup photons and neutral hadrons is handled by the discriminator, which also takes as input the p_T density ρ .

The isolation parameter of electrons and muons is defined relative to their transverse momentum p_T^ℓ as

$$R_{\text{Iso}}^\ell \equiv \left(\sum_{\text{charged}} p_T + \text{MAX} \left[0, \sum_{\text{neut. had.}} p_T + \sum_{\gamma} p_T - \rho_{\text{neutral}} \times A_{\text{eff}} \right] \right) / p_T^\ell, \quad (1)$$

Table 1: Summary information on the analyses included in this paper. The column ‘‘H prod.’’ indicates the production mechanism targeted by an analysis; it does not imply 100% purity (e.g. analyses targeting vector-boson fusion (VBF) production are expected to have 30%–50% of their signal events coming from gluon-gluon fusion production). The main contribution in the untagged and inclusive categories is always gluon-gluon fusion. A final state can be further subdivided into multiple categories based on additional jet multiplicity, reconstructed mass, transverse momentum, or multivariate discriminators. Notations used are: $(jj)_{\text{VBF}}$ stands for a dijet pair consistent with topology (VBF-tag); $V = W$ and Z bosons; same flavour (SF) dileptons = ee or $\mu\mu$ pairs; different flavour (DF) dileptons = $e\mu$ pairs; $\tau_h = \tau$ leptons decaying hadronically. VH stands for associated production with a vector boson.

H decay	H prod.	Exclusive final states analysed	No. of channels	m_H range (GeV)	m_H resolution	\mathcal{L} (fb^{-1})	
						7 TeV	8 TeV
$\gamma\gamma$	untagged	4 diphoton categories	4	110–150	1–2%	5.1	5.3
	VBF-tag	$\gamma\gamma + (jj)_{\text{VBF}}$ 2 m_{jj} categories for 8 TeV	1 or 2	110–150	1–2%	5.1	5.3
$ZZ \rightarrow 4\ell$	inclusive	$4e, 4\mu, 2e2\mu$	3	110–180	1–2%	5.0	5.3
$WW \rightarrow \ell\nu\ell\nu$	0 or 1 jet	DF or SF dileptons	4	110–160	20%	4.9	5.1
	VBF-tag	$\ell\nu\ell\nu + (jj)_{\text{VBF}}$ DF or SF dileptons for 8 TeV	1 or 2	110–160	20%	4.9	5.1
$\tau\tau$	0 or 1 jet	$(e\tau_h, \mu\tau_h, e\mu, \mu\mu)$ 2 $p_T^{\tau\tau}$ categories and 0 or 1 jet	16	110–145	20%	4.9	5.1
	VBF-tag	$(e\tau_h, \mu\tau_h, e\mu, \mu\mu) + (jj)_{\text{VBF}}$	4	110–145	20%	4.9	5.1
bb	VH-tag	$(\nu\nu, ee, \mu\mu, e\nu, \mu\nu + 2 \text{ b jets})$ 2 p_T^V categories	10	110–135	10%	5.0	5.1

where $\sum_{\text{charged}} p_T$, $\sum_{\text{neut. had.}} p_T$, and $\sum_{\gamma} p_T$ are, respectively, the scalar sums of the transverse momenta of charged hadrons, neutral hadrons, and photons located in a cone centred on the lepton direction in (η, ϕ) space. The cone size ΔR is taken to be 0.3 or 0.4 depending on the analysis. Charged hadrons associated with pileup vertices are not considered, and the contribution of pileup photons and neutral hadrons is estimated as the product of the neutral-particle p_T density ρ_{neutral} and an effective cone area A_{eff} . The neutral-particle p_T density is obtained with FASTJET using all PF photons and neutral hadrons in the event, and the effective cone area is slightly different from the actual cone area, being computed in such a way so as to absorb the residual dependence of the isolation efficiency on the number of pileup collisions.

4 Data sample and analyses performance

The data have been collected by the CMS experiment at a centre-of-mass energy of 7 TeV in the year 2011, corresponding to an integrated luminosity of about 5.1 fb^{-1} , and a centre-of-mass energy of 8 TeV in the year 2012, corresponding to an integrated luminosity of about 5.3 fb^{-1} .

A summary of all analyses described in this paper is presented in Table 1, where we list their main characteristics, namely: exclusive final states, Higgs boson mass range of the search, integrated luminosity used, and the approximate experimental mass resolution. The presence of a signal in one of the channels at a certain value of the Higgs boson mass, m_H , should manifest itself as an excess in the corresponding invariant-mass distribution extending around that value for a range corresponding to the m_H resolution.

4.1 Simulated samples

MC simulation samples for the SM Higgs boson signal and background processes are used to optimize the event selection, evaluate the acceptance and systematic uncertainties, and predict the expected yields. They are processed through a detailed simulation of the CMS detector based on GEANT4 [49] and are reconstructed with the same algorithms used for the data. The simulations include pileup interactions properly reweighted to match the distribution of the number of such interactions observed in data. For leading-order generators the default set of parton distribution functions (PDF) used to produce these samples is CTEQ6L [50], while CT10 [51] is employed for next-to-leading-order (NLO) generators. For all generated samples the hadronization is handled by PYTHIA 6.4 [52] or HERWIG++ [53], and the TAUOLA [54] package is used for τ decays. The PYTHIA parameters for the underlying event and pileup interactions are set to the Z2 tune [55] for the 7 TeV data sample and to the Z2* tune [55] for the 8 TeV data sample.

4.2 Signal simulation

The Higgs boson can be produced in pp collisions via four different processes: gluon-gluon fusion, vector-boson fusion, associated production with a vector boson, and associated production with a $t\bar{t}$ pair. Simulated Higgs boson signals from gluon-gluon fusion ($gg \rightarrow H$), and vector-boson fusion (VBF) ($qq \rightarrow qqH$), are generated with POWHEG [56–58] at NLO. The simulation of associated-production samples uses PYTHIA, with the exception of the $H \rightarrow b\bar{b}$ analysis that uses POWHEG interfaced to HERWIG++. Events at the generator level are reweighted according to the total cross section $\sigma(pp \rightarrow H)$, which contains contributions from gluon-gluon fusion up to next-to-next-to-leading order (NNLO) and next-to-next-to-leading-log (NNLL) terms [25, 59–73], vector-boson fusion including NNLO quantum chromodynamic (QCD) and NLO electroweak (EW) terms [25, 74–78], associated production VH (where $V = Z, W$) at NNLO QCD and NLO EW [79–84], and the production in association with $t\bar{t}$ at NLO QCD [85–88].

For the four-fermion final states the total cross section is scaled by the branching fraction $\mathcal{B}(H \rightarrow 4\ell)$ calculated with the PROPHECY4F program [89, 90]. The calculations include NLO QCD and EW corrections, and all interference effects up to NLO [25, 26, 89–94]. For all the other final states HDECAY [91, 92] is used, which includes NLO QCD and NLO EW corrections. The predicted signal cross sections at 8 TeV and branching fraction for a low-mass Higgs boson are shown in the left and right plots of Fig. 2, respectively [25, 26].

The uncertainty in the signal cross section related to the choice of PDFs is determined with the PDF4LHC prescription [95–99]. The uncertainty due to the higher-order terms is calculated by varying the renormalization and factorization scales in each process, as explained in Ref. [25].

For the dominant gluon-gluon fusion process, the transverse momentum spectrum of the Higgs boson in the 7 TeV MC simulation samples is reweighted to match the NNLL + NLO distribution computed with HqT [100, 101] (and FEHIPRO [102, 103] for the high- p_T range in the $\tau\tau$ analysis), except in the $H \rightarrow ZZ$ analysis, where the reweighting is not necessary. At 8 TeV, POWHEG was tuned to reach a good agreement of the p_T spectrum with the NNLL + NLO prediction in order to make reweighting unnecessary [26].

4.3 Background simulation

The background contribution from ZZ production via $q\bar{q}$ is generated at NLO with POWHEG, while other diboson processes (WW, WZ) are generated with MADGRAPH [104, 105] with cross sections rescaled to NLO predictions. The PYTHIA generator is also used to simulate all diboson

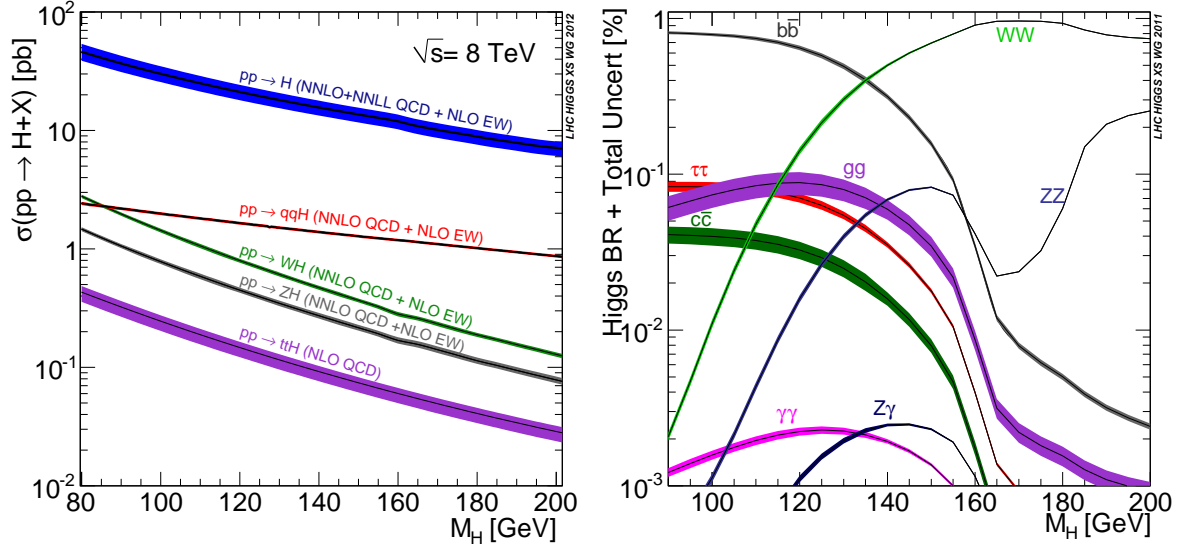


Figure 2: Higgs boson production cross sections at $\sqrt{s} = 8$ TeV (left) and branching fractions (right) as a function of the Higgs boson mass from Refs. [25, 26]. The width of the lines represents the total theoretical uncertainty in the cross section and in the branching fractions.

processes. The $gg \rightarrow VV$ contributions are generated with GG2VV [106]. The V +jets and $V\gamma$ samples are generated with MADGRAPH, as are contributions to inclusive Z and W production, with cross sections rescaled to NNLO predictions. Single-top-quark and $t\bar{t}$ events are generated at NLO with POWHEG. The PYTHIA generator takes into account the initial-state and final-state radiation effects that can lead to the presence of additional hard photons in an event. The MADGRAPH generator is also used to generate samples of $t\bar{t}$ events. QCD events are generated with PYTHIA. Table 2 summarizes the generators used for the different analyses.

4.4 Search sensitivities

The search sensitivities of the different channels, for the recorded luminosity used in the analyses, expressed in terms of the median expected 95% CL upper limit on the ratio of the measured signal cross section, σ , and the predicted SM Higgs boson cross section, σ_{SM} , are shown in Fig. 3 (left) as a function of the Higgs boson mass. A channel showing values below unity (dashed horizontal line) for a given mass hypothesis would be expected, in the absence of a Higgs boson signal, to exclude the standard model Higgs boson at 95% CL or more at that mass. Figure 3 (right) shows the expected sensitivities for the observation of the Higgs boson in terms of local p -values and significances as a function of the Higgs boson mass. The local p -value is defined as the probability of a background fluctuation; it measures the consistency of the data with the background-only hypothesis.

The overall statistical methodology used in this paper was developed by the ATLAS and CMS Collaborations in the context of the LHC Higgs Combination Group [107]. A summary of our usage of this methodology in the search for the Higgs boson is given in Section 10.

5 $H \rightarrow \gamma\gamma$

In the $H \rightarrow \gamma\gamma$ analysis, a search is made for a narrow peak, of width determined by the experimental resolution of $\sim 1\%$, in the diphoton invariant-mass distribution for the range 110–150 GeV, on top of a large irreducible background from the production of two photons originat-

Table 2: Summary of the generators used for the simulation of the main backgrounds for the analyses presented in this paper.

Analysis	Physics Process	Generator used
$H \rightarrow \gamma\gamma$	QCD	PYTHIA
	Z+jet	MADGRAPH
$H \rightarrow ZZ$	$qq \rightarrow 4\ell$	POWHEG
	$gg \rightarrow 4\ell$	GG2ZZ
	Z+jet	MADGRAPH
	$Z + \gamma$	MADGRAPH
	$t\bar{t}$	POWHEG
	$qq \rightarrow WW, WZ$	MADGRAPH
$H \rightarrow WW$	$qq \rightarrow WW$	MADGRAPH
	$gg \rightarrow WW$	GG2WW
	V+jet	MADGRAPH
	$t\bar{t}$	POWHEG
	tW	POWHEG
	QCD	PYTHIA
$H \rightarrow \tau\tau$	Z+jet	MADGRAPH
	$t\bar{t}$	MADGRAPH
	$qq \rightarrow ZZ, ZW, WW$	PYTHIA
	QCD	PYTHIA
$H \rightarrow bb$	$qq \rightarrow ZZ, ZW, WW$	PYTHIA
	Z+jet	MADGRAPH
	W+jet	MADGRAPH
	$t\bar{t}$	MADGRAPH
	tW	POWHEG
	QCD	PYTHIA

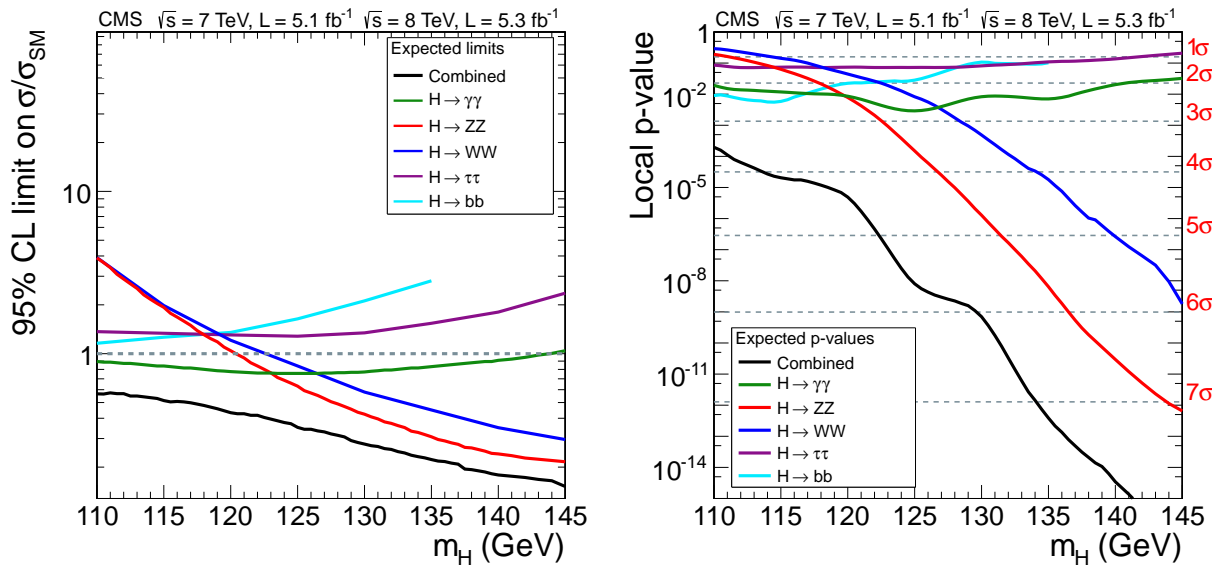


Figure 3: The median expected 95% CL upper limits on the cross section ratio $\sigma/\sigma_{\text{SM}}$ in the absence of a Higgs boson (left) and the median expected local p -value for observing an excess, assuming that a Higgs boson with that mass exists (right), as a function of the Higgs boson mass for the five Higgs boson decay channels and their combination.

ing directly from the hard-scattering process. In addition, there is a sizable amount of reducible background in which one or both of the reconstructed photons originate from the misidentification of particles in jets that deposit substantial energy in the ECAL, typically photons from the decay of π^0 or η mesons. Early studies indicated this to be one of the most promising channels in the search for a SM Higgs boson in the low-mass range [108].

To enhance the sensitivity of the analysis, candidate diphoton events are separated into mutually exclusive classes with different expected signal-to-background ratios, based on the properties of the reconstructed photons and the presence or absence of two jets satisfying criteria aimed at selecting events in which a Higgs boson is produced through the VBF process. The analysis uses multivariate techniques for the selection and classification of the events. As independent cross-checks, two additional analyses are performed. The first is almost identical to the CMS analysis described in Ref. [109], but uses simpler criteria based on the properties of the reconstructed photons to select and classify events. The second analysis incorporates the same multivariate techniques described here, however, it relies on a completely independent modelling of the background. These two analyses are described in more detail in Section 5.6.

5.1 Diphoton trigger

All the data under consideration have passed at least one of a set of diphoton triggers, each using transverse energy thresholds and a set of additional photon selections, including criteria on the isolation and the shapes of the reconstructed energy clusters. The transverse energy thresholds were chosen to be at least 10% lower than the envisaged final-selection thresholds. This set of triggers enabled events passing the later offline $H \rightarrow \gamma\gamma$ selection criteria to be collected with a trigger efficiency greater than 99.5%.

5.2 Interaction vertex location

In order to construct a photon four-momentum from the measured ECAL energies and the impact position determined during the supercluster reconstruction, the photon production vertex, i.e. the origin of the photon trajectory, must be determined. Without incorporating any additional information, any of the reconstructed pp event vertices is potentially the origin of the photon. If the distance in the longitudinal direction between the assigned and the true interaction point is larger than 10 mm, the resulting contribution to the diphoton mass resolution becomes comparable to the contribution from the ECAL energy resolution. It is, therefore, desirable to use additional information to assign the correct interaction vertex for the photon with high probability. This can be achieved by using the kinematic properties of the tracks associated with the vertices and exploiting their correlation with the diphoton kinematic properties, including the transverse momentum of the diphoton ($p_T^{\gamma\gamma}$). In addition, if either of the photons converts into an e^+e^- pair and the tracks from the conversion are reconstructed and identified, the direction of the converted photon, determined by combining the conversion vertex position and the position of the ECAL supercluster, can be extrapolated to identify the diphoton interaction vertex.

For each reconstructed interaction vertex the following set of variables are calculated: the sum of the squared transverse momenta of all tracks associated with the vertex and two variables that quantify the p_T balance with respect to the diphoton system. In the case of a reconstructed photon conversion, an additional ‘‘pull’’ variable is used, defined as the distance between the vertex z position and the beam-line extrapolated z position coming from the conversion reconstruction, divided by the uncertainty in this extrapolated z position. These variables are used as input to a BDT algorithm trained on simulated Higgs signal events and the interaction point ranking highest in the constructed classifier is chosen as the origin of the photons.

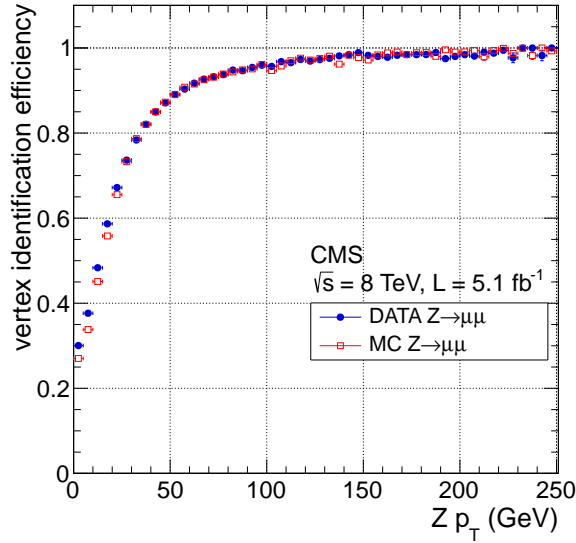


Figure 4: Comparison of the vertex-identification efficiency between data (circles) and MC simulated $Z \rightarrow \mu\mu$ events (squares), as a function of the Z boson p_T .

The vertex-finding efficiency, defined as the efficiency to locate the vertex to within 10 mm of its true position, is studied using $Z \rightarrow \mu\mu$ events where the muon tracks were removed from the tracks considered, and the muon momenta were replaced by the photon momenta. The result is shown in Fig. 4. The overall efficiency in signal events with a Higgs boson mass of 120 GeV, integrated over its p_T spectrum, is $(83.0 \pm 0.4)\%$ in the 7 TeV data set, and $(79.0 \pm 0.2)\%$ in the 8 TeV data set. The statistical uncertainties in these numbers are propagated to the uncertainties in the final result.

A second vertex related multivariate discriminant is employed to estimate, event-by-event, the probability for the vertex assignment to be within 10 mm of the diphoton interaction point. This BDT is trained using simulated $H \rightarrow \gamma\gamma$ events. The input variables are the classifier values of the vertex BDT described above for the three vertices with the highest score BDT values, the number of vertices, the diphoton transverse momentum, the distances between the chosen vertex and the second and third choices, and the number of photons with an associated conversion track. These variables allow for a reliable quantification of the probability that the selected vertex is close to the diphoton interaction point.

The resulting vertex-assignment probability from simulated events is used when constructing the Higgs boson signal models. The signal modelling is described in Section 5.5.

5.3 Photon selection

The event selection requires two photon candidates with transverse momenta satisfying $p_T^\gamma(1) > m_{\gamma\gamma}/3$ and $p_T^\gamma(2) > m_{\gamma\gamma}/4$, where $m_{\gamma\gamma}$ is the diphoton invariant mass, within the ECAL fiducial region $|\eta| < 2.5$, and excluding the barrel-endcap transition region $1.44 < |\eta| < 1.57$. The fiducial region requirement is applied to the supercluster position in the ECAL and the p_T threshold is applied after the vertex assignment. The requirements on the mass-scaled transverse momenta are mainly motivated by the fact that by dividing the transverse momenta by the diphoton mass, turn-on effects on the background-shape in the low mass region are strongly reduced. In the rare cases where the event contains more than two photons passing all the selection requirements, the pair with the highest summed (scalar) p_T is chosen.

The relevant backgrounds in the $H \rightarrow \gamma\gamma$ channel consist of the irreducible background from prompt diphoton production, i.e. processes in which both photons originate directly from the hard-scattering process, and the reducible backgrounds from $\gamma + \text{jet}$ and dijet events, where the objects misidentified as photons correspond to particles in jets that deposit substantial energy in the ECAL, typically photons from the decay of isolated π^0 or η mesons. These misidentified objects are referred to as *fake* or *nonprompt* photons.

In order to optimize the photon identification to exclude such nonprompt photons, a BDT classifier is trained using simulated $pp \rightarrow \gamma + \text{jet}$ event samples, where prompt photons are used as the signal and nonprompt photons as the background. The variables used in the training are divided into two groups. The first contains information on the detailed electromagnetic shower topology, the second has variables describing the photon isolation, i.e. kinematic information on the particles in the geometric neighbourhood of the photon. Examples of variables in the first group are the energy-weighted shower width of the cluster of ECAL crystals assigned to the photon and the ratio of the energy of the most energetic 3×3 crystal cluster to the total cluster energy. The isolation variables include the magnitude of the sum of the transverse momenta of all other reconstructed particles inside a cone of size $\Delta R = 0.3$ around the candidate photon direction. In addition, the geometric position of the ECAL crystal cluster, as well as the event energy density ρ , are used. The photon ID classifier is based on the measured properties of a single photon and makes no use of the any properties that are specific to the production mechanism. Any small residual dependence on the production mechanism, e.g. through the isolation distribution, arises from the different event environments in Higgs decays and in photon plus jets events.

Instead of having a requirement on the trained multivariate classifier value to select photons with a high probability of being prompt photons, the classifier value itself is used as input to subsequent steps of the analysis. To reduce the number of events, a loose requirement is imposed on the classifier value (> -0.2) for candidate photons to be considered further. This requirement retains more than 99% of signal photons. The efficiency of this requirement, as well as the differential shape of the classifier variable for prompt photons, have been studied by comparing $Z \rightarrow ee$ data to simulated events, given the similar response of the detector to photon and electrons. The comparisons between the differential shape in data and MC simulation for the 8 TeV analysis are shown in Fig. 5, for electrons in the barrel (left) and endcap (right) regions.

5.4 Event classification

The strategy of the analysis is to look for a narrow peak over the continuum in the diphoton invariant-mass spectrum. To increase the sensitivity of the search, events are categorized according to their expected diphoton mass resolution and signal-to-background ratio. Categories with good resolution and a large signal-to-background ratio dominate the sensitivity of the search. To accomplish this, an event classifier variable is constructed based on multi-variate techniques, that assigns a high classifier value to events with signal-like kinematic characteristics and good diphoton mass resolution, as well as prompt-photon-like values for the photon identification classifier. However, the classifier should not be sensitive to the value of the diphoton invariant mass, in order to avoid biasing the mass distribution that is used to extract a possible signal. To achieve this, the input variables to the classifier are made dimensionless. Those that have units of energy (transverse momenta and resolutions) are divided by the diphoton invariant-mass value. The variables used to train this diphoton event classifier are the scaled photon transverse momenta ($p_{\text{T}}^{\gamma}(1)/m_{\gamma\gamma}$ and $p_{\text{T}}^{\gamma}(2)/m_{\gamma\gamma}$), the photon pseudo-rapidities ($\eta(1)$ and $\eta(2)$), the cosine of the angle between the two photons in the transverse

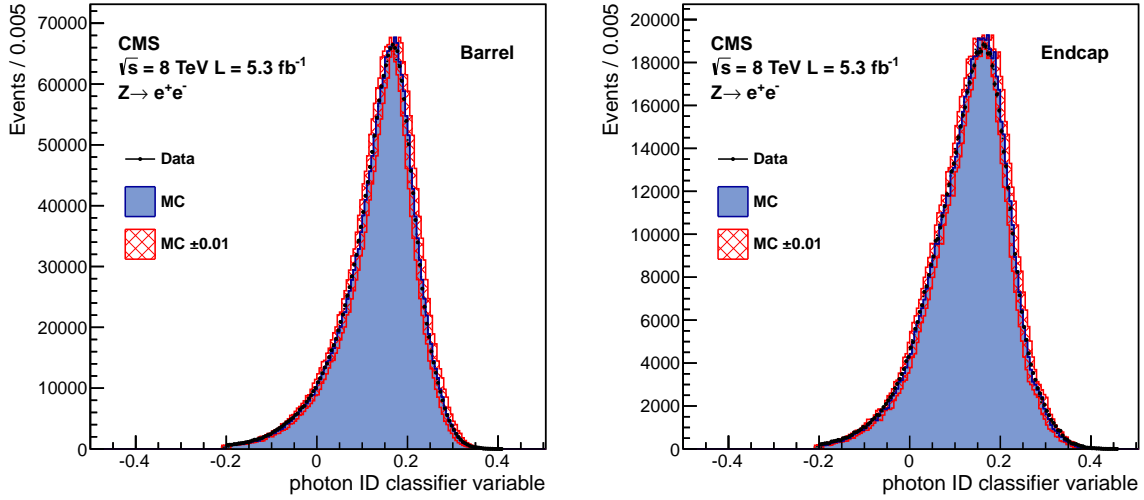


Figure 5: Comparison of the photon identification (ID) classifier variable distribution between 8 TeV data (points) and MC simulated events (histogram), separated into barrel (left) and end-cap (right) electrons originating from $Z \rightarrow ee$ events. The uncertainties in the distributions from simulation are shown by the cross-hatched histogram.

plane ($\cos(\phi(1) - \phi(2))$), the expected relative diphoton invariant-mass resolutions under the hypotheses of selecting a correct/incorrect interaction vertex ($\sigma_m^{\text{correct}(\text{incorrect})}/m_{\gamma\gamma}$), the probability of selecting a correct vertex (p_{vtx}), and the photon identification classifier values for both photons. The $\sigma_m^{\text{correct}(\text{incorrect})}/m_{\gamma\gamma}$ is computed using the single photon resolution estimated by the dedicated BDT described in Section 3. A vertex is being labeled as correct if the distance from the true interaction point is smaller than 10 mm.

To ensure the classifier assigns a high value to events with good mass resolution, the events are weighted by a factor inversely proportional to the mass resolution,

$$w_{\text{sig}} = \frac{p_{\text{vtx}}}{\sigma_m^{\text{correct}}/m_{\gamma\gamma}} + \frac{1 - p_{\text{vtx}}}{\sigma_m^{\text{incorrect}}/m_{\gamma\gamma}}. \quad (2)$$

This factor incorporates the resolutions under both correct- and incorrect-interaction-vertex hypotheses, properly weighted by the probabilities of having assigned the vertex correctly. The training is performed on simulated background and Higgs boson signal events. The training procedure makes full use of the signal kinematic properties that are assumed to be those of the SM Higgs boson. The classifier, though still valid, would not be fully optimal for a particle produced with significantly different kinematic properties.

The uncertainties in the diphoton event classifier output come from potential mismodelling of the input variables. The dominant sources are the uncertainties in the shapes of the photon identification (ID) classifier and the individual photon energy resolutions, which are used to compute the relative diphoton invariant-mass resolutions.

The first of these amounts to a potential shift in the photon ID classifier value of at most ± 0.01 in the 8 TeV and ± 0.025 in the 7 TeV analysis. These values are set looking to the observed differences between the photon ID classifier value distributions from data and simulation. This comparison for the 7 TeV analysis is shown in Fig. 6, where the distribution for the leading (highest

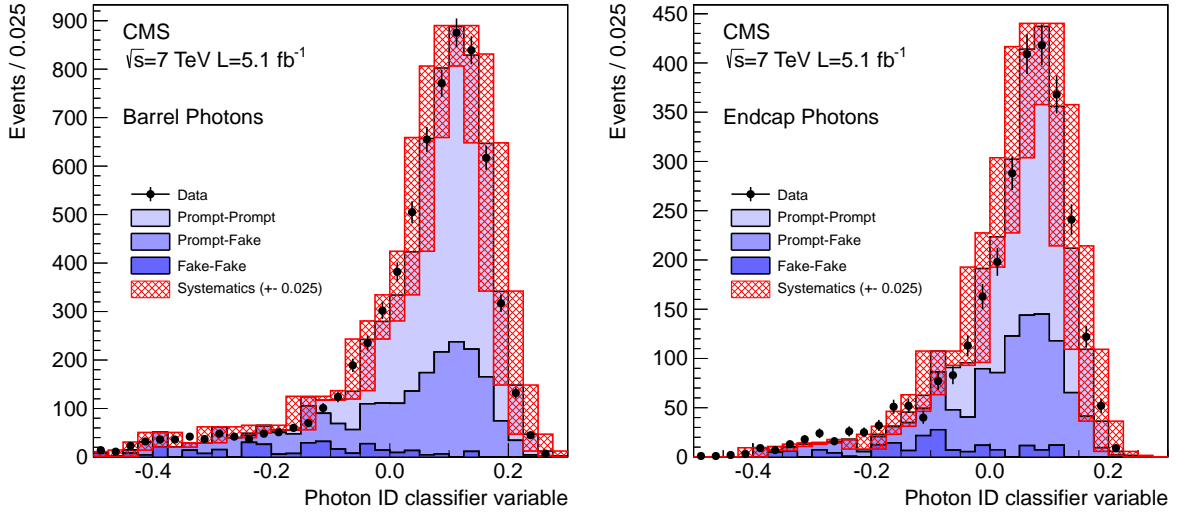


Figure 6: Distribution of the photon ID classifier value for the larger transverse momentum photon in the ECAL barrel (left) and endcaps (right) from candidate diphoton data events (points) with $m_{\gamma\gamma} > 160$ GeV. The predicted distributions for the various diphoton backgrounds as determined from simulation are shown by the histograms. The variations of the classifier value due to the systematic uncertainties are shown by the cross-hatched histogram.

p_T) candidate photons in the ECAL barrel (left) and endcaps (right) are compared between data and MC simulation for $m_{\gamma\gamma} > 160$ GeV, where most photons are prompt ones. In addition to the three background components described in Section 5.3 (prompt-prompt, prompt-nonprompt, and nonprompt-nonprompt), the additional component composed by Drell–Yan events, in which both final-state electrons are misidentified as photons, has been studied and found to be negligible. As discussed previously a variation of the classifier value by ± 0.025 , represented by the cross-hatched histogram, covers the differences.

For the second important variable, the photon energy resolution estimate (calculated by a BDT, as discussed in Section 3), a similar comparison is shown in Fig. 7. Again, the 7 TeV data distributions for candidate photons in the ECAL barrel (left) and endcap (right) are compared to MC simulation for $m_{\gamma\gamma} > 160$ GeV. The systematic uncertainty of $\pm 10\%$ is again shown as the cross-hatched histogram.

The effect of both these uncertainties propagated to the diphoton event classifier distribution can be seen in Fig. 8, where the 7 TeV data diphoton classifier variable is compared to the MC simulation predictions. The data and MC simulation distributions in both the left and right plots of Fig. 8 are the same. In the left plot, the uncertainty band arises from propagating the photon ID classifier uncertainty, while in the right plot, it is from propagating the energy resolution uncertainty. From these plots one can see that the uncertainty in the photon ID classifier dominates the overall uncertainty, and by itself almost covers the full difference between the data and MC simulation distributions. Both uncertainties are propagated into the final result.

The diphoton event classifier output is then used to divide events into different classes, prior to fitting the diphoton invariant-mass spectrum. The procedure successively splits events into classes by introducing a boundary value for the diphoton classifier output. The first boundary results in two classes, and then these classes are further split. Each split is introduced using the boundary value that gives rise to the best expected exclusion limit. The procedure is termi-

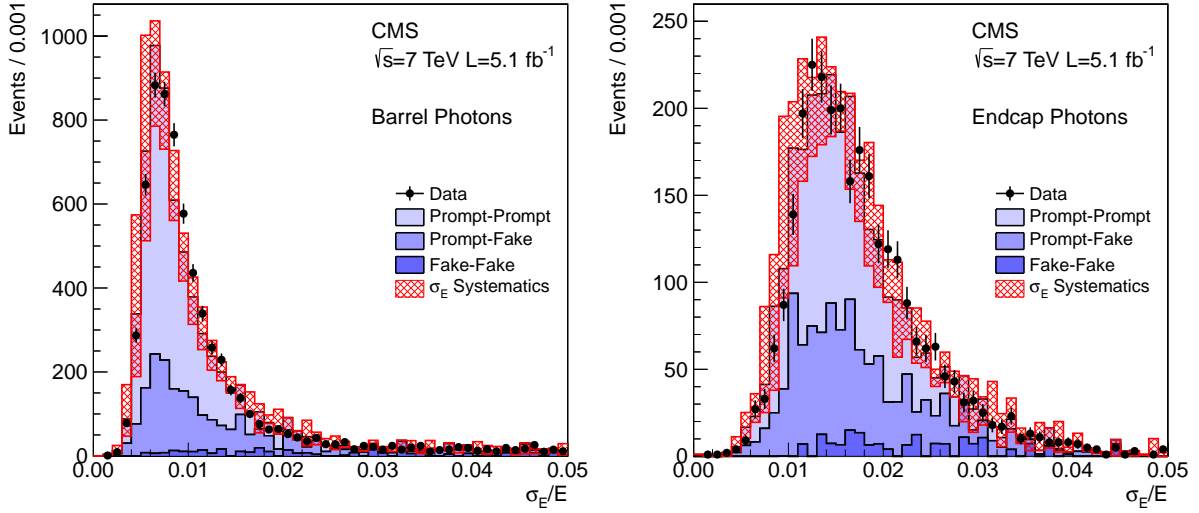


Figure 7: Distribution of the photon resolution estimate σ_E/E for the leading photon in the ECAL barrel (left) and endcaps (right) from candidate diphoton data events (points) with $m_{\gamma\gamma} > 160$ GeV. The predicted distributions for the various diphoton backgrounds, as determined from simulation, are shown by the histograms. The variations of the resolution due to the systematic uncertainties are shown by the cross-hatched histogram.

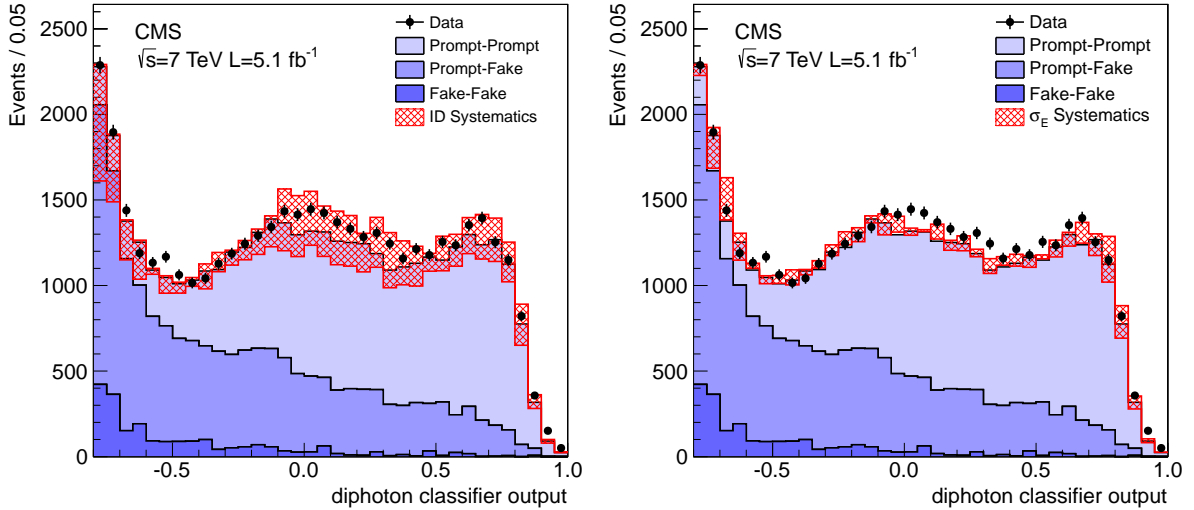


Figure 8: The effect of the systematic uncertainty assigned to the photon identification classifier output (left) and the photon resolution estimate (right) on the diphoton BDT output for background MC simulation ($100 \text{ GeV} < m_{\gamma\gamma} < 180 \text{ GeV}$) and for data. The nominal BDT output is shown as a stacked histogram and the variation due to the uncertainty is shown as a cross-hatched band. These plots show only the systematic uncertainties that are common to both signal and background. There are additional significant uncertainties that are not shown here.

nated once additional splitting results in a negligible ($<1\%$) gain in sensitivity. Additionally, the lowest score class is dropped since it does not contribute significantly to the sensitivity. This procedure results in four event classes for both the 7 and 8 TeV data sets. The systematic uncertainties in the diphoton identification classifier and photon energy resolution discussed above can cause events to migrate between classes. In the 8 TeV analysis, these class migrations are up to 4.3% and 8.1%, respectively. They are defined as the relative change of expected signal yield in each category under the variation of the photon ID BDT classifier and the per-photon energy resolution estimate, within their uncertainties as explained above.

The sensitivity of the analysis is enhanced by using the special kinematics of Higgs bosons produced by the VBF process [110]. Dedicated classes of events are selected using dijet-tagging criteria. The 7 TeV data set has one class of dijet-tagged events, while the 8 TeV data set has two.

In the 7 TeV analysis, dijet-tagged events are required to contain two jets with transverse energies exceeding 20 and 30 GeV, respectively. The dijet invariant mass is required to be greater than 350 GeV, and the absolute value of the difference of the pseudorapidities of the two jets has to be larger than 3.5. In the 8 TeV analysis, dijet-tagged events are required to contain two jets and are categorized as “Dijet tight” or “Dijet loose”. The jets in Dijet tight events must have transverse energies above 30 GeV and a dijet invariant mass greater than 500 GeV. For the jets in the Dijet loose events, the leading (subleading) jet transverse energy must exceed 30 (20) GeV and the dijet invariant mass be greater than 250 GeV, where leading and subleading refer to the jets with the highest and next-to-highest transverse momentum, respectively. The pseudorapidity separation between the two jets is also required to be greater than 3.0. Additionally, in both analyses the difference between the average pseudorapidity of the two jets and the pseudorapidity of the diphoton system must be less than 2.5 [111], and the difference in azimuthal angle between the diphoton system and the dijet system is required to be greater than 2.6 radians. To further reduce the background in the dijet classes, the p_T threshold on the leading photon is increased to $p_T^\gamma(1) > m_{\gamma\gamma}/2$.

Systematic uncertainties in the efficiency of dijet tagging for signal events arise from the uncertainty in the MC simulation modelling of the jet energy corrections and resolution, and from uncertainties in simulating the number of jets and their kinematic properties. These uncertainties are estimated by using different underlying-event tunes, PDFs, and renormalization and factorization scales as suggested in Refs. [25, 26]. A total systematic uncertainty of 10% is assigned to the efficiency for VBF signal events to pass the dijet-tag criteria, and an uncertainty of 50%, dominated by the uncertainty in the underlying-event tune, to the efficiency for signal events produced by gluon-gluon fusion.

Table 3 shows the predicted number of signal events for a SM Higgs boson with $m_H = 125$ GeV, as well as the estimated number of background events per GeV of invariant mass at $m_{\gamma\gamma} = 125$ GeV, for each of the eleven event classes in the 7 and 8 TeV data sets. The table also gives the fraction of each Higgs boson production process in each class (as predicted by MC simulation) and the mass resolution, represented both as σ_{eff} , half the width of the narrowest interval containing 68.3% of the distribution, and as the full-width-at-half-maximum (FWHM) of the invariant-mass distribution divided by 2.35.

5.5 Signal and background modelling

The modelling of the Higgs boson signal used in the estimation of the sensitivity has two aspects. First, the normalization, i.e. the expected number of signal events for each of the considered Higgs boson production processes; second, the diphoton invariant-mass shape. To model both aspects, including their respective uncertainties, the MC simulation events and theoretical

Table 3: Expected number of SM Higgs boson events ($m_H = 125$ GeV) and estimated background (at $m_{\gamma\gamma} = 125$ GeV) for the event classes in the 7 (5.1 fb^{-1}) and 8 TeV (5.3 fb^{-1}) data sets. The composition of the SM Higgs boson signal in terms of the production processes and its mass resolution are also given.

Event classes		SM Higgs boson expected signal ($m_H = 125$ GeV)						Background	
		Events	ggH	VBF	VH	ttH	σ_{eff} (GeV)	FWHM/2.35 (GeV)	$m_{\gamma\gamma} = 125$ GeV (events/GeV)
7 TeV	BDT 0	3.2	61%	17%	19%	3%	1.21	1.14	3.3 ± 0.4
	BDT 1	16.3	88%	6%	6%	–	1.26	1.08	37.5 ± 1.3
	BDT 2	21.5	92%	4%	4%	–	1.59	1.32	74.8 ± 1.9
	BDT 3	32.8	92%	4%	4%	–	2.47	2.07	193.6 ± 3.0
	Dijet tag	2.9	27%	72%	1%	–	1.73	1.37	1.7 ± 0.2
8 TeV	BDT 0	6.1	68%	12%	16%	4%	1.38	1.23	7.4 ± 0.6
	BDT 1	21.0	87%	6%	6%	1%	1.53	1.31	54.7 ± 1.5
	BDT 2	30.2	92%	4%	4%	–	1.94	1.55	115.2 ± 2.3
	BDT 3	40.0	92%	4%	4%	–	2.86	2.35	256.5 ± 3.4
	Dijet tight	2.6	23%	77%	–	–	2.06	1.57	1.3 ± 0.2
	Dijet loose	3.0	53%	45%	2%	–	1.95	1.48	3.7 ± 0.4

considerations described in Section 4 are used. To account for the interference between the signal and background diphoton final states [112], the expected gluon-gluon fusion process cross section is reduced by 2.5% for all values of m_H .

Additional systematic uncertainties in the normalization of each event class arise from potential class-to-class migration of signal events caused by uncertainties in the diphoton event classifier value. The instrumental uncertainties in the classifier value and their effect have been discussed previously. The theoretical ones, arising from the uncertainty in the theoretical predictions for the photon kinematics, are estimated by measuring the amount of class migration under variation of the renormalization and factorization scales within the range $m_H/2 < \mu < 2m_H$, (class migrations up to 12.5%) and the PDFs (class migrations up to 1.3%). These uncertainties are propagated to the final statistical analysis.

To model the diphoton invariant-mass spectrum properly, it is essential that the simulated diphoton mass and scale are accurately predicted. This is done by comparing the dielectron invariant-mass distribution in $Z \rightarrow ee$ events between data and MC simulation, where the electrons have been reconstructed as photons. This comparison is shown for the 8 TeV data in Fig. 9, where the points represent data, and the histogram MC simulation. Before correction, the dielectron invariant-mass distribution from simulation is narrower than the one from data, caused by an inadequate modelling of the photon energy resolution in the simulation. To correct this effect, the photon energies in the Higgs boson signal MC simulation events are smeared and the data events scaled, so that the dielectron invariant-mass scale and resolution as measured in $Z \rightarrow ee$ events agree between data and MC simulation. These scaling and smearing factors are determined in a total of eight photon categories, i.e. separately for photons in four pseudorapidity regions ($|\eta| < 1$, $1 \leq |\eta| < 1.5$, $1.5 \leq |\eta| < 2$, and $|\eta| \geq 2$), and separately for high $R9$ (>0.94) and low $R9$ (≤ 0.94) photons, where $R9$ is the ratio of the energy of the most energetic 3×3 crystal cluster and the total cluster energy.

Additionally, the factors are computed separately for different running periods in order to account for changes in the running conditions, for example the change in the average beam in-

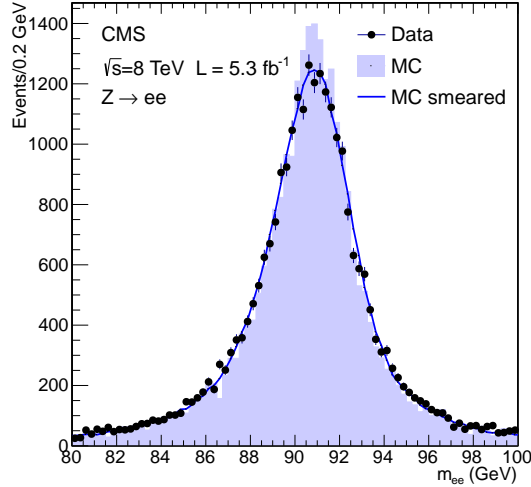


Figure 9: Comparison of the dielectron invariant-mass spectrum from $Z \rightarrow ee$ events between 8 TeV data (points) and the simulated events (histogram), where the selected electrons are reconstructed as photons. The simulated distribution after applying smearing and scaling corrections of the electron energies is shown by the solid line.

tensity. These modifications reconcile the discrepancy between data and simulation, as seen in the comparison of the dots and solid curve of Fig. 9. The uncertainties in the scaling and smearing factors, which range from 0.2% to 0.9% depending on the photon properties, are taken as systematic uncertainties in the signal evaluation and mass measurement.

The final signal model is then constructed separately for each event class and each of the four production processes as the weighted sum of two submodels that assume either the correct or incorrect primary vertex selection (as described in Section 5.2). The two submodels are weighted by the corresponding probability of picking the right (p_{vtx}) or wrong ($1 - p_{\text{vtx}}$) vertex. The uncertainty in the parameter p_{vtx} is taken as a systematic uncertainty.

To describe the signal invariant-mass shape in each submodel, two different approaches are used. In the first, referred to as the parametric model, the MC simulated diphoton invariant-mass distribution is fitted to a sum of Gaussian distributions. The number of Gaussian functions ranges from one to three depending on the event class, and whether the model is a correct- or incorrect-vertex hypothesis. The systematic uncertainties in the signal shape are estimated from the variations in the parameters of the Gaussian functions. In the second approach, referred to as the binned model, the signal mass shape for each event class is taken directly from the binned histogram of the corresponding simulated Higgs boson events. The systematic uncertainties are included by parametrizing the change in each bin of the histogram as a linear function under variation of the corresponding nuisance parameter, i.e. the variable that parametrizes this uncertainty in the statistical interpretation of the data. The two approaches yield consistent final results and serve as an additional verification of the signal modelling. The presented results are derived using the parametric-model approach.

The parametric signal models for a Higgs boson mass of 120 GeV in two of the 8 TeV BDT event classes are shown in Fig. 10. The signal models are summed over the four production processes, each weighted by their respective expected yield as computed from MC simulation. The two plots in Fig. 10 illustrate how the diphoton invariant-mass resolution improves with increasing diphoton classifier value. The left distribution is for classifier values greater than 0.88 and has

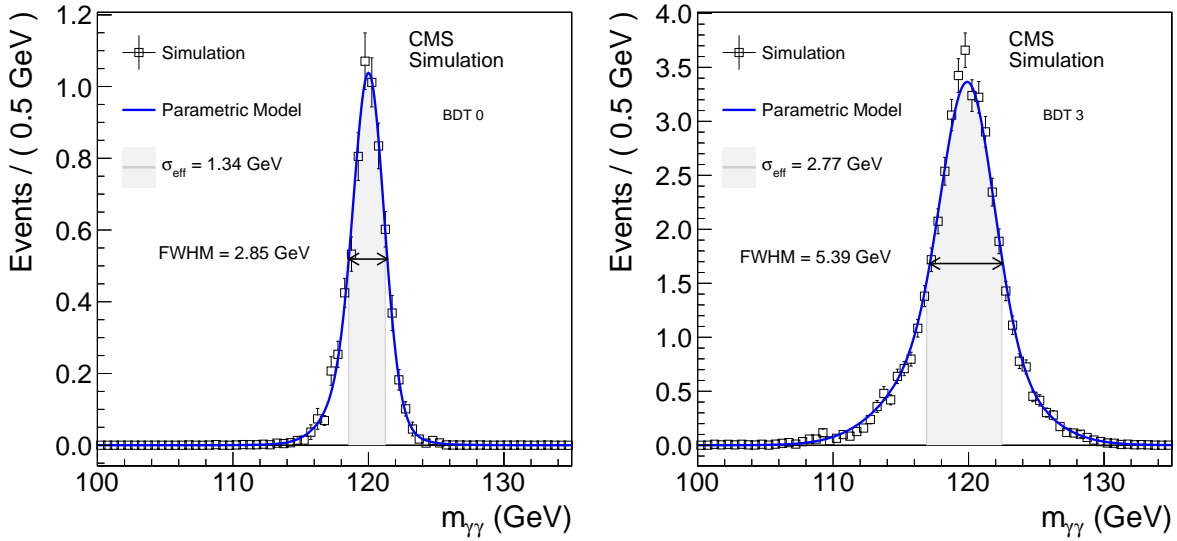


Figure 10: Comparison of the diphoton invariant-mass distribution from the parametric signal model (blue line) and simulated MC events (open squares) for a Higgs mass hypothesis of $m_H = 120$ GeV for two (BDT 0 on the left, BDT 3 on the right) of the four 8 TeV BDT event classes.

a mass resolution $\sigma_{\text{eff}} = 1.34$ GeV, while the right distribution is for classifier values between -0.05 and 0.50 and has $\sigma_{\text{eff}} = 2.77$ GeV. This is the intended behaviour of the event class implementation.

The uncertainties in the weighting factors for each of the production processes arise from variations in the renormalization and factorization scales, and uncertainties in the PDFs. They range from several percent for associated production with W/Z to almost 20% for the gluon-gluon fusion process. The detailed values for the 8 TeV analysis, together with all the other systematic uncertainties discussed above, are summarized in Table 4. The corresponding uncertainties in the 7 TeV analysis are very similar, with the exception of the already mentioned uncertainty on the photon ID classifier, which was significantly larger in the 7 TeV analysis. The reason for this is a worse agreement between data and MC simulation.

In addition to the per-photon energy scale uncertainties, that are derived in the eight $\eta - R9$ categories, additional fully correlated energy scale uncertainties are assigned in order to account for possible non-linearity as a function of energy and for additional electron-photon differences. The uncertainty associated with possible non-linearities in the energy measurement as a function of the cluster energy are evaluated by measuring the energy scale of $Z \rightarrow ee$ events as a function of the scalar sum of transverse momentum of the two electrons. The change in energy scale due to possible non-linearities in the energy measurement is estimated around 0.2%; since this correction is not applied, a systematic uncertainty of 0.4% is assigned. An additional fully correlated uncertainty related to difference of 0.25% between electron and photon is assigned, amounting to half of the absolute energy scale difference between electrons and photons for non-showering electrons/photons in the barrel. Adding these two numbers in quadrature results in the additional energy scale uncertainty of 0.47%, that is treated as fully correlated among all event classes.

The modelling of the background relies entirely on the data. The observed diphoton invariant-mass distributions for the eleven event classes (five in the 7 and eight in the 8 TeV analysis) are

Table 4: Largest sources of systematic uncertainty in the analysis of the 8 TeV data set. Eight photon categories are defined, depending on their η and $R9$, where $R9$ is the ratio of the energy of the most energetic 3×3 crystal cluster and the total cluster energy. The four pseudorapidity regions are: $|\eta| < 1$ (low η), $1 \leq |\eta| < 1.5$ (high η) for the barrel, and $1.5 \leq |\eta| < 2$ (low η), $|\eta| \geq 2$ (high η) for the endcaps; the two $R9$ regions are: high $R9$ (> 0.94) and low $R9$ (≤ 0.94).

Sources of systematic uncertainty		Uncertainty	
Per photon		Barrel	Endcap
Photon selection efficiency		0.8%	2.2%
Energy resolution ($\Delta\sigma/E_{MC}$)	$R9 > 0.94$ (low η , high η)	0.22%, 0.60%	0.90%, 0.34%
	$R9 \leq 0.94$ (low η , high η)	0.24%, 0.59%	0.30%, 0.52%
Energy scale ($(E_{data} - E_{MC})/E_{MC}$)	$R9 > 0.94$ (low η , high η)	0.19%, 0.71%	0.88%, 0.19%
	$R9 \leq 0.94$ (low η , high η)	0.13%, 0.51%	0.18%, 0.28%
Energy scale (fully correlated)		0.47%	
Photon identification classifier		0.01	
Photon energy resolution BDT		10%	
Per event			
Integrated luminosity		4.4%	
Vertex finding efficiency		0.2%	
Trigger efficiency — One or both photons $R9 \leq 0.94$ in endcap		0.4%	
Other events		0.1%	
Dijet selection			
Dijet tagging efficiency	VBF	10%	
	Gluon-gluon fusion	50%	
Production cross sections		Scale	PDF
Gluon-gluon fusion		+12.5% -8.2%	+7.9% -7.7%
VBF		+0.5% -0.3%	+2.7% -2.1%
Associated production with W/Z		1.8%	4.2%
Associated production with $t\bar{t}$		+3.6% -9.5%	8.5%

fitted separately over the range $100 < m_{\gamma\gamma} < 180$ GeV. This has the advantage that there are no systematic uncertainties due to potential mismodelling of the background processes by the MC simulation. The procedure is to fit the diphoton invariant-mass distribution to the sum of a signal mass peak and a background distribution. Since the exact functional form of the background in each event class is not known, the parametric model has to be flexible enough to describe an entire set of potential underlying functions. Using a wrong background model can lead to biases in the measured signal strength. Such a bias can, depending on the Higgs boson mass and the event class, reach or even exceed the size of the expected signal, and therefore dramatically reduce the sensitivity of the analysis to any potential signal. In what follows, a procedure for selecting the background function is described that results in a potential bias small enough to be neglected.

If the true underlying background model could be used in the extraction of the signal strength, and no signal is present in the fitted data, the median fitted signal strength would be zero in the entire mass region of interest. The deviation of the median fitted signal strength from zero in background-only pseudo-experiments can thus be used to quantify the potential bias. These pseudodata sets are generated from a set of hypothetical truth models, with each model using a different analytical function that adequately describes the observed diphoton invariant-mass distribution. The set of truth-models contains exponential and power-law functions, as well as polynomials (Bernstein polynomials) and Laurent series of different orders. None of these functions is required to describe the actual (unknown) underlying background distribution. Instead, we argue that they span the phase-space of potential underlying models in such a way that a fit model resulting in a negligible bias against all of them would also result in a negligible bias against the (unknown) true underlying distribution.

The first step in generating such pseudodata sets consists of constructing a truth model, from which the pseudodata set is drawn. This is done by fitting the data in each of the eleven event classes separately, and for each of the four general types of background functions, resulting in four truth-models for each event class. The order of the background function required to adequately describe the data for each of the models is determined by increasing the order until an additional increase does not result in a significant improvement of the fit to the observed data. A χ^2 -goodness-of-fit is used to quantify the fit quality, and an F-test to determine the termination criterion. "Increasing the order" here means adding additional terms of higher order in the case of the polynomial and the Laurent series, and adding additional exponential or power-law terms with different parameters in the case of the exponential and power-law truth models.

Once the four truth models are determined for a given event class, $\sim 40\,000$ pseudodata sets are generated for each by randomly drawing diphoton mass values from them. The next step is then to find a function (in what follows referred to as *fit model*), that results in a negligible bias against all four sets of toy data in the entire mass region of interest, i.e. an analytical function that when used to extract the signal strength in all the 40 000 pseudodata sets, gives a mean value for the fitted strength consistent with zero.

The criterion for the bias to be negligible is that it must be five times smaller than the statistical uncertainty in the number of fitted events in a mass window corresponding to the FWHM of the corresponding signal model. With this procedure, any potential bias from the background fit function can be neglected in comparison with the statistical uncertainty from the finite data sample. We find that only the polynomial background function produces a sufficiently small bias for all four truth models. Therefore, we only use this background function to fit the data. The required order of the polynomial function needed to reach the sufficiently small bias is

determined separately for each of the 11 event classes, and ranges from 3 to 5.

The entire procedure results in a background model for each of the event classes as a polynomial function of a given, class-dependent order. The parameters of this polynomial, i.e. the coefficients for each term, are left free in the fit, and their variations are therefore the only source of uncertainty from the modelling of the background.

The simultaneous fit to the signal-plus-background models, derived as explained above, together with the $m_{\gamma\gamma}$ distributions for the data, are shown for the eleven event classes in Figs. 11 and 12 for the 7 and 8 TeV data samples, respectively. The uncertainty bands shown in the background component of the fit arise from the variation of the background fit parameters, and correspond to the uncertainties in the expected background yield. The fit is performed on the data from all event class distributions simultaneously, with an overall floating signal strength. In these fits, the mass hypothesis is scanned in steps of 0.5 GeV between 110 and 150 GeV. At the point with the highest significant excess over the background-only hypothesis ($m_H = 125$ GeV), the best fit value is $\sigma/\sigma_{\text{SM}} = 1.56 \pm 0.43$.

In order to better visualize any overall excess/significance in the data, each event is weighted by a class-dependent factor, and its corresponding diphoton invariant mass is plotted with that weight in a single distribution. The weight depends on the event class and is proportional to $S/(S+B)$, where S and B are the number of expected signal and background events in a mass window corresponding to $2\sigma_{\text{eff}}$, centered on $m_{\gamma\gamma} = 125$ GeV and calculated from the signal-plus-background fit to all data event classes simultaneously. The particular choice of the weights is motivated in Ref. [113]. The resulting distribution is shown in Fig. 13, where for reference the distribution for the unweighted sum of events is shown as an inset. The binning for the distributions is chosen to optimize the visual effect of the excess at 125 GeV, which is evident in both the weighted and unweighted distributions. It should be emphasized that this figure is for visualization purposes only, and no results are extracted from it.

5.6 Alternative analyses

In order to verify the results described above, two alternative analyses are performed. The first (referred to as the *cut-based* analysis) refrains from relying on multivariate techniques, except for the photon energy corrections described in Section 3. Instead, the photon identification is performed by an optimized set of requirements on the discriminating variables explained in Section 5.3. Additionally, instead of using a BDT event-classifier variable to separate events into classes, the event classes are built using requirements on the photons directly. Four mutually exclusive classes are constructed by splitting the events according to whether both candidate photons are reconstructed in the ECAL barrel or endcaps, and whether the $R9$ variable exceeds 0.94. This categorization is motivated by the fact that photons in the barrel with high $R9$ values are typically measured with better energy resolution than ones in the endcaps with low $R9$. Thus, the classification serves a similar purpose to the one using the BDT event classifier: events with good diphoton mass resolution are grouped together into one class. The four event classes used in this analysis are then:

- both photons are in the barrel, with $R9 > 0.94$,
- both photons are in the barrel and at least one of them with $R9 \leq 0.94$,
- at least one photon is in the endcap and both photons with $R9 > 0.94$,
- at least one photon is in the endcap and at least one of them with $R9 \leq 0.94$.

The second alternative analysis (referred to as the *sideband* analysis) uses the identical multivariate technique as the baseline analysis, as well as an identical event sample, but relies on dif-

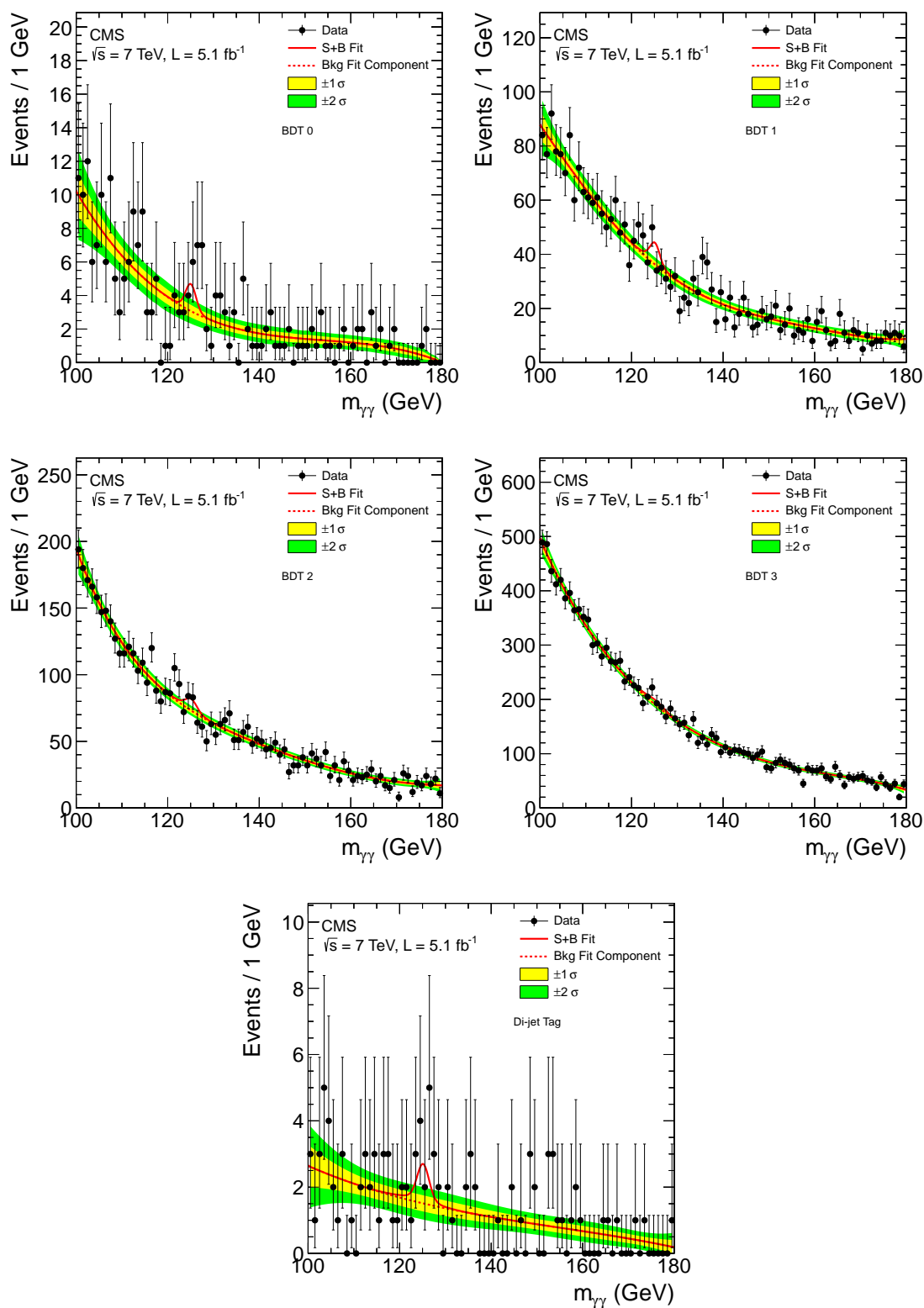


Figure 11: The diphoton invariant-mass distributions for the five classes of the 7 TeV data set (points) and the results of the signal-plus-background fits for $m_{\gamma\gamma} = 125$ GeV (lines). The background fit components are shown by the dotted lines. The light and dark bands represent the ± 1 and ± 2 standard deviation uncertainties, respectively, on the background estimate.

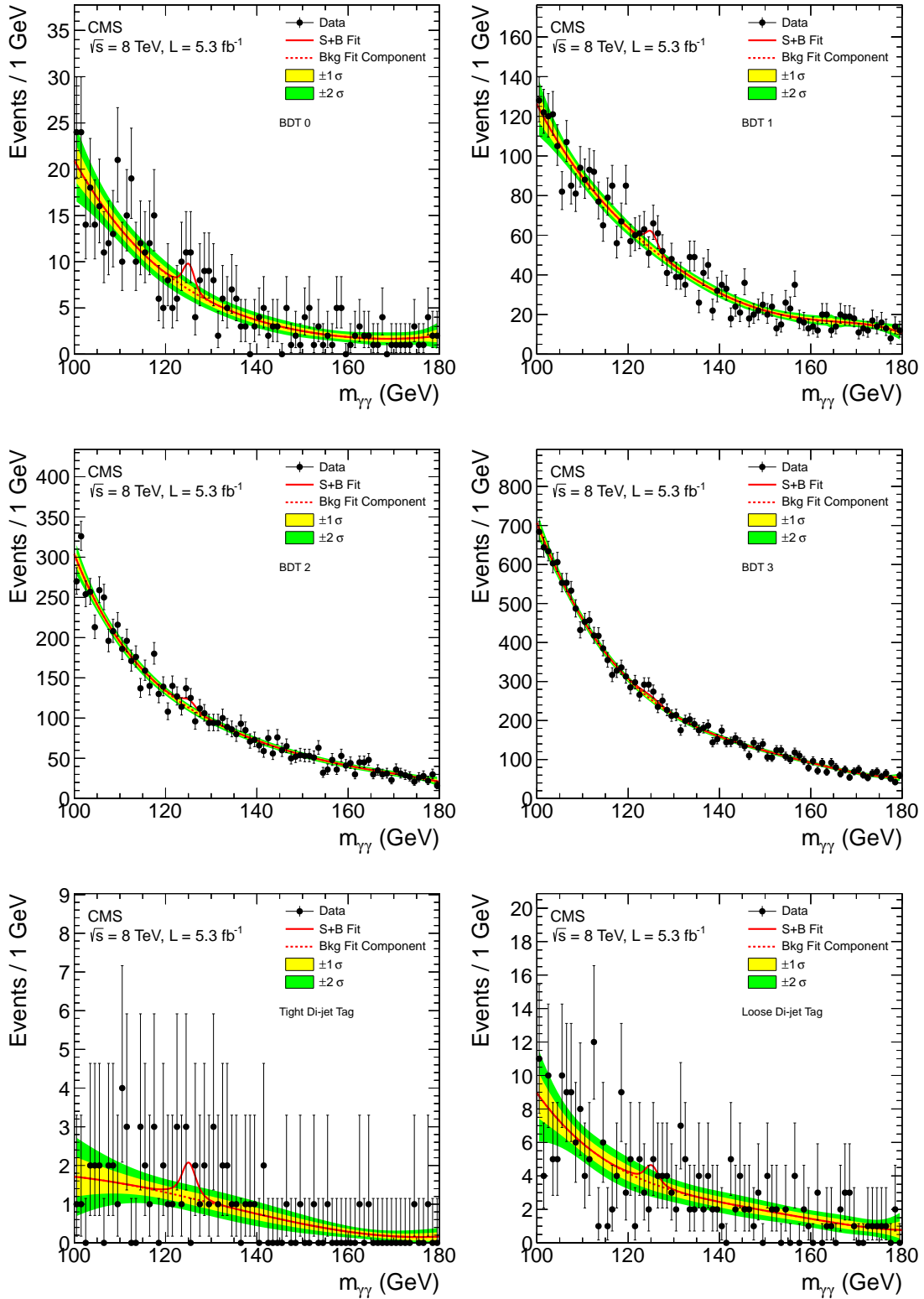


Figure 12: The diphoton invariant-mass distributions for the six classes of the 8 TeV data set (points) and the results of the signal-plus-background fits for $m_{\gamma\gamma} = 125$ GeV (lines). The background fit components are shown by the dotted lines. The light and dark bands represent the ± 1 and ± 2 standard deviation uncertainties, respectively, on the background estimate.

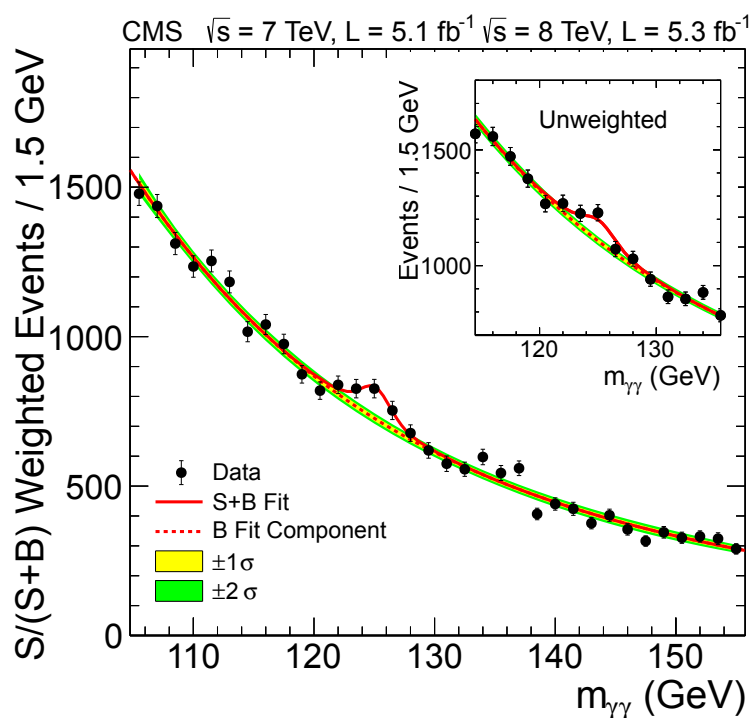


Figure 13: The diphoton invariant-mass distribution for the 7 and 8 TeV data sets (points), with each event weighted by the predicted $S/(S+B)$ ratio of its event class. The solid and dotted lines give the results of the signal-plus-background and background-only fit, respectively. The light and dark bands represent the ± 1 and ± 2 standard deviation uncertainties respectively on the background estimate. The inset shows the corresponding unweighted invariant-mass distribution around $m_{\gamma\gamma} = 125$ GeV.

ferent procedures to model the signal and background contributions. This approach uses data in the sidebands of the invariant mass distribution to model the background. Consequently, this analysis is much less sensitive to the parametric form used to describe the diphoton mass spectrum and allows the explicit inclusion of a systematic uncertainty for the possible bias in the background mass fit. For any given mass hypothesis m_H , a signal region is defined to be in the range $\pm 2\%$ on either side of m_H . A contiguous set of sidebands is defined in the mass distribution on either side of the signal region, from which the background is extracted. Each sideband is defined to have the equivalent width of $\pm 2\%$ relative to the mass hypothesis that corresponds to the centre of the sideband. A total of six sidebands are used in the analysis (three on either side of the signal region), with the two sidebands adjacent to the signal region omitted in order to avoid signal contamination, as illustrated in Fig. 14.

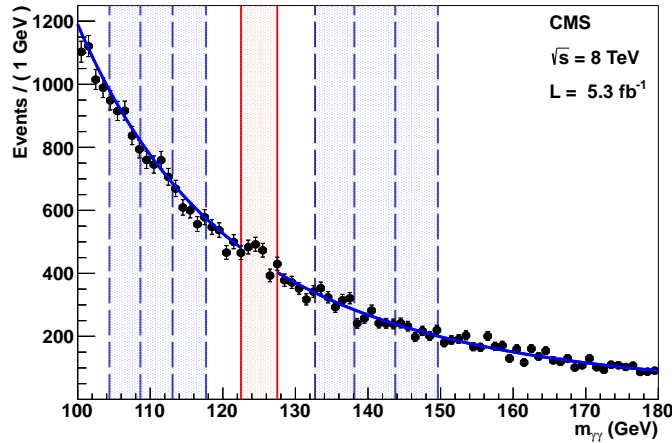


Figure 14: The six sidebands (dashed lines) around the signal region (solid line) in the sideband analysis.

The result is extracted by counting events in the signal region, in classes that are defined by the output distribution of a BDT. This mass-window BDT takes two dimensionless inputs: the diphoton BDT output (as described in Section 5.4), and the mass, in the form $\Delta m / m_H$, where $\Delta m = m_{\gamma\gamma} - m_H$ and m_H is the Higgs boson mass hypothesis. The output of the BDT is binned to define the event classes. The bin boundaries are optimized to give the maximum expected significance in the presence of a Standard Model Higgs boson signal, and the number of bins is chosen such that any additional increase in the number of bins results in an improvement in the expected significance of less than 0.1%. The same bin boundaries are used for the signal region and for the six sidebands. The dijet-tagged events constitute an additional bin (two bins for the 8 TeV data set) appended to the bins of the mass-window BDT output value.

The background model (i.e. the BDT output distribution for background events in the signal region) is constructed from the BDT output distributions of the data in each of the six sidebands. The only assumptions made concerning the background model shape, both verified within the assigned systematic errors, are that the fraction of events in each BDT output bin varies linearly as a function of invariant mass (and thus with sideband position), and that there is negligible signal contamination in the sidebands. Only the overall normalization of the background model (the total number of background events in the signal region) is obtained from a parametric fit to the mass spectrum. The signal region is excluded from this fit. The bias incurred by the choice of the functional form used in the fit has been studied in a similar fashion to that described in Section 5.5, and is covered with a systematic uncertainty of 1%.

The mass-window BDT is trained using simulated Higgs boson events with $m_H = 123$ GeV and simulated background events, including prompt-prompt, prompt-fake, and fake-fake processes. The training samples are not used in any other part of the analysis, except as input to the binning algorithm, thus avoiding any biases from overtraining.

The signal region for mass hypothesis $m_H = 125$ GeV is estimated from simulation to contain 93% of the signal. The number of expected signal events in each bin is determined using MC simulation, as in the baseline analysis. Systematic uncertainties in the signal modelling lead to event migrations between the BDT bins, that are accounted for as additional nuisance parameters in the limit-setting procedure.

Examples of distributions in this analysis are shown in Fig. 15, for the 7 (left) and 8 TeV (right) data sets. The different event classes are listed along the x axis. The first seven classes are the mass-window BDT classes. They are ordered by increasing expected signal-to-background ratio. The class labeled as ‘‘Dijet’’ contains the dijet-tagged events. The number of data events, displayed as points, is compared to the expected background events determined from the sideband population, shown by the histogram. The expected signal yield for a Higgs boson mass of $m_H = 125$ GeV is shown with the dotted line.

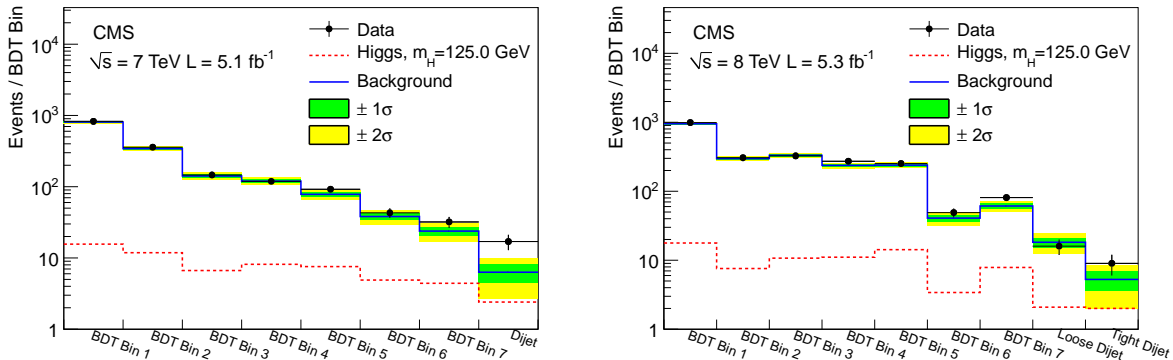


Figure 15: The number of observed events (points) for each of the mass-window BDT classes in the sideband analysis of $H \rightarrow \gamma\gamma$ for the 7 (left) and 8 TeV (right) data sets. The expected number of background events in each class, determined from the sidebands of the diphoton invariant-mass distribution, is shown by the solid line. The dark and light bands display the ± 1 and ± 2 standard deviation uncertainties in the background predictions, respectively. The expected number of signal events in each class for a 125 GeV Higgs boson, as determined from MC simulation, is shown by the dotted line.

The statistical interpretation of the results is given in Section 10.

6 $H \rightarrow ZZ$

6.1 Event selection and kinematics

The search for the decay $H \rightarrow ZZ \rightarrow 4\ell$ with $\ell = e, \mu$ is performed by looking for a narrow four-lepton invariant-mass peak in the presence of a small continuum background. The background sources include an irreducible four-lepton contribution from direct ZZ ($Z\gamma^*$) production via the $q\bar{q}$ annihilation and gg fusion processes. Reducible contributions arise from $Z + b\bar{b}$ and $t\bar{t}$ production, where the final state contains two isolated leptons and two b -quark jets that produce two nonprompt leptons. Additional background arises from Z +jets and WZ +jets

events, where jets are misidentified as leptons. Since there are differences in the reducible background rates and mass resolutions between the subchannels $4e$, 4μ , and $2e2\mu$, they are analyzed separately and the results are then combined statistically.

Compared to the first CMS $ZZ \rightarrow 4\ell$ analysis reported in Ref. [114], this analysis employs improved muon reconstruction, lepton identification and isolation, recovery of final-state-radiation (FSR) photons, and the use of a kinematic discriminant that exploits the expected decay kinematics of the signal events. New mass and spin-parity results obtained from a $H \rightarrow ZZ \rightarrow 4\ell$ analysis using additional integrated luminosity at the centre-of-mass energy of 8 TeV are described in a recent CMS publication [115], and not discussed further here.

Candidate events are first selected by triggers that require the presence of a pair of electrons or muons. An additional trigger requiring an electron and a muon in the event is also used for the 8 TeV data. The requirements on the minimum p_T of the two leptons are 17 and 8 GeV. The trigger efficiency is determined by first adjusting the simulation to reproduce the efficiencies obtained on single lepton legs in special tag-and-probe measurements, and then using the simulation to combine lepton legs within the acceptance of the analysis. The efficiency for a Higgs boson of mass > 120 GeV, is greater than 99% (98%, 95%) in the 4μ ($2e2\mu$, $4e$) channel. The candidate events are selected using identified and isolated leptons. The electrons are required to have transverse momentum $p_T^e > 7$ GeV and pseudorapidity within the tracker geometrical acceptance of $|\eta^e| < 2.5$. The corresponding requirements for muons are $p_T^\mu > 5$ GeV and $|\eta^\mu| < 2.4$. No gain in expected significance for a Higgs boson signal is obtained by lowering the p_T thresholds for the leptons, since the improvement in signal detection efficiency is accompanied by a large increase in the Z +jets background.

The lepton-identification techniques have been described in Section 3. The multivariate electron identification is trained using a Higgs boson MC simulation sample for the $H \rightarrow ZZ$ signal and a sample of W +1-jet events from data for the background. The working point is optimized using a Z +1-jet data sample. For each lepton, $\ell = e, \mu$, an isolation requirement of $R_{\text{Iso}}^\ell < 0.4$ is applied to suppress the Z +jet, $Z+b\bar{b}$, and $t\bar{t}$ backgrounds. In addition, the lepton impact parameter significance with respect to the primary vertex, defined as $\text{SIP}_{3\text{D}} = \frac{\text{IP}}{\sigma_{\text{IP}}}$, with IP the impact parameter in three dimensions and σ_{IP} its uncertainty, is used to further reduce background. The criteria of $|\text{SIP}_{3\text{D}}| < 4$ suppresses the $Z + b\bar{b}$ and $t\bar{t}$ backgrounds with negligible effect on the signal efficiency.

The efficiencies for reconstruction, identification, and isolation of electrons and muons are measured in data, using a tag-and-probe technique [116] based on an inclusive sample of $Z \rightarrow \ell\ell$ events. The measurements are performed in bins of p_T^ℓ and $|\eta|$. Additional samples of dileptons with $p_T^\ell < 15$ GeV from J/ψ decays are used for the efficiency measurements (in the case of muons) or for consistency checks (in the case of electrons). Examples of tag-and-probe results for the lepton identification efficiencies obtained with data and MC simulation are shown for electrons (top) and muons (bottom) in Fig. 16. The efficiencies measured with data are in agreement with those obtained using MC simulation. The mean differences (at the percent level) are used to correct the MC simulation predictions, and the uncertainty in the difference is propagated as a systematic uncertainty per lepton. The overall lepton selection efficiencies are obtained as the product of the reconstruction, identification, and isolation efficiencies. The overall efficiency for selecting electrons in the ECAL barrel (endcaps) varies from about 71% (65%) for $7 < p_T^e < 10$ GeV to 82% (73%) at $p_T^e \simeq 10$ GeV, and reaches 90% (89%) for $p_T^e \simeq 20$ GeV. The efficiency for electrons drops to about 85% in the transition region, $1.44 < |\eta^e| < 1.57$, between the ECAL barrel and endcaps. The muons are selected with an efficiency above 98% in the full $|\eta^\mu| < 2.4$ range for $p_T^\mu > 5$ GeV.

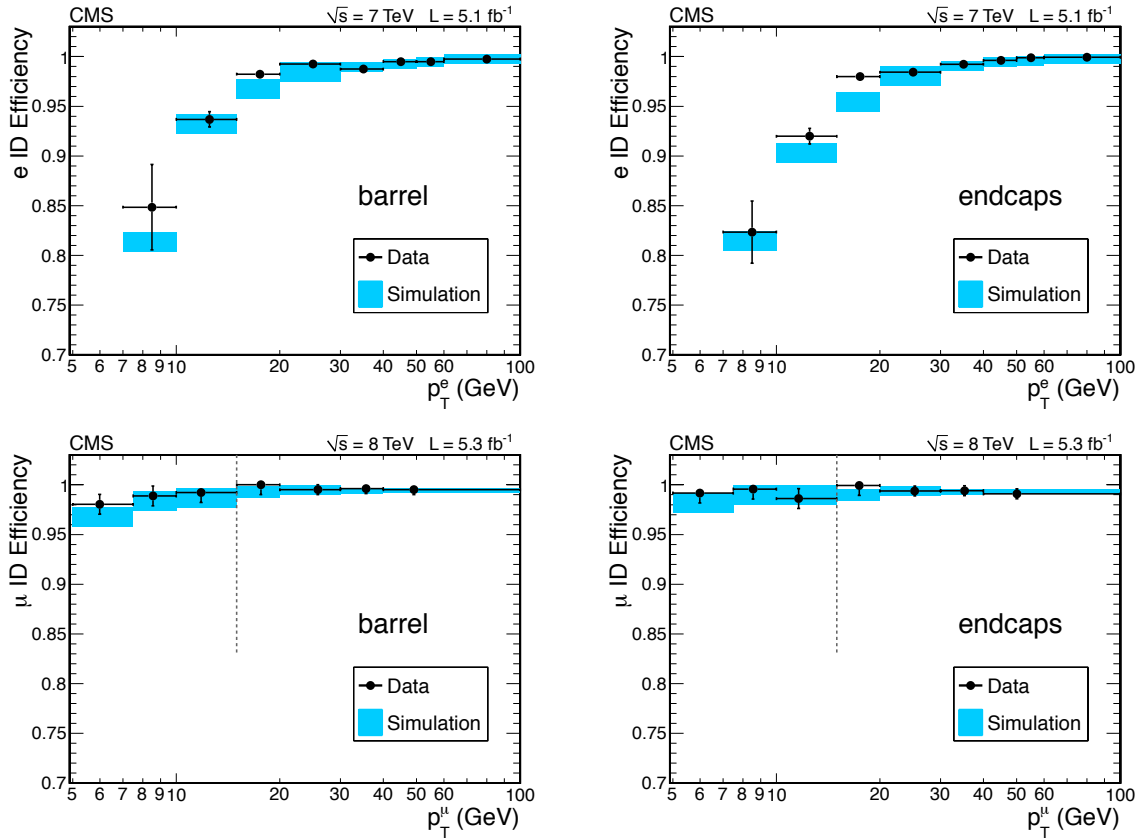


Figure 16: Measurements of the lepton identification efficiency using a tag-and-probe technique based on samples of Z and J/ψ dilepton events. The measurements are shown for electrons (top) at 7 TeV and muons (bottom) at 8 TeV as a function of p_T^ℓ for the $|\eta|$ regions of the barrel (left) and endcaps (right). For muons, the efficiencies at $p_T^\mu < 15$ GeV (dashed line on bottom plots) is obtained using J/ψ . The results obtained from data (points with error bars) are compared to results obtained from MC simulation (histograms), with the shaded region representing the combined statistical and systematic uncertainties.

Photons reconstructed with pseudorapidity $|\eta^\gamma| < 2.4$ are possible FSR candidates. The photon selection criteria are optimized as a function of the angular distance between the photon and the closest lepton in (η, ϕ) space. In an inner cone $\Delta R = 0.07$, photons are accepted if $p_T > 2$ GeV, with no further requirements. In an outer annulus $0.07 < \Delta R < 0.5$, where the rate of photons from the underlying event and pileup is much larger, a tighter threshold of 4 GeV is used, and the photons are also required to be isolated: the sum of the p_T of all charged hadrons, neutral hadrons, and photons in a cone of radius $\Delta R = 0.3$ centred on the photon should not exceed the p_T of the photon itself. In contrast to lepton isolation, and in order to take into account the fact that the photon might come from a pileup interaction, the photon isolation also uses the charged hadrons associated with other primary vertices. The selection criteria have been tuned to achieve approximately the same purity in the two angular regions. When reconstructing the $Z \rightarrow \ell\ell$ candidates, only FSR photons associated with the closest lepton, and that make the dilepton-plus-photon invariant mass closer to the nominal Z mass than the dilepton invariant mass, are kept. The dilepton-plus-photon invariant mass must also be less than 100 GeV. The performance of the FSR selection algorithm is measured using MC $H \rightarrow ZZ$ simulation samples, and the rate is verified with inclusive Z-boson events in data. Photons within the acceptance for the FSR selection are measured with an efficiency of $\simeq 50\%$ and a mean purity of 80%. The FSR photons are selected in 5% of inclusive Z-boson events in the muon channel and 0.5% in the electron channels. In the case of electrons, the FSR photons are often implicitly combined into the electron superclusters, resulting in a lower FSR recovery efficiency.

The Z boson candidates are reconstructed from pairs of leptons of the same flavour and opposite charge ($\ell^+\ell^-$). The lepton pair with an invariant mass closest to the nominal Z mass is denoted as Z_1 with mass m_{Z_1} and is retained if it satisfies $40 < m_{Z_1} < 120$ GeV. The invariant mass of the second Z candidate, denoted Z_2 , must satisfy $12 < m_{Z_2} < 120$ GeV. The minimum value of 12 GeV is found from simulation to provide the optimal sensitivity for a Higgs boson mass in the range $110 < m_H < 160$ GeV. If more than one Z_2 candidate satisfies all the criteria, we choose the candidate reconstructed from the two leptons with the highest scalar sum of their p_T . Among the four selected leptons forming Z_1 and Z_2 , at least one is required to have $p_T > 20$ GeV and another $p_T > 10$ GeV. These p_T thresholds ensure that the selected leptons are on the high-efficiency plateau for the trigger. To further reject leptons originating from weak semileptonic hadron decays or decays of low-mass hadronic resonances, we require that all opposite-charge pairs of leptons chosen from among the four selected leptons (irrespective of flavour) have an invariant mass greater than 4 GeV. The phase space for the Higgs boson search is defined by restricting the four-lepton mass range to $m_{4\ell} > 100$ GeV. The predicted lepton p_T distributions from the MC simulation for a Higgs boson with $m_H = 125$ GeV are shown in Fig. 17 for the $4e$, 4μ , and $2e2\mu$ channels. Also given in Fig. 17 (bottom right) are the event selection efficiencies for each of the three lepton channels, as a function of the Higgs boson mass. These distributions clearly emphasize the importance of low lepton- p_T thresholds and high lepton efficiencies. The selection efficiencies shown in Fig. 17 are relative to events where all four leptons are within the geometrical acceptance and all dilepton invariant masses satisfy $m_{\ell\ell} > 1$ GeV. The combined signal reconstruction and selection efficiency, for a Higgs boson with $m_H = 125$ GeV, is 18% for the $4e$ channel, 40% for the 4μ channel, and 27% for the $2e2\mu$ channel. The expected resolution on the per-event mass measurement is on average 2.2% for the $4e$ channel, 1.1% for the 4μ channel, and 1.6% for the $2e2\mu$ channel.

The kinematics of the $H \rightarrow ZZ \rightarrow 4\ell$ process, as well as for any boson decaying to ZZ , has been extensively studied in the literature [117–129]. Since the Higgs boson is spinless, the angular distribution of its decay products is independent of the production mechanism. In the Higgs

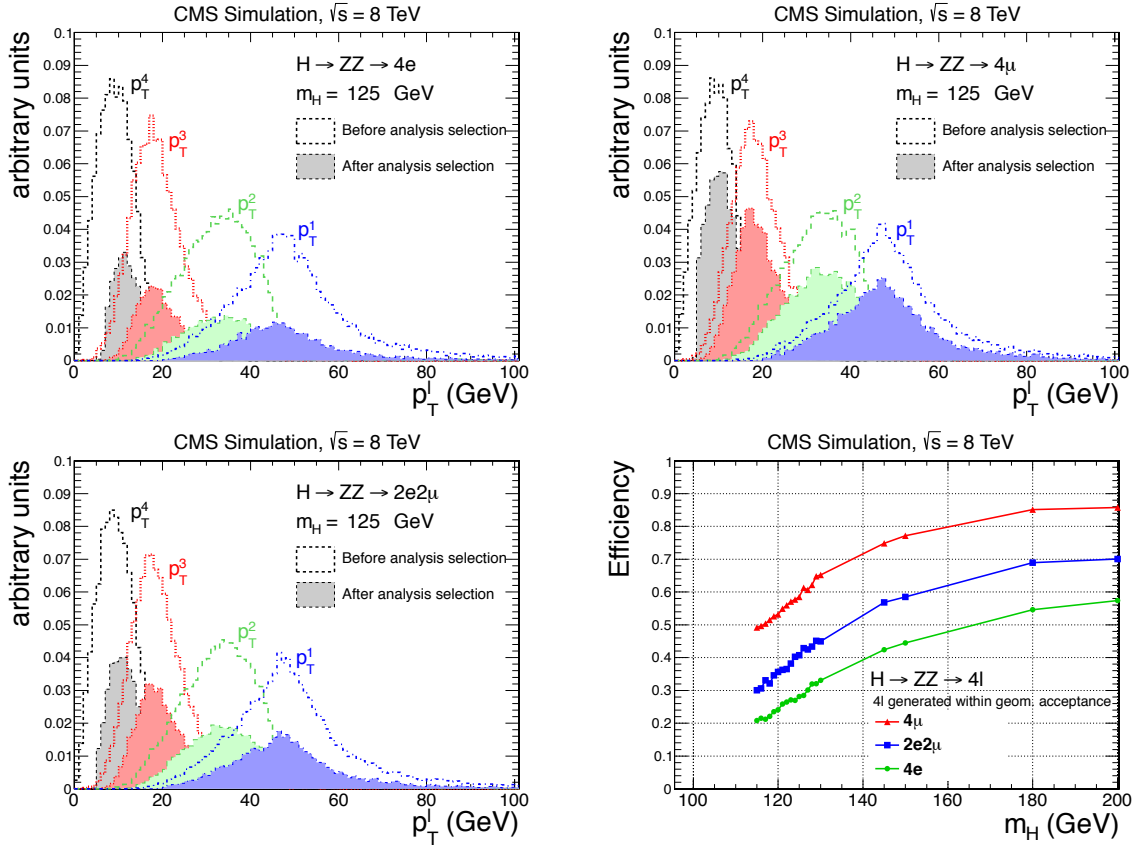


Figure 17: The MC simulation distributions of the lepton transverse momentum p_T^ℓ for each of the four leptons, ordered by p_T^ℓ , from the process $H \rightarrow ZZ \rightarrow 4\ell$ for a Higgs boson mass of 125 GeV in the $4e$ (top left), 4μ (top right), and $2e2\mu$ (bottom left) channels. The distributions are shown for events when all four leptons are within the geometrical acceptance of the analysis (open histograms), and for events passing the final selection criteria (solid histograms). The bottom-right plot displays the event selection efficiencies for $H \rightarrow ZZ \rightarrow 4\ell$ determined from MC simulation, as a function of the Higgs boson mass, for the $4e$, 4μ , and $2e2\mu$ channels. The efficiencies are relative to events where all four leptons are within the geometrical acceptance. Divergent contributions from $Z\gamma^*$ with $\gamma^* \rightarrow \ell\ell$ at generator level are avoided by requiring that all dilepton invariant masses are greater than 1 GeV.

boson rest frame, for a given invariant mass of the 4ℓ system, the kinematics are fully described by five angles, denoted $\vec{\Omega}$, and the invariant masses of the two lepton pairs Z_1 and Z_2 . These seven variables provide significant discriminating power between signal and background.

A kinematic discriminant (K_D) is introduced using the full probability density in the dilepton masses and angular variables, $\mathcal{P}(m_{Z_1}, m_{Z_2}, \vec{\Omega} | m_{4\ell})$. The K_D is constructed for each candidate event based on the probability ratio of the signal and background hypotheses, $K_D = \mathcal{P}_{\text{sig}} / (\mathcal{P}_{\text{sig}} + \mathcal{P}_{\text{bkg}})$, as described in Refs. [23, 130]. For the signal, the phase-space and Z-propagator terms [119] are included in a fully analytic parametrization of the Higgs boson signal [126]. An analytic parametrization is also used for the background probability distribution for the mass range above the ZZ threshold, while it is tabulated using a MC simulation of the $q\bar{q} \rightarrow ZZ(Z\gamma^*)$ process below this threshold.

6.2 Background estimation and systematic uncertainties

The small number of observed candidate events precludes a precise direct determination of the background by extrapolating from the signal region mass sidebands. Instead, we rely on MC simulation to evaluate the local density ($\Delta N / \Delta m_{4\ell}$) of ZZ background events expected as a function of $m_{4\ell}$. The cross section for ZZ production at NLO is calculated with MCFM [131–133]. This includes the dominant process from $q\bar{q}$ annihilation, as well as from gluon-gluon fusion. The uncertainties in the predicted number of background events owing to the variation in the QCD renormalization and factorization scales and PDF set are on average 8% for each final state [26]. The number of predicted $ZZ \rightarrow 4\ell$ events and their systematic uncertainties after the signal selection are given in Table 5.

The reducible $Z + b\bar{b}$, $t\bar{t}$, $Z + \text{jets}$, $Z + \gamma + \text{jets}$, and $WZ + \text{jets}$ backgrounds contain at least one nonprompt lepton in the four-lepton final state. The main sources of nonprompt leptons are electrons and muons coming from decays of heavy-flavour quark, misidentified jets (usually originating from light-flavour quarks), and electrons from photon conversions. The lepton misidentification probabilities are measured in data samples of $Z + \text{jet}$ events with one additional reconstructed lepton, which are dominated by final states that include a Z boson and a fake lepton. The contamination from WZ production in these events is suppressed by requiring $E_T^{\text{miss}} < 25 \text{ GeV}$. The lepton misidentification probabilities measured from these events are consistent with those derived from MC simulation. These misidentification probabilities are applied to dedicated $Z_1 + X$ control samples, where X contains two reconstructed leptons with relaxed isolation and identification criteria. Starting from these samples, two complementary approaches are used to extract the corresponding reducible $Z + X$ background yield expected in the 4ℓ signal region. The first approach avoids signal contamination in the background sample by reversing the opposite-sign requirement on the Z_2 lepton candidates, and then applies the fake lepton efficiencies to the additional leptons to calculate the expected number of background events in the signal sample. The second approach uses a control region defined by two opposite-sign leptons failing the isolation and identification criteria, and using the misidentification probability to extrapolate to the signal region. In addition, a control region with three passing leptons and one failing lepton is also used to estimate the background with three prompt leptons and one misidentified lepton. Comparable background predictions in the signal region are found from both methods within their uncertainties. The average of the two predictions is used for the background estimate, with an uncertainty that includes the difference between them (see Table 5).

Systematic uncertainties are evaluated from the data for the trigger (1.5%), and the combined four-lepton reconstruction, identification, and isolation efficiencies that vary from 1.2% in the

4μ channel at $m_H = 150$ GeV to about 11% in the $4e$ channel at $m_H = 120$ GeV. The effects of the systematic uncertainties in the lepton energy-momentum calibration (0.4%) and energy resolution on the four-lepton invariant-mass distribution are taken into account. The accuracy of the absolute mass scale and resolution is validated using $Z \rightarrow \ell\ell$, $Y \rightarrow \ell\ell$, and $J/\psi \rightarrow \ell\ell$ events. The effect of the energy resolution uncertainty is taken into account by introducing a 20% variation on the simulated width of the signal mass peak. An uncertainty of 50% is assigned to the reducible background rate. This arises from the finite statistical precision in the reducible background control regions, differences in the background composition between the various control regions, and differences between the data samples used to measure the lepton misidentification probabilities. Since all the reducible and instrumental background are estimated using control regions in the data, they are independent of the uncertainty in the integrated luminosity. However, this uncertainty (2.2% at 7 TeV [134] and 4.4% at 8 TeV [135]) does affect the prediction of the ZZ background and the normalization of the signal in determining the Higgs boson cross section. Finally, the systematic uncertainties in the theoretical Higgs boson cross section (17–20%) and 4ℓ branching fraction (2%) are taken from Ref. [25].

6.3 Results

The number of selected $ZZ \rightarrow 4\ell$ candidate events in the mass range $110 < m_{4\ell} < 160$ GeV for each of the three final states is given in Table 5. The number of predicted background events in each of the three final states and their uncertainties are also given, together with the number of signal events expected from a SM Higgs boson of $m_H = 125$ GeV.

Table 5: The number of observed selected events, compared to the expected background yields and the expected number of signal events ($m_H = 125$ GeV) for each lepton final state in the $H \rightarrow ZZ \rightarrow 4\ell$ analysis. The estimates of the ZZ background are from MC simulation and the $Z + X$ background are based on data. These results are given for the four-lepton invariant-mass range from 110 to 160 GeV. The total expected background and the observed numbers of events are also given integrated over the three bins (“signal region” defined as $121.5 < m_{4\ell} < 130.5$ GeV) of Fig. 18, centred on the bin where the most significant excess is seen. The uncertainties shown include both statistical and systematic components.

Channel	$4e$	4μ	$2e2\mu$	Total
ZZ background	2.7 ± 0.3	5.7 ± 0.6	7.2 ± 0.8	15.6 ± 1.4
Z + X	$1.2^{+1.1}_{-0.8}$	$0.9^{+0.7}_{-0.6}$	$2.3^{+1.8}_{-1.4}$	$4.4^{+2.2}_{-1.7}$
All backgrounds ($110 < m_{4\ell} < 160$ GeV)	$3.9^{+1.1}_{-0.8}$	$6.6^{+0.9}_{-0.8}$	$9.5^{+2.0}_{-1.6}$	$20.0^{+3.2}_{-2.6}$
Observed ($110 < m_{4\ell} < 160$ GeV)	6	6	9	21
Expected Signal ($m_H = 125$ GeV)	1.37 ± 0.44	2.75 ± 0.56	3.44 ± 0.81	7.6 ± 1.1
All backgrounds (signal region)	$0.71^{+0.20}_{-0.15}$	$1.25^{+0.15}_{-0.13}$	$1.83^{+0.36}_{-0.28}$	$3.79^{+0.47}_{-0.45}$
Observed (signal region)	1	3	5	9

The observed $m_{4\ell}$ distribution from data is shown in Fig. 18. There is a clear peak at the Z boson mass from the decay $Z \rightarrow 4\ell$ [136]. The size and shape of the peak are consistent with those from the background prediction. Over the full Higgs boson search region from 110 to 160 GeV, the reducible background from Z+X events is much smaller than the irreducible ZZ($Z\gamma^*$) background. There is an excess of events above the expected background near 125 GeV. The total number of observed events and the expected number of background events in the three bins centred on the excess ($121.5 < m_{4\ell} < 130.5$ GeV), and referred to as the “signal” region, are given in Table 5. The expected four-lepton invariant-mass distribution for a Higgs boson with a mass of 125 GeV is shown by the open histogram in Fig. 18.

The distributions of the reconstructed Z_1 and Z_2 dilepton invariant masses for the events in the signal region are shown in the left and right plots of Fig. 19, respectively. The Z_1 distribution has a tail towards low invariant mass, indicative that also the highest mass Z is often off-shell.

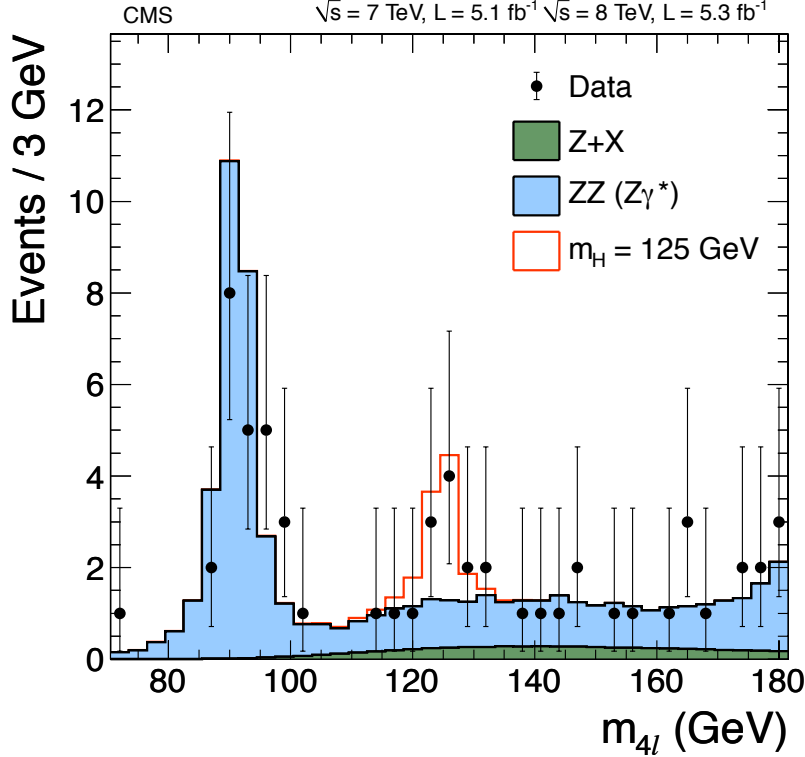


Figure 18: Distribution of the observed four-lepton invariant mass from the combined 7 and 8 TeV data for the $H \rightarrow ZZ \rightarrow 4\ell$ analysis (points). The prediction for the expected $Z+X$ and $ZZ(Z\gamma^*)$ background are shown by the dark and light histogram, respectively. The open histogram gives the expected distribution for a Higgs boson of mass 125 GeV.

The two-dimensional distribution of the kinematic discriminant K_D versus the four-lepton reconstructed mass $m_{4\ell}$ is shown in Fig. 20 for the individual selected events. Superimposed on this figure are the contours of the expected event density for the background (upper) and a SM Higgs boson at $m_H = 125$ GeV (lower). A clustering of events is observed in the region around $m_{4\ell} = 125$ GeV with $K_D \geq 0.7$. The background expectation is low in this region and the signal expectation is high, corresponding to the excess of events above background seen in the one-dimensional $m_{4\ell}$ distribution.

The observed distribution of the K_D discriminant values for invariant masses in the signal range $121.5 < m_{4\ell} < 130.5$ GeV is shown in Fig. 21 (left). The $m_{4\ell}$ distribution of events satisfying $K_D > 0.5$ is shown in Fig. 21 (right). The clustering of events is clearly visible near $m_{4\ell} \approx 125$ GeV.

7 $H \rightarrow WW$

The decay mode $H \rightarrow WW$ is highly sensitive to a SM Higgs boson with a mass around the WW threshold of 160 GeV. With the lepton identification and E_T^{miss} reconstruction optimized for LHC pileup conditions, it is possible to extend the sensitivity down to 120 GeV. The search

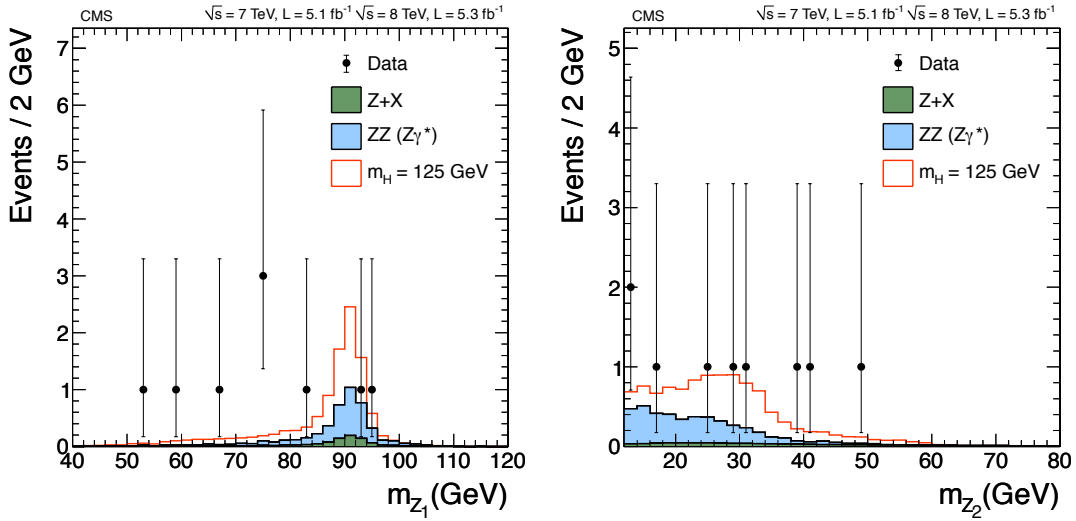


Figure 19: Distributions of the observed Z_1 (left) and Z_2 (right) dilepton invariant masses for four-lepton events in the mass range $121.5 < m_{4\ell} < 130.5$ GeV for the combined 7 and 8 TeV data (points). The shaded histograms show the predictions for the background distributions, and the open histogram for a Higgs boson with a mass of 125 GeV.

strategy for $H \rightarrow WW$ is based on the final state in which both W bosons decay leptonically, resulting in a signature with two isolated, oppositely charged, high- p_T leptons (electrons or muons) and large E_T^{miss} caused by the undetected neutrinos. It is not possible to reconstruct the Higgs mass in this final state, nevertheless there is some mass sensitivity via different kinematic distributions like the dilepton mass or the invariant mass of leptons and E_T^{miss} . The analysis of the 7 TeV data is described in Ref. [137] and remains unchanged, while the 8 TeV analysis is modified to cope with the more difficult conditions induced by the higher pileup in the 2012 data taking, and is explained below.

7.1 WW event selection

To improve the signal sensitivity, events are separated by jet multiplicity into three mutually exclusive categories, which are characterized by different expected signal yields and signal-to-background ratios. We call these the 0-jet, 1-jet, and 2-jet categories. Jets are reconstructed using the selection described in Section 3, and events are classified according to the number of selected jets with $E_T > 30$ GeV and $|\eta| < 4.7$. To exclude electrons and muons from the jet sample, these jets are required to be separated from the selected leptons in ΔR by at least $\Delta R^{\text{jet-lepton}} > 0.3$. Events with more than 2 jets are only considered if there are no additional jets above this threshold present in the pseudorapidity region between the two highest- E_T jets. Furthermore, the search splits candidate signal events into three final states, denoted by: e^+e^- , $\mu^+\mu^-$, and $e^\pm\mu^\mp$.

The bulk of the signal arises through direct WW decays to dileptons of opposite charge, where the small contribution proceeding through an intermediate τ leptonic decays is implicitly included. The events are selected by triggers that require the presence of one or two high- p_T electrons or muons. The trigger efficiency for signal events that pass the full event selection is measured to be above 97% in the $\mu^+\mu^-$ final state, and above 98% in the e^+e^- and $e^\pm\mu^\mp$ final states for a Higgs boson mass of about 125 GeV. The trigger efficiencies increase along with Higgs boson mass. These efficiencies are measured using $Z/\gamma^* \rightarrow \ell^+\ell^-$ events [116], with associated uncertainties of about 1%.

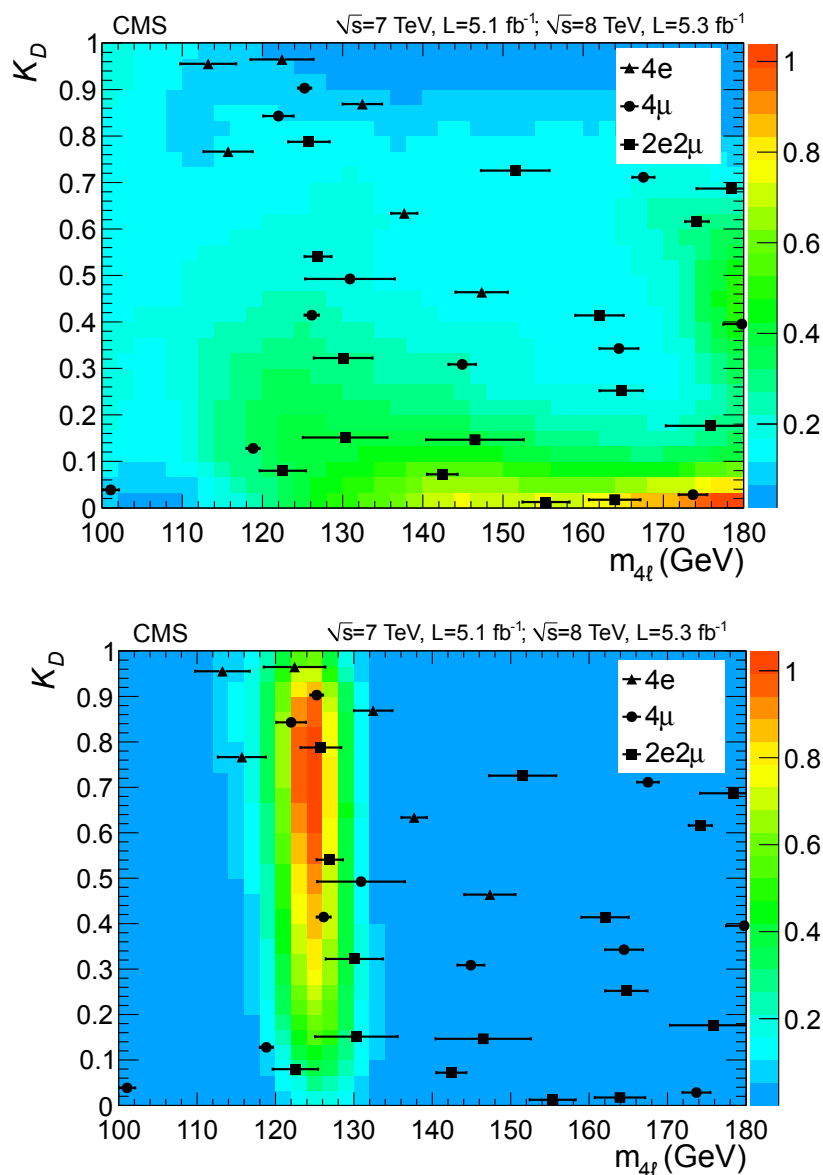


Figure 20: The two-dimensional distribution of the kinematic discriminant K_D versus $m_{4\ell}$ for selected 4ℓ events in the combined 7 and 8 TeV data. Events in the three different final states are designated by symbols shown in the legend. The horizontal error bars indicate the estimated per-event mass resolution deduced from the combination of the per-lepton momentum uncertainties. The contours in the upper plot show the event density for the background expectation, and in the lower plot the contours for a SM Higgs boson with $m_H = 125$ GeV (both in arbitrary units).

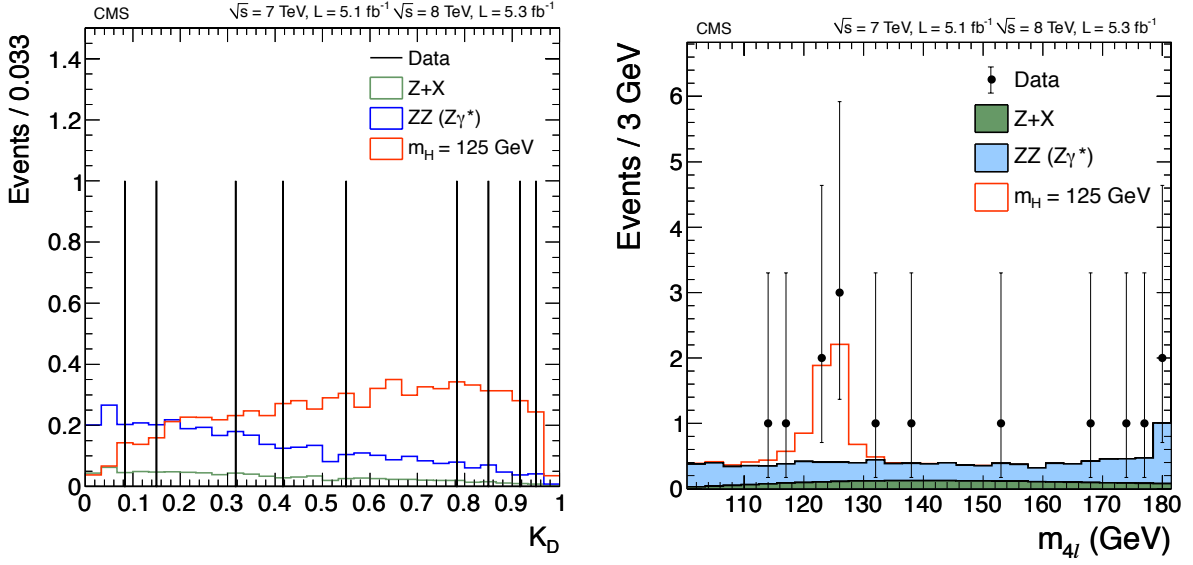


Figure 21: Left: Distribution of the kinematic discriminant K_D for $H \rightarrow ZZ \rightarrow 4\ell$ candidate events from the combined 7 and 8 TeV data (vertical lines) in the signal mass region $121.5 < m_{4\ell} < 130.5$ GeV. The predicted distributions for the Z+X and ZZ($Z\gamma^*$) backgrounds and for a Higgs boson with a mass of 125 GeV are shown by the histograms. Right: The $m_{4\ell}$ distribution for data events with $K_D > 0.5$ (points) and the predicted distributions for the backgrounds and a Higgs boson with a mass of 125 GeV (histograms).

Two oppositely charged lepton candidates are required, with $p_T > 20$ GeV for the higher- p_T lepton ($p_T^{\ell,\max}$) and $p_T > 10$ GeV for the lower- p_T lepton ($p_T^{\ell,\min}$). Only electrons (muons) with $|\eta| < 2.5$ (2.4) are considered in the analysis.

A tight muon selection is applied, as described in Section 3. Muons are required to be isolated to distinguish between muon candidates from W boson decays and those from QCD background processes, which are usually in or near jets. For each muon candidate, the scalar sum of the transverse energy of all particles consistent with originating from the primary vertex is reconstructed in cones of several widths around the muon direction, excluding the contribution from the muon itself. This information is combined using a multivariate algorithm that exploits the differences in the energy deposition between prompt muons and muons from hadron decays inside a jet.

Electron candidates are identified using the multivariate approach described in Section 3. Electrons are required to be isolated by applying a threshold on the sum of the transverse energy of the particles that are reconstructed in a cone around them, excluding the contribution from the electron itself. For both electrons and muons, a correction is applied to account for the contribution to the energy in the isolation cone from pileup, as explained in Section 3.

In addition to high-momentum, isolated leptons and minimal jet activity, missing transverse momentum is present in signal events, but generally not in the background. In this analysis, a projected E_T^{miss} variable is employed. It is equal to the component of the E_T^{miss} vector transverse to the nearest lepton direction, if the difference in azimuthal angle between this lepton and the E_T^{miss} vector is less than 90° . If there is no lepton within 90° of the E_T^{miss} direction in azimuth, the value of E_T^{miss} is used. Since the projected E_T^{miss} resolution is degraded by pileup, the minimum of two E_T^{miss} observables is used in the determination of the projected E_T^{miss} value: the first is the standard E_T^{miss} , while the second uses only charged particles associated with the primary

vertex to measure the missing transverse energy. Events with projected E_T^{miss} above 20 GeV are selected for the analysis.

To suppress the top-quark background, a *top-quark tagging* technique, based on low-momentum muon identification and b-jet tagging [31], is applied. The first selection is designed to veto events containing muons from b hadrons coming from top-quark decays. The second selection uses a b-jet tagging algorithm that looks for tracks with large impact parameter within jets. The rejection when combining the two selections for the top-quark background is about 50% in the 0-jet category and above 80% for events with at least one jet passing the selection criteria.

Various selection criteria are used to reduce the other background contributions. For the W+jets background, a minimum dilepton transverse momentum ($p_T^{\ell\ell}$) of 45 GeV is required. To reduce the background from WZ production, any event that has a third lepton passing the identification and isolation requirements is rejected. This requirement rejects less than 1% of the $WW \rightarrow 2\ell 2\nu$ events, while rejecting around 35% of the remaining WZ events. The contribution from $W\gamma$ production, where the photon converts into an electron pair, is reduced by about 90% in the dielectron final state by requirements that reject γ conversions. Those requirements consist in finding tracks that associated with the electron give good conversion candidates. The background from low-mass resonances is rejected by requiring a dilepton mass ($m_{\ell\ell}$) greater than 12 GeV.

The Drell–Yan process produces same-flavour lepton pairs (e^+e^- and $\mu^+\mu^-$). In order to suppress this background, a few additional requirements are applied in the same-flavour final states. First, the resonant Z component of the Drell–Yan production is rejected by requiring a dilepton mass outside a 30 GeV window centred on the Z mass. Then, the remaining off-peak contribution is suppressed by exploiting different E_T^{miss} -based approaches depending on the number of jets and the Higgs boson mass hypothesis. At large Higgs boson masses ($m_H > 140$ GeV), signal events are associated with large E_T^{miss} and, thus, to suppress the Drell–Yan background it is sufficient to require the minimum of the two projected E_T^{miss} variables to be greater than 45 GeV. On the contrary, in low-mass Higgs boson events ($m_H \leq 140$ GeV) it is more difficult to separate the signal from the Drell–Yan background; therefore in this case, a dedicated multivariate selection, combining the missing transverse momentum with kinematic and topological variables, is used to reject Drell–Yan events and maximize the signal yield. A third approach is employed in events with two jets. Here, the dominant source of E_T^{miss} is the mismeasurement of the hadronic jet energy, and the optimal performance is obtained by requiring $E_T^{\text{miss}} > 45$ GeV. Finally, the momenta of the dilepton system and the most energetic jet must have an angle in the transverse plane smaller than 165° . These selections reduce the Drell–Yan background by three orders of magnitude, while rejecting less than 50% of the signal, as determined from simulation.

After applying the full set of selection criteria, referred to as the WW selection, the observed yields in the combined 7 and 8 TeV data set are 1594, 1186, and 1295 events in the 0-jet, 1-jet, and 2-jet categories, respectively. This sample is dominated by nonresonant WW events in the 0-jet category and by a similar fraction of WW and top events in the other two categories. The main efficiency loss is due to the lepton selection and the stringent E_T^{miss} requirements. Figures 22 and 23 show the observed distributions of the azimuthal angle difference ($\Delta\phi_{\ell\ell}$) and the dilepton mass ($m_{\ell\ell}$) after the WW selection, respectively, and the expected distributions for a SM Higgs boson with $m_H = 125$ GeV and for backgrounds in the 0- and 1-jet categories. The clear difference in the shape between the $H \rightarrow WW$ and the nonresonant WW processes is because of the spin-0 nature of the Higgs boson.

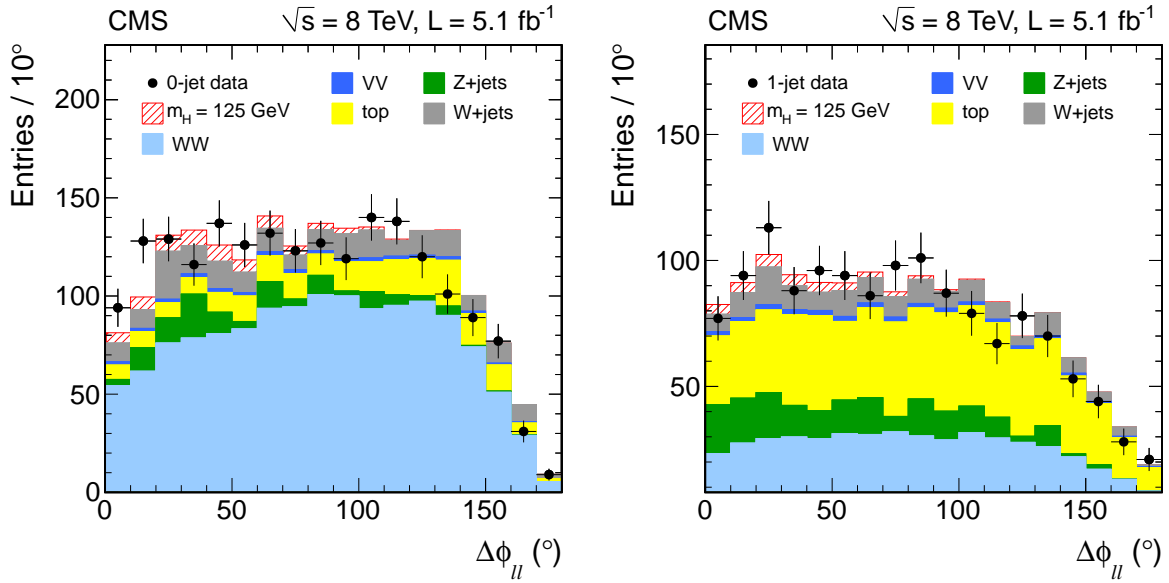


Figure 22: Distributions of the azimuthal angle difference $\Delta\phi_{\ell\ell}$ between selected leptons in the 0-jet (left) and 1-jet (right) categories, for data (points), the main backgrounds (solid histograms), and a SM Higgs boson signal with $m_H = 125$ GeV (hatched histogram) at 8 TeV. The standard WW selection is applied.

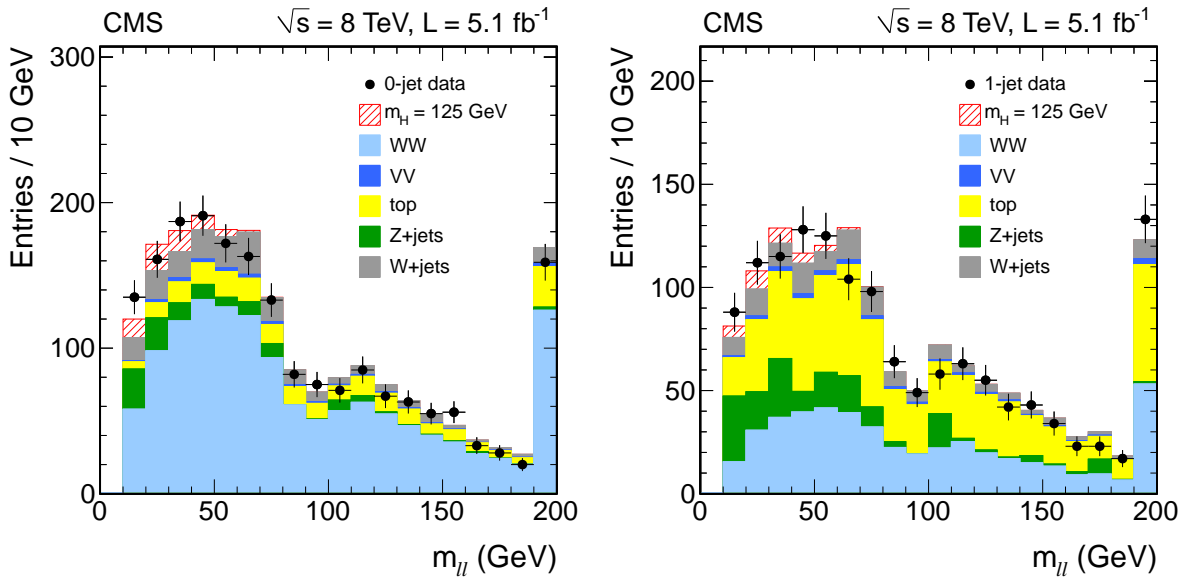


Figure 23: Distributions of the dilepton invariant mass $m_{\ell\ell}$ of selected dileptons in the 0-jet (left) and 1-jet (right) categories, for data (points), the main backgrounds (solid histograms), and a SM Higgs boson with $m_H = 125$ GeV (hatched histogram) at 8 TeV. The standard WW selection is applied. The last bin contains overflows.

7.2 $H \rightarrow WW$ search strategy

To enhance the sensitivity for a Higgs boson signal, a cut-based approach is chosen for the final event selection. Because the kinematics of signal events change as a function of the Higgs boson mass, separate optimizations are performed for different m_H hypotheses. The extra requirements, designed to optimize the sensitivity for a SM Higgs boson, are placed on $p_T^{\ell, \max}$, $p_T^{\ell, \min}$, $m_{\ell\ell}$, $\Delta\phi_{\ell\ell}$ and the transverse mass m_T , defined as $\sqrt{2p_T^{\ell\ell}E_T^{\text{miss}}(1 - \cos\Delta\phi_{E_T^{\text{miss}}\ell\ell})}$, where $\Delta\phi_{E_T^{\text{miss}}\ell\ell}$ is the difference in azimuthal angle between the E_T^{miss} direction, and the transverse momentum of the dilepton system. The requirements, which are the same for both the 0- and 1-jet categories, are summarized in Table 6. The $m_{\ell\ell}$ distribution in the 0-jet (left) and 1-jet (right) categories for the $e\mu$ candidate events are shown in Fig. 24, along with the predictions for the background and a SM Higgs boson with $m_H = 125$ GeV.

Table 6: Final event selection requirements for the cut-based analysis of the 0- and 1-jet event samples. Values for other Higgs boson mass hypotheses follow a smooth behavior with respect to the reported values.

m_H (GeV)	$p_T^{\ell, \max}$ (GeV)	$p_T^{\ell, \min}$ (GeV)	$m_{\ell\ell}$ (GeV)	$\Delta\phi_{\ell\ell}$ ($^\circ$)	m_T (GeV)
125	>23	>10	<43	<100	80–123
130	>25	>10	<45	<90	80–125

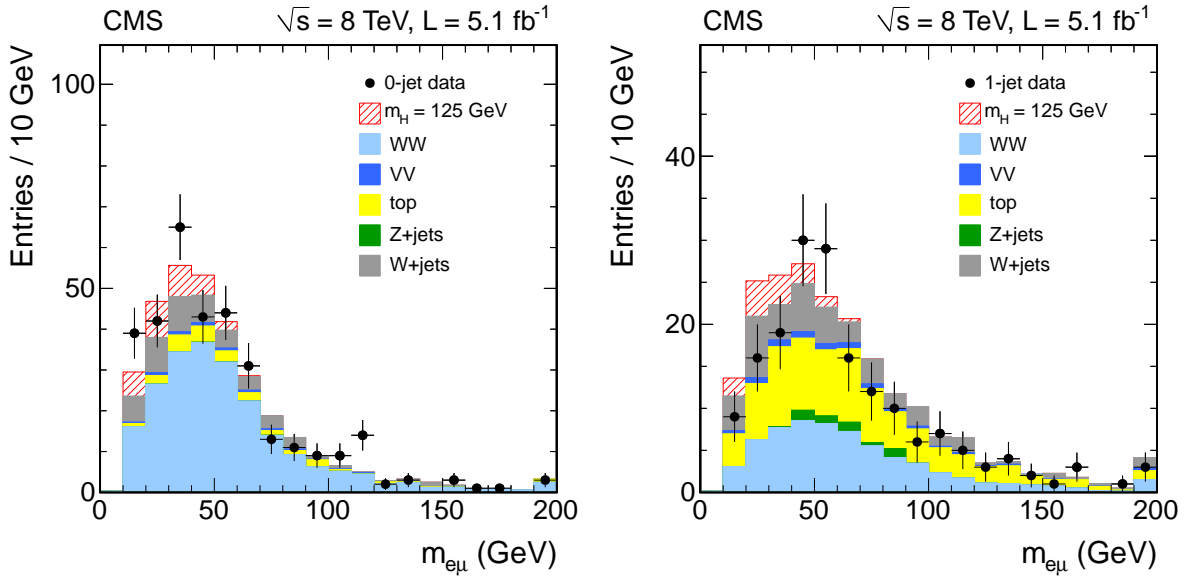


Figure 24: Dilepton invariant mass distribution from the 0-jet (left) and 1-jet (right) $e\mu$ events from the 8 TeV data (points with error bars), and the prediction for the various backgrounds (solid histograms), and for a SM Higgs boson with $m_H = 125$ GeV (hatched histogram) at 8 TeV. The cut-based $H \rightarrow WW$ selection, except for the requirement on the dilepton mass itself, is applied.

The 2-jet category is mainly sensitive to VBF production [74, 75, 77, 138], whose cross section is roughly ten times smaller than that from gluon-gluon fusion. The VBF channel offers a different production mechanism to test the consistency of a signal with the SM Higgs boson hypothesis. The VBF signal can be extracted using simple selection criteria, especially in the relatively low-background environment of the fully leptonic WW decay mode, providing additional search

sensitivity. The $H \rightarrow WW$ events from VBF production are characterized by two energetic forward-backward jets and very little hadronic activity in the rest of the event. Events passing the WW criteria are further required to satisfy $p_T > 30$ GeV for the two highest- E_T jets, with no jets above this threshold present in the pseudorapidity region between these two jets. Both leptons are required to be within the pseudorapidity region between the two jets. To reject the main background from top-quark decays, the two jets must have a pseudorapidity difference larger than 3.5 and a dijet invariant mass greater than 450 GeV. In addition, m_T is required to be between 30 GeV and the Higgs boson mass hypothesis. Finally, a m_H -dependent upper limit on the dilepton mass is applied.

7.3 Background predictions

A combination of techniques is used to determine the contributions from the background processes that remain after the final selection. The largest background contributions are estimated directly from data, avoiding uncertainties related to the simulation of these sources. The remaining contributions estimated from simulation are small.

The W +jets and QCD multijet backgrounds arise from semileptonic decays of heavy quarks, hadrons misidentified as leptons, and electrons from photon conversions. Estimations of these contributions are derived directly from data, using a control sample of events in which one lepton passes the standard criteria and the other does not, but instead satisfies a relaxed set of requirements (“loose” selection), resulting in a “tight-loose” sample. Then the efficiency, ϵ_{loose} , for a lepton candidate that satisfies the loose selection to also pass the tight selection is determined, using data from an independent multijet event sample dominated by non-prompt leptons and parametrized as a function of the p_T and η of the lepton. Finally, the background contamination is estimated using the events in the “tight-loose” sample, weighted by $\epsilon_{\text{loose}}/(1 - \epsilon_{\text{loose}})$. The systematic uncertainty in the determination of ϵ_{loose} dominates the overall uncertainty of this method, which is estimated to be about 36%. The uncertainty is obtained by varying the requirements to obtain ϵ_{loose} , and from a closure test, where the tight-loose rate derived from QCD simulated events is applied to a W + jets simulated sample to predict the rate of events with one real and one misidentified lepton.

The normalization of the top-quark background is estimated from data by counting the number (N_{tagged}) of top-quark-tagged events and applying a corresponding top-quark-tagging efficiency ϵ_{top} . The top-quark-tagging efficiency (ϵ_{top}) is measured with a control sample dominated by $t\bar{t}$ and Wt events, which is selected by requiring a b-tagged jet in the event. The number of top-quark background events in the signal region is then given by: $N_{\text{tagged}} \times (1 - \epsilon_{\text{top}})/\epsilon_{\text{top}}$. Background sources from non-top events are subtracted by estimating the misidentification probability from data control samples. The main uncertainty comes from the statistical uncertainty in the b-tagged control sample and from the systematic uncertainties related to the measurement of ϵ_{top} . The uncertainty is about 20% in the 0-jet category and about 5% in the 1-jet category.

For the low-mass $H \rightarrow WW$ signal region, $m_H \leq 200$ GeV, the nonresonant WW background prediction is estimated from data. This contribution is measured using events with a dilepton mass larger than 100 GeV, where the Higgs boson signal contamination is negligible, and the MC simulation is then used to extrapolate into the signal region. The total uncertainty is about 10%, where the statistical uncertainty of the data control region is the largest component. For larger Higgs boson masses there is a significant overlap between the nonresonant WW and Higgs boson signal, and the simulation is used for the estimation of the background.

The $Z/\gamma^* \rightarrow \ell^+\ell^-$ contribution to the e^+e^- and $\mu^+\mu^-$ final states is estimated by extrapolat-

ing the observed number of events with a dilepton mass within ± 7.5 GeV of the Z mass, with the residual background in that region subtracted using $e^\pm\mu^\mp$ events. The extrapolation to the signal region is then performed using the simulation. The results are cross-checked with data, using the same algorithm and subtracting the background in the Z-mass region, estimated from the number of $e^\pm\mu^\mp$ events. The largest uncertainty in the estimate is the statistical uncertainty in the control sample, which is about 20% to 50%. The $Z/\gamma^* \rightarrow \tau^+\tau^-$ contamination is estimated using $Z/\gamma^* \rightarrow e^+e^-$ and $\mu^+\mu^-$ events selected in data, where the leptons are replaced with simulated τ decays, thus providing a better description of the process $Z/\gamma^* \rightarrow \tau^+\tau^-$. The TAUOLA [54] program is used in the simulation of the τ decays to account for τ -polarization effects.

Finally, to estimate the $W\gamma^*$ background contribution from asymmetric virtual photon decays to dileptons [139], where one lepton escapes detection, the MADGRAPH generator [104] with dedicated cuts is used. In particular, all the leptons are required to have a p_T larger than 5 GeV and the mass of each lepton is considered in the generation of the samples. To normalize the simulated events, a control sample of high-purity $W\gamma^*$ events from data with three reconstructed leptons is compared to the simulation prediction. A normalization factor of 1.6 ± 0.5 with respect to the theoretical leading-order $W\gamma^*$ cross section is found.

Other minor backgrounds from WZ, ZZ (when the two selected leptons come from different boson decays), and $W\gamma$ are estimated from simulation. The $W\gamma$ background estimate is cross-checked in data using events passing all the selection requirements, except the two leptons must have the same charge; this sample is dominated by W +jets and $W\gamma$ events. The agreement between data and the background prediction in this test is at the 20% level.

The number of observed events and the expected number of events from all background processes after the WW selection are summarized in Table 7. The number of events observed in data and the signal and background predictions after the final selection are listed in Table 8 for two Higgs boson mass hypotheses.

Table 7: Observed number of events and background estimates for the 8 TeV data sample, after applying the WW selection requirements. The uncertainties are statistical only.

	WW	$t\bar{t} + tW$	W+jets	WZ + ZZ	Z/γ^*	$W\gamma^{(*)}$	tot. bkg.	data
0-jet	1046.1 ± 7.2	164.2 ± 5.4	158.2 ± 7.1	32.6 ± 0.6	73 ± 17	27.1 ± 3.9	1501 ± 21	1594
1-jet	381.0 ± 4.0	527.3 ± 8.4	122.6 ± 6.7	30.3 ± 0.6	77 ± 24	23.7 ± 5.2	1162 ± 27	1186
2-jet	177.0 ± 2.8	886.5 ± 11.1	94.9 ± 6.4	20.8 ± 0.5	227 ± 20	5.6 ± 2.1	1412 ± 24	1295

7.4 Efficiencies and systematic uncertainties

The signal efficiency is estimated using simulations. All Higgs boson production mechanisms are considered: gluon-gluon fusion, associated production with a W or Z boson (VH), and VBF processes.

Residual discrepancies in the lepton reconstruction and identification efficiencies between data and simulation are corrected for by data-to-simulation scale factors measured using $Z/\gamma^* \rightarrow \ell^+\ell^-$ events in the Z-peak region [116], recorded with dedicated unbiased triggers. These factors depend on the lepton p_T and $|\eta|$, and are typically in the range 0.9–1.0. The uncertainties on the lepton and trigger efficiencies are about 2% per lepton leg.

Experimental effects, theoretical predictions, and the choice of MC event generators are considered as sources of systematic uncertainty, and their impact on the signal efficiency is assessed. The experimental uncertainties in lepton efficiency, momentum scale and resolution,

Table 8: The signal predictions, background estimates, and numbers of events in data for two different Higgs boson mass hypotheses with the 8 TeV data set, after applying the final $H \rightarrow WW$ cut-based requirements, which depend on the Higgs boson mass hypothesis. The different jet categories and dilepton final states are shown separately. The combined statistical, experimental, and theoretical systematic uncertainties are given.

m_H	$H \rightarrow WW$	WW	WZ + ZZ + Z/ γ^*	$t\bar{t} + tW$	W+jets	$W\gamma^{(*)}$	all bkg.	data
0-jet category $e\mu$ final state								
125	23.9 ± 5.2	87.6 ± 9.5	2.2 ± 0.2	9.3 ± 2.7	19.1 ± 7.2	6.0 ± 2.3	124.2 ± 12.4	158
130	35.3 ± 7.6	96.8 ± 10.5	2.5 ± 0.3	10.1 ± 2.8	20.7 ± 7.8	6.3 ± 2.4	136.3 ± 13.6	169
0-jet category $ee/\mu\mu$ final state								
125	14.9 ± 3.3	60.4 ± 6.7	37.7 ± 12.5	1.9 ± 0.5	10.8 ± 4.3	4.6 ± 2.5	115.5 ± 15.0	123
130	23.5 ± 5.1	67.4 ± 7.5	41.3 ± 15.9	2.3 ± 0.6	11.0 ± 4.3	4.8 ± 2.5	126.8 ± 18.3	134
1-jet category $e\mu$ final state								
125	10.3 ± 3.0	19.5 ± 3.7	2.4 ± 0.3	22.3 ± 2.0	11.7 ± 4.6	5.9 ± 3.2	61.7 ± 7.0	54
130	15.7 ± 4.7	22.0 ± 4.1	2.6 ± 0.3	25.1 ± 2.2	12.8 ± 5.1	6.0 ± 3.2	68.5 ± 7.6	64
1-jet category $ee/\mu\mu$ final state								
125	4.4 ± 1.3	9.7 ± 1.9	8.7 ± 4.9	9.5 ± 1.1	3.9 ± 1.7	1.3 ± 1.2	33.1 ± 5.7	43
130	7.1 ± 2.2	11.2 ± 2.2	9.1 ± 5.4	10.7 ± 1.2	3.7 ± 1.7	1.3 ± 1.2	36.0 ± 6.3	53
2-jet category $e\mu$ final state								
125	1.5 ± 0.2	0.4 ± 0.1	0.1 ± 0.0	3.4 ± 1.9	0.3 ± 0.3	0.0 ± 0.0	4.1 ± 1.9	6
130	2.5 ± 0.4	0.5 ± 0.2	0.1 ± 0.0	3.0 ± 1.8	0.3 ± 0.3	0.0 ± 0.0	3.9 ± 1.9	6
2-jet category $ee/\mu\mu$ final state								
125	0.8 ± 0.1	0.3 ± 0.1	3.1 ± 1.8	2.0 ± 1.2	0.0 ± 0.0	0.0 ± 0.0	5.4 ± 2.2	7
130	1.3 ± 0.2	0.4 ± 0.2	3.8 ± 2.2	2.0 ± 1.2	0.0 ± 0.0	0.0 ± 0.0	6.2 ± 2.5	7

E_T^{miss} modelling, and jet energy scale are applied to the reconstructed objects in simulated events by smearing and scaling the relevant observables, and propagating the effects to the kinematic variables used in the analysis. The 36% normalization uncertainty in the $W + \text{jets}$ background is included by varying the efficiency for misidentified leptons to pass the tight lepton selection and by comparing the results of a closure test using simulated samples.

The relative systematic uncertainty on the signal efficiency from pileup is evaluated to be 1%. This corresponds to shifting the mean of the expected distribution of the number of pp collision per beam-crossing that is used to reweight the simulation up and down by one pp interaction. The systematic uncertainty on the integrated luminosity measurement is 4.4% [135].

The systematic uncertainties from theoretical input are separated into two components, which are assumed to be independent. The first component is the uncertainty in the fraction of events classified into the different jet categories and the effect of migration between categories. The second component is the uncertainty in the lepton acceptance and the selection efficiency of the other requirements. The effect of variations in the PDF, the value of α_s , and the higher-order corrections are considered for both components, using the PDF4LHC prescription [95–99] and the recommendations from [25]. For the jet categorization, the effects of higher-order logarithmic terms via the uncertainty in the parton shower model and the underlying event are also considered by comparing different generators. These uncertainties range between 10% and 30%, depending on the jet category. The uncertainties related to the diboson cross sections are calculated using the MCFM program [131].

The systematic uncertainty in the overall signal efficiency is estimated to be about 20% and is dominated by the theoretical uncertainty in the missing higher-order corrections and PDF uncertainties. The total uncertainty in the background estimations in the $H \rightarrow WW$ signal

region is about 15%, dominated by the statistical uncertainty in the observed number of events in the background-control regions.

The interpretation of the results in terms of upper limits on the Higgs boson production cross section will be given in Section 10.

8 $H \rightarrow \tau\tau$

The $H \rightarrow \tau\tau$ decay mode is sensitive to a SM Higgs boson with a mass below about 145 GeV, for which the branching fraction is large. The search uses final states where the two τ leptons are identified either by their leptonic decay to an electron or muon, or by their hadronic decay designated as τ_h . Four independent channels are studied: $e\tau_h$, $\mu\tau_h$, $e\mu$, and $\mu\mu$. In each channel, the signal is separated from the background, and in particular from the irreducible $Z \rightarrow \tau\tau$ process, using the τ -lepton pair invariant mass $m_{\tau\tau}$, reconstructed from the four-momentum of the visible decay products of the two τ leptons and the E_T^{miss} vector, as explained in Section 8.2. Events are classified by the number of additional jets in the final state, in order to enhance the contribution of different Higgs boson production mechanisms. The 0- and 1-jet categories select primarily signal events with a Higgs boson produced by gluon-gluon fusion, or in association with a W or Z vector boson that decays hadronically. These two categories are further classified according to the p_T of the τ -lepton decay products, because high- p_T events benefit from a higher signal-to-background ratio. Events in the VBF category are required to have two jets separated by a large rapidity, which preferentially selects signal events from the vector-boson fusion production mechanism and strongly enhances the signal purity.

8.1 Trigger and inclusive event selection

The high-level trigger requires a combination of electron, muon, and τ_h trigger objects [42, 140, 141]. The electron and muon HLT reconstruction is seeded by electron and muon level-1 trigger objects, respectively, while the τ_h trigger object reconstruction is entirely done at HLT stage. A specific version of the particle-flow algorithm is used in the HLT to reconstruct these objects and quantify their isolation, as done in the offline reconstruction. The identification and isolation criteria and the transverse momentum thresholds for these objects were progressively tightened as the LHC instantaneous luminosity increased over the data taking period. In the $e\tau_h$ and $\mu\tau_h$ channels, the trigger requires the presence of a lepton and a τ_h , both loosely isolated with respect to the offline isolation criteria described below. In the $e\mu$ and $\mu\mu$ channels, the lepton trigger objects are not required to be isolated. For the $e\tau_h$, $\mu\tau_h$, and $\mu\mu$ channels, the muon and electron trigger efficiencies are measured with respect to the offline selection in the data and the simulation using $Z \rightarrow \ell\ell$ ($\ell = e, \mu$) events passing a single-lepton trigger. For the $e\mu$ channel, they are determined using $Z \rightarrow \tau\tau \rightarrow e\mu$ events passing a single-lepton trigger. The τ_h triggering efficiency is obtained using $Z \rightarrow \tau\tau \rightarrow \mu\tau_h$ events passing a single-muon trigger. In the analysis, simulated events are weighted by the ratio between the efficiency measured in the data and the simulation, which are parametrized as a function of the lepton or τ_h transverse momentum and pseudorapidity.

To be considered in the offline event selection, electrons and muons must fulfill tight isolation criteria. The electron and muon isolation parameter R_{iso}^ℓ is calculated as in Eq. (1) using a cone size $\Delta R = 0.4$, but with the following differences. The sum $\sum_{\text{charged}} p_T$ is performed considering all charged particles associated with the primary vertex, including other electrons and muons. The contribution of neutral pileup particles is estimated as $0.5 \sum_{\text{charged,PU}} p_T$, where the sum is computed for all charged hadrons from pileup interactions in the isolation cone, and where the factor 0.5 corresponds approximately to the ratio of neutral-to-charged hadron energy in

the hadronization process, as estimated from simulation. Electrons and muons are required to have $R_{\text{iso}}^{\ell} < 0.1$. This criterion is relaxed to 0.15 in the $e\mu$ channel for leptons in the barrel, and in the $\mu\mu$ channel for muons with $p_{\text{T}} < 20$ GeV. The τ -isolation discriminator R_{iso}^{τ} defined in Section 3 is used to select loosely isolated τ_h so that the overall τ_h identification efficiency is 60–65%, for a jet misidentification probability of 2–3%. Finally, electrons and muons misidentified as τ_h are suppressed using dedicated criteria based on the consistency between the tracker, calorimeter, and muon-chamber measurements.

In the $e\tau_h$ and $\mu\tau_h$ channels, we select events containing either an electron with $p_{\text{T}} > 20$ GeV or a muon with $p_{\text{T}} > 17$ GeV, and $|\eta| < 2.1$, accompanied by an oppositely charged τ_h with $p_{\text{T}} > 20$ GeV and $|\eta| < 2.3$. In the 8 TeV data set analysis, the electron and muon p_{T} thresholds are increased to 24 and 20 GeV, respectively, to account for the higher trigger thresholds. In these channels, events with more than one loosely identified electron or muon with $p_{\text{T}} > 15$ GeV are rejected to reduce the Drell–Yan background. In the $e\mu$ channel, we demand an electron within $|\eta| < 2.3$ and an oppositely charged muon within $|\eta| < 2.1$. The higher- p_{T} lepton must have $p_{\text{T}} > 20$ GeV and the other lepton $p_{\text{T}} > 10$ GeV. In the $\mu\mu$ channel, the higher- p_{T} muon is required to have $p_{\text{T}} > 20$ GeV and the other muon $p_{\text{T}} > 10$ GeV. Both muons must be within $|\eta| < 2.1$.

Neutrinos produced in the τ -lepton decay are nearly collinear with the visible decay products because the τ -lepton energy is much larger than its mass after event selection. Conversely, in W +jets events where a jet is misidentified as τ_h , one of the main backgrounds in the $\ell\tau_h$ channels, the high mass of the W results in a neutrino direction approximately opposite to the lepton in the transverse plane. In the $e\tau_h$ and $\mu\tau_h$ channels, we therefore require the transverse mass

$$m_{\text{T}} = \sqrt{2p_{\text{T}}E_{\text{T}}^{\text{miss}}(1 - \cos(\Delta\phi))} \quad (3)$$

to be less than 40 GeV, where p_{T} is the lepton transverse momentum and $\Delta\phi$ is the azimuthal angle difference between the lepton momentum and the $E_{\text{T}}^{\text{miss}}$ vector. In the $e\mu$ channel, instead of an m_{T} requirement, we demand $D_{\zeta} \equiv \not{p}_{\zeta} - 0.85 \cdot p_{\zeta}^{\text{vis}} > -25$ GeV, where

$$\not{p}_{\zeta} = \vec{p}_{\text{T},1} \cdot \hat{\zeta} + \vec{p}_{\text{T},2} \cdot \hat{\zeta} + \vec{E}_{\text{T}}^{\text{miss}} \cdot \hat{\zeta}, \quad (4)$$

$$p_{\zeta}^{\text{vis}} = \vec{p}_{\text{T},1} \cdot \hat{\zeta} + \vec{p}_{\text{T},2} \cdot \hat{\zeta}. \quad (5)$$

Here, as illustrated in Fig. 25, $\hat{\zeta}$ is a unit vector along the ζ axis, defined as the bisector of the lepton directions in the transverse plane [142], $\vec{p}_{\text{T},i}$ are the lepton transverse momenta, and $\vec{E}_{\text{T}}^{\text{miss}}$ is the missing transverse energy vector.

The D_{ζ} distribution is shown in Fig. 27(b). Requiring a large D_{ζ} rejects W +jets and $t\bar{t}$ events, for which the $E_{\text{T}}^{\text{miss}}$ vector is typically oriented in the opposite direction of the two-lepton system, resulting in a small D_{ζ} . Conversely, in $H \rightarrow \tau\tau$ or $Z \rightarrow \tau\tau$ events, the neutrinos are emitted along the directions of the two τ leptons, resulting in a large D_{ζ} . The 0.85 factor is introduced to bring the mean of the D_{ζ} distribution to 0 for $Z \rightarrow \tau\tau$.

In the $\mu\mu$ channel, the sample of dimuon events is largely dominated by the $Z \rightarrow \mu\mu$ background, which is suppressed using a BDT discriminant combining a set of variables related to the kinematics of the dimuon system, and the distance of closest approach between the two muons.

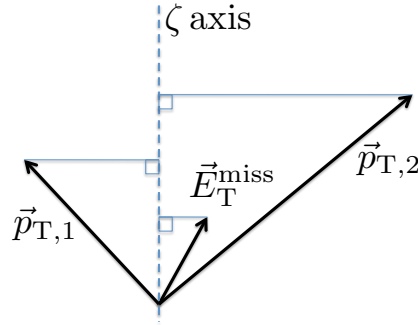


Figure 25: The ζ axis and the projections onto this axis of \vec{E}_T^{miss} and transverse momenta $\vec{p}_{T,1}$ and $\vec{p}_{T,2}$ of the two leptons.

8.2 The $\tau\tau$ invariant-mass reconstruction

The invariant mass m_{vis} of the visible decay products of the two τ leptons can be used as an estimator of the mass of a possible parent boson, in order to separate the $H \rightarrow \tau\tau$ signal from the irreducible $Z \rightarrow \tau\tau$ background. However, the neutrinos from τ -lepton decays can have substantial energy limiting the separation power of this estimator. An alternative approach is to reconstruct the neutrino energy using a collinear approximation [143], which has the disadvantage of providing an unphysical solution for about 20% of the events, in particular when the E_T^{miss} and the parent boson p_T are small. The SVFit algorithm described below reconstructs the $\tau\tau$ invariant-mass $m_{\tau\tau}$ with improved resolution and gives a physical solution for every event.

Six parameters are needed to specify τ -lepton decays to hadrons: the polar and azimuthal angles of the visible decay product system in the τ -lepton rest frame, the three boost parameters from the τ -lepton rest frame to the laboratory frame, and the invariant mass m_{vis} of the visible decay products. In the case of a leptonic τ -lepton decay, two neutrinos are produced, and the invariant mass of the two-neutrino system constitutes a seventh parameter. The unknown parameters are constrained by four observables that are the components of the four-momentum of the system formed by the visible τ -lepton decay products, measured in the laboratory frame. For each hadronic (leptonic) τ -lepton decay, 2 (3) parameters are thus left unconstrained. We choose these parameters to be:

- x , the fraction of the τ -lepton energy in the laboratory frame carried by the visible decay products.
- ϕ , the azimuthal angle of the τ -lepton direction in the laboratory frame.
- $m_{\nu\nu}$, the invariant mass of the two-neutrino system. For hadronic τ -lepton decay, $m_{\nu\nu} \equiv 0$.

The two components E_x^{miss} and E_y^{miss} of the missing transverse energy vector provide two further constraints, albeit with an experimental resolution of 10–15 GeV on each [144].

The fact that the reconstruction of the τ -lepton pair decay kinematics is underconstrained by the measured observables is addressed by a maximum-likelihood fit method. The mass $m_{\tau\tau}$ is reconstructed by combining the measured observables E_x^{miss} and E_y^{miss} with a likelihood model that includes terms for the τ -lepton decay kinematics and the E_T^{miss} resolution. The model gives the probability density $f(\vec{z}|\vec{y}, \vec{a}_1, \vec{a}_2)$ to observe the values $\vec{z} = (E_x^{\text{miss}}, E_y^{\text{miss}})$ in an event, given that the unknown parameters specifying the kinematics of the two τ -lepton decays have values $\vec{a}_1 = (x_1, \phi_1, m_{\nu\nu,1})$ and $\vec{a}_2 = (x_2, \phi_2, m_{\nu\nu,2})$, and that the four-momenta of the visible

decay products have the measured values $\vec{y} = (p_1^{\text{vis}}, p_2^{\text{vis}})$. The likelihood model is used to compute the probability

$$P(m_{\tau\tau}^i) = \int \delta\left(m_{\tau\tau}^i - m_{\tau\tau}(\vec{y}, \vec{a}_1, \vec{a}_2)\right) f(\vec{z}|\vec{y}, \vec{a}_1, \vec{a}_2) d\vec{a}_1 d\vec{a}_2, \quad (6)$$

as a function of mass hypothesis $m_{\tau\tau}^i$. The best estimate $\hat{m}_{\tau\tau}$ for $m_{\tau\tau}$ is taken to be the value of $m_{\tau\tau}^i$ that maximizes $P(m_{\tau\tau}^i)$.

The probability density $f(\vec{z}|\vec{y}, \vec{a}_1, \vec{a}_2)$ is the product of three likelihood functions. The first two model the decay parameters \vec{a}_1 and \vec{a}_2 of the two τ leptons, and the last one quantifies the consistency of a τ -lepton decay hypothesis with the measured E_T^{miss} . The likelihood functions modelling the τ -lepton decay kinematics are different for leptonic and hadronic τ -lepton decays. Matrix elements from Ref. [145] are used to model the differential distributions in the leptonic decays,

$$L_{\tau,l} = \frac{d\Gamma}{dx dm_{\nu\nu} d\phi} \propto \frac{m_{\nu\nu}}{4m_\tau^2} [(m_\tau^2 + 2m_{\nu\nu}^2)(m_\tau^2 - m_{\nu\nu}^2)], \quad (7)$$

within the physically allowed region $0 \leq x \leq 1$ and $0 \leq m_{\nu\nu} \leq m_\tau\sqrt{1-x}$. For hadronic τ -lepton decays, a model based on two-body phase-space [146] is used, treating all the τ -lepton visible decay products as a single system,

$$L_{\tau,h} = \frac{d\Gamma}{dx d\phi} \propto \frac{1}{1 - \frac{m_{\text{vis}}^2}{m_\tau^2}}, \quad (8)$$

within the physically allowed region $\frac{m_{\text{vis}}^2}{m_\tau^2} \leq x \leq 1$. We have verified that the two-body phase space model is adequate for representing hadronic τ -lepton decays by comparing distributions generated by a parameterized MC simulation based on the two-body phase-space model with the detailed simulation implemented in TAUOLA. The likelihood functions for leptonic (hadronic) τ -lepton decays do not depend on the parameters x and ϕ (x , ϕ , and $m_{\nu\nu}$). The dependence on x enters via the integration boundaries, and the dependence on ϕ comes from the E_T^{miss} likelihood function.

The E_T^{miss} likelihood function L_{MET} quantifies the compatibility of a τ -lepton decay hypothesis with the reconstructed missing transverse momentum in an event, assuming the neutrinos from the τ -lepton decays are the only source of E_T^{miss} , and is defined as

$$L_{\text{MET}}(E_x^{\text{miss}}, E_y^{\text{miss}}) = \frac{1}{2\pi\sqrt{|V|}} \cdot \exp\left(-\frac{1}{2} \begin{pmatrix} E_x^{\text{miss}} - \sum p_x^\nu \\ E_y^{\text{miss}} - \sum p_y^\nu \end{pmatrix}^T \cdot V^{-1} \cdot \begin{pmatrix} E_x^{\text{miss}} - \sum p_x^\nu \\ E_y^{\text{miss}} - \sum p_y^\nu \end{pmatrix}\right). \quad (9)$$

In this expression, the expected E_T^{miss} resolution is represented by the covariance matrix V , estimated on an event-by-event basis using a E_T^{miss} -significance algorithm [144], and $|V|$ is the determinant of this matrix.

The $m_{\tau\tau}$ resolution achieved by the SVFit algorithm is estimated to be about 20% from simulation. Figure 26 shows the normalized distributions of m_{vis} and $m_{\tau\tau}$ in the $\mu\tau_h$ channel from simulated $Z \rightarrow \tau\tau$ events and simulated SM Higgs boson events with $m_H = 125$ GeV. The SVFit mass reconstruction allows for a better separation between signal and background than m_{vis} .

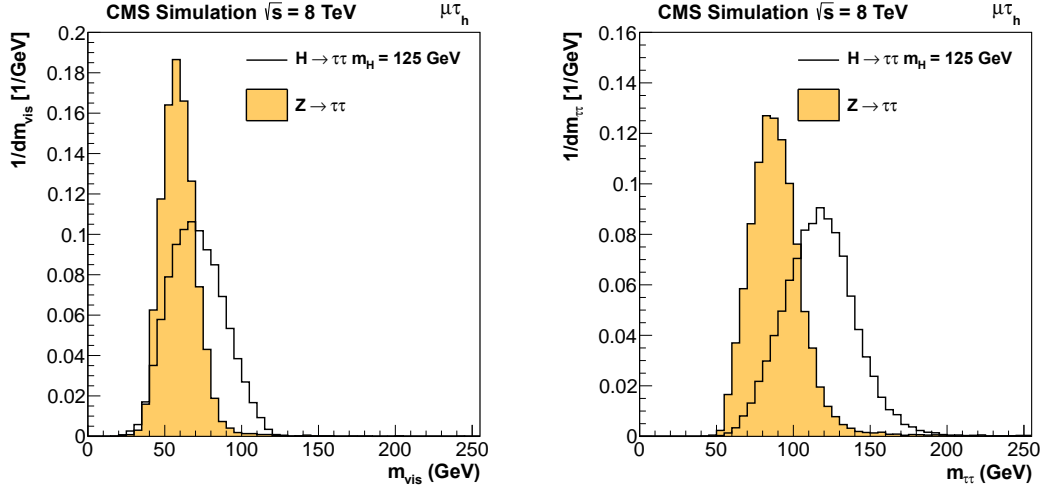


Figure 26: Normalized distribution of the visible invariant mass m_{vis} (left) and SVFit mass $m_{\tau\tau}$ (right) obtained from MC simulation in the $\mu\tau_h$ channel for the $Z \rightarrow \tau\tau$ background (solid histogram) and a SM Higgs boson signal of mass $m_H = 125$ GeV (open histogram).

8.3 Event categories

To further enhance the sensitivity of the search for the SM Higgs boson, the selected events are split into mutually exclusive categories based on the jet multiplicity, and the transverse momentum of the visible τ -lepton decay products. The jet multiplicity categories are defined using jets within $|\eta| < 5$. In some cases, events are rejected if they contain a b-tagged jet, identified using the CSV algorithm described in Section 3. From simulation, the efficiency for b-jet tagging is 75%, with a misidentification rate of 1%. The event categories are:

- **VBF:** In this category, two jets with $p_T > 30$ GeV are required in the event. A rapidity gap is demanded by requiring there be no third jet with $p_T > 30$ GeV between these two jets. A BDT discriminator is used to discriminate between VBF Higgs boson production and the background processes. This discriminator takes as input the invariant mass of the two jets, the differences in η and ϕ between the directions of the two jets, the p_T of the $\tau_h\tau_h$ system, the p_T of the $\tau_h\tau_h-E_T^{\text{miss}}$ system, the p_T of the dijet system, and the difference in η between the $\tau_h\tau_h$ system direction and the closest jet. In the $e\mu$ channel, the large $t\bar{t}$ background is suppressed by rejecting events with a b-tagged jet with $p_T > 20$ GeV.
- **1-jet:** Events in this category are required to have ≥ 1 jet with $p_T > 30$ GeV, not fulfill the VBF criteria, and not contain any b-tagged jet with $p_T > 20$ GeV. This category addresses the production of a high- p_T Higgs boson recoiling against a jet. Events with high- p_T Higgs bosons typically have much larger E_T^{miss} and thus benefit from a more precise measurement of $m_{\tau\tau}$, owing to the improved E_T^{miss} resolution. In the $e\tau_h$ channel, the large background from $Z \rightarrow ee + \text{jets}$ events with one electron misidentified as τ_h is reduced by requiring $E_T^{\text{miss}} > 30$ GeV.
- **0-jet:** This category requires events to have no jet with $p_T > 30$ GeV and no b-tagged jet with $p_T > 20$ GeV. In the $e\tau_h$ channel, E_T^{miss} is required to be larger than 30 GeV as in the 1-jet category.

The 0- and 1-jet categories are each further divided into two subsets, using the p_T of the visible τ -lepton decay products, either hadronic or leptonic. We label these subsets “low- p_T ” and

“high- p_T ”. In the $e\tau_h$ and $\mu\tau_h$ channels, the boundary between the two subsets is defined as $p_T(\tau_h) = 40$ GeV. In the $e\mu$ and $\mu\mu$ channels, the threshold is at 35 GeV on the muon p_T and 30 GeV on the leading muon p_T , respectively. Thus, five independent categories of events are used in the SM Higgs boson search: VBF, 1-jet/high- p_T , 1-jet/low- p_T , 0-jet/high- p_T , and 0-jet/low- p_T .

8.4 Background estimation and systematic uncertainties

For each channel and each category, Table 9 shows the overall number of events observed in the 7 and 8 TeV data, as well as the corresponding number of expected events from the various background contributions, in the full $m_{\tau\tau}$ range. The expected number of events from a SM Higgs boson signal of mass $m_H = 125$ GeV is also shown. The numbers in Table 9 cannot be used to estimate the global significance of a possible signal since the expected significance varies considerably with $m_{\tau\tau}$, and the sensitive 1-jet/high- p_T category is merged with the 1-jet/low- p_T category.

The largest source of background is the Drell–Yan production of $Z \rightarrow \tau\tau$. This contribution is greatly reduced by the 1-jet and VBF selection criteria, and is modelled using a data sample of $Z \rightarrow \mu\mu$ events, in which the reconstructed muons are replaced by the reconstructed particles from simulated τ -lepton decays, a technique called “embedding”. The background yield is rescaled to the $Z \rightarrow \mu\mu$ yield in the data before any jet selection, thus, for this dominant background, the systematic uncertainties in the efficiency of the jet-category selections and the luminosity measurement are negligible. In the $e\tau_h$ and $\mu\tau_h$ channels, the largest remaining systematic uncertainty affecting this background yield is in the τ_h selection efficiency. This uncertainty, which includes the uncertainty in the τ_h triggering efficiency, is estimated to be 7% from an independent study based on a tag-and-probe technique [116].

The Drell–Yan production of $Z \rightarrow \ell\ell$, labelled as Z+jets in Table 9, is an important source of background in the $e\tau_h$ channel, owing to the 2–3% probability for electrons to be misidentified as τ_h [48], and the fact that the reconstructed $\tau\tau$ invariant-mass distribution peaks in the Higgs boson mass search range. The contribution of this background in the $e\tau_h$ and $\mu\tau_h$ channels is estimated from simulation. The simulated Drell–Yan yield is rescaled to the data using $Z \rightarrow \mu\mu$ events, and the efficiencies of the jet category selections are measured in a $Z \rightarrow \mu\mu$ data sample. The dominant systematic uncertainty in the background yield is from the $\ell \rightarrow \tau_h$ misidentification rate, which is obtained by comparing tag-and-probe measurements from $Z \rightarrow \ell\ell$ events in the data and the simulation, and is 30% for electrons and 100% for muons. The very small probability for a muon to be misidentified as τ_h makes it difficult to estimate the systematic uncertainty in this probability, but also makes this background very small in the $\mu\tau_h$ channel.

The background from W+jets production contributes significantly to the $e\tau_h$ and $\mu\tau_h$ channels when the W boson decays leptonically and one jet is misidentified as a τ_h . The background is modelled for these channels using the simulation. The W+jets background yield is normalized to the data in a high- m_T control region dominated by the background in each of the five categories. The factor for extrapolating to the low- m_T signal region is obtained from the simulation, and has a 30% systematic uncertainty. In the 1-jet/high- p_T and VBF categories, where the number of simulated events is marginal, mass-shape templates are obtained by relaxing the τ_h isolation requirement, ensuring that the bias introduced in the shape is negligible. Figure 27 (upper left) shows the m_T distribution obtained in the $\mu\tau_h$ channel after the inclusive selection from data and simulation. In the high- m_T region, the agreement between the observed and expected yields comes from the normalization of the W+jets prediction to the data.

Table 9: Observed and expected numbers of events in the four $H \rightarrow \tau\tau$ decay channels and the 3 event categories, for the combined 7 and 8 TeV data. The uncertainties include the statistical and systematic uncertainties added in quadrature. In the 0- and 1-jet categories, the low- and high- p_T subcategories have been combined. The expected number of signal events for a SM Higgs boson of mass $m_H = 125$ GeV is also given.

Process	0-jet	1-jet	VBF
$e\tau_h$			
$Z \rightarrow \tau\tau$	2550 ± 200	2130 ± 170	53 ± 6
QCD	910 ± 70	410 ± 30	35 ± 8
W+jets	1210 ± 70	1111 ± 75	46 ± 10
Z+jets	560 ± 99	194 ± 24	13 ± 2
$t\bar{t}$	162 ± 21	108 ± 13	7 ± 2
Dibosons	20 ± 5	60 ± 14	1.1 ± 0.9
Total Background	5410 ± 270	4020 ± 220	155 ± 15
$H \rightarrow \tau\tau$ (125 GeV)	15 ± 2	26 ± 4	4.4 ± 0.7
Data	5273	3972	142
$\mu\tau_h$			
$Z \rightarrow \tau\tau$	$50\,500 \pm 3800$	$10\,570 \pm 830$	100 ± 11
QCD	$14\,100 \pm 1600$	3980 ± 510	41 ± 9
W+jets	$13\,300 \pm 1300$	5600 ± 480	72 ± 15
Z+jets	1620 ± 230	658 ± 97	2.5 ± 0.6
$t\bar{t}$	651 ± 82	479 ± 61	15 ± 3
Dibosons	298 ± 70	256 ± 58	3 ± 2
Total Background	$80\,400 \pm 4500$	$21\,500 \pm 1200$	234 ± 22
$H \rightarrow \tau\tau$ (125 GeV)	141 ± 21	86 ± 12	8 ± 1
Data	80 229	22 009	263
$e\mu$			
$Z \rightarrow \tau\tau$	$22\,030 \pm 850$	5030 ± 230	56 ± 5
QCD	940 ± 200	550 ± 120	7 ± 2
$t\bar{t}$	39 ± 3	831 ± 86	24 ± 6
Dibosons	796 ± 96	550 ± 120	11 ± 2
Total Background	$23\,800 \pm 930$	6960 ± 350	99 ± 9
$H \rightarrow \tau\tau$ (125 GeV)	53 ± 7	35 ± 4	3.5 ± 0.5
Data	23 274	6847	110
$\mu\mu$			
$Z \rightarrow \tau\tau$	9120 ± 490	1980 ± 120	5.3 ± 0.4
QCD	759 ± 53	341 ± 27	<1
W+jets	145 ± 10	19 ± 1	<1
$Z \rightarrow \mu\mu$	$(1263 \pm 73) \times 10^3$	$(380 \pm 24) \times 10^3$	71 ± 10
$t\bar{t}$	2440 ± 200	1330 ± 130	7 ± 2
Dibosons	1500 ± 1100	2210 ± 790	2.4 ± 0.9
Total Background	$(1277 \pm 73) \times 10^3$	$(386 \pm 24) \times 10^3$	85 ± 11
$H \rightarrow \tau\tau$ (125 GeV)	26 ± 4	16 ± 2	0.8 ± 0.1
Data	1 291 874	385 494	83

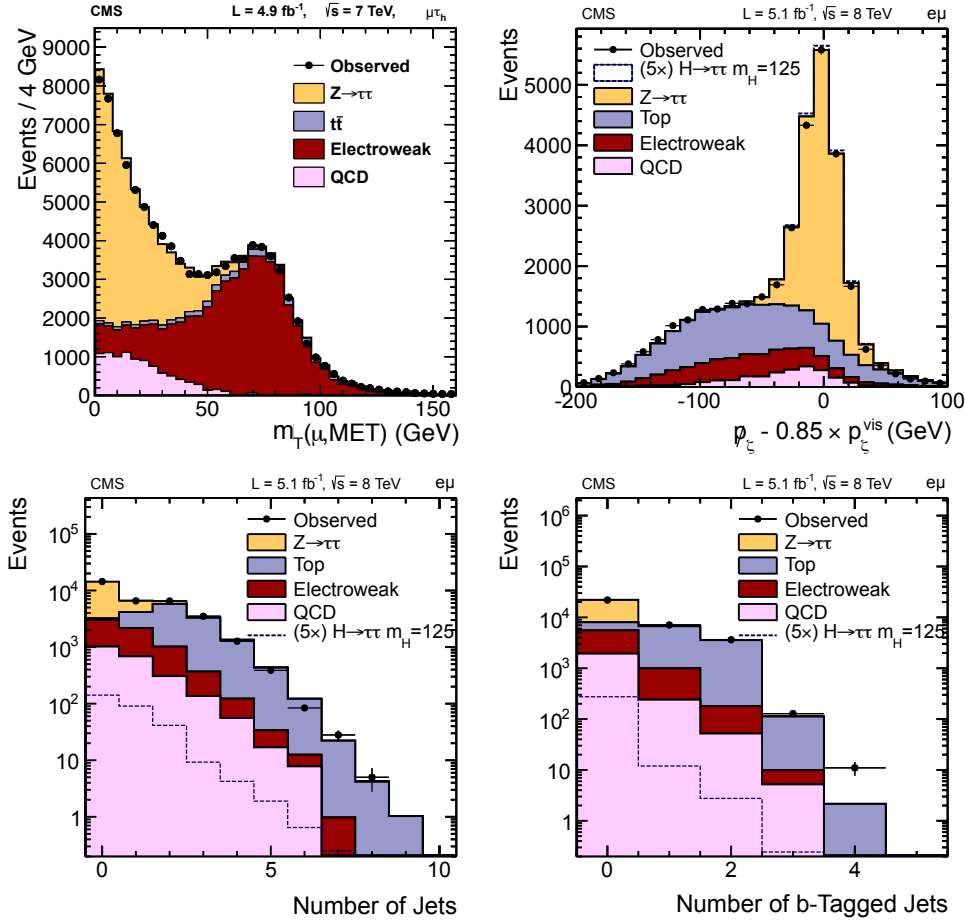


Figure 27: The observed distributions (points with error bars) for the (upper left) transverse mass m_T in the $\mu\tau_h$ channel at $\sqrt{s} = 7$ TeV; (upper right) $p_{\zeta} - 0.85 \cdot p_{\zeta}^{\text{vis}}$, (lower left) number of jets, and (lower right) number of b-tagged jets in the $e\mu$ channel at $\sqrt{s} = 8$ TeV. The expected distributions from the various background sources are shown by the shaded histograms. In particular, the Electroweak background combines the expected contributions from W +jets, Z +jets, and diboson processes. The predictions for a SM Higgs boson with $m_H = 125$ GeV are given by the dotted histograms, multiplied by a factor of 5 for clarity.

The agreement in shape indicates good modelling of E_T^{miss} in the simulation.

The $t\bar{t}$ production process is the main remaining background in the $e\mu$ channel. The predicted yield for all channels is obtained from simulation, with the yield rescaled to the one observed in the data from a $t\bar{t}$ -enriched control sample, extracted by requiring b-tagged jets. The systematic uncertainty in the yield includes a 10% systematic uncertainty in the b-tagging efficiency. Figures 27 (upper right), (lower left), and (lower right) show the distributions of D_{ζ} , the number of jets, and the number of b-tagged jets in the $e\mu$ channel. There is good agreement between the data and the background predictions in the distributions at low D_{ζ} values in Fig. 27 (upper right), and at high numbers of jets in Fig. 27 (lower left) and (lower right), where the $t\bar{t}$ process dominates.

QCD multijet events, in which one jet is misidentified as τ_h and another as a lepton, constitute another important source of background in the $e\tau_h$ and $\mu\tau_h$ channels. In the 0- and 1-jet categories, the QCD multijet background prediction is obtained using a control sample where

the lepton and the τ_h are required to have the same charge. In this control sample, the QCD multijet distribution and yield are obtained by subtracting from the data the contribution of the Drell–Yan, $t\bar{t}$, and W +jets processes, estimated as explained above. The expected contribution of the QCD multijet background in the opposite-charge signal sample is then derived by rescaling the yield obtained in the same-charge control sample by a factor of 1.1, which is measured in the data using a pure QCD multijet sample obtained by inverting the lepton isolation and relaxing the τ_h isolation. The 10% systematic uncertainty in this factor covers its small dependence on $p_T(\tau_h)$ and the statistical uncertainty in its measurement, and dominates the uncertainty in this background contribution. In the VBF category, the number of events in the same-charge control sample is too small to use this procedure. Instead, the QCD multijet yield is obtained by multiplying the inclusive QCD yield by the VBF selection efficiency measured in data using a QCD-dominated sample in which the lepton and the τ_h are not isolated. The mass shape template is obtained from data by relaxing the muon and τ_h isolation criteria.

The small background from W +jets and QCD multijet events in the $e\mu$ channel is estimated from the number of events with one identified lepton and a second lepton that passes relaxed selection criteria, but fails the nominal lepton selection. This number is converted to the expected background yield using the efficiencies for such loosely identified lepton candidates to pass the nominal lepton selection. These efficiencies are measured in data using QCD multijet events.

Finally, the small background contribution in each channel from diboson and single top-quark production is estimated using the simulation. The main experimental systematic uncertainties affecting the expected signal yield are from the τ_h identification efficiency (7%), the E_T^{miss} scale (5%), owing to the m_T requirement and the E_T^{miss} selection applied to the 0- and 1-jet categories of the $e\tau_h$ channel, the integrated luminosity (5%), and the jet energy scale ($< 4\%$). The uncertainties in the muon and electron selection efficiencies, including trigger, identification, and isolation, are both 2%. The theoretical uncertainty in the signal yield comes from the uncertainties in the PDFs, the renormalization and factorization scales, and the modelling of the underlying event and parton showers. The magnitude of the theoretical uncertainty depends on the production process (gluon-gluon fusion, VBF, or associated production) and on the event category. In particular, the scale uncertainty in the VBF production yield is 10%. The scale uncertainty in the gluon-gluon fusion production yield is 10% in the 1-jet/high- p_T category and 30% in the VBF category. The τ_h (3%) and electron (1%) energy scale uncertainties cause an uncertainty in the $m_{\tau\tau}$ spectrum shape, and are discussed in the next section. The muon energy scale uncertainty is negligible.

8.5 Results

The statistical methodology described in Section 10.1 is used to search for the presence of a SM Higgs boson signal, combining the five categories of the four final states in the 7 and 8 TeV data sets as forty independent channels in a binned likelihood based on the $m_{\tau\tau}$ distributions obtained for each channel. Systematic uncertainties are represented by nuisance parameters in the likelihood. A log-normal prior is assumed for the systematic uncertainties affecting the background normalization, discussed in the previous section. The τ_h and electron energy scale uncertainties, which affect the shape of the $m_{\tau\tau}$ spectrum, are represented by nuisance parameters whose variation results in a continuous change of this shape [147].

Figures 28 and 29 show the observed $m_{\tau\tau}$ distributions in the $e\tau_h$, $\mu\tau_h$, $e\mu$, and $\mu\mu$ channels, for each event category, compared with the background predictions. The 7 and 8 TeV data sets are merged, as well as the low- and high- p_T subcategories of the 0- and 1-jet categories. The

binning given in the figures corresponds to the binning used in the likelihood. The background mass distributions are the result of the global maximum-likelihood fit under the background-only hypothesis. This fit finds the best set of values for the nuisance parameters to match the data, assuming no signal is present. The variation of the nuisance parameters is limited by the systematic uncertainties estimated for each of the background contributions and used as input to the fit. For example, in the VBF category of the $e\tau_h$ channel, the most important nuisance parameters related to background normalization are the ones affecting the $Z \rightarrow \tau\tau$ yield (τ_h selection efficiency), the $Z \rightarrow ee$ yield ($e \rightarrow \tau_h$ misidentification rate), the W +jets yield (extrapolation from the high m_T to the low m_T region), and the QCD yield (ratio between the yields in the opposite-charge and same-charge regions). The fit makes use of the high- $m_{\tau\tau}$ region of the VBF category to constrain the nuisance parameters affecting the W +jets yield. The nuisance parameter related to the τ_h identification efficiency is mostly constrained by the 0- and 1-jet categories, where the number of events in the $Z \rightarrow \tau\tau$ peak is much larger. It is also the case for the nuisance parameter related to the τ_h energy scale, which affects the shape of the $Z \rightarrow \tau\tau$ distribution.

The interpretation of the results in terms of upper limits on the Higgs boson production cross section is given in Section 10.

9 $H \rightarrow b\bar{b}$

The decay $H \rightarrow b\bar{b}$ has the largest branching fraction of the five search modes for $m_H \leq 135$ GeV, but the signal is overwhelmed by the QCD multijet production of b quarks. The analysis is therefore designed to search for a dijet resonance in events where a Higgs boson is produced at high p_T , in association with a W or Z boson that decays leptonically, which largely suppresses the QCD multijet background. The following final states are included in the search: $W(\mu\nu)H$, $W(e\nu)H$, $Z(\mu\mu)H$, $Z(ee)H$, and $Z(\nu\nu)H$, all with the Higgs boson decaying to $b\bar{b}$. Backgrounds arise from the production of vector bosons in association with jets (from all quark flavours), singly- and pair-produced top quarks, dibosons, and QCD multijet processes. Simulated samples of signal and background events are used to optimize the analysis. Control regions in data are selected to adjust the predicted event yields from simulation for the main background processes and to estimate their contribution in the signal region.

Several different high-level triggers are used to collect events consistent with the signal hypothesis in all five channels. For the WH channels, the trigger paths consist of several single-lepton triggers with tight lepton identification. Leptons are also required to be isolated from other tracks and calorimeter energy depositions to maintain an acceptable trigger rate. For the $W(\mu\nu)H$ channel, in the 7 TeV data set, the trigger thresholds for the muon transverse momentum, p_T , vary from 17 to 40 GeV. The higher thresholds are implemented for periods of higher instantaneous luminosity. For the 8 TeV data set, the muon p_T threshold is 24 GeV for the isolated-muon trigger, and 40 GeV for muons without any isolation requirements. The combined single-muon trigger efficiency is $\approx 90\%$ for signal events that pass all offline requirements, described in Section 9.1. For the $W(e\nu)H$ channel, in the 7 TeV data set, the electron p_T threshold ranges from 17 to 30 GeV. In addition, two jets and a minimum value on the missing transverse energy are required. These additional requirements help to maintain acceptable trigger rates during the periods of high instantaneous luminosity. For the 8 TeV data set, a single-isolated-electron trigger is used with a 27 GeV p_T threshold. The combined efficiency for these triggers for signal events that pass the final offline selection criteria is larger than 95%.

The $Z(\mu\mu)H$ channel uses the same single-muon triggers as the $W(\mu\nu)H$ channel. For the $Z(ee)H$ channel, dielectron triggers with lower- p_T thresholds of 17 and 8 GeV and tight isola-

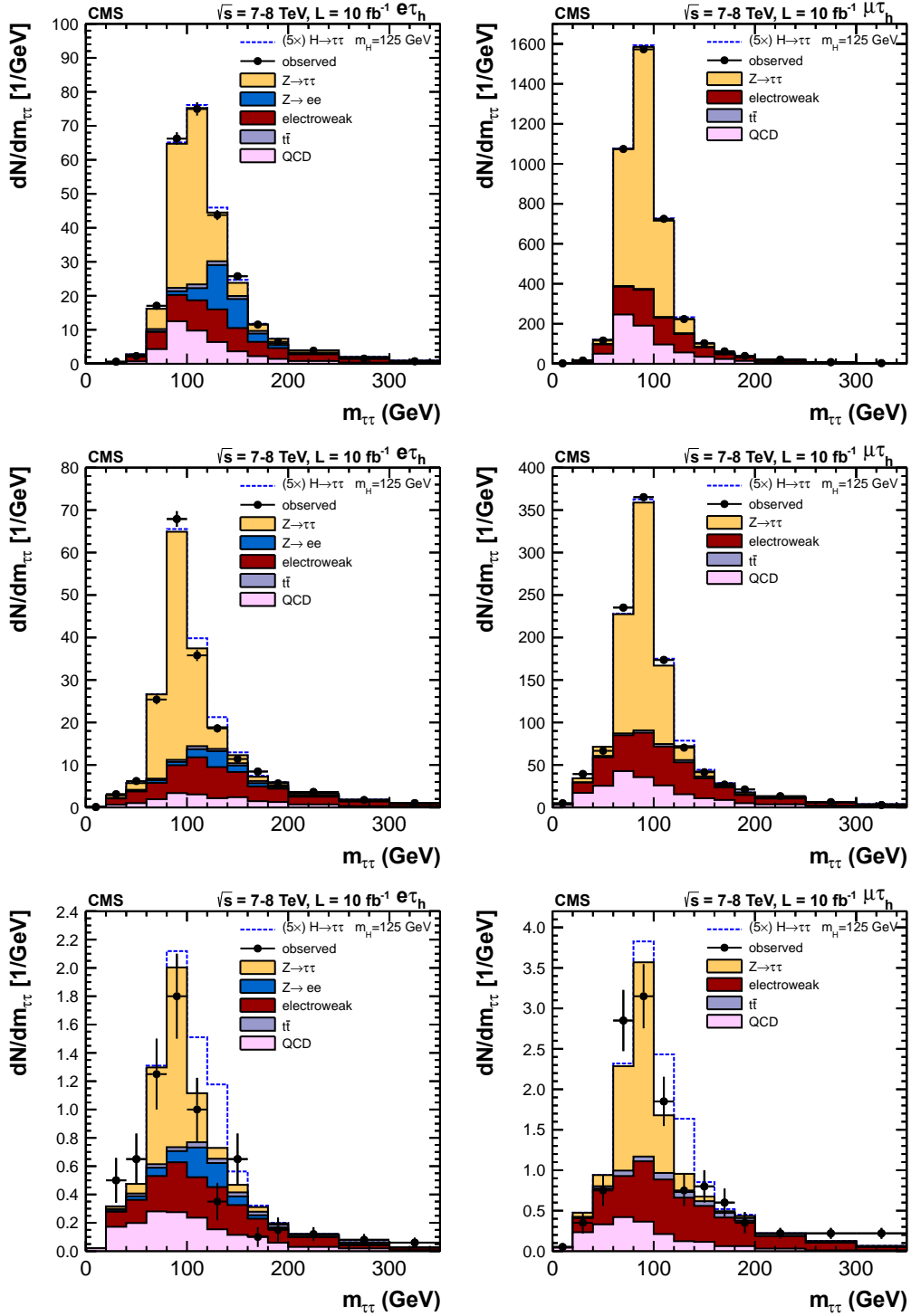


Figure 28: Observed (points with error bars) and expected (histograms) $m_{\tau\tau}$ distributions for the $e\tau_h$ (left) and $\mu\tau_h$ (right) channels, and, from top to bottom, the 0-jet, 1-jet, and VBF categories for the combined 7 and 8 TeV data sets. In the 0- and 1-jet categories, the low- and high- p_T subcategories have been summed. The electroweak background combines the expected contributions from W +jets, Z +jets, and diboson processes. In the case of $e\tau_h$, the $Z \rightarrow ee$ background is shown separately. The dotted histogram shows the expected distribution for a SM Higgs boson with $m_H = 125$ GeV (multiplied by a factor of 5 for clarity).

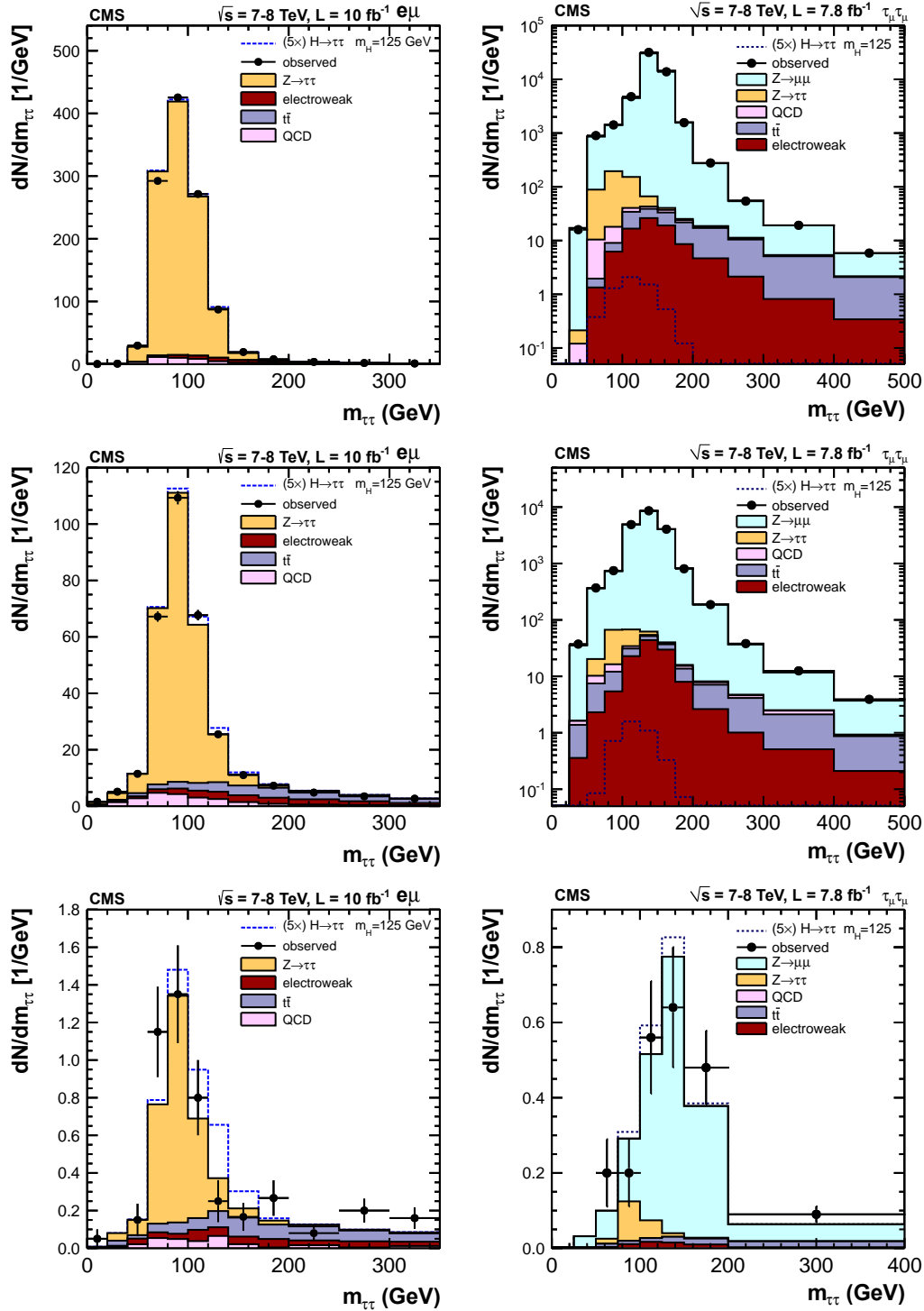


Figure 29: Observed (points with error bars) and expected (histograms) $m_{\tau\tau}$ distributions for the $e\mu$ (left) and $\mu\mu$ (right) channels, and, from top to bottom, the 0-jet, 1-jet, and VBF categories for the combined 7 and 8 TeV data sets. In the 0- and 1-jet categories, the low- and high- p_T subcategories have been summed. The electroweak background combines the contributions from W +jets, Z +jets, and diboson processes. In the case of $\mu\mu$, the $Z \rightarrow \mu\mu$ background is shown separately. The dotted histogram shows the expected distribution for a SM Higgs boson with $m_H = 125$ GeV (multiplied by a factor of 5 for clarity).

tion requirements are used. These triggers are $\approx 99\%$ efficient for ZH signal events that pass the final offline selection criteria. For the $Z(\nu\nu)H$ channel, combinations of several triggers are used, all with the requirement that the missing transverse energy be above a certain threshold. Additional jet requirements are made to keep the trigger rates acceptable as the luminosity increases and to reduce the E_T^{miss} thresholds, in order to increase the signal acceptance. A trigger with $E_T^{\text{miss}} > 150$ GeV requirement is implemented for both the 7 and 8 TeV data sets. For the 7 TeV data, triggers that require the presence of two jets with $|\eta| < 2.6$, $p_T > 20$ GeV, and E_T^{miss} thresholds of 80 and 100 GeV, depending on the instantaneous luminosity, are also used. For the 8 TeV data set, a trigger that requires two jets, each with $|\eta| < 2.6$ and $p_T > 30$ GeV, and $E_T^{\text{miss}} > 80$ GeV is also implemented. As the instantaneous luminosity increased further, this trigger was replaced by one requiring $E_T^{\text{miss}} > 100$ GeV, two jets with $|\eta| < 2.6$, one with $p_T > 60$ GeV and the other with $p_T > 25$ GeV, the dijet $p_T > 100$ GeV, and no jet with $p_T > 40$ GeV within 0.5 radians in azimuthal angle of the E_T^{miss} vector. For $Z(\nu\nu)H$ signal events with missing transverse energy > 160 GeV, the overall trigger efficiency is $\approx 98\%$ with respect to the offline event reconstruction and selection described below. The corresponding efficiency for $120 < E_T^{\text{miss}} < 160$ GeV is about 66%.

9.1 Event selection

The final-state objects used in the $H \rightarrow bb$ event reconstruction are described in Section 3. Electron candidates are considered in the pseudorapidity range $|\eta| < 2.5$, excluding the $1.44 < |\eta| < 1.57$ transition region between the ECAL barrel and endcaps. Tight muon candidates are considered in the $|\eta| < 2.4$ range. An isolation requirement on R_{Iso}^ℓ of approximately 10%, as calculated in Eq. (1), that is consistent with the expectation for leptons originating from W and Z boson decays, is applied to electron and muon candidates. The exact requirement depends on the lepton η , p_T , and flavour. To identify b jets, different values for the CSV output discriminant, which can range between 0 and 1, are used, with corresponding different efficiencies and misidentification rates. For example, with a CSV > 0.90 requirement, the efficiencies to tag b quarks, c quarks, and light quarks, are 50%, 6%, and 0.15%, respectively [31]. The corresponding efficiencies for CSV > 0.50 are 72%, 23%, and 3%. All events from data and simulation are required to pass the same trigger and event reconstruction algorithms. Scale factors that account for differences in the performance of these algorithms between data and simulation are computed and used in the analysis.

The background processes to VH production are V+jets, $t\bar{t}$, single-top-quark, diboson (VV), and QCD multijet production. These overwhelm the signal by several orders of magnitude. The event selection is based on the kinematic reconstruction of the vector boson and the Higgs boson decay into two b-tagged jets. Backgrounds are then substantially reduced by requiring a significant boost of the p_T of the vector boson and the Higgs boson [148], which tend to recoil from each other with a large azimuthal opening angle, $\Delta\phi(V,H)$, between them. For each channel, two ranges of $p_T(V)$ are considered. These are referred to as “low” and “high”. Owing to different signal and background compositions, each $p_T(V)$ range has a different sensitivity, and the analysis is performed separately for each range. The results from all the ranges are then combined for each channel. The ranges for the WH channels are $120 < p_T(V) < 170$ GeV and $p_T(V) > 170$ GeV, for the $Z(\nu\nu)H$ channel $120 < p_T(V) < 160$ GeV and $p_T(V) > 160$ GeV, and for the $Z(\ell\ell)H$ channel $50 < p_T(V) < 100$ GeV and $p_T(V) > 100$ GeV.

Candidate $W \rightarrow \ell\nu$ decays are identified by requiring the presence of a single isolated lepton and missing transverse energy. Muons (electrons) are required to have a p_T above 20 (30) GeV. For the $W(e\nu)H$ channel only, to reduce contamination from QCD multijet processes, E_T^{miss} is required to be greater than 35 GeV. Candidate $Z \rightarrow \ell\ell$ decays are reconstructed by combin-

ing isolated, oppositely charged pairs of electrons or muons with $p_T > 20$ GeV and a dilepton invariant mass satisfying $75 < m_{\ell\ell} < 105$ GeV. The identification of $Z \rightarrow \nu\bar{\nu}$ decays requires the E_T^{miss} in the event to be within the $p_T(V)$ ranges described above. Two requirements suppress events from QCD multijet processes with an E_T^{miss} arising from mismeasured jets. First, the E_T^{miss} vector must be isolated from jet activity, using the requirement that the azimuthal angle difference $\Delta\phi(E_T^{\text{miss}}, j)$ between the E_T^{miss} direction and any jet with $|\eta| < 2.5$ and $p_T > 20$ (30) GeV be greater than 0.5 radians for the 7 (8) TeV data sample. Second, the azimuthal angle between the E_T^{miss} vector calculated using only charged particles with $p_T > 0.5$ GeV and $|\eta| < 2.5$ and the direction of the standard E_T^{miss} vector (calculated using all particles, charged and neutral) must be greater than 0.5 radians. Subject to these two requirements, background from QCD multijet processes is reduced to a negligible level in the $Z(\nu\nu)H$ channel. To reduce the $t\bar{t}$ and WZ background in the WH and $Z(\nu\nu)H$ channels, events where the number of additional isolated leptons with $p_T > 20$ GeV is greater than 0 are rejected.

Reconstruction of the $H \rightarrow b\bar{b}$ decay is done by requiring two jets above the minimum p_T thresholds listed in Table 10, having $|\eta| < 2.5$, and tagged by the CSV algorithm. If more than two such jets are found in the event, the pair with the highest total dijet transverse momentum, $p_T(jj)$, is selected. The background from V +jets and dibosons is reduced significantly through b tagging, and subprocesses where the two jets originate from genuine b quarks dominate the final selected data sample. After all the event selection criteria are applied, the invariant-mass resolution for the Higgs boson decay to $b\bar{b}$ is approximately 10%, as found in a previous CMS analysis [149]. The mass resolution is improved here by applying regression techniques similar to those used by the CDF experiment [150]. Through this procedure, a further correction, beyond the standard jet energy corrections, is computed for individual b jets in order to better measure the true parton energy. A BDT algorithm is trained on simulated $H \rightarrow b\bar{b}$ signal events, with inputs that include detailed information about each jet that helps to differentiate b -quark jets from light-flavour jets. The resulting improvement in the $b\bar{b}$ invariant-mass resolution is approximately 15%, resulting in an increase in the analysis sensitivity of 10–20%, depending on the specific channel. The BDT regression is implemented in the TMVA framework [40]. The complete set of input variables is (though not all variables are used for every channel):

- transverse momentum of the jet before and after energy corrections;
- transverse energy and mass of the jet after energy correction;
- uncertainty in the jet energy correction;
- transverse momentum of the highest- p_T constituent in the jet;
- pseudorapidity of the jet;
- total number of jet constituents;
- length and uncertainty of the displacement of the jet's secondary vertex;
- mass and transverse momentum of the jet's secondary vertex;
- number and fraction of jet constituents that are charged;
- event energy density, ρ , calculated using constituents with $|\eta| < 2.5$;
- missing transverse energy in the event;
- azimuthal angle between the missing transverse energy vector and the direction of the nearest jet in pseudorapidity.

To better discriminate the signal from background for different Higgs boson mass hypotheses, an event classification BDT algorithm is trained separately for each mass value using simu-

Table 10: Selection criteria for the simulated event samples used in training of the signal and background BDT algorithm. Variables marked “-” are not used in the given channel. Entries in parentheses indicate the selection for the high- $p_T(V)$ range. The second and third rows refer to the p_T threshold for the highest- and second-highest- p_T jet, respectively, for the pair with the highest total dijet transverse momentum, $p_T(jj)$. The parameter N_{al} is the number of additional isolated leptons in the event. Kinematic variables are given in GeV and angles in radians.

Variable	$W(\ell\nu)H$	$Z(\ell\ell)H$	$Z(\nu\nu)H$
$m_{\ell\ell}$	-	$\in [75 - 105]$	-
$p_T(j_1)$	> 30	> 20	> 80
$p_T(j_2)$	> 30	> 20	> 30
$p_T(jj)$	> 120	-	$\in [120 - 160] (> 160)$
$m(jj)$	< 250	$\in [80 - 150] (-)$	< 250
$p_T(V)$	$\in [120 - 170] (> 170)$	$\in [50 - 100] (> 100)$	-
CSV_{max}	> 0.40	0.50 (0.244)	> 0.679
CSV_{min}	> 0.40	0.244	> 0.244
N_{al}	$= 0$	-	$= 0$
E_T^{miss}	$> 35(e)$	-	$\in [120 - 160] (> 160)$
$\Delta\phi(E_T^{miss}, j)$	-	-	> 0.5
$\Delta\phi(V,H)$	-	-	> 2.0

Table 11: Variables used for training the signal and background BDT algorithm.

Variable	definition
p_{T_j}	transverse momentum of each b jet from the Higgs boson decay
$m(jj)$	dijet invariant mass
$p_T(jj)$	dijet transverse momentum
$p_T(V)$	vector boson transverse momentum
CSV_{max}	value of CSV for the b-tagged jet with the largest CSV value
CSV_{min}	value of CSV for the b-tagged jet with the second largest CSV value
$\Delta\phi(V,H)$	azimuthal angle between the vector boson (or E_T^{miss} vector) and the dijet direction
$ \Delta\eta(jj) $	difference in η between b jets from Higgs boson decay
$\Delta R(j_1, j_2)$	distance in η - ϕ between b jets from Higgs boson decay (not for $Z(\ell\ell)H$)
N_{aj}	number of additional jets
$\Delta\phi(E_T^{miss}, j)$	azimuthal angle between E_T^{miss} and the closest jet (only for $Z(\nu\nu)H$)

lated samples of signal and background events that pass the selection criteria described above, together with the requirements listed in Table 10. The set of input variables used in training this BDT is chosen by iterative optimization from a larger number of potentially discriminating variables. Table 11 lists these variables. The number N_{aj} of additional jets in an event counts jets that satisfy $p_T > 20$ GeV and $|\eta| < 4.5$ for $W(\ell\nu)H$, $p_T > 20$ GeV and $|\eta| < 2.5$ for $Z(\ell\ell)H$, or $p_T > 30$ GeV and $|\eta| < 4.5$ for $Z(\nu\nu)H$. The output distribution of this BDT algorithm is fitted to search for events from Higgs boson production. Fitting this distribution, rather than simply counting events in a range of the distribution with a good signal-to-background ratio, as in Ref. [149], improves the sensitivity of the analysis by approximately 20%.

Table 12: Definitions of the control regions for the simulated sample of Z+jets and $t\bar{t}$ backgrounds in the $Z(\ell\ell)H$ channel. The same selection is used for the low- and high- $p_T(V)$ ranges. The values of kinematical variables are in GeV.

Variable	Z+jets	$t\bar{t}$
$m_{\ell\ell}$	$\in [75 - 105]$	$\notin [75 - 105]$
$p_T(j_1)$	> 20	> 20
$p_T(j_2)$	> 20	> 20
$p_T(V)$	$\in [50 - 100]$	$\in [50 - 100]$
CSV_{\max}	> 0.244	> 0.244
CSV_{\min}	> 0.244	> 0.244
$m(jj)$	$\notin [80 - 150], < 250$	$\notin [80 - 150], < 250$

9.2 Background control regions

Control regions are identified in the data and used to correct the estimated yields from the MC simulation for two of the important background processes: $t\bar{t}$ production and V+jets, originating from light-flavour partons (u, d, s, or c quarks and gluons) or from heavy-flavour (b quarks). Simultaneous fits are then performed to the distributions of the discriminating variables in the control regions to obtain scale factors by which the simulation yields are adjusted. This procedure is performed separately for each channel. For the $Z(\ell\ell)H$ and WH modes the scale factors derived for the electron and muon decay channels are combined. These scale factors account not only for possible simulation cross-section discrepancies with the data, but also for potential differences in the selection efficiencies for the various physics object. Therefore, separate scale factors are used for each background process in the different channels. The uncertainties in the scale factor determination include a statistical uncertainty from the fits (owing to the finite size of the samples) and an associated systematic uncertainty. The latter is estimated by refitting the distributions in the control regions after applying estimates for sources of potential systematic shifts such as b-jet-tagging efficiency, jet energy scale, and jet energy resolution.

Tables 12–14 list the selection criteria used for the control regions in the $Z(\ell\ell)H$, $Z(\nu\nu)H$ and WH channels, respectively. Table 15 summarizes the fit results for all channels separately for the 7 TeV and 8 TeV data sets. The fit results are found to be robust and the fitted scale factors are consistent with the values from the previous analysis [149].

9.3 Systematic uncertainties

Sources of systematic uncertainty in the expected signal and background yields and distribution shapes are listed in Table 16. The uncertainty in the integrated luminosity measurement is 2.2% for the 7 TeV data [151] and 4.4% for the 8 TeV data [135]. Muon and electron trigger, reconstruction, and identification efficiencies are determined in data from samples of leptonic Z boson decays. The uncertainty in the yields due to the trigger efficiency is 2% per charged lepton and the uncertainty in the identification efficiency is also 2% per lepton. The parameters describing the $Z(\nu\nu)H$ trigger efficiency turn-on curve are varied within their statistical uncertainties and for different assumptions on the methodology. A 2% systematic uncertainty in the yield is estimated.

The jet energy scale is varied by ± 1 standard deviation as a function of the jet p_T and η , and the efficiency of the analysis selection is recomputed. A 2–3% yield variation is found, depending

Table 13: Definitions of the control regions for the simulated samples of V+jets and $t\bar{t}$ background processes in the $Z(\nu\nu)H$ channel for the low- and high- $p_T(V)$ regions. The values in parentheses are for the high- $p_T(V)$ region. The labels LF and HF refer to light- and heavy-flavour jets. The parameter N_{al} is the number of additional isolated leptons in the event. The values for kinematical variables are in GeV.

Variable	Z+jets (LF)	Z+jets (HF)	$t\bar{t}$	W+jets (LF)	W+jets (HF)
$p_T(j_1)$	$> 60(> 80)$	$> 60(> 80)$	$> 60(> 80)$	$> 60(> 80)$	$> 60(> 80)$
$p_T(j_2)$	> 30	> 30	> 30	> 30	> 30
$p_T(jj)$	$> 120(> 160)$	$> 120(> 160)$	$> 120(> 160)$	$> 120(> 160)$	$> 120(> 160)$
CSV_{max}	-	>0.898	>0.898	-	>0.898
N_{aj}	-	-	1	0	0
N_{al}	0	0	1	1	1
E_T^{miss}	$\in[120-160] (> 160)$	$\in[120-160] (> 160)$	$\in[120-160] (> 160)$	$\in[120-160] (> 160)$	$\in[120-160] (> 160)$
$m(jj)$	-	$\notin[90-150]$	$\notin[90-150]$	-	$\notin[90-150]$

Table 14: Definitions of the control regions for the simulated samples of three background processes in the $W(\ell\nu)H$ channel for the low- and high- $p_T(V)$ regions. The values in parentheses are used for the high- $p_T(V)$ region. The labels LF and HF refer to light- and heavy-flavour jets. The parameter N_{al} is the number of additional isolated leptons in the event, and METsig is the ratio of the E_T^{miss} value to its uncertainty [144]. The values for kinematical variables are in GeV. The symbols e and μ mean that the selection is used only for the $W(e\nu)H$ mode or $W(\mu\nu)H$ mode, respectively.

Variable	W+jets (LF)	$t\bar{t}$	W+jets (HF)
$p_T(j_1)$	>30	>30	>30
$p_T(j_2)$	>30	>30	>30
$p_T(jj)$	>120	>120	>120
$p_T(V)$	$\in [120 - 170] (>170)$	$\in [120 - 170] (>170)$	$\in [120 - 170] (>170)$
CSV_{max}	-	>0.898	>0.898
N_{aj}	<2	>1	$=0$
N_{al}	$=0$	$=0$	$=0$
E_T^{miss}	>35 (e)	>35 (e)	>35 (e)
METsig	$>2.0(\mu), >3.0(e)$	-	-
$m(jj)$	<250	<250	$\notin [90 - 150]$

Table 15: Data/MC scale factors for the control region in each Higgs boson production process with the 7 TeV and 8 TeV data sets in the low- and high- $p_T(V)$ ranges. The uncertainties shown are statistical and systematic, respectively. The labels LF and HF refer to light- and heavy-flavour jets.

Process	WH	WH	Z($\ell\ell$)H	Z($\ell\ell$)H	Z($\nu\nu$)H	Z($\nu\nu$)H
Low- $p_T(V)$	7 TeV	8 TeV	7 TeV	8 TeV	7 TeV	8 TeV
W+jets (LF)	$0.88 \pm 0.01 \pm 0.03$	$0.97 \pm 0.01 \pm 0.03$	–	–	$0.89 \pm 0.01 \pm 0.03$	$0.91 \pm 0.03 \pm 0.03$
W+jets (HF)	$1.91 \pm 0.14 \pm 0.31$	$2.05 \pm 0.21 \pm 0.33$	–	–	$1.36 \pm 0.10 \pm 0.15$	$1.63 \pm 0.29 \pm 0.14$
Z+jets (LF)	–	–	$1.11 \pm 0.03 \pm 0.11$	$1.41 \pm 0.03 \pm 0.16$	$0.87 \pm 0.01 \pm 0.03$	$1.01 \pm 0.05 \pm 0.03$
Z+jets (HF)	–	–	$0.98 \pm 0.05 \pm 0.12$	$1.04 \pm 0.05 \pm 0.20$	$0.96 \pm 0.02 \pm 0.03$	$1.00 \pm 0.10 \pm 0.04$
$t\bar{t}$	$0.93 \pm 0.02 \pm 0.05$	$1.12 \pm 0.01 \pm 0.06$	$1.03 \pm 0.04 \pm 0.11$	$1.06 \pm 0.03 \pm 0.11$	$0.97 \pm 0.02 \pm 0.04$	$1.02 \pm 0.03 \pm 0.03$
High- $p_T(V)$	7 TeV	8 TeV	7 TeV	8 TeV	7 TeV	8 TeV
W+jets (LF)	$0.79 \pm 0.01 \pm 0.02$	$0.88 \pm 0.01 \pm 0.02$	–	–	$0.78 \pm 0.02 \pm 0.03$	$0.86 \pm 0.03 \pm 0.03$
W+jets (HF)	$1.49 \pm 0.14 \pm 0.19$	$1.30 \pm 0.20 \pm 0.17$	–	–	$1.48 \pm 0.15 \pm 0.20$	$1.43 \pm 0.28 \pm 0.18$
Z+jets (LF)	–	–	$1.11 \pm 0.03 \pm 0.11$	$1.41 \pm 0.03 \pm 0.16$	$0.97 \pm 0.02 \pm 0.04$	$1.01 \pm 0.04 \pm 0.04$
Z+jets (HF)	–	–	$0.98 \pm 0.05 \pm 0.12$	$1.03 \pm 0.05 \pm 0.20$	$1.08 \pm 0.09 \pm 0.06$	$1.06 \pm 0.06 \pm 0.07$
$t\bar{t}$	$0.84 \pm 0.02 \pm 0.03$	$0.97 \pm 0.02 \pm 0.03$	$1.03 \pm 0.04 \pm 0.11$	$1.06 \pm 0.03 \pm 0.11$	$0.97 \pm 0.02 \pm 0.04$	$1.03 \pm 0.04 \pm 0.04$

on the particular decay channel and production process. The effect of the uncertainty in the jet energy resolution is evaluated by smearing the jet energies by the measured uncertainty, giving a 3–6% variation in yields. The uncertainties in the jet energy scale and resolution also affect the shape of the BDT output distribution. The impact of the jet energy scale uncertainty is determined by recomputing the BDT distribution after shifting the energy scale up and down by its uncertainty. Similarly, the impact of the jet energy resolution is determined by recomputing the BDT distribution after increasing or reducing the jet energy resolution.

Data-to-simulation b-tagging-efficiency scale factors, measured in $t\bar{t}$ events and multijet events, are applied to the jets in signal and background events. The estimated systematic uncertainties in the b-tagging scale factors are: 6% per b tag, 12% per c tag, and 15% per mistagged jet (originating from gluons and light quarks) [31]. These translate into yield uncertainties in the 3–15% range, depending on the channel and the production process. The shape of the BDT output distribution is also affected by the shape of the CSV distribution, and therefore recomputed according to the range of variations of the CSV distributions.

The theoretical VH signal cross section is calculated to NNLO, and the systematic uncertainty is 4% [25], including the effects of scale and PDF variations [95–99]. The analysis described in this paper is performed in the regime where the V and H have a significant boost in p_T , and thus, potential differences in the p_T spectrum of the V and H between the data and the MC simulation generators could introduce systematic effects in the estimates of the signal acceptance and efficiency. Theoretical calculations are available that estimate the NLO electroweak (EW) [83, 152, 153] and NNLO QCD [84] corrections to VH production in the boosted regime. The estimated effect from electroweak corrections for a boost of ≈ 150 GeV are 5% for ZH and 10% for WH. For the QCD correction, a 10% uncertainty is estimated for both ZH and WH, which includes effects due to additional jet activity from initial- and final-state radiation. The finite size of the signal MC simulation samples, after all selection criteria are applied, contributes an uncertainty of 1–5% in the various channels.

The total uncertainty in the prediction of the background yields from estimates using data is approximately 10%. For the V+jets background, the differences in the BDT output distribution for events from the MADGRAPH and HERWIG++ MC simulation generators are considered. For the single-top-quark and diboson yield predictions, which are obtained solely from simulation, a 30% systematic uncertainty in the cross sections is used.

Table 16: Systematic uncertainties in the predicted signal and background yields from the sources listed. The ranges give the variations over the 7 and 8 TeV data sets, different search channels, specific processes, and Higgs boson mass hypotheses. The acronym EWK stands for electroweak.

Source	Range (%)
Integrated luminosity	2.2–4.4
Lepton identification and trigger efficiency (per lepton)	3
$Z(\nu\nu)H$ triggers	2
Jet energy scale	2–3
Jet energy resolution	3–6
Missing transverse energy	3
b-tagging efficiency	3–15
Signal cross section (scale and PDF)	4
Signal cross section (p_T boost, EWK/QCD)	5–10/10
Statistical precision of signal simulation	1–5
Backgrounds estimated from data	10
Backgrounds estimated from simulation	30

9.4 Results

Maximum-likelihood fits are performed to the output distributions of the BDT algorithms, trained separately for each channel and each Higgs boson mass value hypothesis in the 110–135 GeV range. In the fit, the BDT shapes and normalizations, for signal and each background component, are allowed to vary within the systematic and statistical uncertainties described in Section 9.3. These uncertainties are treated as nuisance parameters, with appropriate correlations taken into account.

Tables 17–20 summarize the expected signal and background yields for both $p_T(V)$ bins in each channel from the 7 TeV and 8 TeV data. All the data/MC scale factors determined in Section 9.2 have been applied to the corresponding background yields. Examples of output BDT distributions, for the $m_H = 125$ GeV training and for the high $p_T(V)$ bin, are shown in Figure 30. The signal and background shapes and normalizations are those returned by the fits. Figure 30 also shows the dijet invariant-mass distribution for the combination of all five channels in the combined 7 and 8 TeV data sets, using an event selection that is more restrictive than the one used in the BDT analysis and that is more suitable for a counting experiment in just this observable. The events considered are those in the high $p_T(V)$ bin with tighter b-tagging requirements on both jets, and with requirements that there be no additional jets in the events and that the azimuthal opening angle between the dijet system and the reconstructed vector boson be large. The $H \rightarrow bb$ search with such a selection is significantly less sensitive than the search using the BDT discriminant and it is therefore not elaborated on further in this article.

The interpretation of the results from the BDT discriminant analysis, in terms of upper limits on the Higgs boson production cross section, is given in Section 10.

10 Combined results

In this section, we present the results obtained by combining the measurements from all five search channels described above. We begin with a short summary of the statistical method used to combine the analyses.

Table 17: Predicted signal and background yields (statistical uncertainty only) in the BDT output distribution for the low- $p_T(V)$ range with the 7 TeV data for each of the five channels. The labels LF and HF refer to light- and heavy-flavour jets. The numbers in parentheses refer to the Higgs boson mass hypothesis in GeV.

Process	Z($\mu\mu$)H	Z(ee)H	Z($\nu\nu$)H	W($\mu\nu$)H	W($e\nu$)H
Z+jets (LF)	176 \pm 14	255 \pm 18	158.3 \pm 6.1	11.0 \pm 1.5	1.87 \pm 0.56
Z+jets (HF)	235 \pm 16	225 \pm 16	254.9 \pm 5.5	23.2 \pm 2.1	2.71 \pm 0.68
W+jets (LF)	–	–	133.1 \pm 8.1	124.6 \pm 4.6	58.5 \pm 3.1
W+jets (HF)	–	–	171.85 \pm 7.1	248.3 \pm 9.5	135.3 \pm 7.0
$t\bar{t}$	74.2 \pm 1.9	64.3 \pm 1.7	898.5 \pm 5.2	894.6 \pm 4.1	575.5 \pm 3.3
Single Top	3.73 \pm 0.72	2.67 \pm 0.64	98.5 \pm 5.9	123.1 \pm 3.0	67.7 \pm 2.2
VV	10.77 \pm 0.53	10.07 \pm 0.55	33.5 \pm 1.5	15.10 \pm 0.72	7.89 \pm 0.54
ZH(110)	2.72 \pm 0.03	2.19 \pm 0.03	6.19 \pm 0.05	0.28 \pm 0.02	0.08 \pm 0.01
WH(110)	–	–	3.19 \pm 0.04	4.98 \pm 0.08	2.96 \pm 0.06
ZH(115)	2.34 \pm 0.03	1.88 \pm 0.03	4.52 \pm 0.05	0.21 \pm 0.01	0.07 \pm 0.01
WH(115)	–	–	2.36 \pm 0.03	4.57 \pm 0.07	2.58 \pm 0.05
ZH(120)	1.93 \pm 0.02	1.56 \pm 0.02	4.10 \pm 0.04	0.19 \pm 0.01	0.07 \pm 0.01
WH(120)	–	–	2.15 \pm 0.04	3.90 \pm 0.05	2.17 \pm 0.04
ZH(125)	1.52 \pm 0.02	1.23 \pm 0.02	3.67 \pm 0.04	0.18 \pm 0.01	0.06 \pm 0.01
WH(125)	–	–	1.94 \pm 0.04	3.19 \pm 0.04	1.90 \pm 0.03
ZH(130)	1.19 \pm 0.01	0.95 \pm 0.01	2.81 \pm 0.04	0.15 \pm 0.01	0.05 \pm 0.01
WH(130)	–	–	1.25 \pm 0.03	2.56 \pm 0.04	1.50 \pm 0.03
ZH(135)	0.83 \pm 0.01	0.67 \pm 0.01	2.10 \pm 0.02	0.11 \pm 0.01	0.03 \pm 0.01
WH(135)	–	–	0.87 \pm 0.02	1.92 \pm 0.02	1.13 \pm 0.02
Sum	500 \pm 22	558 \pm 24	1749 \pm 16	1440 \pm 12	850 \pm 9
Data	493	512	1793	1411	925

Table 18: Predicted signal and background yields (statistical uncertainty only) in the BDT output distribution for the high- $p_T(V)$ range with the 7 TeV data for each of the five channels. The labels LF and HF refer to light- and heavy-flavour jets. The numbers in parentheses refer to the Higgs boson mass hypothesis in GeV.

Process	Z($\mu\mu$)H	Z(ee)H	Z($\nu\nu$)H	W($\mu\nu$)H	W($e\nu$)H
Z+jets (LF)	291 \pm 15	275 \pm 15	107.7 \pm 3.1	3.47 \pm 0.79	1.63 \pm 0.52
Z+jets (HF)	180 \pm 11	160 \pm 10	117.0 \pm 4.6	6.7 \pm 1.2	2.13 \pm 0.59
W+jets (LF)	–	–	81.4 \pm 3.8	61.9 \pm 3.0	41.4 \pm 2.5
W+jets (HF)	–	–	171.7 \pm 5.9	129.5 \pm 6.1	67.8 \pm 4.4
$t\bar{t}$	41.7 \pm 1.4	39.4 \pm 1.3	275.7 \pm 3.0	302.4 \pm 2.3	225.0 \pm 2.0
Single Top	1.49 \pm 0.45	3.44 \pm 0.71	37.9 \pm 3.4	60.8 \pm 2.1	41.6 \pm 1.7
VV	14.02 \pm 0.67	11.68 \pm 0.60	24.6 \pm 2.8	9.71 \pm 0.58	6.28 \pm 0.47
ZH(110)	3.19 \pm 0.04	2.69 \pm 0.03	5.75 \pm 0.04	0.14 \pm 0.01	0.07 \pm 0.01
WH(110)	–	–	1.88 \pm 0.06	4.39 \pm 0.07	3.18 \pm 0.06
ZH(115)	2.78 \pm 0.03	2.37 \pm 0.027	5.87 \pm 0.05	0.08 \pm 0.01	0.04 \pm 0.01
WH(115)	–	–	1.71 \pm 0.05	3.93 \pm 0.06	2.82 \pm 0.05
ZH(120)	2.41 \pm 0.02	2.09 \pm 0.023	5.15 \pm 0.04	0.10 \pm 0.01	0.06 \pm 0.01
WH(120)	–	–	1.42 \pm 0.04	3.57 \pm 0.05	2.51 \pm 0.04
ZH(125)	1.99 \pm 0.02	1.67 \pm 0.02	4.46 \pm 0.04	0.08 \pm 0.01	0.04 \pm 0.01
WH(125)	–	–	1.15 \pm 0.03	3.04 \pm 0.04	2.14 \pm 0.04
ZH(130)	1.58 \pm 0.02	1.37 \pm 0.01	3.54 \pm 0.03	0.06 \pm 0.01	0.04 \pm 0.01
WH(130)	–	–	0.70 \pm 0.02	2.51 \pm 0.04	1.83 \pm 0.03
ZH(135)	1.24 \pm 0.01	1.03 \pm 0.01	2.76 \pm 0.02	0.05 \pm 0.01	0.03 \pm 0.01
WH(135)	–	–	0.77 \pm 0.02	1.94 \pm 0.03	1.39 \pm 0.02
Sum	529 \pm 19	490 \pm 18	816 \pm 10	575 \pm 6	386 \pm 6
Data	565	491	783	551	383

Table 19: Predicted signal and background yields (statistical uncertainty only) in the BDT output distribution for the low- $p_T(V)$ range with the 8 TeV data for each of the five channels. The labels LF and HF refer to light- and heavy-flavour jets. The numbers in parentheses refer to the Higgs boson mass hypothesis in GeV.

Process	Z($\mu\mu$)H	Z(ee)H	Z($\nu\nu$)H	W($\mu\nu$)H	W($e\nu$)H
Z+jets (LF)	296 \pm 20	254 \pm 23	156.3 \pm 2.6	13.7 \pm 2.5	6.7 \pm 1.9
Z+jets (HF)	250 \pm 15	228 \pm 17	355.1 \pm 4.7	21.7 \pm 2.9	8.5 \pm 2.0
W+jets (LF)	–	–	202.6 \pm 3.1	92.8 \pm 6.9	58.2 \pm 5.7
W+jets (HF)	–	–	384.6 \pm 5.0	177.7 \pm 14.1	102.4 \pm 10.7
$t\bar{t}$	86.3 \pm 3.7	75.7 \pm 3.6	1573 \pm 29	1308 \pm 15	970 \pm 13
Single Top	5.4 \pm 1.9	2.45 \pm 0.82	102.2 \pm 2.2	64.3 \pm 5.2	49.6 \pm 4.8
VV	13.7 \pm 1.1	12.4 \pm 1.0	48.3 \pm 2.5	19.0 \pm 1.8	13.0 \pm 1.8
ZH(110)	2.83 \pm 0.06	2.21 \pm 0.05	7.78 \pm 0.02	0.31 \pm 0.02	0.14 \pm 0.01
WH(110)	–	–	1.14 \pm 0.02	4.87 \pm 0.17	3.39 \pm 0.14
ZH(115)	2.37 \pm 0.05	1.89 \pm 0.04	6.64 \pm 0.02	0.25 \pm 0.01	0.11 \pm 0.01
WH(115)	–	–	1.11 \pm 0.02	4.73 \pm 0.15	3.28 \pm 0.13
ZH(120)	1.92 \pm 0.04	1.54 \pm 0.03	5.78 \pm 0.04	0.23 \pm 0.01	0.10 \pm 0.01
WH(120)	–	–	1.07 \pm 0.02	3.79 \pm 0.12	2.59 \pm 0.10
ZH(125)	1.52 \pm 0.03	1.24 \pm 0.03	4.39 \pm 0.02	0.18 \pm 0.01	0.08 \pm 0.01
WH(125)	–	–	0.95 \pm 0.03	3.19 \pm 0.10	2.41 \pm 0.09
ZH(130)	1.15 \pm 0.02	0.92 \pm 0.02	3.37 \pm 0.04	0.15 \pm 0.01	0.05 \pm 0.01
WH(130)	–	–	0.79 \pm 0.03	2.61 \pm 0.09	1.85 \pm 0.08
ZH(135)	0.83 \pm 0.02	0.65 \pm 0.02	2.31 \pm 0.03	0.11 \pm 0.01	0.04 \pm 0.01
WH(135)	–	–	0.61 \pm 0.02	1.85 \pm 0.06	1.40 \pm 0.05
Sum	651 \pm 26	572 \pm 29	2822 \pm 30	1697 \pm 22	1208 \pm 19
Data	707	547	2804	1727	1289

Table 20: Predicted signal and background yields (statistical uncertainty only) in the BDT output distribution for the high- $p_T(V)$ range with the 8 TeV data for each of the five channels. The labels LF and HF refer to light- and heavy-flavour jets. The numbers in parentheses refer to the Higgs boson mass hypothesis in GeV.

Process	Z($\mu\mu$)H	Z(ee)H	Z($\nu\nu$)H	W($\mu\nu$)H	W($e\nu$)H
Z+jets (LF)	426 \pm 17	353 \pm 16	109.6 \pm 3.0	4.1 \pm 1.2	1.33 \pm 0.41
Z+jets (HF)	238 \pm 11	199 \pm 10	182.0 \pm 3.6	6.3 \pm 1.4	3.17 \pm 0.99
W+jets (LF)	–	–	79.0 \pm 2.8	42.8 \pm 4.8	32.2 \pm 4.4
W+jets (HF)	–	–	97.4 \pm 4.9	64.4 \pm 7.1	45.7 \pm 5.9
$t\bar{t}$	55.0 \pm 3.0	48.0 \pm 2.8	488 \pm 16	458.8 \pm 8.1	361.8 \pm 7.4
Single Top	4.5 \pm 1.5	5.9 \pm 2.2	43.2 \pm 2.4	35.6 \pm 4.4	28.6 \pm 4.1
VV	16.5 \pm 1.3	13.4 \pm 1.2	34.8 \pm 1.8	16.1 \pm 1.7	9.0 \pm 1.2
ZH(110)	3.66 \pm 0.06	2.95 \pm 0.06	8.05 \pm 0.07	0.14 \pm 0.01	0.08 \pm 0.01
WH(110)	–	–	2.63 \pm 0.06	4.49 \pm 0.16	3.92 \pm 0.16
ZH(115)	3.17 \pm 0.05	2.64 \pm 0.05	6.81 \pm 0.05	0.12 \pm 0.01	0.06 \pm 0.01
WH(115)	–	–	1.52 \pm 0.05	4.30 \pm 0.14	3.52 \pm 0.13
ZH(120)	2.77 \pm 0.04	2.26 \pm 0.04	5.81 \pm 0.04	0.10 \pm 0.01	0.06 \pm 0.01
WH(120)	–	–	1.00 \pm 0.04	3.86 \pm 0.12	3.09 \pm 0.11
ZH(125)	2.31 \pm 0.04	1.84 \pm 0.03	5.40 \pm 0.04	0.09 \pm 0.01	0.06 \pm 0.01
WH(125)	–	–	0.74 \pm 0.03	3.29 \pm 0.10	2.67 \pm 0.09
ZH(130)	1.84 \pm 0.03	1.53 \pm 0.03	3.99 \pm 0.03	0.07 \pm 0.01	0.04 \pm 0.01
WH(130)	–	–	0.70 \pm 0.02	2.56 \pm 0.09	2.07 \pm 0.08
ZH(135)	1.39 \pm 0.02	1.16 \pm 0.02	2.80 \pm 0.02	0.06 \pm 0.01	0.03 \pm 0.01
WH(135)	–	–	0.67 \pm 0.02	2.00 \pm 0.06	1.76 \pm 0.06
Sum	740 \pm 20	620 \pm 19	1034 \pm 18	628 \pm 13	482 \pm 11
Data	776	635	1045	689	544

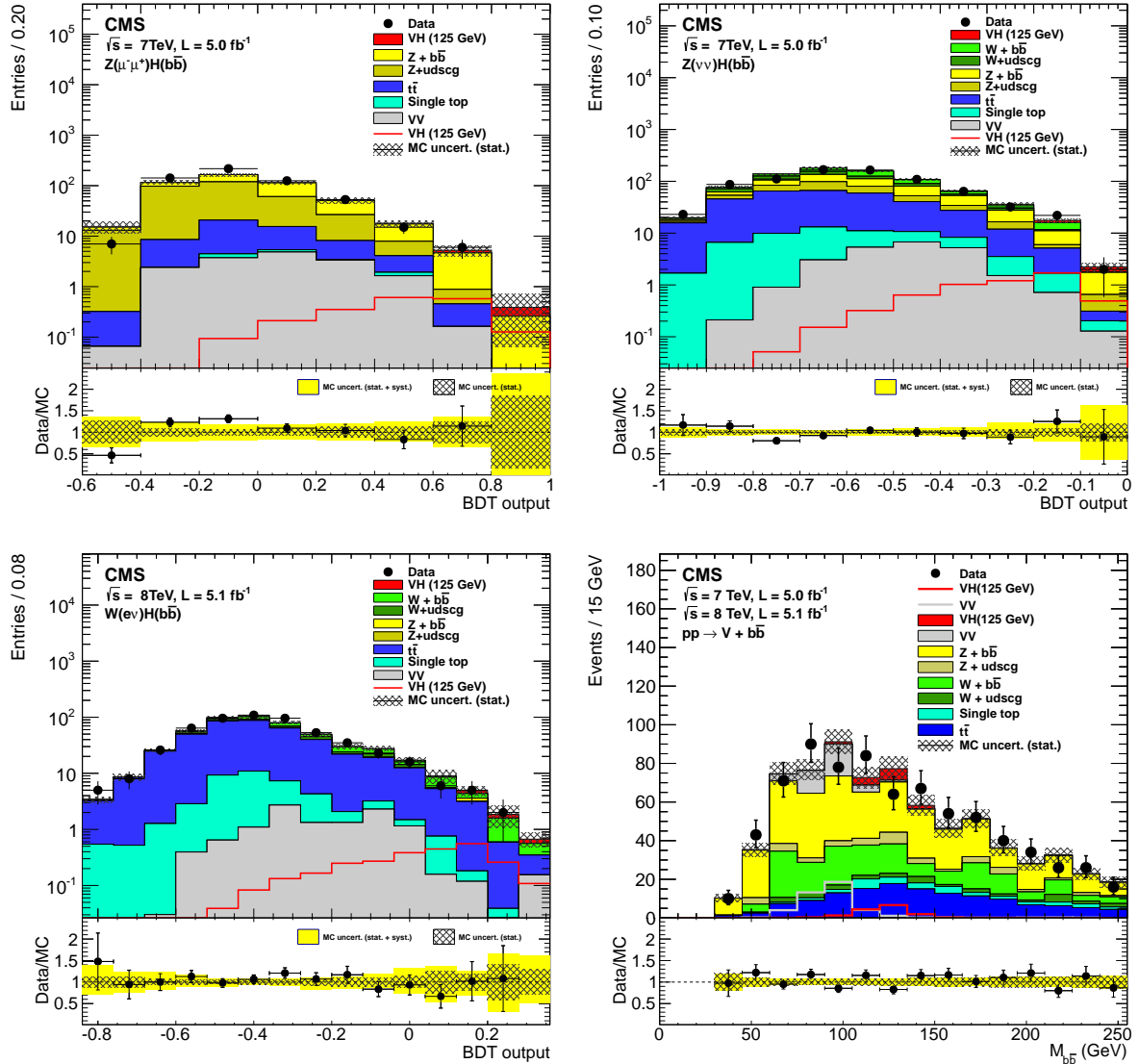


Figure 30: Example of BDT output distributions in the high $p_T(V)$ bin, after all the selection criteria have been applied, for $Z(\mu\mu)H$ (top left), $Z(\nu\nu)H$ (top right), and $W(e\nu)H$ (bottom left). Bottom right: the b-tagged dijet invariant-mass distribution from the combination of all VH channels for the combined 7 and 8 TeV data sets. Only events that pass a more restrictive selection are included (see text). For all figures the solid histograms show the signal and the various backgrounds, with the hatched region denoting the statistical uncertainties in the MC simulation. The data are represented by points with error bars. The VH signal is represented by a red line histogram. The ratio of the data to the sum of the expected background distributions is shown at the bottom of each figure.

10.1 Combination methodology

Combining the Higgs boson search results requires a simultaneous analysis of the data selected by the individual decay modes, accounting for their correlations and for all the statistical and systematic uncertainties. The statistical methodology used in this combination was developed by the ATLAS and CMS Collaborations in the context of the LHC Higgs Combination Group. A description of the general methodology can be found in Refs. [20, 107]. Results presented in this paper are obtained using asymptotic formulae from Ref. [154] and recent updates available in the ROOSTATS package [155]. The Higgs boson mass is tested in steps accordant with the expected Higgs boson width and the experimental mass resolution [107].

10.1.1 Characterizing the absence of a signal: limits

For the calculation of exclusion limits, we adopt the modified frequentist criterion CL_s [156, 157]. The chosen test statistic q , used to determine how signal- or background-like the data are, is based on a profile likelihood ratio. Systematic uncertainties are incorporated via nuisance parameters and are treated according to the frequentist paradigm, as described in Ref [107]. The profile likelihood ratio is defined as

$$q_\mu = -2 \ln \frac{\mathcal{L}(\text{obs} | \mu \cdot s + b, \hat{\theta}_\mu)}{\mathcal{L}(\text{obs} | \hat{\mu} \cdot s + b, \hat{\theta})}, \quad (10)$$

where “obs” stands for the observed data; s stands for the number and distribution of signal events expected under the SM Higgs boson hypothesis; μ is a signal-strength modifier, introduced to accommodate deviations from the SM Higgs boson predictions; b is the number and distribution of background events; $\mu \cdot s + b$ is the signal-plus-background hypothesis, with the expected SM signal event yields s multiplied by the signal-strength modifier μ ; θ are nuisance parameters describing the systematic uncertainties. The value $\hat{\theta}_\mu$ maximizes the likelihood in the numerator for a given μ , while $\hat{\mu}$ and $\hat{\theta}$ define the point at which the likelihood reaches its global maximum.

The ratio of the probabilities to observe a value of the test statistic at least as large as the one observed in data, q_μ^{obs} , under the signal+background ($\mu \cdot s + b$) and background-only (b) hypotheses,

$$CL_s(\mu) = \frac{P(q_\mu \geq q_\mu^{\text{obs}} | \mu \cdot s + b)}{P(q_\mu \geq q_\mu^{\text{obs}} | b)} \leq \alpha, \quad (11)$$

is used as the criterion for excluding the presence of a signal at the $1 - \alpha$ confidence level.

A signal with a cross section $\sigma = \mu \cdot \sigma_{\text{SM}}$ is defined to be excluded at 95% CL if $CL_s(\mu) \leq 0.05$. Here, σ_{SM} stands for the SM Higgs boson cross section.

10.1.2 Characterizing an excess of events: p-values and significance

To quantify the presence of an excess of events beyond what is expected for the background, we use a test statistic:

$$q_0 = -2 \ln \frac{\mathcal{L}(\text{obs} | b, \hat{\theta}_0)}{\mathcal{L}(\text{obs} | \hat{\mu} \cdot s + b, \hat{\theta})}, \quad (12)$$

where the likelihood in the numerator is for the background-only hypothesis. The local statistical significance Z_{local} of a signal-like excess is computed from the probability p_0

$$p_0 = P(q_0 \geq q_0^{\text{obs}} | b), \quad (13)$$

henceforth referred to as the local p -value, using the one-sided Gaussian-tail convention:

$$p_0 = \int_{Z_{\text{local}}}^{+\infty} \frac{1}{\sqrt{2\pi}} \exp(-x^2/2) dx. \quad (14)$$

In the Higgs boson search, we scan over the Higgs boson mass hypotheses and find the value giving the minimum local p -value $p_{\text{local}}^{\text{min}}$, which describes the probability of a background fluctuation for that particular Higgs boson mass hypothesis. The probability to find a fluctuation with a local p -value lower or equal to the observed $p_{\text{local}}^{\text{min}}$ anywhere in the explored mass range is referred to as the global p -value, p_{global} :

$$p_{\text{global}} = P(p_0 \leq p_{\text{local}}^{\text{min}} | b). \quad (15)$$

The fact that the global p -value can be significantly larger than $p_{\text{local}}^{\text{min}}$ is often referred to as the “look-elsewhere effect” (LEE). The global significance (and global p -value) of an observed excess can be evaluated following the method described in Ref. [158], using:

$$p_{\text{global}} = p_{\text{local}}^{\text{min}} + C \cdot e^{-Z_{\text{local}}^2/2}. \quad (16)$$

The constant C is found by generating a set of pseudo-experiments and using it to evaluate the global p -value corresponding to the $p_{\text{local}}^{\text{min}}$ value observed in the data. Pseudo-experiments are a simulated outcome of an experiment obtained by randomly varying the average expected event yields and their distributions according to a specified model of statistical and systematic uncertainties. For example, a Poisson distribution is used to model statistical variations, while a Gaussian distribution is used to describe the systematic uncertainties.

10.1.3 Extracting signal-model parameters

The values of a set of signal-model parameters a (the signal-strength modifier μ is one of them) are evaluated from a scan of the profile likelihood ratio $q(a)$:

$$q(a) = -2 \ln \frac{\mathcal{L}(\text{obs} | s(a) + b, \hat{\theta}_a)}{\mathcal{L}(\text{obs} | s(\hat{a}) + b, \hat{\theta})}. \quad (17)$$

The values of the parameters \hat{a} and $\hat{\theta}$ that maximize the likelihood $\mathcal{L}(\text{obs} | s(\hat{a}) + b, \hat{\theta})$, are called the best-fit set. The 68% (95%) CL interval for a given signal-model parameter a_i is evaluated from $q(a_i) = 1$ (3.84), with all other unconstrained model parameters treated as nuisance parameters. The two-dimensional (2D) 68% (95%) CL contours for pairs of signal-model parameters a_i, a_j are derived from $q(a_i, a_j) = 2.3$ (6.0). Note that the boundaries of the 2D confidence-level region projected onto either parameter axis are not identical to the one-dimensional (1D) confidence intervals for this parameter.

10.2 Exclusion limits on the SM Higgs boson

10.2.1 Results of searches in the five decay modes

Figures 31 and 32 show the 95% CL upper limits on the signal-strength modifier, $\mu = \sigma/\sigma_{\text{SM}}$, as a function of m_{H} for the five decay modes: $\gamma\gamma$, ZZ , WW , $\tau\tau$, and bb . The observed values are shown by the solid lines. The SM Higgs boson mass regions where the line is below $\sigma/\sigma_{\text{SM}} = 1$ are excluded at 95% CL. The dashed lines indicate the median of the expected results for the background-only hypothesis. The dark and light bands indicate the ranges in which the observed results are expected to reside in 68% and 95% of the experiments, should multiple experiments be performed under the background-only hypothesis. The probabilities for an observation to lie above and below the 68% (95%) bands are each 16% (2.5%).

In the $H \rightarrow \gamma\gamma$ analysis, the SM Higgs boson signal is searched for in a simultaneous statistical analysis of the diphoton invariant-mass distributions for the eleven exclusive event classes: five classes (four untagged and one VBF-tagged) for the 7 TeV data and six classes (four untagged and two VBF-tagged) for the 8 TeV data, as described in Section 5. Figure 31 shows the 95% CL upper limits on the Higgs boson production cross section obtained in (a) the *baseline* analysis and the two alternative analyses: (b) the *cut-based* analysis and (c) the *sideband* analysis. The observed limits in the sideband analysis [Fig. 31 (lower right)] are not smooth because, when changing the mass hypothesis, the event class boundaries move as well. This is true for the $\pm 2\%$ signal window and each sideband window. This leads to events moving in and out of the classes in a discrete manner. Figure 31 (top) shows that the $H \rightarrow \gamma\gamma$ search has reached the sensitivity for excluding the SM Higgs boson at 95% CL in the mass range 110–144 GeV, while the observed data exclude it in the following three mass ranges: 113–122 GeV, 128–133 GeV, and 138–149 GeV. All three diphoton analyses give observed exclusion limits near $m_{\text{H}} = 125$ GeV that are much weaker than the expected for the background-only hypothesis, which implies a significant excess of events with diphoton masses around 125 GeV. The consistency of the results obtained with the three alternative approaches confirms the robustness of the measurement.

In the $H \rightarrow ZZ \rightarrow 4\ell$ analysis, the SM Higgs boson signal is searched for in a simultaneous statistical analysis of six 2D distributions of the four-lepton invariant mass $m_{4\ell}$ and the matrix-element-based kinematic discriminant K_D , as described in Section 6. The six distributions correspond to the three lepton final states ($4e$, 4μ , $2e2\mu$) and the 7 and 8 TeV data sets. Figure 32 (upper left) shows the 95% CL upper limits on the Higgs boson production cross section. The $H \rightarrow ZZ \rightarrow 4\ell$ search has reached the sensitivity for excluding the SM Higgs boson at 95% CL in the mass range 120–180 GeV, while the observed data exclude it in the following two mass ranges: 130–164 GeV and 170–180 GeV. The observed exclusion limits for $m_{\text{H}} = 120$ –130 GeV are much weaker than the expected limits for the background-only hypothesis, suggesting a significant excess of four-lepton events in this mass range. As a cross-check, the statistical analysis using only the $m_{4\ell}$ distributions has been performed. The results are found to be consistent with the 2D analysis, although with less sensitivity.

In the $H \rightarrow WW \rightarrow \ell\nu\ell\nu$ analysis, the SM Higgs boson signal is searched for in a simultaneous statistical analysis of eleven exclusive final states: same-flavour (e^+e^- and $\mu^+\mu^-$) dilepton events with 0 and 1 jet for the 7 and 8 TeV data sets, different-flavour $e^\pm\mu^\mp$ dilepton events with 0 and 1 jet for the 7 and 8 TeV data sets, dilepton events in the VBF-tag category for the 7 TeV data set, and same-flavour and different-flavour dilepton events in the VBF-tag category for the 8 TeV data set. All analysis details can be found in Section 7. Figure 32 (upper right) shows the 95% CL upper limits on the Higgs boson production cross section. The $H \rightarrow WW \rightarrow \ell\nu\ell\nu$ search has reached a sensitivity for excluding the SM Higgs boson at 95% CL in the mass range

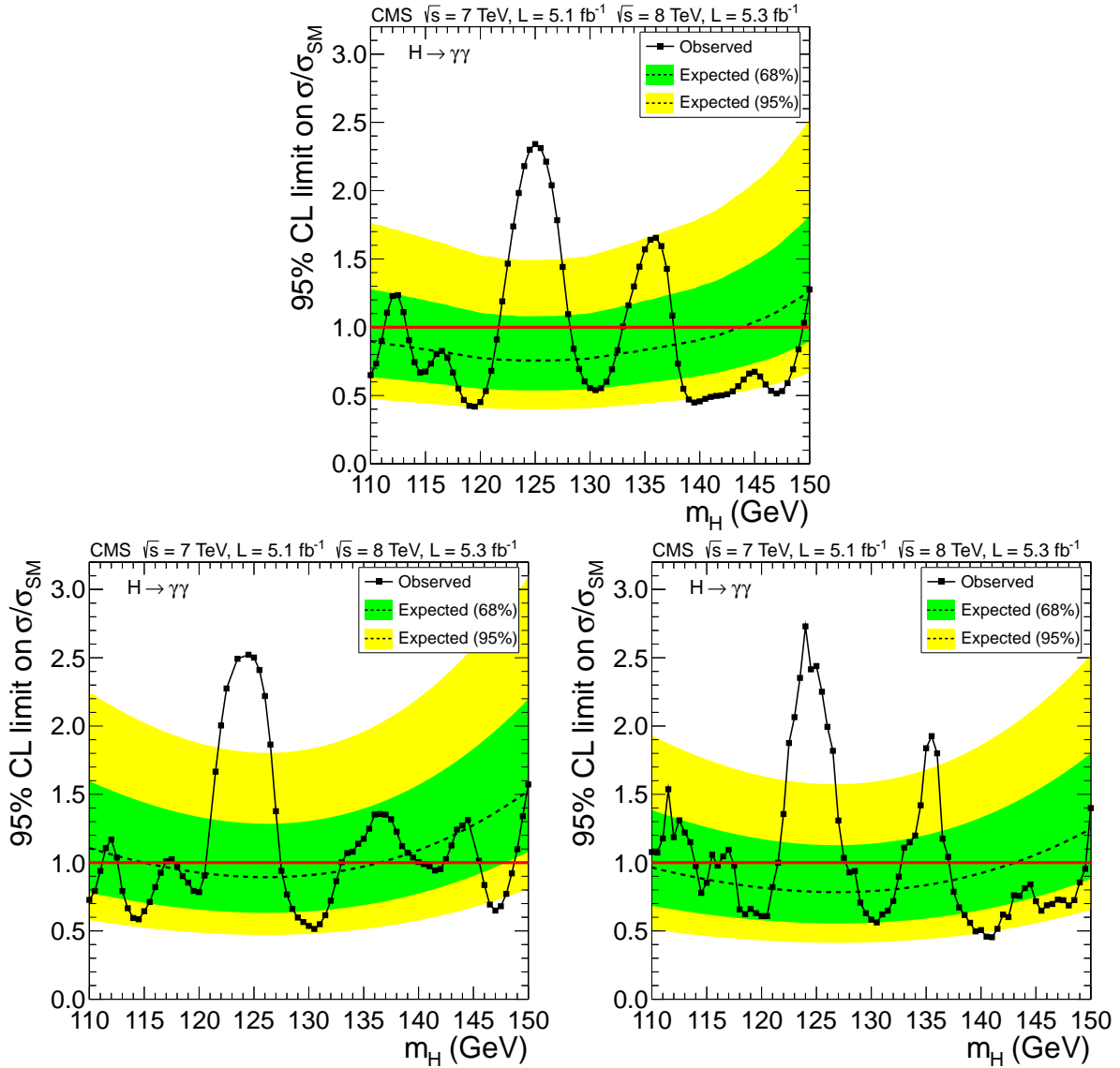


Figure 31: The 95% CL upper limits on the production cross section of a Higgs boson expressed in units of the SM Higgs boson production cross section, $\sigma/\sigma_{\text{SM}}$, as obtained in the $H \rightarrow \gamma\gamma$ search channel for (top) the baseline analysis, (lower left) the cut-based analysis, and (lower right) the sideband analysis. The solid lines represent the observed limits; the background-only hypotheses are represented by their median (dashed lines) and by their 68% (dark) and 95% (light) CL bands.

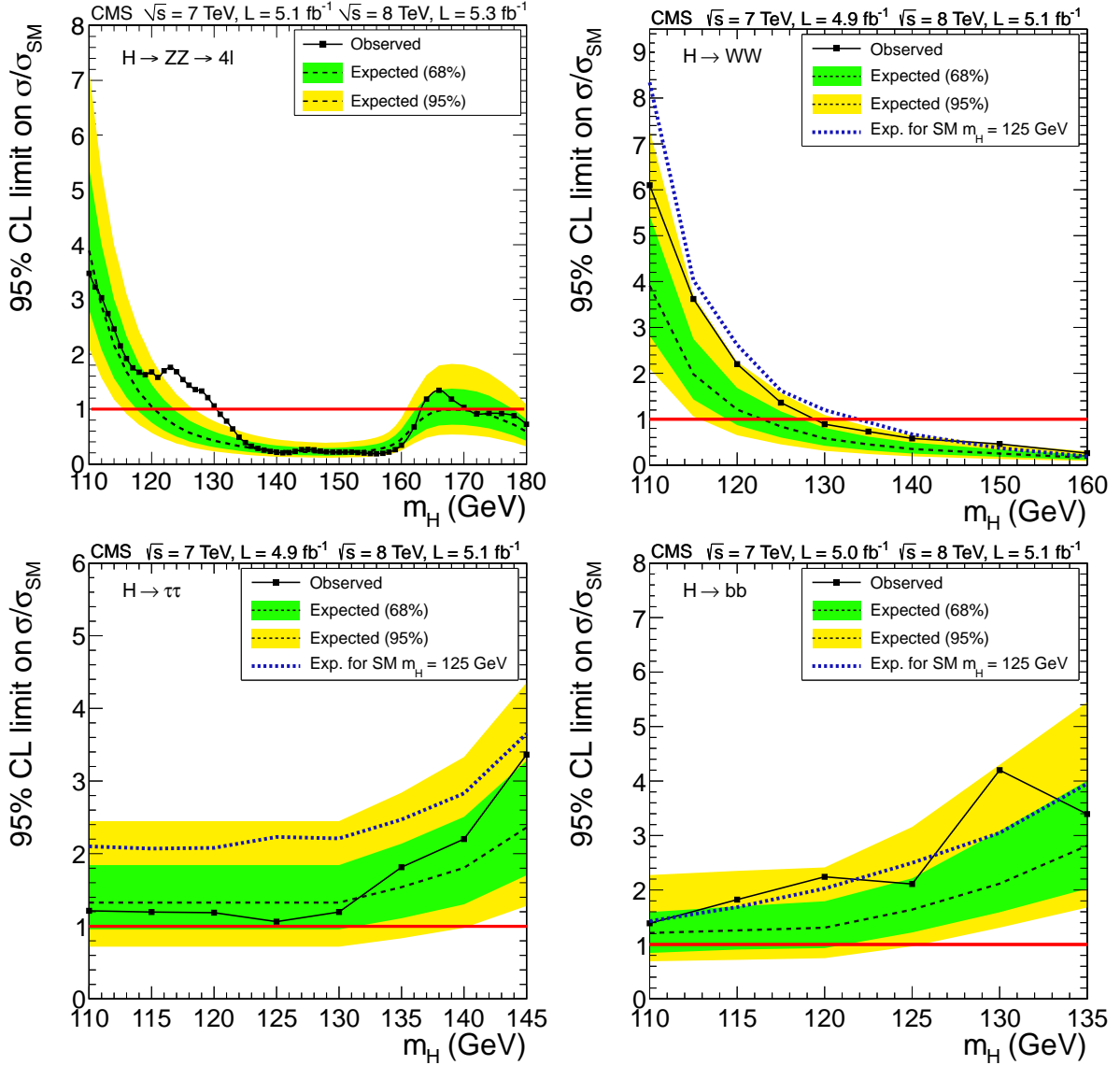


Figure 32: The 95% CL upper limits on the production cross section of a Higgs boson expressed in units of the SM Higgs boson production cross section, $\sigma/\sigma_{\text{SM}}$, for the following search modes: (upper left) $H \rightarrow ZZ \rightarrow 4\ell$, (upper right) $H \rightarrow WW$, (lower left) $H \rightarrow \tau\tau$, and (lower right) $H \rightarrow bb$. The solid lines represent the observed limits; the background-only hypotheses are represented by their median (dashed lines) and by the 68% and 95% CL bands. The signal-plus-background expectation (dotted lines) from a Higgs boson with mass $m_H = 125$ GeV is also shown for the final states with a poor mass resolution, WW , $\tau\tau$, and bb .

122–160 GeV (the higher-mass range is not discussed in this paper), while the observed data exclude it in the mass range 129–160 GeV. The observed exclusion limits are weaker than the expected ones for the background-only hypothesis in the entire mass range, suggesting an excess of events in data. However, given the mass resolution of about 20% in this channel, owing to the presence of the two undetectable neutrinos, a broad excess is observed across the mass range from 110 to about 130 GeV. The dotted line in Fig. 32 (b) indicates the median expected exclusion limits in the presence of a SM Higgs boson with a mass near 125 GeV. The observed limits in this channel are consistent with the expectation for a SM Higgs boson of 125 GeV.

In the $H \rightarrow \tau\tau$ channel, the 0-, 1-jet, and VBF categories are used to set 95% CL upper limits on the Higgs boson production. The ditau system is reconstructed in four final states: $e\tau_h$, $\mu\tau_h$, $e\mu$, $\mu\mu$, where the leptons come from $\tau \rightarrow e\nu$ or $\tau \rightarrow \mu\nu$ decays. The 0- and 1-jet categories are further split into two categories of low or high ditau transverse momentum. The 7 and 8 TeV data are treated independently giving a total of 40 ditau mass distributions. All analysis details can be found in Section 8. Figure 32 (lower left) shows the 95% CL upper limits on the Higgs boson production cross section in this channel. The $H \rightarrow \tau\tau$ search has not yet reached the SM Higgs boson exclusion sensitivity; the expected limits on the signal event rates are 1.3–2.4 times larger than the event rates expected for the SM Higgs boson in this channel.

In the $H \rightarrow bb$ analysis, five final states are considered: two b-tagged jets with E_T^{miss} ($Z \rightarrow \nu\nu$), e^+e^- , $\mu^+\mu^-$ ($Z \rightarrow \ell^+\ell^-$), $e + E_T^{\text{miss}}$, and $\mu + E_T^{\text{miss}}$ ($W \rightarrow \ell\nu$). Each of these categories is further split into two categories of low or high bb transverse momentum. The 7 and 8 TeV data are treated independently giving a total of 20 BDT-output distributions. All analysis details can be found in Section 9. Figure 32 (lower right) shows the 95% upper CL limits on the Higgs boson production cross section in this channel. The $H \rightarrow bb$ search has not yet reached the SM Higgs boson exclusion sensitivity; the expected limits on the signal event rates are 1.2–2.8 times larger than the event rates expected for the SM Higgs boson in this channel.

10.2.2 Combined results

The five individual search channels described above are combined into a single search for the SM Higgs boson. Figure 33 (left) shows the 95% CL upper limits on the signal-strength modifier, $\mu = \sigma/\sigma_{\text{SM}}$, as a function of m_H . We exclude a SM Higgs boson at 95% CL in two mass ranges: 110–121.5 GeV and 128.0–145 GeV.

The CL_s value for the SM Higgs boson hypothesis as a function of its mass is shown in Fig. 33 (right). The horizontal lines indicate CL_s values of 0.05, 0.01, and 0.001. The mass regions where the observed CL_s values are below these lines are excluded with the corresponding $(1 - \text{CL}_s)$ confidence levels of 95%, 99%, and 99.9%, respectively. The 95% CL exclusion range for the SM Higgs boson is identical to that shown in Fig. 33 (left), as both results are simply different representations of the same underlying information. At 99% CL, we exclude the SM Higgs boson in three mass ranges: 110.0–111.5 GeV, 113.5–121.0 GeV, and 128.5–145.0 GeV.

Figure 33 (right) shows that, in the absence of a signal, we would expect to exclude the entire m_H range of 110–145 GeV at the 99.9% CL or higher. In most of the Higgs boson mass range, the differences between the observed and expected limits are consistent since the observed limits are generally within the 68% or 95% bands of the expected limit values. However, in the range $121.5 < m_H < 128.0$ GeV, we observe an excess of events, making the observed limits considerably weaker than expected in the absence of the SM Higgs boson and, hence, not allowing the exclusion of the SM Higgs boson in this range.

10.3 Significance of the observed excess

10.3.1 Results of searches in the $H \rightarrow \gamma\gamma$ and $H \rightarrow ZZ \rightarrow 4\ell$ decay modes

As presented in Section 10.2.1, the searches for the SM Higgs boson in the $\gamma\gamma$ and $ZZ \rightarrow 4\ell$ modes reveal a substantial excess of events with diphoton and four-lepton invariant masses near 125 GeV.

Figure 34 shows the local p -value as a function of the SM Higgs boson mass in the $\gamma\gamma$ channel. The results are presented for the three analyses: (a) *baseline* analysis, and in the two alternative analyses: (b) *cut-based* analysis, and (c) *sideband* analysis. Figure 34 (top) shows about a 3σ excess near 125 GeV in both the 7 and 8 TeV data. The minimum local p -value $p_0 = 1.8 \times 10^{-5}$, corresponding to a local maximum significance of 4.1σ , occurs at a mass of 125.0 GeV for the combined 7 and 8 TeV data sets. The median expected significance for a SM Higgs boson of this mass is 2.7σ . In the asymptotic approximation, 68% (95%) of repeated experiments would give results within $\pm 1\sigma$ ($\pm 2\sigma$) around the median expected significance. Therefore, the excess seen in data, even being larger than the expected median for a Higgs boson signal, is consistent with a SM Higgs boson with a probability of about 16%. The consistency of the results from the three analyses is a good check on the robustness of the measurement.

The local p -value as a function of the Higgs boson mass m_H for the $ZZ \rightarrow 4\ell$ channel is shown in Fig. 35. The minimum of the local p -value is at $m_H = 125.5$ GeV and corresponds to a local significance of 3.2σ . A local significance of 2.2σ is found for a 1D fit of the invariant mass without using the K_D discriminant. The median expected significance for a SM Higgs boson of this mass is 3.8σ and 3.2σ for the 2D and 1D fits, respectively.

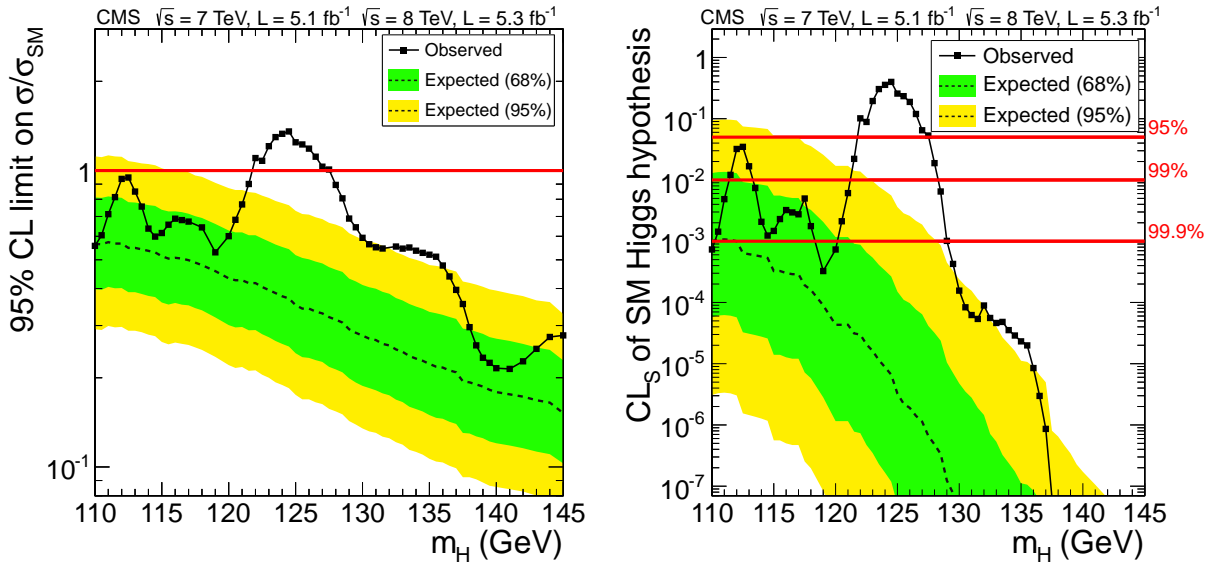


Figure 33: The 95% CL upper limits on the production cross section of a Higgs boson expressed in units of the SM Higgs boson production cross section, $\sigma/\sigma_{\text{SM}}$, (left) and the CL_s values (right) for the SM Higgs boson hypothesis, as a function of the Higgs boson mass for the five decay modes and the 7 and 8 TeV data sample combined. The solid lines represent the observed limits; the background-only hypotheses are represented by their median (dashed lines) and by the 68% and 95% CL bands. The three horizontal lines on the right plot show the CL_s values 0.05, 0.01, and 0.001, corresponding to 95%, 99%, and 99.9% confidence levels, defined as $(1 - \text{CL}_s)$.

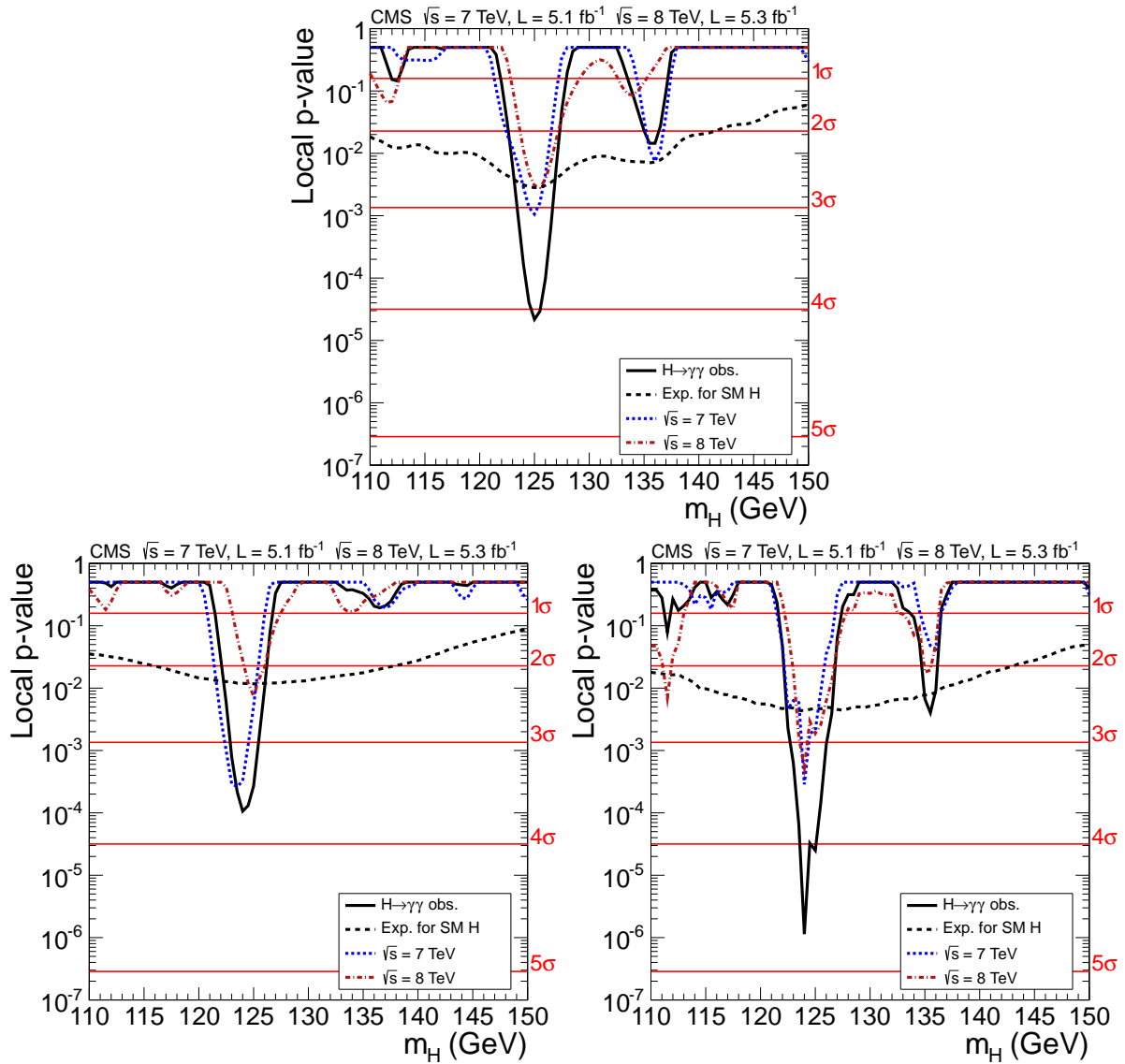


Figure 34: The local p -value as a function of m_H for the 7 and 8 TeV data sets and their combination for the $\gamma\gamma$ mode from (top) the primary analysis, (lower left) the cut-based analysis, and (lower right) the side-band analysis. The observed p -values for the combined 7 and 8 TeV data sets are shown by the solid lines; the median expected p -values for a SM Higgs boson with mass m_H , are shown by the dashed lines. The horizontal lines show the relationship between the p -value (left y axis) and the significance in standard deviations (right y axis).

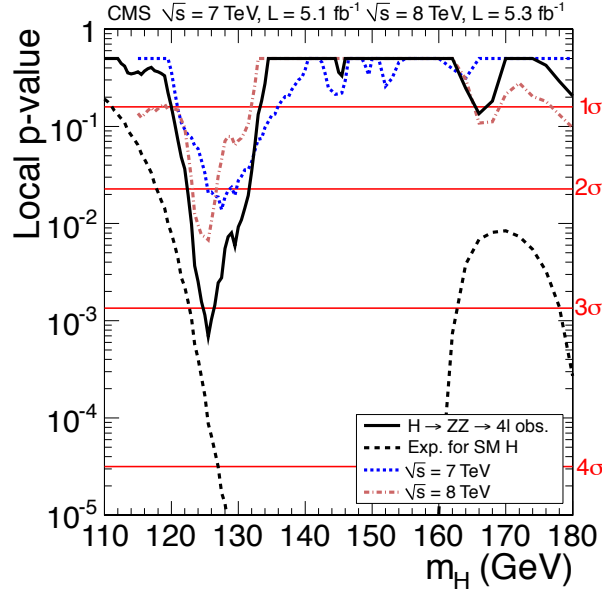


Figure 35: The local p -value as a function of m_H for the 7 and 8 TeV data sets and their combination for the $ZZ \rightarrow 4\ell$ channel. The observed p -values for the combined 7 and 8 TeV data sets are shown by the solid line; the median expected p -values for a SM Higgs boson with mass m_H are shown by the dashed line. The observed p -values for the 7 and 8 TeV data sets are shown by the dotted lines. The horizontal lines show the relationship between the p -value (left y axis) and the significance in standard deviations (right y axis).

10.3.2 Combined results

To quantify the inconsistency of the observed excesses with the background-only hypothesis, we show in Fig. 36 (left) the local p -value p_0 for the five decay modes combined for the 7 and 8 TeV data sets. The 7 and 8 TeV data sets exhibit excesses of 3.2σ and 3.8σ , respectively, for a SM Higgs boson with a mass near 125 GeV. In the combination, the minimum local p -value of $p_{\min} = 3 \times 10^{-7}$, corresponding to a local significance of 5.0σ , occurs at $m_H = 125.5$ GeV.

Figure 36 (right) gives the p -value distribution for each of the decay channels. The largest contributions to the overall excess are from the $\gamma\gamma$ and $ZZ \rightarrow 4\ell$ channels. Both channels have good mass resolution and allow a precise measurement of the mass of the resonance corresponding to the excess. Their combined significance is 5.0σ , as displayed in Fig. 37 (left). Figure 37 (right) shows the combined p -value distribution for the channels with poorer mass resolution: WW , $\tau\tau$, and bb .

Table 21 summarizes the median expected and observed local significance for a SM Higgs boson mass hypothesis of 125.5 GeV from the individual decay modes and their combinations. In the $\tau\tau$ channel, we do not observe an excess of events at this mass. The expected significance is evaluated assuming the expected background and signal rates. The observed significance is expected to be within $\pm 1\sigma$ of the expected significance with a 68% probability.

The LEE-corrected significance is evaluated by generating 10 000 pseudo-experiments. After fitting for the constant C in Eq. (16), we find that the global significance of the signal at $m_H = 125.5$ GeV is 4.6σ (4.5σ) for the mass search range 115–130 GeV (110–145 GeV).

The low probability for an excess at least as large as the observed one to arise from a statistical fluctuation of the background leads to the conclusion that we observe a new particle with a

Table 21: The median expected and observed significances of the excesses in the individual decay modes and their various combinations for a SM Higgs boson mass hypothesis of 125.5 GeV. There is no observed excess in the $\tau\tau$ channel.

Decay mode or combination	Expected (σ)	Observed (σ)
ZZ	3.8	3.2
$\gamma\gamma$	2.8	4.1
WW	2.5	1.6
bb	1.9	0.7
$\tau\tau$	1.4	–
$\gamma\gamma + ZZ$	4.7	5.0
$WW + \tau\tau + bb$	3.4	1.6
$\gamma\gamma + ZZ + WW + \tau\tau + bb$	5.8	5.0

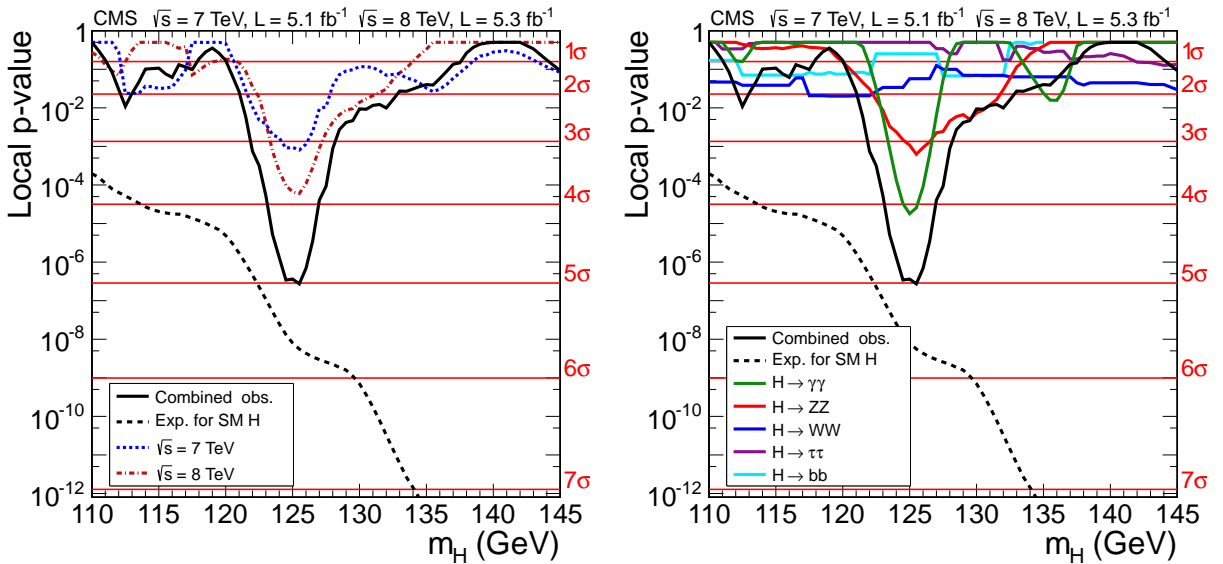


Figure 36: (Left) The observed local p -value for the combination of all five decay modes with the 7 and 8 TeV data sets, and their combination as a function of the Higgs boson mass. (Right) The observed local p -value for each separate decay mode and their combination, as a function of the Higgs boson mass. The dashed lines show the mean expected local p -values for a SM Higgs boson with mass m_H .

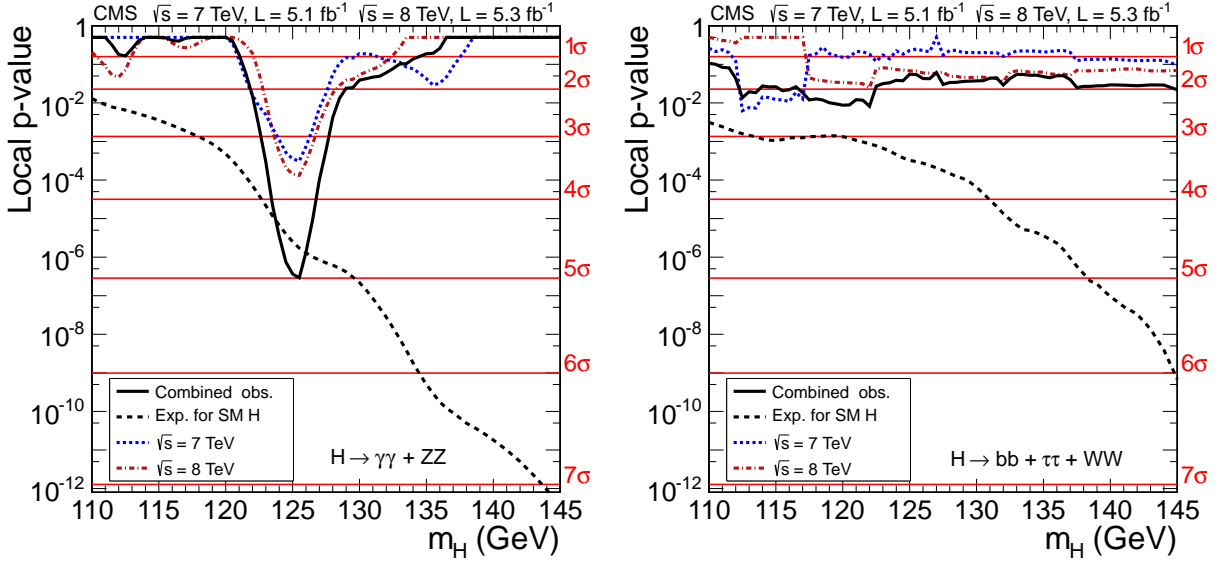


Figure 37: The observed local p -value for the $\gamma\gamma$ and $ZZ \rightarrow 4\ell$ decay channels with good mass resolution (left) and the WW , bb , and $\tau\tau$ modes with poorer mass resolution (right), as a function of the Higgs boson mass, for the 7 and 8 TeV data sets and their combination. The dashed lines show the expected local p -values for a SM Higgs boson with mass m_H .

mass near 125 GeV. The $\gamma\gamma$ and $ZZ \rightarrow 4\ell$ decay modes indicate that the new particle is a boson, and the diphoton decay implies that its spin is different from 1 [159, 160].

10.4 Mass of the observed state

To measure the mass of the observed state, we use the $\gamma\gamma$ and $ZZ \rightarrow 4\ell$ decay modes. Figure 38 (left) shows the 2D 68% CL regions for the signal cross section (normalized to the SM Higgs boson cross section) versus the new boson's mass m_χ , separately for untagged $\gamma\gamma$, VBF-tagged $\gamma\gamma$, and $ZZ \rightarrow 4\ell$ events, and their combination. The combined 68% CL contour shown with a solid line in Fig. 38 (left) assumes that the relative event yields between the three channels are fixed to the SM expectations, while the overall signal strength is a free parameter.

The energy scale uncertainties for photons, electrons, and muons are treated as independent. The $Z \rightarrow ee$ peak is used for correcting both photon and electron energy scales. However, we find that they have a very weak correlation, since photons in $H \rightarrow \gamma\gamma$ decays and electrons in $H \rightarrow ZZ \rightarrow 4\ell$ decays have substantially different energy scales. Moreover, the photons have an additional systematic uncertainty associated with the extrapolation of the energy scale corrections derived for the electrons to the energy scale corrections to be used for the photons.

To measure the value of m_χ in a model-independent way, the untagged $\gamma\gamma$, VBF-tagged $\gamma\gamma$, and $ZZ \rightarrow 4\ell$ channels are assumed to have independent signal cross sections. This is achieved by scaling the expected SM Higgs boson event yields in these channels by independent factors μ_i , where i denotes the individual channel. The signal is assumed to be a particle with a unique mass m_χ . The mass and its uncertainty are extracted from a scan of the combined test statistic q , frequently referred to as $-2 \Delta \ln \mathcal{L}$, versus m_χ . The signal-strengths μ_i in such a scan are treated in the same way as the other nuisance parameters. Figure 38 (right) shows the test statistic as a function of m_χ for the three final states separately and their combination. The crossing of the $q(m_\chi)$ curves with the horizontal thick (thin) lines at $q = 1$ (3.8) defines the 68% (95%) CL interval for the mass of the observed particle. These intervals include both the statistical and systematic uncertainties. The resulting mass measurement and 68% CL interval in such a

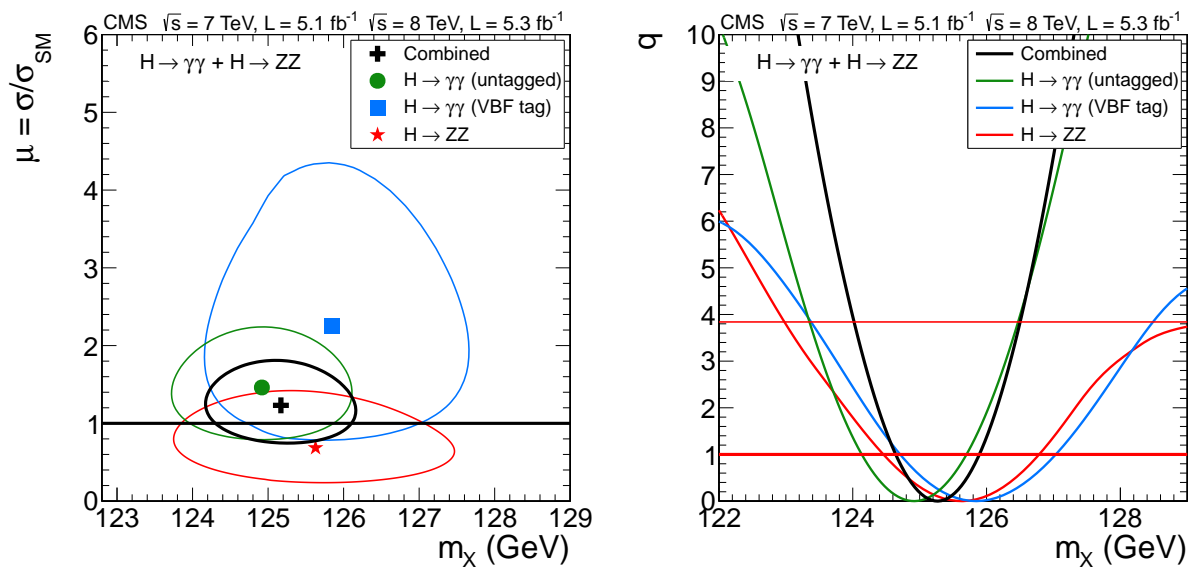


Figure 38: (Left) The 2D 68% CL contours for a hypothesized boson mass m_X versus $\mu = \sigma/\sigma_{\text{SM}}$ for the untagged $\gamma\gamma$, VBF-tagged $\gamma\gamma$, and $ZZ \rightarrow 4\ell$ decay channels, and their combination from the combined 7 and 8 TeV data. In the combination, the relative signal strengths for the three final states are fixed to those for the SM Higgs boson. (Right) The maximum-likelihood test statistic q versus m_X for the untagged $\gamma\gamma$, VBF-tagged $\gamma\gamma$, and $ZZ \rightarrow 4\ell$ final states, and their combination from the combined 7 and 8 TeV data. Neither the absolute nor the relative signal strengths for the three final states are constrained to the SM Higgs boson expectations. The crossings with the thick (thin) horizontal line $q = 1$ (3.8) define the 68% (95%) CL interval for the measured mass, shown by the vertical lines.

combination is $m_\chi = 125.3 \pm 0.6$ GeV.

To determine the statistical component in the overall uncertainty, we evaluate the test statistic $q(m_\chi)$ with all the nuisance parameters fixed to their best-fit values. The result is shown by the dashed line in Fig. 39. The crossing of the dashed line with the thick horizontal line $q = 1$ gives the statistical uncertainty (68% CL interval) in the mass measurements: ± 0.4 GeV. The quadrature difference between the overall and statistical-only uncertainties determines the systematic uncertainty component in the mass measurements: ± 0.5 GeV. Therefore, the final result for the mass measurement is $m_\chi = 125.3 \pm 0.4$ (stat.) ± 0.5 (syst.) GeV.

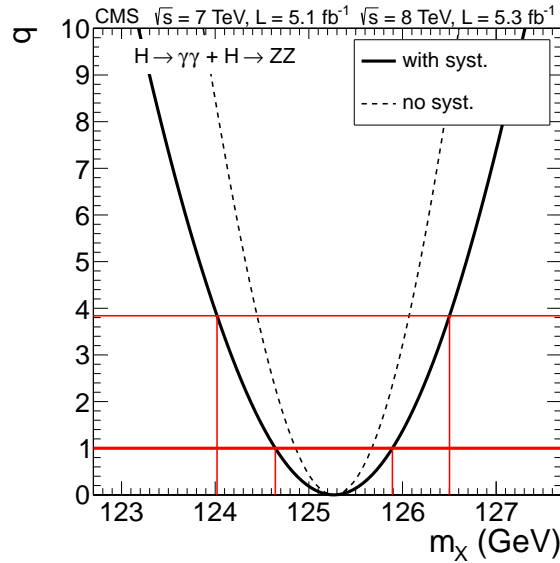


Figure 39: The maximum-likelihood test statistic q versus the hypothesized boson mass m_χ for the combination of the $\gamma\gamma$ and $ZZ \rightarrow 4\ell$ modes from the combined 7 and 8 TeV data. The solid line is obtained including all the nuisance parameters and, hence, includes both the statistical and systematic uncertainties. The dashed line is found with all nuisance parameters fixed to their best-fit values and, hence, represents the statistical uncertainties only. The crossings with the thick (thin) horizontal line $q = 1$ (3.8) define the 68% (95%) CL interval for the measured mass, shown by the vertical lines.

10.5 Consistency of the observed state with the SM Higgs boson hypothesis

The p -value characterizes the probability of the background producing the observed excess of events or greater, but it does not give information about the consistency of the observed excess with the expected signal. The current data sample allows for only a limited number of such consistency tests, which we present in this section. These consistency tests do not constitute measurements of any physics parameters per se, but rather show the consistency of the various observations with the expectations for the SM Higgs boson. Unless stated otherwise, all consistency tests presented in this section are for the hypothesis of the SM Higgs boson with mass 125.5 GeV and all quoted uncertainties include both the statistical and systematic ones.

10.5.1 Measurement of the signal strength

The value for the signal-strength modifier $\hat{\mu} = \sigma/\sigma_{\text{SM}}$, obtained by combining all the search channels, provides the first consistency test. Note that $\hat{\mu}$ becomes negative if the observed number of events is smaller than the expected rate for the background-only hypothesis. Figure 40 shows the $\hat{\mu}$ value versus the hypothesized Higgs boson mass m_H . The band corresponds

to the 68% CL region when including the statistical and systematic uncertainties. The value of μ is found in 0.5 GeV steps of m_H . The measured $\hat{\mu}$ value for a Higgs boson mass of 125.5 GeV is 0.87 ± 0.23 , consistent with the value $\mu = 1$ expected for the SM Higgs boson.

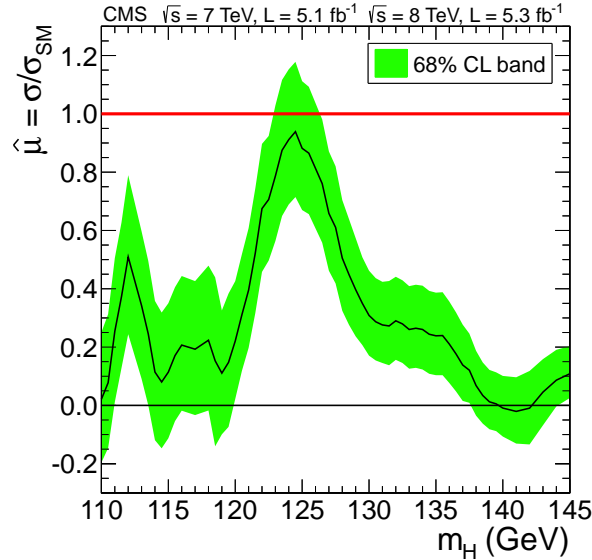


Figure 40: The signal-strength $\hat{\mu} = \sigma/\sigma_{SM}$ as a function of the hypothesized SM Higgs boson mass m_H using all the decay modes and the combined 7 and 8 TeV data sets. The bands correspond to ± 1 standard deviation including both statistical and systematic uncertainties.

Figure 41 shows a consistency test of the $\hat{\mu}$ values obtained in different combinations of search channels. The combinations are organized by decay mode and additional features that allow the selection of events with an enriched purity of a particular production mechanism. The expected purities of different combinations are discussed in the sections describing the individual analyses. For example, assuming the SM Higgs boson cross sections, the channels with the VBF dijet requirements have a substantial fraction (20–50%) of gluon-gluon fusion events. There is consistency among all the channels contributing to the overall measurement and their various combinations.

The four main Higgs boson production mechanisms can be associated with either top-quark couplings (gluon-gluon fusion and ttH) or vector-boson couplings (VBF and VH). Therefore, combinations of channels associated with a particular decay mode and explicitly targeting different production mechanisms can be used to test the relative strengths of the couplings of the new state to the vector bosons and top quark. Figure 42 shows the 68% and 95% CL contours for the signal-strength modifiers $\mu_{ggH+ttH}$ of the gluon-gluon fusion plus ttH, and μ_{VBF+VH} of the VBF plus VH production mechanisms. The three sets of contours correspond to the channels associated with the $\gamma\gamma$, $\tau\tau$, and WW decay modes; searches in these decay modes have subchannels with VBF dijet tags. The SM Higgs boson point shown by the diamond at $\mu_{ggH+ttH}, \mu_{VBF+VH} = (1, 1)$ is within the 95% CL intervals for each of the three decay modes.

10.5.2 Consistency of the data with the SM Higgs boson couplings

The event yield N of Higgs bosons produced in collisions of partons x ($xx \rightarrow H$) and decaying to particles y ($H \rightarrow yy$), is proportional to the partial and total Higgs boson decay widths as follows:

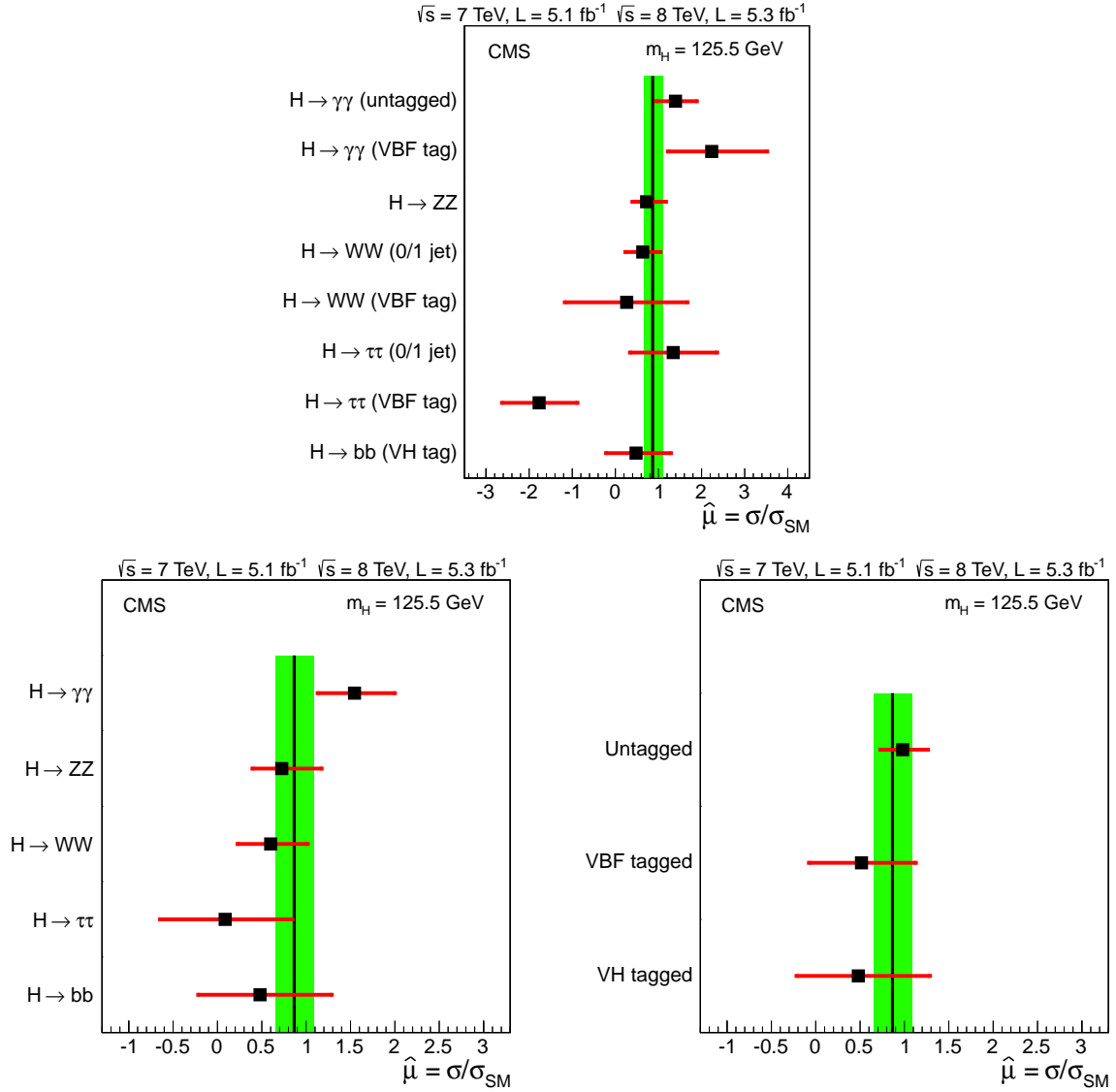


Figure 41: Signal-strength values $\hat{\mu} = \sigma/\sigma_{\text{SM}}$ for various combinations of the search channels with $m_H = 125.5 \text{ GeV}$. The horizontal bars indicate the $\pm 1\sigma$ statistical-plus-systematic uncertainties. The vertical line with the band shows the combined $\hat{\mu}$ value with its uncertainty. (Top) Combinations by decay mode and additional requirements that select events with an enriched purity of a particular production mechanism. (Bottom-left) Combinations by decay mode. (Bottom-right) Combinations by selecting events with additional requirements that select events with an enriched purity of a particular production mechanism.

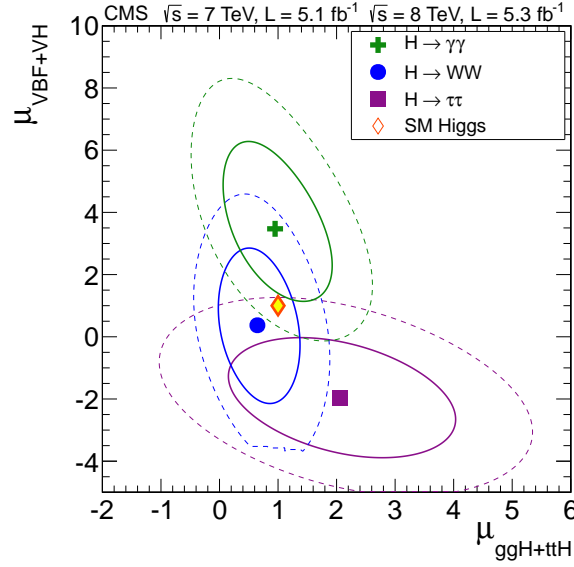


Figure 42: The 68% (solid lines) and 95% (dashed lines) CL contours for the signal strength of the gluon-gluon fusion plus ttH production mechanisms ($\mu_{ggH+ttH}$), versus VBF plus VH (μ_{VBF+VH}). The three different lines show the results for the decay modes: $\gamma\gamma$, WW , and $\tau\tau$. The markers indicate the best-fit values for each mode. The diamond at (1,1) indicates the expected values for the SM Higgs boson.

$$N \propto \sigma(xx \rightarrow H) \cdot \mathcal{B}(H \rightarrow yy) \propto \frac{\Gamma_{xx} \Gamma_{yy}}{\Gamma_{\text{tot}}}, \quad (18)$$

where $\sigma(xx \rightarrow H)$ is the Higgs boson production cross section, $\mathcal{B}(H \rightarrow yy)$ is the branching fraction for the decay mode, Γ_{xx} and Γ_{yy} are the partial widths associated with the $H \rightarrow xx$ and $H \rightarrow yy$ processes, and Γ_{tot} is the total width.

Seven partial widths (Γ_{WW} , Γ_{ZZ} , Γ_{tt} , Γ_{bb} , $\Gamma_{\tau\tau}$, Γ_{gg} , $\Gamma_{\gamma\gamma}$) and the total width Γ_{tot} are relevant for the current analysis, where Γ_{gg} is the partial width for the Higgs boson decay to two gluons. The partial widths Γ_{gg} and $\Gamma_{\gamma\gamma}$ are generated by loop diagrams and thus are directly sensitive to the presence of new physics. The possibility of Higgs boson decays to beyond-the-standard-model (BSM) particles, with a partial width Γ_{BSM} , is accommodated by making Γ_{tot} equal to the sum of all partial widths of allowed decays to the SM particles plus Γ_{BSM} .

The partial widths are proportional to the square of the effective Higgs boson couplings to the corresponding particles. To test for possible deviations of the measurements from the rates expected in different channels for the SM Higgs boson, we introduce different sets of coupling scale factors κ and fit the data to these new parameters. One can introduce up to eight independent parameters relevant for the current analysis. Significant deviations of the scale factors from unity would imply new physics beyond the SM Higgs boson hypothesis.

The current data set is insufficient to measure all eight independent parameters. Therefore, we measure different subsets, with the remaining unmeasured parameters either constrained to equal the SM Higgs boson expectations or included in the likelihood fit as unconstrained nuisance parameters.

A. Test of custodial symmetry

In the SM, the Higgs boson sector possesses a global $SU(2)_L \times SU(2)_R$ symmetry, which is broken by the Higgs boson vacuum expectation value down to the diagonal subgroup $SU(2)_{L+R}$.

As a result, the tree-level relations between the ratios of the W and Z boson masses, m_W/m_Z , and their couplings to the Higgs boson, g_W/g_Z , are protected against large radiative corrections, a phenomenon known as “custodial symmetry” [161, 162]. However, large violations of custodial symmetry are possible in BSM theories. To test custodial symmetry, we introduce two scaling factors κ_W and κ_Z that modify the SM Higgs boson couplings to W and Z bosons, and perform two different procedures to determine the consistency of the ratio $\lambda_{WZ} = \kappa_W/\kappa_Z$ with unity.

The dominant Higgs boson production mechanism for the inclusive $H \rightarrow ZZ$ and untagged $H \rightarrow WW$ channels is $gg \rightarrow H$. Therefore, the ratio of the event yields for these channels provides a test of custodial symmetry. To quantify the test, we introduce two event-rate modifiers μ_{ZZ} and R_{WZ} . The expected $H \rightarrow ZZ \rightarrow 4\ell$ event yield is scaled by μ_{ZZ} , while the expected untagged $H \rightarrow WW \rightarrow \ell\nu\ell\nu$ event yield is scaled by $R_{WZ} \cdot \mu_{ZZ}$. The mass of the observed state is fixed to 125.5 GeV. The test statistic $q(R_{WZ})$ as a function of R_{WZ} , with μ_{ZZ} included with the other nuisance parameters, is shown in Fig. 43 (left) and yields $R_{WZ} = 0.9^{+1.1}_{-0.6}$, where the uncertainty is the combined statistical and systematic. The contributions from VBF and VH production to the fit give a small bias of 0.02 when relating the observed event-yield ratio R_{WZ} to the square of the ratio of the couplings λ_{WZ}^2 . Hence, the current measurements are consistent, within the uncertainties, with the expectation from custodial symmetry.

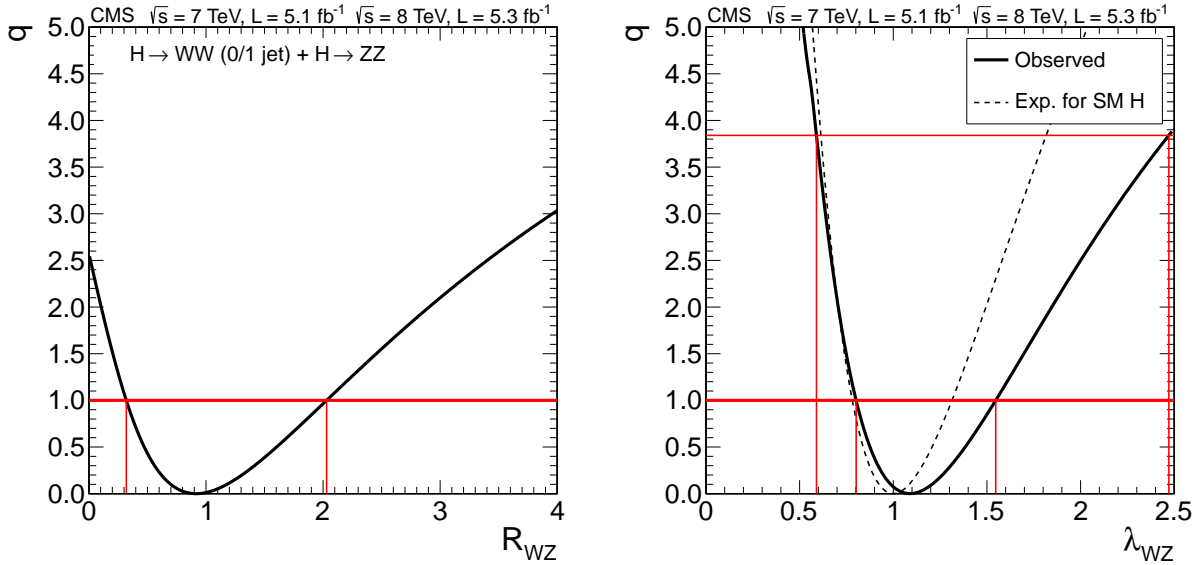


Figure 43: (Left) The likelihood test statistic $q(R_{WZ})$ as a function of the event-rate modifier R_{WZ} from the combined untagged $H \rightarrow WW \rightarrow \ell\nu\ell\nu$ and inclusive $H \rightarrow ZZ \rightarrow 4\ell$ searches. (Right) The test statistic $q(\lambda_{WZ})$ as a function of the ratio of the couplings to W and Z bosons, λ_{WZ} , from the combination of all channels. The intersection of the curves with the horizontal lines $q = 1$ and 3.8 give the 68% and 95% CL intervals, respectively.

In the second method, we extract λ_{WZ} directly from the combination of all search channels. In this approach, we use three parameters: λ_{WZ} , κ_Z , and κ_F . The latter variable is a single event-rate modifier for all Higgs boson couplings to fermions. The BSM Higgs boson width Γ_{BSM} is set to zero. The partial width Γ_{gg} , induced by quark loops, scales as κ_F^2 . The partial width $\Gamma_{\gamma\gamma}$ is also induced via loop diagrams, with the W boson and top quark being the dominant contributors; hence, it scales as $|\alpha\kappa_W + \beta\kappa_F|^2$, where $\kappa_W = \lambda_{WZ} \cdot \kappa_Z$ and the ratio of the factors α and β , $\beta/\alpha \approx -0.22$, is taken from the prediction for the SM Higgs boson with $m_H = 125.5$ GeV [66]. In the evaluation of $q(\lambda_{WZ})$, both κ_Z and κ_F are included with the other nuisance parameters. Assuming a common scaling factor for all fermions makes this measurement model dependent,

but using all the channels gives it greater sensitivity. The results are shown in Fig. 43 (right) by the solid line. The dashed line indicates the median expected result for the SM Higgs boson, given the integrated luminosity. The measured value is $\lambda_{WZ} = 1.1^{+0.5}_{-0.3}$, where the uncertainty is the combined statistical and systematic. The result is consistent with the expectation of $\lambda_{WZ} = 1$ from custodial symmetry. In all further combinations presented below, we assume $\lambda_{WZ} = 1$ and use a common factor κ_V to modify the Higgs boson couplings to W and Z bosons.

B. Test of the couplings to vector bosons and fermions

We further test the consistency of the measurements with the SM Higgs boson hypothesis by fitting for the two free parameters κ_V and κ_F introduced above. We assume $\Gamma_{\text{BSM}} = 0$, i.e. no BSM Higgs boson decay modes. At lowest order, all partial widths, except for $\Gamma_{\gamma\gamma}$, scale either as κ_V^2 or κ_F^2 . As discussed above, the partial width $\Gamma_{\gamma\gamma}$ scales as $|\alpha \kappa_V + \beta \kappa_F|^2$. Hence, $\gamma\gamma$ is the only channel sensitive to the relative sign of κ_V and κ_F .

Figure 44 shows the 2D likelihood test statistic over the (κ_V, κ_F) plane. The left plot allows for different signs of κ_V and κ_F , while the right plot constrains both of them to be positive. The 68%, 95%, and 99.7% CL contours are shown by the solid, dashed, and dotted lines, respectively. The global minimum in the left plot occurs in the $(+, -)$ quadrant, which is due to the observed excess in the $\gamma\gamma$ channel. If the relative sign between κ_V and κ_F is negative, the interference term between the W and top-quark loops responsible for the $H \rightarrow \gamma\gamma$ decays becomes positive and helps boost the $\gamma\gamma$ branching fraction. However, the difference between the global minimum in the $(+, -)$ quadrant and the local minimum in the $(+, +)$ quadrant is not statistically significant since the 95% CL contours encompass both of them. The data are consistent with the expectation for the SM Higgs boson: the point at $(\kappa_V, \kappa_F) = (1, 1)$, shown by the diamond, is within the 95% CL contour. Any significant deviation from $(\kappa_V, \kappa_F) = (1, 1)$ would imply BSM physics, with the magnitude and sign of the κ_V and κ_F measurements providing a clue to the most plausible BSM scenarios.

Figure 45 displays the corresponding 68% and 95% contours of κ_V versus κ_F from each of the individual decay modes, restricting the parameters to the $(+, +)$ and $(+, -)$ quadrants (left), and the $(+, +)$ quadrant (right). The hypothesis of a “fermiophobic” Higgs boson that couples only to bosons is represented by the point at $(1, 0)$. The point is just outside the 95% CL contour, which implies that a fermiophobic Higgs boson with $m_H = 125.5 \text{ GeV}$ is excluded at 95% CL.

The 1D likelihood scans versus κ_V and κ_F , setting one parameter at a time to the SM value of 1, are given in the left and right plots of Fig. 46, respectively. The resulting fit values are: $\kappa_V = 1.00 \pm 0.13$ and $\kappa_F = 0.5 \pm 0.2$, where the uncertainties are combined statistical and systematic, with corresponding 95% CL intervals of $[0.7; 1.3]$ and $[0.2; 1.0]$, respectively.

C. Test for the presence of BSM particles

The presence of BSM particles can considerably modify the Higgs boson phenomenology, even if the underlying Higgs boson sector in the model remains unaltered. Processes induced by loop diagrams ($H \rightarrow \gamma\gamma$ and $gg \rightarrow H$) can be particularly sensitive to the presence of new particles. Therefore, we combine and fit the data to the scale factors κ_γ and κ_g for these two processes. The partial widths associated with the tree-level production processes and decay modes are assumed to be unaltered.

Figure 47 displays the likelihood test statistic in the κ_g versus κ_γ plane, under the assumption that $\Gamma_{\text{BSM}} = 0$. The results are consistent with the expectation for the SM Higgs boson of $(\kappa_\gamma, \kappa_g) = (1, 1)$. The best-fit value is $(\kappa_\gamma, \kappa_g) = (1.5, 0.75)$.

Figure 48 gives the likelihood test statistic versus $\text{BR}_{\text{BSM}} = \Gamma_{\text{BSM}}/\Gamma_{\text{tot}}$, with κ_g and κ_γ included

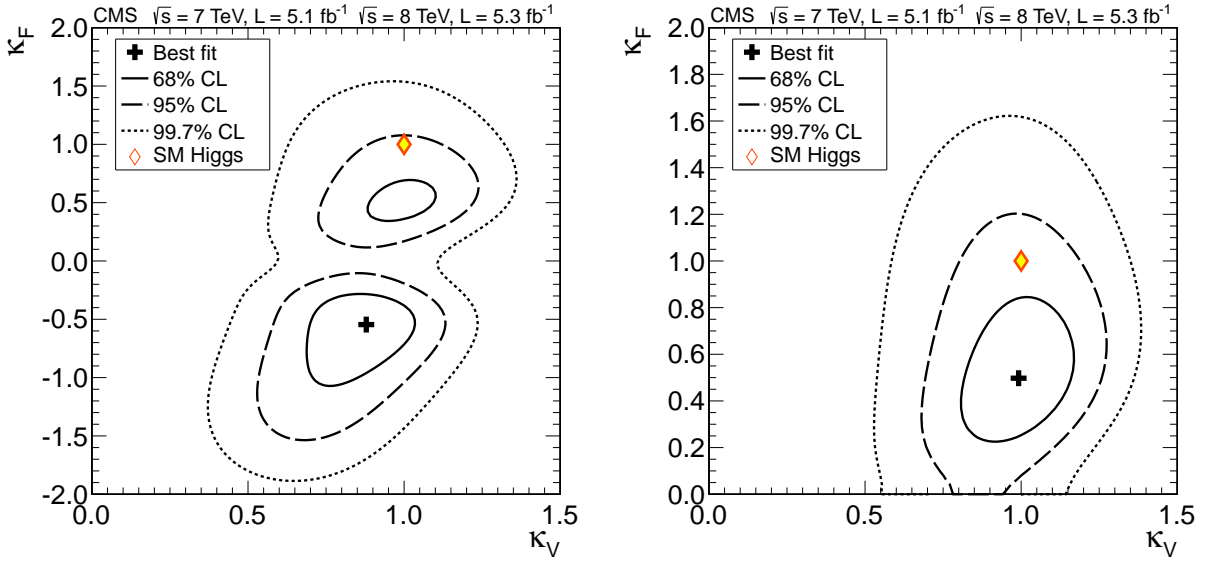


Figure 44: The likelihood test statistic in the κ_V versus κ_F plane. The cross indicates the best-fit values. The solid, dashed, and dotted lines show the 68%, 95%, and 99.7% CL contours, respectively. The diamond shows the SM point $(\kappa_V, \kappa_F) = (1, 1)$. The left plot allows for different signs of κ_V and κ_F , while the right plot constrains them both to be positive.

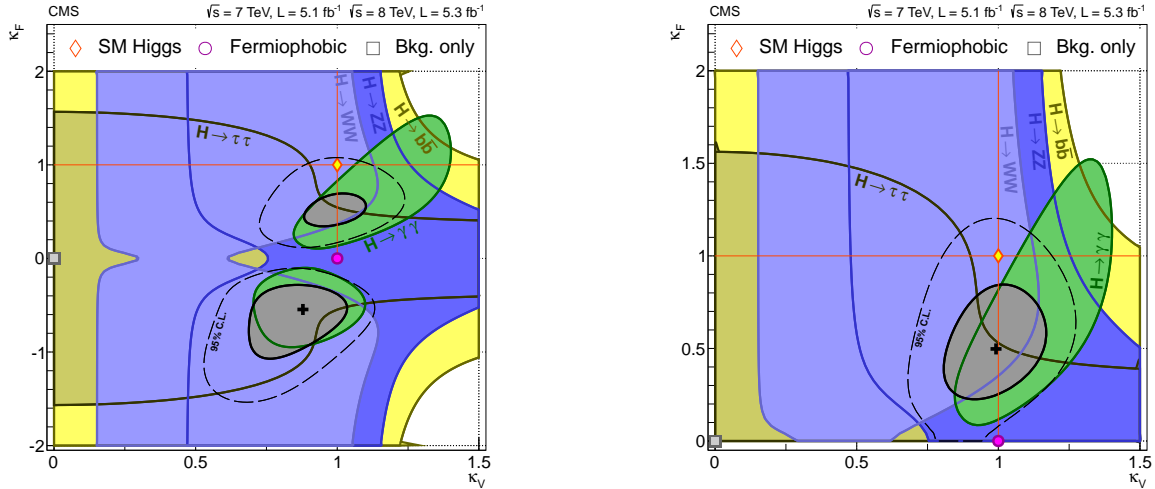


Figure 45: The 68% CL contours for the test statistic in the $(\kappa_V$ versus $\kappa_F)$ plane for individual channels (coloured regions) and the overall combination (solid thick lines). The thin dashed lines show the 95% CL range for the overall combination. The black cross indicates the global best-fit values. The diamond shows the SM Higgs boson point $(\kappa_V, \kappa_F) = (1, 1)$. The point $(\kappa_V, \kappa_F) = (1, 0)$, indicated by the circle, corresponds to the fermiophobic Higgs boson scenario. The left plot allows for different signs of κ_V and κ_F , while the right plot constrains them both to be positive.

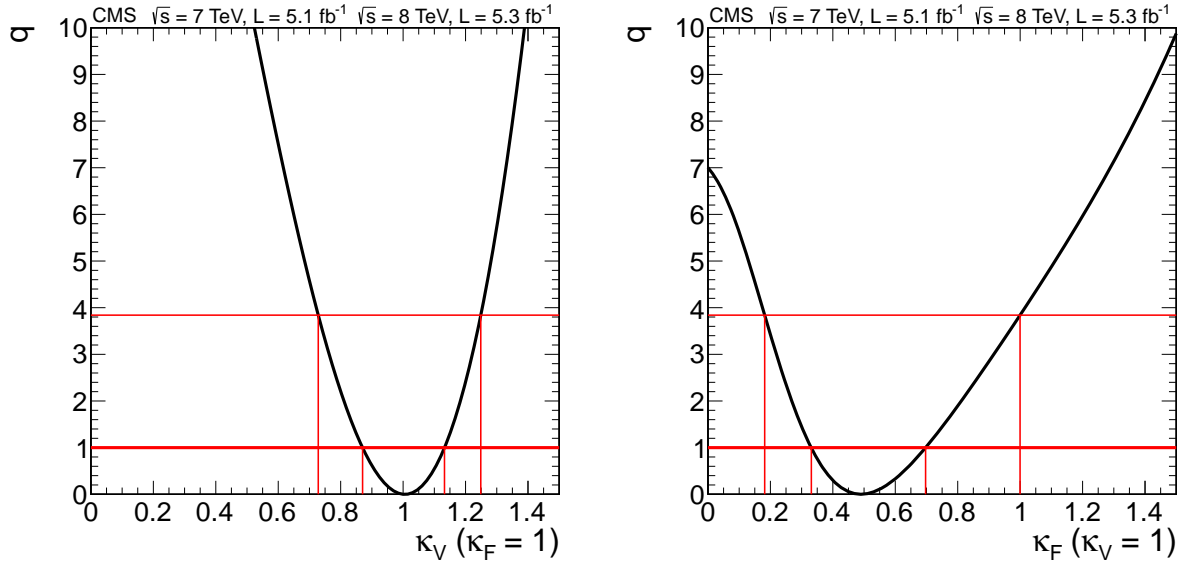


Figure 46: The likelihood test statistic $q(\kappa_V; \kappa_F = 1)$ (left) and $q(\kappa_F; \kappa_V = 1)$ (right). The intersections with the horizontal lines $q = 1$ and $q = 3.84$ mark the 68% and 95% CL intervals, respectively, as shown by the vertical lines.

as unconstrained nuisance parameters. The resulting 95% CL upper limit is $\text{BR}_{\text{BSM}} < 0.89$.

D. Test for differences in the couplings to fermions

In two-Higgs-boson doublet models (2HDM) [163], the couplings of the neutral Higgs bosons to fermions can be substantially modified with respect to the Yukawa couplings of the SM Higgs boson. For example, in the minimal supersymmetric model (MSSM), the couplings of the neutral Higgs bosons to up-type and down-type fermions are modified, with the modification being the same for all three generations and for quarks and leptons. In more general 2HDMs, leptons can be nearly decoupled from the Higgs boson that otherwise would behave like a SM Higgs boson with respect to the W and Z bosons and the quarks. To test for such modifications to the fermion couplings, we evaluate two different combinations of the corresponding parameters: one in which we allow different ratios of couplings to the up- and down-type fermions ($\lambda_{\text{du}} = \kappa_{\text{d}}/\kappa_{\text{u}}$), and the other where we allow different ratios of the couplings to the leptons and quarks ($\lambda_{\ell\text{q}} = \kappa_{\ell}/\kappa_{\text{q}}$). We assume that $\Gamma_{\text{BSM}} = 0$.

Figure 49 (left) shows the resulting test statistic versus λ_{du} , with the other free coupling modifiers, κ_V and κ_u , included as unconstrained nuisance parameters. The relative sign between the couplings to up- and down-type fermions is nearly degenerate, which manifests itself in the left-right symmetry observed in the plot. The symmetry is not perfect since there is some sensitivity to the sign of λ_{du} because of the nonvanishing role of the b quark (in comparison to the top quark) in generating the Higgs boson coupling to gluons. Figure 49 (right) displays the corresponding results versus $\lambda_{\ell\text{q}}$, with the two coupling modifiers, κ_V and κ_q , treated as unconstrained nuisance parameters. There are no loop-induced processes measurably sensitive to the relative sign of the couplings to leptons and quarks; hence, the plot exhibits a perfect left-right symmetry. Both $|\lambda_{\text{du}}|$ and $|\lambda_{\ell\text{q}}|$ are consistent with 0 and 1, with a 95% CL upper limit of 1.5 for both. The main reason for both parameters having their best-fit values close to 0 is the lack of any event excess in the $H \rightarrow \tau\tau$ channel. However, neither the $H \rightarrow \tau\tau$ nor the $H \rightarrow \text{bb}$ channels have reached sufficient sensitivity to place strong constraints on the parameters associated with the corresponding Higgs boson couplings.

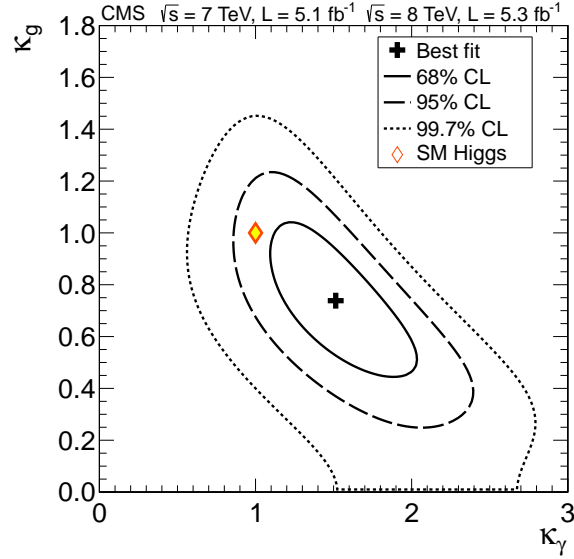


Figure 47: The likelihood test statistic $q(\kappa_\gamma, \kappa_g)$ assuming $\Gamma_{\text{BSM}} = 0$. The cross indicates the best-fit values. The solid, dashed, and dotted contours show the 68%, 95%, and 99.7% CL contours, respectively. The diamond shows the SM point $(\kappa_\gamma, \kappa_g) = (1, 1)$. The partial widths associated with the tree-level production processes and decay modes are assumed to be unaltered ($\kappa = 1$).

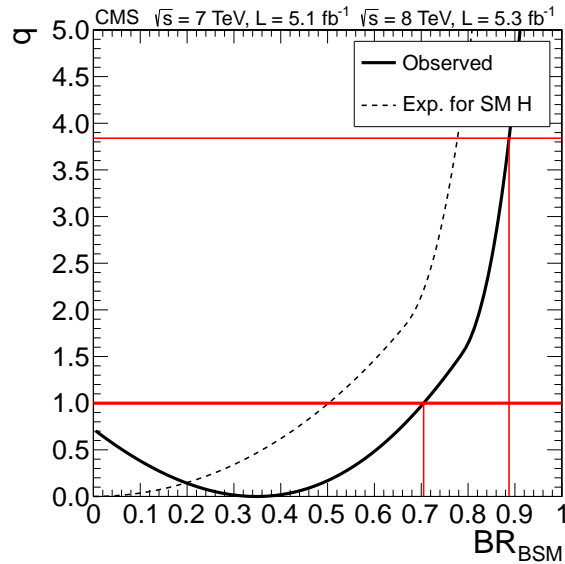


Figure 48: The likelihood test statistic q versus $\text{BR}_{\text{BSM}} = \Gamma_{\text{BSM}}/\Gamma_{\text{tot}}$, with the parameters κ_g and κ_γ included as nuisance parameters. The solid curve is the data; the dashed curve indicates the expected median results in the presence of the SM Higgs boson. The intersections with the horizontal lines $q = 1$ and 3.8 give the 68% and 95% CL intervals, respectively. The partial widths associated with the tree-level production processes and decay modes are assumed to be unaltered ($\kappa = 1$).

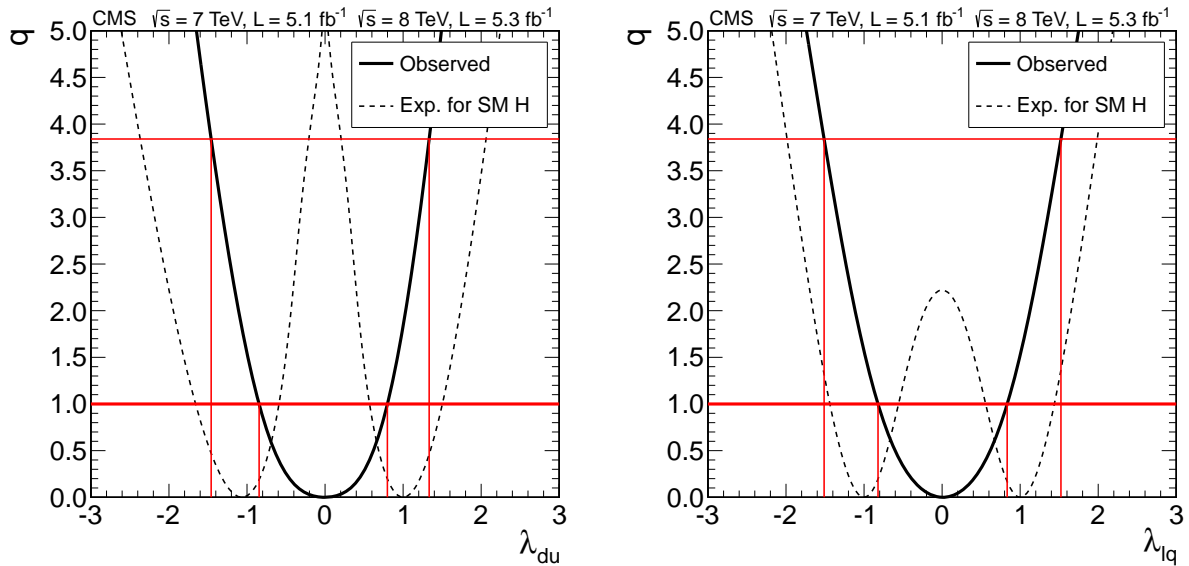


Figure 49: (Left) Likelihood test statistic q as a function of the ratio λ_{du} of the coupling to the up- and down-type fermions with the coupling modifiers κ_V and κ_u treated as nuisance parameters. (Right) The likelihood test statistic as a function of the ratio $\lambda_{\ell q}$ of the couplings to leptons and quarks with the coupling modifiers κ_V and κ_q treated as nuisance parameters. The solid curves are the results from the data. The dashed curves show the expected distributions for the SM Higgs boson. The intersection of the curves with the horizontal lines $q = 1$ and 3.8 give the 68% and 95% CL intervals, respectively.

11 Summary

In this paper, the analyses that were the basis for the discovery of a new boson at a mass of approximately 125 GeV have been described in detail. The data were collected by the CMS experiment at the LHC in proton-proton collisions at $\sqrt{s} = 7$ and 8 TeV, corresponding to integrated luminosities of up to 5.1 fb^{-1} and 5.3 fb^{-1} , respectively.

The particle is observed in the search for the SM Higgs boson using five decay modes $\gamma\gamma$, ZZ , WW , $\tau\tau$, and bb . An excess of events is found above the expected background, with a local significance of 5.0σ , signaling the production of a new particle. The expected significance for a SM Higgs boson of that mass is 5.8σ .

The excess is most significant in the two decay modes with the best mass resolution, $\gamma\gamma$ and $ZZ \rightarrow 4\ell$, and a fit to these invariant-mass peaks gives a mass of 125.3 ± 0.4 (stat.) ± 0.5 (syst.) GeV. The decay to two photons indicates that the new particle is a boson with spin different from one. Within the SM hypothesis, the couplings of the new particle to vector bosons, fermions, gluons, and photons have been measured. All the results are consistent, within their uncertainties, with expectations for a SM Higgs boson. More data are needed to ascertain whether the properties of this new state imply physics beyond the SM.

Acknowledgements

We congratulate our colleagues in the CERN accelerator departments for the excellent performance of the LHC and thank the technical and administrative staffs at CERN and at other CMS institutes for their contributions to the success of the CMS effort. In addition, we gratefully acknowledge the computing centres and personnel of the Worldwide LHC Computing Grid

for delivering so effectively the computing infrastructure essential to our analyses. Finally, we acknowledge the enduring support for the construction and operation of the LHC and the CMS detector provided by the following funding agencies: the Austrian Federal Ministry of Science and Research and the Austrian Science Fund; the Belgian Fonds de la Recherche Scientifique, and Fonds voor Wetenschappelijk Onderzoek; the Brazilian Funding Agencies (CNPq, CAPES, FAPERJ, and FAPESP); the Bulgarian Ministry of Education, Youth and Science; CERN; the Chinese Academy of Sciences, Ministry of Science and Technology, and National Natural Science Foundation of China; the Colombian Funding Agency (COLCIENCIAS); the Croatian Ministry of Science, Education and Sport; the Research Promotion Foundation, Cyprus; the Ministry of Education and Research, Recurrent financing contract SF0690030s09 and European Regional Development Fund, Estonia; the Academy of Finland, Finnish Ministry of Education and Culture, and Helsinki Institute of Physics; the Institut National de Physique Nucléaire et de Physique des Particules / CNRS, and Commissariat à l'Énergie Atomique et aux Énergies Alternatives / CEA, France; the Bundesministerium für Bildung und Forschung, Deutsche Forschungsgemeinschaft, and Helmholtz-Gemeinschaft Deutscher Forschungszentren, Germany; the General Secretariat for Research and Technology, Greece; the National Scientific Research Foundation, and National Office for Research and Technology, Hungary; the Department of Atomic Energy and the Department of Science and Technology, India; the Institute for Studies in Theoretical Physics and Mathematics, Iran; the Science Foundation, Ireland; the Istituto Nazionale di Fisica Nucleare, Italy; the Korean Ministry of Education, Science and Technology and the World Class University program of NRF, Republic of Korea; the Lithuanian Academy of Sciences; the Mexican Funding Agencies (CINVESTAV, CONACYT, SEP, and UASLP-FAI); the Ministry of Science and Innovation, New Zealand; the Pakistan Atomic Energy Commission; the Ministry of Science and Higher Education and the National Science Centre, Poland; the Fundação para a Ciência e a Tecnologia, Portugal; JINR (Armenia, Belarus, Georgia, Ukraine, Uzbekistan); the Ministry of Education and Science of the Russian Federation, the Federal Agency of Atomic Energy of the Russian Federation, Russian Academy of Sciences, and the Russian Foundation for Basic Research; the Ministry of Science and Technological Development of Serbia; the Secretaría de Estado de Investigación, Desarrollo e Innovación and Programa Consolider-Ingenio 2010, Spain; the Swiss Funding Agencies (ETH Board, ETH Zurich, PSI, SNF, UniZH, Canton Zurich, and SER); the National Science Council, Taipei; the Thailand Center of Excellence in Physics, the Institute for the Promotion of Teaching Science and Technology of Thailand and the National Science and Technology Development Agency of Thailand; the Scientific and Technical Research Council of Turkey, and Turkish Atomic Energy Authority; the Science and Technology Facilities Council, UK; the US Department of Energy, and the US National Science Foundation.

Individuals have received support from the Marie-Curie programme and the European Research Council and EPLANET (European Union); the Leventis Foundation; the A. P. Sloan Foundation; the Alexander von Humboldt Foundation; the Belgian Federal Science Policy Office; the Fonds pour la Formation à la Recherche dans l'Industrie et dans l'Agriculture (FRIA-Belgium); the Agentschap voor Innovatie door Wetenschap en Technologie (IWT-Belgium); the Ministry of Education, Youth and Sports (MEYS) of Czech Republic; the Council of Science and Industrial Research, India; the Compagnia di San Paolo (Torino); and the HOMING PLUS programme of Foundation for Polish Science, cofinanced from European Union, Regional Development Fund.

References

- [1] S. L. Glashow, "Partial-symmetries of weak interactions", *Nucl. Phys.* **22** (1961) 579, doi:10.1016/0029-5582(61)90469-2.
- [2] S. Weinberg, "A Model of Leptons", *Phys. Rev. Lett.* **19** (1967) 1264, doi:10.1103/PhysRevLett.19.1264.
- [3] A. Salam, "Weak and electromagnetic interactions", in *Elementary particle physics: relativistic groups and analyticity*, N. Svartholm, ed., p. 367. Almqvist & Wiksell, 1968. Proceedings of the eighth Nobel symposium.
- [4] ALEPH, CDF, D0, DELPHI, L3, OPAL, SLD Collaborations, the LEP Electroweak Working Group, the Tevatron Electroweak Working Group, and the SLD Electroweak and Heavy Flavour Groups, "Precision Electroweak Measurements and Constraints on the Standard Model", CERN PH-EP-2010-095, (2010). At this time, the most up-to-date Higgs boson mass constraints come from <http://lepewwg.web.cern.ch/LEPEWWG/plots/winter2012/>.
- [5] F. Englert and R. Brout, "Broken symmetry and the mass of gauge vector mesons", *Phys. Rev. Lett.* **13** (1964) 321, doi:10.1103/PhysRevLett.13.321.
- [6] P. W. Higgs, "Broken symmetries, massless particles and gauge fields", *Phys. Lett.* **12** (1964) 132, doi:10.1016/0031-9163(64)91136-9.
- [7] P. W. Higgs, "Broken symmetries and the masses of gauge bosons", *Phys. Rev. Lett.* **13** (1964) 508, doi:10.1103/PhysRevLett.13.508.
- [8] G. S. Guralnik, C. R. Hagen, and T. W. B. Kibble, "Global conservation laws and massless particles", *Phys. Rev. Lett.* **13** (1964) 585, doi:10.1103/PhysRevLett.13.585.
- [9] P. W. Higgs, "Spontaneous symmetry breakdown without massless bosons", *Phys. Rev.* **145** (1966) 1156, doi:10.1103/PhysRev.145.1156.
- [10] T. W. B. Kibble, "Symmetry breaking in non-Abelian gauge theories", *Phys. Rev.* **155** (1967) 1554, doi:10.1103/PhysRev.155.1554.
- [11] Y. Nambu and G. Jona-Lasinio, "Dynamical Model of Elementary Particles Based on an Analogy with Superconductivity. 1.", *Phys. Rev.* **122** (1961) 345, doi:10.1103/PhysRev.122.345.
- [12] Y. Nambu, "Spontaneous Symmetry Breaking in Particle Physics: a Case of Cross Fertilization". The Nobel Foundation, 2008.
- [13] M. Gell-Mann and M. Levy, "The axial vector current in beta decay", *Nuovo Cim.* **16** (1960) 705, doi:10.1007/BF02859738.
- [14] J. M. Cornwall, D. N. Levin, and G. Tiktopoulos, "Uniqueness of spontaneously broken gauge theories", *Phys. Rev. Lett.* **30** (1973) 1268, doi:10.1103/PhysRevLett.30.1268.
- [15] J. M. Cornwall, D. N. Levin, and G. Tiktopoulos, "Derivation of gauge invariance from high-energy unitarity bounds on the S matrix", *Phys. Rev. D* **10** (1974) 1145, doi:10.1103/PhysRevD.10.1145. Erratum-ibid. D11 (1975) 972, doi:10.1103/PhysRevD.11.972.

- [16] C. H. Llewellyn Smith, "High energy behaviour and gauge symmetry", *Phys. Lett. B* **46** (1973) 233, doi:10.1016/0370-2693(73)90692-8.
- [17] B. W. Lee, C. Quigg, and H. B. Thacker, "Weak interactions at very high energies: The role of the Higgs-boson mass", *Phys. Rev. D* **16** (1977) 1519, doi:10.1103/PhysRevD.16.1519.
- [18] ALEPH, DELPHI, L3, OPAL Collaborations, and LEP Working Group for Higgs Boson Searches, "Search for the standard model Higgs boson at LEP", *Phys. Lett. B* **565** (2003) 61, doi:10.1016/S0370-2693(03)00614-2, arXiv:hep-ex/0306033.
- [19] CDF and D0 Collaborations, "Combination of Tevatron Searches for the Standard Model Higgs Boson in the W^+W^- Decay Mode", *Phys. Rev. Lett.* **104** (2010) 061802, doi:10.1103/PhysRevLett.104.061802.
- [20] CMS Collaboration, "Combined results of searches for the standard model Higgs boson in pp collisions at $\sqrt{s} = 7$ TeV", *Phys. Lett. B* **710** (2012) 26, doi:10.1016/j.physletb.2012.02.064, arXiv:1202.1488.
- [21] ATLAS Collaboration, "Combined search for the Standard Model Higgs boson in pp collisions at $\sqrt{s} = 7$ TeV with the ATLAS detector", *Phys. Rev. D* **86** (2012) 032003, doi:10.1103/PhysRevD.86.032003, arXiv:1207.0319.
- [22] ATLAS Collaboration, "Observation of a new particle in the search for the Standard Model Higgs boson with the ATLAS detector at the LHC", *Phys. Lett. B* (2012) 1, doi:10.1016/j.physletb.2012.08.020, arXiv:1207.7214.
- [23] CMS Collaboration, "Observation of a new boson at a mass of 125 GeV with the CMS experiment at the LHC", *Phys. Lett. B* (2012) 30, doi:10.1016/j.physletb.2012.08.021, arXiv:1207.7235.
- [24] CDF and D0 Collaboration, "Evidence for a Particle Produced in Association with Weak Bosons and Decaying to a Bottom-Antibottom Quark Pair in Higgs Boson Searches at the Tevatron", *Phys. Rev. Lett.* **109** (Aug, 2012) 071804, doi:10.1103/PhysRevLett.109.071804.
- [25] LHC Higgs Cross Section Working Group, "Handbook of LHC Higgs Cross Sections: 1. Inclusive Observables", (CERN-2011-02, Geneva, 2011). arXiv:1101.0593.
- [26] LHC Higgs Cross Section Working Group, "Handbook of LHC Higgs Cross Sections: 2. Differential Distributions", (CERN-2012-02, Geneva, 2012). arXiv:1201.3084.
- [27] M. Della Negra et al., "Muon trigger and identification", in *Proceedings of the Large Hadron Collider Workshop*, G. Jarlskog and D. Rein, eds., p. 467. Aachen, Germany, 1990. CERN 90-10-V-3/ECFA 90-133-V-3.
- [28] CMS Collaboration, "Letter of intent by the CMS Collaboration for a general purpose detector at the LHC", Technical Report CERN-LHCC-92-03, CERN-LHCC-I-1, CERN, (1992).
- [29] N. Ellis and T. S. Virdee, "Experimental challenges in high luminosity collider physics", *Ann. Rev. Nucl. Part. Sci.* **44** (1994) 609, doi:10.1146/annurev.ns.44.120194.003141.

- [30] CMS Collaboration, “The CMS experiment at the CERN LHC”, *JINST* **3** (2008) S08004, doi:10.1088/1748-0221/3/08/S08004.
- [31] CMS Collaboration, “Identification of b-quark jets with the CMS experiment”, (2013). arXiv:1211.4462. Submitted to JINST.
- [32] CMS Collaboration, “Upsilon production cross section in pp collisions at $\sqrt{s} = 7$ TeV”, *Phys. Rev. D* **83** (2011) 112004, doi:10.1103/PhysRevD.83.112004, arXiv:1012.5545.
- [33] K. Rose, “Deterministic annealing for clustering, compression, classification, regression and related optimization problems”, *Proceedings of the IEEE* **86** (1998) 2210, doi:10.1109/5.726788.
- [34] CMS Collaboration, “Particle-Flow Event Reconstruction in CMS and Performance for Jets, Taus, and E_T^{miss} ”, CMS Physics Analysis Summary CMS-PAS-PFT-09-001, (2009).
- [35] CMS Collaboration, “Commissioning of the Particle-flow Event Reconstruction in Minimum-Bias and Jet Events from pp Collisions at 7 TeV”, CMS Physics Analysis Summary CMS-PAS-PFT-10-002, (2010).
- [36] P. Adzic et al., “Energy resolution of the barrel of the CMS Electromagnetic Calorimeter”, *JINST* **2** (2007) S08004, doi:10.1088/1748-0221/2/04/P04004.
- [37] M. Anfreville et al., “Laser monitoring system for the CMS lead tungstate crystal calorimeter”, *Nucl. Instr. and Meth. A* **594** (2008) 292, doi:10.1016/j.nima.2008.01.104.
- [38] CMS Collaboration, “Electromagnetic calorimeter calibration with 7 TeV data”, CMS Physics Analysis Summary CMS-PAS-EGM-10-003, (2010).
- [39] CMS Collaboration, “Role of the CMS electromagnetic calorimeter in the hunt for the Higgs boson in the two-gamma channel”, *J. Phys. Conf. Ser.* **404** (2012) 012002, doi:10.1088/1742-6596/404/1/012002.
- [40] H. Voss et al., “TMVA: Toolkit for Multivariate Data Analysis with ROOT”, in *XI Int. Workshop on Advanced Computing and Analysis Techniques in Physics Research*. 2007. arXiv:physics/0703039. PoS ACAT:040.
- [41] S. Baffioni et al., “Electron reconstruction in CMS”, *Eur. Phys. J. C* **49** (2007) 1099, doi:10.1140/epjc/s10052-006-0175-5.
- [42] CMS Collaboration, “Electron Reconstruction and Identification at $\sqrt{s} = 7$ TeV”, CMS Physics Analysis Summary CMS-PAS-EGM-10-004, (2010).
- [43] CMS Collaboration, “Commissioning of the particle-flow event reconstruction with leptons from J/ψ and W decays at 7 TeV”, CMS Physics Analysis Summary CMS-PAS-PFT-10-003, (2010).
- [44] W. Adam et al., “Reconstruction of electrons with the Gaussian-sum filter in the CMS tracker at the LHC”, *J. Phys. G* **31** (2005) N9, doi:10.1088/0954-3899/31/9/N01.
- [45] M. Cacciari, G. P. Salam, and G. Soyez, “The anti- k_r jet clustering algorithm”, *JHEP* **04** (2008) 063, doi:10.1088/1126-6708/2008/04/063, arXiv:0802.1189.

- [46] M. Cacciari, G. P. Salam, “Dispelling the N^3 myth for the k_t jet-finder”, *Phys. Lett. B* **641** (2006) 57, doi:10.1016/j.physletb.2006.08.037, arXiv:hep-ph/0512210.
- [47] CMS Collaboration, “Determination of jet energy calibration and transverse momentum resolution in CMS”, *JINST* **6** (2011) 11002, doi:10.1088/1748-0221/6/11/P11002, arXiv:1107.4277.
- [48] CMS Collaboration, “Performance of tau-lepton reconstruction and identification in CMS”, *JINST* **7** (2012) P01001, doi:10.1088/1748-0221/7/01/P01001.
- [49] GEANT4 Collaboration, “GEANT4—a simulation toolkit”, *Nucl. Instrum. Meth. A* **506** (2003) 250, doi:10.1016/S0168-9002(03)01368-8.
- [50] J. Pumplin et al., “New generation of parton distributions with uncertainties from global QCD analysis”, *JHEP* **02** (2002) 012, doi:10.1088/1126-6708/2002/07/012, arXiv:arXiv:hep-ph/0201195.
- [51] M. Guzzi et al., “CT10 parton distributions and other developments in the global QCD analysis”, (2011). arXiv:1101.0561.
- [52] T. Sjöstrand, S. Mrenna, and P. Z. Skands, “PYTHIA 6.4 physics and manual”, *JHEP* **05** (2006) 026, doi:10.1088/1126-6708/2006/05/026.
- [53] S. Gieseke et al., “Herwig++ 2.0 Release Note”, (2006). arXiv:hep-ph/0609306.
- [54] S. Jadach, J. H. Kuhn, and Z. Wąs, “TAUOLA - a library of Monte Carlo programs to simulate decays of polarized tau leptons”, *Comp. Phys. Commun.* **64** (1991) 275, doi:10.1016/0010-4655(91)90038-M.
- [55] CMS Collaboration, “Measurement of the underlying event activity at the LHC with $\sqrt{s} = 7$ TeV and comparison with $\sqrt{s} = 0.9$ TeV”, *JHEP* **09** (2011) 109, doi:10.1007/JHEP09(2011)109.
- [56] S. Frixione, P. Nason, and C. Oleari, “Matching NLO QCD computations with Parton Shower simulations: the POWHEG method”, *JHEP* **11** (2007) 070, doi:10.1088/1126-6708/2007/11/070, arXiv:0709.2092.
- [57] S. Alioli et al., “NLO Higgs boson production via gluon fusion matched with shower in POWHEG”, *JHEP* **04** (2009) 002, doi:10.1088/1126-6708/2009/04/002.
- [58] P. Nason and C. Oleari, “NLO Higgs boson production via vector-boson fusion matched with shower in POWHEG”, *JHEP* **02** (2010) 037, doi:10.1007/JHEP02(2010)037.
- [59] D. de Florian and M. Grazzini, “Higgs production at the LHC: updated cross sections at $\sqrt{s} = 8$ TeV”, *Phys. Lett. B* **718** (2012) 117, doi:10.1016/j.physletb.2012.10.019, arXiv:1206.4133.
- [60] C. Anastasiou et al., “Inclusive Higgs boson cross-section for the LHC at 8 TeV”, *JHEP* **04** (2012) 004, doi:10.1007/JHEP04(2012)004, arXiv:1202.3638.
- [61] C. Anastasiou, R. Boughezal, and F. Petriello, “Mixed QCD-electroweak corrections to Higgs boson production in gluon fusion”, *JHEP* **04** (2009) 003, doi:10.1088/1126-6708/2009/04/003, arXiv:0811.3458.

- [62] D. de Florian and M. Grazzini, "Higgs production through gluon fusion: updated cross sections at the Tevatron and the LHC", *Phys. Lett. B* **674** (2009) 291, doi:10.1016/j.physletb.2009.03.033, arXiv:0901.2427.
- [63] J. Baglio and A. Djouadi, "Higgs production at the LHC", *JHEP* **03** (2011) 055, doi:10.1007/JHEP03(2011)055, arXiv:1012.0530.
- [64] A. Djouadi, M. Spira, and P. M. Zerwas, "Production of Higgs bosons in proton colliders: QCD corrections", *Phys. Lett. B* **264** (1991) 440, doi:10.1016/0370-2693(91)90375-Z.
- [65] S. Dawson, "Radiative corrections to Higgs boson production", *Nucl. Phys. B* **359** (1991) 283, doi:10.1016/0550-3213(91)90061-2.
- [66] M. Spira et al., "Higgs boson production at the LHC", *Nucl. Phys. B* **453** (1995) 17, doi:10.1016/0550-3213(95)00379-7, arXiv:hep-ph/9504378.
- [67] R. V. Harlander and W. B. Kilgore, "Next-to-next-to-leading order Higgs production at hadron colliders", *Phys. Rev. Lett.* **88** (2002) 201801, doi:10.1103/PhysRevLett.88.201801, arXiv:hep-ph/0201206.
- [68] C. Anastasiou and K. Melnikov, "Higgs boson production at hadron colliders in NNLO QCD", *Nucl. Phys. B* **646** (2002) 220, doi:10.1016/S0550-3213(02)00837-4, arXiv:hep-ph/0207004.
- [69] V. Ravindran, J. Smith, and W. L. van Neerven, "NNLO corrections to the total cross section for Higgs boson production in hadron hadron collisions", *Nucl. Phys. B* **665** (2003) 325, doi:10.1016/S0550-3213(03)00457-7, arXiv:hep-ph/0302135.
- [70] S. Catani et al., "Soft-gluon resummation for Higgs boson production at hadron colliders", *JHEP* **07** (2003) 028, doi:10.1088/1126-6708/2003/07/028.
- [71] S. Actis et al., "NLO electroweak corrections to Higgs boson production at hadron colliders", *Phys. Lett. B* **670** (2008) 12, doi:10.1016/j.physletb.2008.10.018, arXiv:0809.1301.
- [72] U. Aglietti et al., "Two-loop light fermion contribution to Higgs production and decays", *Phys. Lett. B* **595** (2004) 432, doi:10.1016/j.physletb.2004.06.063, arXiv:hep-ph/0404071.
- [73] G. Degrossi and F. Maltoni, "Two-loop electroweak corrections to Higgs production at hadron colliders", *Phys. Lett. B* **600** (2004) 255, doi:10.1016/j.physletb.2004.09.008, arXiv:hep-ph/0407249.
- [74] M. Ciccolini, A. Denner, and S. Dittmaier, "Strong and Electroweak Corrections to the Production of a Higgs Boson+2 Jets via Weak Interactions at the Large Hadron Collider", *Phys. Rev. Lett.* **99** (2007) 161803, doi:10.1103/PhysRevLett.99.161803, arXiv:0707.0381.
- [75] M. Ciccolini, A. Denner, and S. Dittmaier, "Electroweak and QCD corrections to Higgs production via vector-boson fusion at the LHC", *Phys. Rev. D* **77** (2008) 013002, doi:10.1103/PhysRevD.77.013002, arXiv:0710.4749.

- [76] T. Figy, C. Oleari, and D. Zeppenfeld, "Next-to-leading order jet distributions for Higgs boson production via weak-boson fusion", *Phys. Rev. D* **68** (2003) 073005, doi:10.1103/PhysRevD.68.073005, arXiv:hep-ph/0306109.
- [77] K. Arnold et al., "VBFNLO: A parton level Monte Carlo for processes with electroweak bosons", *Comput. Phys. Commun.* **180** (2009) 1661, doi:10.1016/j.cpc.2009.03.006, arXiv:0811.4559.
- [78] P. Bolzoni et al., "Higgs production via vector-boson fusion at NNLO in QCD", *Phys. Rev. Lett.* **105** (2010) 011801, doi:10.1103/PhysRevLett.105.011801, arXiv:1003.4451.
- [79] T. Han and S. Willenbrock, "QCD correction to the $pp \rightarrow WH$ and ZH total cross-sections", *Phys. Lett. B* **273** (1991) 167, doi:10.1016/0370-2693(91)90572-8.
- [80] O. Brein, A. Djouadi, and R. Harlander, "NNLO QCD corrections to the Higgs-strahlung processes at hadron colliders", *Phys. Lett. B* **579** (2004) 149, doi:10.1016/j.physletb.2003.10.112, arXiv:hep-ph/0307206.
- [81] M. L. Ciccolini, S. Dittmaier, and M. Krämer, "Electroweak radiative corrections to associated WH and ZH production at hadron colliders", *Phys. Rev. D* **68** (2003) 073003, doi:10.1103/PhysRevD.68.073003, arXiv:hep-ph/0306234.
- [82] R. Hamberg, W. L. van Neerven, and T. Matsuura, "A complete calculation of the order α_s^2 correction to the Drell-Yan K factor", *Nucl. Phys. B* **359** (1991) 343, doi:10.1016/0550-3213(91)90064-5.
- [83] A. Denner et al., "Electroweak corrections to Higgs-strahlung off W/Z bosons at the Tevatron and the LHC with HAWK", *JHEP* **1203** (2012) 075, doi:10.1007/JHEP03(2012)075, arXiv:1112.5142.
- [84] G. Ferrera, M. Grazzini, and F. Tramontano, "Associated WH production at hadron colliders: a fully exclusive QCD calculation at NNLO", *Phys. Rev. Lett.* **107** (2011) 152003, doi:10.1103/PhysRevLett.107.152003, arXiv:1107.1164.
- [85] W. Beenakker et al., "Higgs radiation off top quarks at the Tevatron and the LHC", *Phys. Rev. Lett.* **87** (2001) 201805, doi:10.1103/PhysRevLett.87.201805, arXiv:hep-ph/0107081.
- [86] W. Beenakker et al., "NLO QCD corrections to $t\bar{t}H$ production in hadron collisions.", *Nucl. Phys. B* **653** (2003) 151, doi:10.1016/S0550-3213(03)00044-0, arXiv:hep-ph/0211352.
- [87] S. Dawson et al., "Associated top quark Higgs boson production at the LHC", *Phys. Rev. D* **67** (2003) 071503, doi:10.1103/PhysRevD.67.071503, arXiv:hep-ph/0211438.
- [88] S. Dawson et al., "Associated Higgs production with top quarks at the Large Hadron Collider: NLO QCD corrections", *Phys. Rev. D* **68** (2003) 034022, doi:10.1103/PhysRevD.68.034022, arXiv:hep-ph/0305087.
- [89] A. Bredenstein et al., "Radiative corrections to the semileptonic and hadronic Higgs-boson decays $H \rightarrow WW/ZZ \rightarrow 4$ fermions", *JHEP* **02** (2007) 080, doi:10.1088/1126-6708/2007/02/080, arXiv:hep-ph/0611234.

- [90] A. Bredenstein et al., “Precise predictions for the Higgs-boson decay $H \rightarrow WW/ZZ \rightarrow 4$ leptons”, *Phys. Rev. D* **74** (2006) 013004, doi:10.1103/PhysRevD.74.013004, arXiv:hep-ph/0604011.
- [91] A. Djouadi, J. Kalinowski, and M. Spira, “HDECAY: A program for Higgs boson decays in the standard model and its supersymmetric extension”, *Comput. Phys. Commun.* **108** (1998) 56, doi:10.1016/S0010-4655(97)00123-9, arXiv:hep-ph/9704448.
- [92] A. Djouadi et al., “An update of the program HDECAY”, in *The Les Houches 2009 workshop on TeV colliders: The tools and Monte Carlo working group summary report*. 2010. arXiv:1003.1643.
- [93] S. Actis et al., “NNLO Computational Techniques: the Cases $H \rightarrow \gamma\gamma$ and $H \rightarrow gg$ ”, *Nucl. Phys. B* **811** (2009) 182, doi:10.1016/j.nuclphysb.2008.11.024, arXiv:0809.3667.
- [94] A. Denner et al., “Standard Model Higgs-Boson Branching Ratios with Uncertainties”, *Eur. Phys. J. C* **71** (2011) 1753, doi:10.1140/epjc/s10052-011-1753-8, arXiv:1107.5909.
- [95] S. Alekhin et al., “The PDF4LHC Working Group Interim Report”, (2011). arXiv:1101.0536.
- [96] M. Botje et al., “The PDF4LHC Working Group Interim Recommendations”, (2011). arXiv:1101.0538.
- [97] H.-L. Lai et al., “New parton distributions for collider physics”, *Phys. Rev. D* **82** (2010) 074024, doi:10.1103/PhysRevD.82.074024, arXiv:1007.2241.
- [98] A. D. Martin et al., “Parton distributions for the LHC”, *Eur. Phys. J. C* **63** (2009) 189, doi:10.1140/epjc/s10052-009-1072-5, arXiv:0901.0002.
- [99] NNPDF Collaboration, “Impact of Heavy Quark Masses on Parton Distributions and LHC Phenomenology”, *Nucl. Phys. B* **849** (2011) 296, doi:10.1016/j.nuclphysb.2011.03.021, arXiv:1101.1300.
- [100] G. Bozzi et al., “Transverse-momentum resummation and the spectrum of the Higgs boson at the LHC”, *Nucl. Phys. B* **737** (2006) 73, doi:10.1016/j.nuclphysb.2005.12.022, arXiv:hep-ph/0508068.
- [101] D. de Florian et al., “Transverse-momentum resummation: Higgs boson production at the Tevatron and the LHC”, *JHEP* **11** (2011) 064, doi:10.1007/JHEP11(2011)064.
- [102] C. Anastasiou, K. Melnikov, and F. Petriello, “Fully differential Higgs boson production and the di-photon signal through next-to-next-to-leading order”, *Nucl. Phys. B* **724** (2005) 197, doi:10.1016/j.nuclphysb.2005.06.036.
- [103] C. Anastasiou, S. Bucherer, and Z. Kunszt, “HPro: A NLO Monte-Carlo for Higgs production via gluon fusion with finite heavy quark masses”, *JHEP* **10** (2009) 068, doi:10.1088/1126-6708/2009/10/068.
- [104] J. Alwall et al., “MadGraph 5 : going beyond”, *JHEP* **06** (2011) 128, doi:10.1007/JHEP06(2011)128, arXiv:1106.0522.

- [105] J. Alwall et al., “MadGraph/MadEvent v4: the new web generation”, *JHEP* **09** (2007) 028, doi:10.1088/1126-6708/2007/09/028, arXiv:0706.2334.
- [106] T. Binoth, N. Kauer, and P. Mertsch, “Gluon-induced QCD corrections to $pp \rightarrow ZZ \rightarrow \ell\bar{\ell}\ell'\bar{\ell}'$ ”, (2008). arXiv:0807.0024.
- [107] ATLAS and CMS Collaborations, LHC Higgs Combination Group, “Procedure for the LHC Higgs boson search combination in Summer 2011”, Technical Report ATL-PHYS-PUB 2011-11, CMS NOTE 2011/005, (2011).
- [108] C. J. Seez et al., “Photon decay modes of the intermediate mass Higgs”, in *Proceedings of the Large Hadron Collider Workshop*, G. Jarlskog and D. Rein, eds., p. 474. Aachen, Germany, 1990. CERN 90-10-V-2/ECFA 90-133-V-2.
- [109] CMS Collaboration, “Search for the standard model Higgs boson decaying into two photons in pp collisions at $\sqrt{s} = 7$ TeV”, *Phys. Lett. B* **710** (2012) 403, doi:10.1016/j.physletb.2012.03.003, arXiv:1202.1487.
- [110] A. Ballestrero, G. Bevilacqua, and E. Maina, “A complete parton level analysis of boson-boson scattering and ElectroWeak Symmetry Breaking in $lv +$ four jets production at the LHC”, *JHEP* **05** (2009) 015, doi:10.1088/1126-6708/2009/05/015.
- [111] D. L. Rainwater, R. Szalapski, and D. Zeppenfeld, “Probing color singlet exchange in $Z +$ two jet events at the CERN LHC”, *Phys. Rev. D* **54** (1996) 6680, doi:10.1103/PhysRevD.54.6680.
- [112] L. Dixon and M. S. Siu, “Resonance-continuum interference in the diphoton Higgs signal at the LHC”, *Phys. Rev. Lett.* **90** (2003) 252001, doi:10.1103/PhysRevLett.90.252001, arXiv:hep-ph/0302233.
- [113] R. J. Barlow, “Event classification using weighting methods”, *J. Comp. Phys.* **72** (1987) 202, doi:10.1016/0021-9991(87)90078-7.
- [114] CMS Collaboration, “Search for the standard model Higgs boson in the decay channel $H \rightarrow ZZ \rightarrow 4\ell$ in pp collisions at $\sqrt{s} = 7$ TeV”, *Phys. Rev. Lett.* **108** (2012) 111804, doi:10.1103/PhysRevLett.108.111804, arXiv:1202.1997.
- [115] CMS Collaboration, “Study of the mass and spin-parity of the Higgs boson candidate via its decays to Z boson pairs”, *Phys. Rev. Lett.* **110** (2013) 081803, doi:10.1103/PhysRevLett.110.081803, arXiv:1212.6639.
- [116] CMS Collaboration, “Measurement of the inclusive W and Z production cross sections in pp collisions at $\sqrt{s} = 7$ TeV with the CMS experiment”, *JHEP* **10** (2011) 132, doi:10.1007/JHEP10(2011)132.
- [117] A. Soni and R. M. Xu, “Probing CP violation via Higgs decays to four leptons”, *Phys. Rev. D* **48** (1993) 5259, doi:10.1103/PhysRevD.48.5259, arXiv:hep-ph/9301225.
- [118] V. D. Barger et al., “Higgs bosons: Intermediate mass range at e^+e^- colliders”, *Phys. Rev. D* **49** (1994) 79, doi:10.1103/PhysRevD.49.79, arXiv:hep-ph/9306270.
- [119] S. Y. Choi et al., “Identifying the Higgs spin and parity in decays to Z pairs”, *Phys. Lett. B* **553** (2003) 61, doi:10.1016/S0370-2693(02)03191-X, arXiv:hep-ph/0210077.

- [120] B. C. Allanach et al., “Exploring small extra dimensions at the Large Hadron Collider”, *JHEP* **0212** (2002) 039, doi:10.1088/1126-6708/2002/12/039, arXiv:hep-ph/0211205.
- [121] C. P. Buszello et al., “Prospective analysis of spin- and CP-sensitive variables in $H \rightarrow ZZ \rightarrow l_1^+ l_1^- l_2^+ l_2^-$ at the LHC”, *Eur. Phys. J. C* **32** (2004) 209, doi:10.1140/epjc/s2003-01392-0, arXiv:hep-ph/0212396.
- [122] R. M. Godbole, D. J. Miller, and M. M. Mühlleitner, “Aspects of CP violation in the H ZZ coupling at the LHC”, *JHEP* **07** (2007) 031, doi:10.1088/1126-6708/2007/12/031, arXiv:0708.0458.
- [123] W.-Y. Keung, I. Low, and J. Shu, “Landau-Yang Theorem and Decays of a Z' Boson into Two Z Bosons”, *Phys. Rev. Lett.* **101** (2008) 091802, doi:10.1103/PhysRevLett.101.091802, arXiv:0806.2864.
- [124] O. Antipin and A. Soni, “Towards establishing the spin of warped gravitons”, *JHEP* **10** (2008) 018, doi:10.1088/1126-6708/2008/10/018, arXiv:0806.3427.
- [125] K. Hagiwara, Q. Li, and K. Mawatari, “Jet angular correlation in vector-boson fusion processes at hadron colliders”, *JHEP* **07** (2009) 101, doi:10.1088/1126-6708/2009/07/101, arXiv:0905.4314.
- [126] Y. Gao et al., “Spin determination of single-produced resonances at hadron colliders”, *Phys. Rev. D* **81** (2010) 075022, doi:10.1103/PhysRevD.81.075022, arXiv:1001.3396.
- [127] A. De Rujula et al., “Higgs look-alikes at the LHC”, *Phys. Rev. D* **82** (2010) 013003, doi:10.1103/PhysRevD.82.013003, arXiv:1001.5300.
- [128] J. S. Gainer et al., “Improving the sensitivity of Higgs boson searches in the golden channel”, *JHEP* **11** (2011) 027, doi:10.1007/JHEP11(2011)027, arXiv:1108.2274.
- [129] S. Bolognesi et al., “On the spin and parity of a single-produced resonance at the LHC”, *Phys. Rev. D* **86** (2012) 095031, doi:10.1103/PhysRevD.86.095031, arXiv:1208.4018.
- [130] CMS Collaboration, “Search for a Higgs boson in the decay channel $H \rightarrow ZZ^{(*)} \rightarrow q\bar{q}\ell^-\ell^+$ in pp collisions at $\sqrt{s} = 7$ TeV”, *JHEP* **04** (2012) 036, doi:10.1007/JHEP04(2012)036, arXiv:1202.1416.
- [131] J. Campbell and R. K. Ellis, “MCFM for the Tevatron and the LHC”, *Nucl. Phys. Proc. Suppl.* **205** (2010) 10, doi:10.1016/j.nuclphysbps.2010.08.011, arXiv:1007.3492.
- [132] J. M. Campbell and R. K. Ellis, “An update on vector boson pair production at hadron colliders”, *Phys. Rev. D* **60** (1999) 113006, doi:10.1103/PhysRevD.60.113006, arXiv:hep-ph/9905386.
- [133] J. M. Campbell, R. K. Ellis, and C. Williams, “Vector boson pair production at the LHC”, *JHEP* **07** (2011) 018, doi:10.1007/JHEP07(2011)018, arXiv:1105.0020.
- [134] CMS Collaboration, “Absolute Calibration of the Luminosity Measurement at CMS: Winter 2012 Update”, CMS Physics Analysis Summary CMS-PAS-SMP-12-008, (2012).

- [135] CMS Collaboration, “CMS Luminosity Based on Pixel Cluster Counting - Summer 2012 Update”, CMS Physics Analysis Summary CMS-PAS-LUM-12-001, (2012).
- [136] CMS Collaboration, “Observation of Z decays to four leptons with the CMS detector at the LHC”, *JHEP* **1212** (2012) 034, doi:10.1007/JHEP12(2012)034, arXiv:1210.3844.
- [137] CMS Collaboration, “Search for the standard model Higgs boson decaying to W^+W^- in the fully leptonic final state in pp collisions at $\sqrt{s} = 7$ TeV”, *Phys. Lett. B* **710** (2012) 91, doi:10.1016/j.physletb.2012.02.076, arXiv:1202.1489.
- [138] R. N. Cahn et al., “Transverse momentum signatures for heavy Higgs bosons”, *Phys. Rev. D* **35** (1987) 1626, doi:10.1103/PhysRevD.35.1626.
- [139] R. C. Gray et al., “Backgrounds to Higgs Boson Searches from Asymmetric Internal Conversion”, (2011). arXiv:1110.1368.
- [140] CMS Collaboration, “Performance of muon identification in pp collisions at $\sqrt{s} = 7$ TeV”, CMS Physics Analysis Summary CMS-PAS-MUO-10-002, (2010).
- [141] CMS Collaboration, “Measurement of Inclusive Z Cross Section via Decays to Tau Pairs in pp Collisions at $\sqrt{s} = 7$ TeV”, *JHEP* **08** (2011) 117, doi:10.1007/JHEP08(2011)117.
- [142] C. C. Almenar, “Search for the neutral MSSM Higgs bosons in the $\tau\tau$ decay channels at CDF Run II”. PhD thesis, Universitat de València. FERMILAB-THESIS-2008-86. doi:10.2172/953708.
- [143] R. K. Ellis et al., “Higgs decay to $\tau^+\tau^-$: A possible signature of intermediate mass Higgs bosons at high energy hadron colliders”, *Nucl. Phys. B* **297** (1988) 221, doi:10.1016/0550-3213(88)90019-3.
- [144] CMS Collaboration, “Missing transverse energy performance of the CMS detector”, *JINST* **6** (2011) P09001, doi:10.1088/1748-0221/6/09/P09001, arXiv:1106.5048.
- [145] B. K. Bullock, K. Hagiwara, and A. D. Martin, “Tau polarization and its correlations as a probe of new physics”, *Nucl. Phys. B* **395** (1993) 499, doi:10.1016/0550-3213(93)90045-Q.
- [146] Particle Data Group Collaboration, “Review of Particle Physics”, *Phys. Rev. D* **86** (2012) 010001, doi:10.1103/PhysRevD.86.010001.
- [147] J. S. Conway, “Nuisance Parameters in Likelihoods for Multisource Spectra”, in *Proceedings of PHYSTAT 2011 Workshop on Statistical Issues Related to Discovery Claims in Search Experiments and Unfolding*, p. 115. CERN, 2011. CERN-2011-006.
- [148] J. M. Butterworth et al., “Jet Substructure as a New Higgs-Search Channel at the Large Hadron Collider”, *Phys. Rev. Lett.* **100** (2008) 242001, doi:10.1103/PhysRevLett.100.242001.
- [149] CMS Collaboration, “Search for the standard model Higgs boson decaying to bottom quarks in pp collisions at $\sqrt{s} = 7$ TeV”, *Phys. Lett. B* **710** (2012) 284, doi:10.1016/j.physletb.2012.02.085.

- [150] T. Aaltonen et al., “Improved b -jet Energy Correction for $H \rightarrow b\bar{b}$ Searches at CDF”, (2011). arXiv:1107.3026.
- [151] CMS Collaboration, “Absolute Calibration of the CMS Luminosity Measurement: Summer 2011 Update”, CMS Physics Analysis Summary CMS-PAS-EWK-11-001, (2011).
- [152] M. Ciccolini, A. Denner, and S. Dittmaier, “Strong and Electroweak Corrections to the Production of Higgs Boson+2 Jets via Weak Interactions at the Large Hadron Collider”, *Phys. Rev. Lett.* **99** (2007) 161803, doi:10.1103/PhysRevLett.99.161803, arXiv:0707.0381.
- [153] M. Ciccolini, A. Denner, and S. Dittmaier, “Electroweak and QCD corrections to Higgs production via vector-boson fusion at the LHC”, *Phys. Rev. D* **77** (2008) 013002, doi:10.1103/PhysRevD.77.013002, arXiv:0710.4749.
- [154] G. Cowan et al., “Asymptotic formulae for likelihood-based tests of new physics”, *Eur. Phys. J. C* **71** (2011) 1, doi:10.1140/epjc/s10052-011-1554-0, arXiv:1007.1727.
- [155] L. Moneta et al., “The RooStats Project”, in *13th International Workshop on Advanced Computing and Analysis Techniques in Physics Research (ACAT2010)*. SISSA, 2010. arXiv:1009.1003.
- [156] T. Junk, “Confidence level computation for combining searches with small statistics”, *Nucl. Instrum. Meth. A* **434** (1999) 435, doi:10.1016/S0168-9002(99)00498-2.
- [157] A. L. Read, “Presentation of search results: the CLs technique”, *J. Phys. G* **28** (2002) 2693, doi:10.1088/0954-3899/28/10/313.
- [158] E. Gross and O. Vitells, “Trial factors for the look elsewhere effect in high energy physics”, *Eur. Phys. J. C* **70** (2010) 525, doi:10.1140/epjc/s10052-010-1470-8, arXiv:1005.1891.
- [159] L. D. Landau, “On the angular momentum of a two-photon system”, *Dokl. Akad. Nauk* **60** (1948) 207.
- [160] C. N. Yang, “Selection Rules for the Dematerialization of a Particle into Two Photons”, *Phys. Rev.* **77** (1950) 242, doi:10.1103/PhysRev.77.242.
- [161] M. J. G. Veltman, “Limit on Mass Differences in the Weinberg Model”, *Nucl. Phys. B* **123** (1977) 89, doi:10.1016/0550-3213(77)90342-X.
- [162] P. Sikivie et al., “Isospin Breaking in Technicolor Models”, *Nucl. Phys. B* **173** (1980) 189, doi:10.1016/0550-3213(80)90214-X.
- [163] G. C. Branco et al., “Theory and phenomenology of two-Higgs-doublet models”, *Phys. Rept.* **516** (2012) 1, doi:10.1016/j.physrep.2012.02.002, arXiv:1106.0034.

A The CMS Collaboration

Yerevan Physics Institute, Yerevan, Armenia

S. Chatrchyan, V. Khachatryan, A.M. Sirunyan, A. Tumasyan

Institut für Hochenergiephysik der OeAW, Wien, Austria

W. Adam, T. Bergauer, M. Dragicevic, J. Erö, C. Fabjan¹, M. Friedl, R. Frühwirth¹, V.M. Ghete, N. Hörmann, J. Hrubec, M. Jeitler¹, W. Kiesenhofer, V. Knünz, M. Krammer¹, I. Krätschmer, D. Liko, I. Mikulec, D. Rabady², B. Rahbaran, C. Rohringer, H. Rohringer, R. Schöfbeck, J. Strauss, A. Taurok, W. Treberer-treberspurg, W. Waltenberger, C.-E. Wulz¹

National Centre for Particle and High Energy Physics, Minsk, Belarus

V. Mossolov, N. Shumeiko, J. Suarez Gonzalez

Universiteit Antwerpen, Antwerpen, Belgium

S. Alderweireldt, M. Bansal, S. Bansal, T. Cornelis, E.A. De Wolf, X. Janssen, A. Knutsson, S. Luyckx, L. Mucibello, S. Ochesanu, B. Roland, R. Rougny, H. Van Haevevermaet, P. Van Mechelen, N. Van Remortel, A. Van Spilbeeck

Vrije Universiteit Brussel, Brussel, Belgium

F. Blekman, S. Blyweert, J. D'Hondt, A. Kalogeropoulos, J. Keaveney, M. Maes, A. Olbrechts, S. Tavernier, W. Van Doninck, P. Van Mulders, G.P. Van Onsem, I. Villella

Université Libre de Bruxelles, Bruxelles, Belgium

B. Clerbaux, G. De Lentdecker, A.P.R. Gay, T. Hreus, A. Léonard, P.E. Marage, A. Mohammadi, T. Reis, L. Thomas, C. Vander Velde, P. Vanlaer, J. Wang

Ghent University, Ghent, Belgium

V. Adler, K. Beernaert, L. Benucci, A. Cimmino, S. Costantini, S. Dildick, G. Garcia, B. Klein, J. Lellouch, A. Marinov, J. Mccartin, A.A. Ocampo Rios, D. Ryckbosch, M. Sigamani, N. Strobbe, F. Thyssen, M. Tytgat, S. Walsh, E. Yazgan, N. Zaganidis

Université Catholique de Louvain, Louvain-la-Neuve, Belgium

S. Basegmez, G. Bruno, R. Castello, A. Caudron, L. Ceard, C. Delaere, T. du Pree, D. Favart, L. Forthomme, A. Giammanco³, J. Hollar, V. Lemaître, J. Liao, O. Militaru, C. Nuttens, D. Pagano, A. Pin, K. Piotrkowski, A. Popov⁴, M. Selvaggi, J.M. Vizan Garcia

Université de Mons, Mons, Belgium

N. Belyi, T. Caebergs, E. Daubie, G.H. Hammad

Centro Brasileiro de Pesquisas Fisicas, Rio de Janeiro, Brazil

G.A. Alves, M. Correa Martins Junior, T. Martins, M.E. Pol, M.H.G. Souza

Universidade do Estado do Rio de Janeiro, Rio de Janeiro, Brazil

W.L. Aldá Júnior, W. Carvalho, J. Chinellato⁵, A. Custódio, E.M. Da Costa, D. De Jesus Damiao, C. De Oliveira Martins, S. Fonseca De Souza, H. Malbouisson, M. Malek, D. Matos Figueiredo, L. Mundim, H. Nogima, W.L. Prado Da Silva, A. Santoro, L. Soares Jorge, A. Sznajder, E.J. Tonelli Manganote⁵, A. Vilela Pereira

Universidade Estadual Paulista ^a, Universidade Federal do ABC ^b, São Paulo, Brazil

T.S. Anjos^b, C.A. Bernardes^b, F.A. Dias^{a,6}, T.R. Fernandez Perez Tomei^a, E.M. Gregores^b, C. Lagana^a, F. Marinho^a, P.G. Mercadante^b, S.F. Novaes^a, Sandra S. Padula^a

Institute for Nuclear Research and Nuclear Energy, Sofia, Bulgaria

V. Genchev², P. Iaydjiev², S. Piperov, M. Rodozov, S. Stoykova, G. Sultanov, V. Tcholakov, R. Trayanov, M. Vutova

University of Sofia, Sofia, Bulgaria

A. Dimitrov, R. Hadjiiska, V. Kozhuharov, L. Litov, B. Pavlov, P. Petkov

Institute of High Energy Physics, Beijing, China

J.G. Bian, G.M. Chen, H.S. Chen, C.H. Jiang, D. Liang, S. Liang, X. Meng, J. Tao, J. Wang, X. Wang, Z. Wang, H. Xiao, M. Xu

State Key Laboratory of Nuclear Physics and Technology, Peking University, Beijing, China

C. Asawatangtrakuldee, Y. Ban, Y. Guo, Q. Li, W. Li, S. Liu, Y. Mao, S.J. Qian, D. Wang, L. Zhang, W. Zou

Universidad de Los Andes, Bogota, Colombia

C. Avila, C.A. Carrillo Montoya, J.P. Gomez, B. Gomez Moreno, J.C. Sanabria

Technical University of Split, Split, Croatia

N. Godinovic, D. Lelas, R. Plestina⁷, D. Polic, I. Puljak

University of Split, Split, Croatia

Z. Antunovic, M. Kovac

Institute Rudjer Boskovic, Zagreb, Croatia

V. Brigljevic, S. Duric, K. Kadija, J. Luetic, D. Mekterovic, S. Morovic, L. Tikvica

University of Cyprus, Nicosia, Cyprus

A. Attikis, G. Mavromanolakis, J. Mousa, C. Nicolaou, F. Ptochos, P.A. Razis

Charles University, Prague, Czech Republic

M. Finger, M. Finger Jr.

Academy of Scientific Research and Technology of the Arab Republic of Egypt, Egyptian Network of High Energy Physics, Cairo, Egypt

Y. Assran⁸, A. Ellithi Kamel⁹, M.A. Mahmoud¹⁰, A. Mahrous¹¹, A. Radi^{12,13}

National Institute of Chemical Physics and Biophysics, Tallinn, Estonia

M. Kadastik, M. Müntel, M. Murumaa, M. Raidal, L. Rebane, A. Tiko

Department of Physics, University of Helsinki, Helsinki, Finland

P. Eerola, G. Fedi, M. Voutilainen

Helsinki Institute of Physics, Helsinki, Finland

J. Härkönen, V. Karimäki, R. Kinnunen, M.J. Kortelainen, T. Lampén, K. Lassila-Perini, S. Lehti, T. Lindén, P. Luukka, T. Mäenpää, T. Peltola, E. Tuominen, J. Tuominiemi, E. Tuovinen, L. Wendland

Lappeenranta University of Technology, Lappeenranta, Finland

A. Korpela, T. Tuuva

DSM/IRFU, CEA/Saclay, Gif-sur-Yvette, France

M. Besancon, S. Choudhury, F. Couderc, M. Dejardin, D. Denegri, B. Fabbro, J.L. Faure, F. Ferri, S. Ganjour, A. Givernaud, P. Gras, G. Hamel de Monchenault, P. Jarry, E. Locci, J. Malcles, L. Millischer, A. Nayak, J. Rander, A. Rosowsky, M. Titov

Laboratoire Leprince-Ringuet, Ecole Polytechnique, IN2P3-CNRS, Palaiseau, France

S. Baffioni, F. Beaudette, L. Benhabib, L. Bianchini, M. Bluj¹⁴, P. Busson, C. Charlot, N. Daci, T. Dahms, M. Dalchenko, L. Dobrzynski, A. Florent, R. Granier de Cassagnac, M. Haguenaer, P. Miné, C. Mironov, I.N. Naranjo, M. Nguyen, C. Ochando, P. Paganini, D. Sabes, R. Salerno, Y. Sirois, C. Veelken, A. Zabi

Institut Pluridisciplinaire Hubert Curien, Université de Strasbourg, Université de Haute Alsace Mulhouse, CNRS/IN2P3, Strasbourg, France

J.-L. Agram¹⁵, J. Andrea, D. Bloch, D. Bodin, J.-M. Brom, E.C. Chabert, C. Collard, E. Conte¹⁵, F. Drouhin¹⁵, J.-C. Fontaine¹⁵, D. Gelé, U. Goerlach, C. Goetzmann, P. Juillot, A.-C. Le Bihan, P. Van Hove

Université de Lyon, Université Claude Bernard Lyon 1, CNRS-IN2P3, Institut de Physique Nucléaire de Lyon, Villeurbanne, France

S. Beauceron, N. Beaupere, G. Boudoul, S. Brochet, J. Chasserat, R. Chierici², D. Contardo, P. Depasse, H. El Mamouni, J. Fay, S. Gascon, M. Gouzevitch, B. Ille, T. Kurca, M. Lethuillier, L. Mirabito, S. Perries, L. Sgandurra, V. Sordini, Y. Tschudi, M. Vander Donckt, P. Verdier, S. Viret

Institute of High Energy Physics and Informatization, Tbilisi State University, Tbilisi, Georgia

Z. Tsamalaidze¹⁶

RWTH Aachen University, I. Physikalisches Institut, Aachen, Germany

C. Autermann, S. Beranek, B. Calpas, M. Edelhoff, L. Feld, N. Heracleous, O. Hindrichs, K. Klein, J. Merz, A. Ostapchuk, A. Perieanu, F. Raupach, J. Sammet, S. Schael, D. Sprenger, H. Weber, B. Wittmer, V. Zhukov⁴

RWTH Aachen University, III. Physikalisches Institut A, Aachen, Germany

M. Ata, J. Caudron, E. Dietz-Laursonn, D. Duchardt, M. Erdmann, R. Fischer, A. Güth, T. Hebbeker, C. Heidemann, K. Hoepfner, D. Klingebiel, P. Kreuzer, M. Merschmeyer, A. Meyer, M. Olschewski, K. Padeken, P. Papacz, H. Pieta, H. Reithler, S.A. Schmitz, L. Sonnenschein, J. Steggemann, D. Teyssier, S. Thüer, M. Weber

RWTH Aachen University, III. Physikalisches Institut B, Aachen, Germany

V. Cherepanov, Y. Erdogan, G. Flügge, H. Geenen, M. Geisler, W. Haj Ahmad, F. Hoehle, B. Kargoll, T. Kress, Y. Kuessel, J. Lingemann², A. Nowack, I.M. Nugent, L. Perchalla, O. Pooth, A. Stahl

Deutsches Elektronen-Synchrotron, Hamburg, Germany

M. Aldaya Martin, I. Asin, N. Bartosik, J. Behr, W. Behrenhoff, U. Behrens, M. Bergholz¹⁷, A. Bethani, K. Borras, A. Burgmeier, A. Cakir, L. Calligaris, A. Campbell, F. Costanza, D. Dammann, C. Diez Pardos, T. Dorland, G. Eckerlin, D. Eckstein, G. Flucke, A. Geiser, I. Glushkov, P. Gunnellini, S. Habib, J. Hauk, G. Hellwig, H. Jung, M. Kasemann, P. Katsas, C. Kleinwort, H. Kluge, M. Krämer, D. Krücker, E. Kuznetsova, W. Lange, J. Leonard, K. Lipka, W. Lohmann¹⁷, B. Lutz, R. Mankel, I. Marfin, M. Marienfeld, I.-A. Melzer-Pellmann, A.B. Meyer, J. Mnich, A. Mussgiller, S. Naumann-Emme, O. Novgorodova, F. Nowak, J. Olzem, H. Perrey, A. Petrukhin, D. Pitzl, A. Raspereza, P.M. Ribeiro Cipriano, C. Riedl, E. Ron, M. Rosin, J. Salfeld-Nebgen, R. Schmidt¹⁷, T. Schoerner-Sadenius, N. Sen, M. Stein, R. Walsh, C. Wissing

University of Hamburg, Hamburg, Germany

V. Blobel, H. Enderle, J. Erfle, U. Gebbert, M. Görner, M. Gosselink, J. Haller, K. Heine, R.S. Höing, G. Kaussen, H. Kirschenmann, R. Klanner, J. Lange, T. Peiffer, N. Pietsch, D. Rathjens, C. Sander, H. Schettler, P. Schleper, E. Schlieckau, A. Schmidt, T. Schum, M. Seidel, J. Sibille¹⁸, V. Sola, H. Stadie, G. Steinbrück, J. Thomsen, L. Vanelderren

Institut für Experimentelle Kernphysik, Karlsruhe, Germany

C. Barth, C. Baus, J. Berger, C. Böser, T. Chwalek, W. De Boer, A. Descroix, A. Dierlamm,

M. Feindt, M. Guthoff², C. Hackstein, F. Hartmann², T. Hauth², M. Heinrich, H. Held, K.H. Hoffmann, U. Husemann, I. Katkov⁴, J.R. Komaragiri, A. Kornmayer², P. Lobelle Pardo, D. Martschei, S. Mueller, Th. Müller, M. Niegel, A. Nürnberg, O. Oberst, J. Ott, G. Quast, K. Rabbertz, F. Ratnikov, N. Ratnikova, S. Röcker, F.-P. Schilling, G. Schott, H.J. Simonis, F.M. Stober, D. Troendle, R. Ulrich, J. Wagner-Kuhr, S. Wayand, T. Weiler, M. Zeise

Institute of Nuclear and Particle Physics (INPP), NCSR Demokritos, Aghia Paraskevi, Greece

G. Anagnostou, G. Daskalakis, T. Gerasis, S. Kesisoglou, A. Kyriakis, D. Loukas, A. Markou, C. Markou, E. Ntomari

University of Athens, Athens, Greece

L. Gouskos, T.J. Mertzimekis, A. Panagiotou, N. Saoulidou, E. Stiliaris

University of Ioánnina, Ioánnina, Greece

X. Aslanoglou, I. Evangelou, G. Flouris, C. Foudas, P. Kokkas, N. Manthos, I. Papadopoulos, E. Paradis

KFKI Research Institute for Particle and Nuclear Physics, Budapest, Hungary

G. Bencze, C. Hajdu, P. Hidas, D. Horvath¹⁹, B. Radics, F. Sikler, V. Veszpremi, G. Vesztergombi²⁰, A.J. Zsigmond

Institute of Nuclear Research ATOMKI, Debrecen, Hungary

N. Beni, S. Czellar, J. Molnar, J. Palinkas, Z. Szillasi

University of Debrecen, Debrecen, Hungary

J. Karacsi, P. Raics, Z.L. Trocsanyi, B. Ujvari

Panjab University, Chandigarh, India

S.B. Beri, V. Bhatnagar, N. Dhingra, R. Gupta, M. Kaur, M.Z. Mehta, M. Mittal, N. Nishu, L.K. Saini, A. Sharma, J.B. Singh

University of Delhi, Delhi, India

Ashok Kumar, Arun Kumar, S. Ahuja, A. Bhardwaj, B.C. Choudhary, S. Malhotra, M. Naimuddin, K. Ranjan, P. Saxena, V. Sharma, R.K. Shivpuri

Saha Institute of Nuclear Physics, Kolkata, India

S. Banerjee, S. Bhattacharya, K. Chatterjee, S. Dutta, B. Gomber, Sa. Jain, Sh. Jain, R. Khurana, A. Modak, S. Mukherjee, D. Roy, S. Sarkar, M. Sharan

Bhabha Atomic Research Centre, Mumbai, India

A. Abdulsalam, D. Dutta, S. Kailas, V. Kumar, A.K. Mohanty², L.M. Pant, P. Shukla, A. Topkar

Tata Institute of Fundamental Research - EHEP, Mumbai, India

T. Aziz, R.M. Chatterjee, S. Ganguly, M. Guchait²¹, A. Gurtu²², M. Maity²³, G. Majumder, K. Mazumdar, G.B. Mohanty, B. Parida, K. Sudhakar, N. Wickramage

Tata Institute of Fundamental Research - HECR, Mumbai, India

S. Banerjee, S. Dugad

Institute for Research in Fundamental Sciences (IPM), Tehran, Iran

H. Arfaei²⁴, H. Bakhshiansohi, S.M. Etesami²⁵, A. Fahim²⁴, H. Hesari, A. Jafari, M. Khakzad, M. Mohammadi Najafabadi, S. Paktinat Mehdiabadi, B. Safarzadeh²⁶, M. Zeinali

University College Dublin, Dublin, Ireland

M. Grunewald

INFN Sezione di Bari ^a, Università di Bari ^b, Politecnico di Bari ^c, Bari, Italy

M. Abbrescia^{a,b}, L. Barbone^{a,b}, C. Calabria^{a,b,2}, S.S. Chhibra^{a,b}, A. Colaleo^a, D. Creanza^{a,c}, N. De Filippis^{a,c,2}, M. De Palma^{a,b}, L. Fiore^a, G. Iaselli^{a,c}, G. Maggi^{a,c}, M. Maggi^a, B. Marangelli^{a,b}, S. My^{a,c}, S. Nuzzo^{a,b}, N. Pacifico^a, A. Pompili^{a,b}, G. Pugliese^{a,c}, G. Selvaggi^{a,b}, L. Silvestris^a, G. Singh^{a,b}, R. Venditti^{a,b}, P. Verwilligen^a, G. Zito^a

INFN Sezione di Bologna ^a, Università di Bologna ^b, Bologna, Italy

G. Abbiendi^a, A.C. Benvenuti^a, D. Bonacorsi^{a,b}, S. Braibant-Giacomelli^{a,b}, L. Brigliadori^{a,b}, R. Campanini^{a,b}, P. Capiluppi^{a,b}, A. Castro^{a,b}, F.R. Cavallo^a, M. Cuffiani^{a,b}, G.M. Dallavalle^a, F. Fabbri^a, A. Fanfani^{a,b}, D. Fasanella^{a,b}, P. Giacomelli^a, C. Grandi^a, L. Guiducci^{a,b}, S. Marcellini^a, G. Masetti^a, M. Meneghelli^{a,b,2}, A. Montanari^a, F.L. Navarra^{a,b}, F. Odorici^a, A. Perrotta^a, F. Primavera^{a,b}, A.M. Rossi^{a,b}, T. Rovelli^{a,b}, G.P. Siroli^{a,b}, N. Tosi^{a,b}, R. Travaglini^{a,b}

INFN Sezione di Catania ^a, Università di Catania ^b, Catania, Italy

S. Albergo^{a,b}, M. Chiorboli^{a,b}, S. Costa^{a,b}, R. Potenza^{a,b}, A. Tricomi^{a,b}, C. Tuve^{a,b}

INFN Sezione di Firenze ^a, Università di Firenze ^b, Firenze, Italy

G. Barbagli^a, V. Ciulli^{a,b}, C. Civinini^a, R. D'Alessandro^{a,b}, E. Focardi^{a,b}, S. Frosali^{a,b}, E. Gallo^a, S. Gonzi^{a,b}, P. Lenzi^{a,b}, M. Meschini^a, S. Paoletti^a, G. Sguazzoni^a, A. Tropiano^{a,b}

INFN Laboratori Nazionali di Frascati, Frascati, Italy

L. Benussi, S. Bianco, F. Fabbri, D. Piccolo

INFN Sezione di Genova ^a, Università di Genova ^b, Genova, Italy

P. Fabbriatore^a, R. Musenich^a, S. Tosi^{a,b}

INFN Sezione di Milano-Bicocca ^a, Università di Milano-Bicocca ^b, Milano, Italy

A. Benaglia^a, F. De Guio^{a,b}, L. Di Matteo^{a,b,2}, S. Fiorendi^{a,b}, S. Gennai^{a,2}, A. Ghezzi^{a,b}, P. Govoni, M.T. Lucchini², S. Malvezzi^a, R.A. Manzoni^{a,b}, A. Martelli^{a,b}, A. Massironi^{a,b}, D. Menasce^a, L. Moroni^a, M. Paganoni^{a,b}, D. Pedrini^a, S. Ragazzi^{a,b}, N. Redaelli^a, T. Tabarelli de Fatis^{a,b}

INFN Sezione di Napoli ^a, Università di Napoli 'Federico II' ^b, Università della Basilicata (Potenza) ^c, Università G. Marconi (Roma) ^d, Napoli, Italy

S. Buontempo^a, N. Cavallo^{a,c}, A. De Cosa^{a,b,2}, O. Dogangun^{a,b}, F. Fabozzi^{a,c}, A.O.M. Iorio^{a,b}, L. Lista^a, S. Meola^{a,d,2}, M. Merola^a, P. Paolucci^{a,2}

INFN Sezione di Padova ^a, Università di Padova ^b, Università di Trento (Trento) ^c, Padova, Italy

P. Azzi^a, N. Bacchetta^{a,2}, D. Bisello^{a,b}, A. Branca^{a,b}, R. Carlin^{a,b}, P. Checchia^a, T. Dorigo^a, U. Dosselli^a, M. Galanti^{a,b}, F. Gasparini^{a,b}, U. Gasparini^{a,b}, P. Giubilato^{a,b}, A. Gozzelino^a, K. Kanishchev^{a,c}, S. Lacaprara^a, I. Lazzizzera^{a,c}, M. Margoni^{a,b}, A.T. Meneguzzo^{a,b}, M. Nespolo^a, J. Pazzini^{a,b}, N. Pozzobon^{a,b}, P. Ronchese^{a,b}, F. Simonetto^{a,b}, E. Torassa^a, M. Tosi^{a,b}, A. Triossi^a, S. Vanini^{a,b}, P. Zotto^{a,b}, A. Zucchetta^{a,b}, G. Zumerle^{a,b}

INFN Sezione di Pavia ^a, Università di Pavia ^b, Pavia, Italy

M. Gabusi^{a,b}, S.P. Ratti^{a,b}, C. Riccardi^{a,b}, P. Vitulo^{a,b}

INFN Sezione di Perugia ^a, Università di Perugia ^b, Perugia, Italy

M. Biasini^{a,b}, G.M. Bilei^a, L. Fanò^{a,b}, P. Lariccia^{a,b}, G. Mantovani^{a,b}, M. Menichelli^a, A. Nappi^{a,b†}, F. Romeo^{a,b}, A. Saha^a, A. Santocchia^{a,b}, A. Spiezia^{a,b}

INFN Sezione di Pisa ^a, Università di Pisa ^b, Scuola Normale Superiore di Pisa ^c, Pisa, Italy

K. Androsov^{a,27}, P. Azzurri^a, G. Bagliesi^a, T. Boccali^a, G. Broccolo^{a,c}, R. Castaldi^a, R.T. D'Agnolo^{a,c,2}, R. Dell'Orso^a, F. Fiori^{a,c,2}, L. Foà^{a,c}, A. Giassi^a, A. Kraan^a, F. Ligabue^{a,c},

T. Lomtadze^a, L. Martini^{a,27}, A. Messineo^{a,b}, F. Palla^a, A. Rizzi^{a,b}, A.T. Serban^a, P. Spagnolo^a, P. Squillacioti^a, R. Tenchini^a, G. Tonelli^{a,b}, A. Venturi^a, P.G. Verdini^a, C. Vernieri^{a,c}

INFN Sezione di Roma ^a, Università di Roma ^b, Roma, Italy

L. Barone^{a,b}, F. Cavallari^a, D. Del Re^{a,b}, M. Diemoz^a, C. Fanelli^{a,b}, M. Grassi^{a,b,2}, E. Longo^{a,b}, F. Margaroli^{a,b}, P. Meridiani^{a,2}, F. Micheli^{a,b}, S. Nourbakhsh^{a,b}, G. Organtini^{a,b}, R. Paramatti^a, S. Rahatlou^{a,b}, L. Soffi^{a,b}

INFN Sezione di Torino ^a, Università di Torino ^b, Università del Piemonte Orientale (Novara) ^c, Torino, Italy

N. Amapane^{a,b}, R. Arcidiacono^{a,c}, S. Argiro^{a,b}, M. Arneodo^{a,c}, C. Biino^a, N. Cartiglia^a, S. Casasso^{a,b}, M. Costa^{a,b}, N. Demaria^a, C. Mariotti^{a,2}, S. Maselli^a, E. Migliore^{a,b}, V. Monaco^{a,b}, M. Musich^{a,2}, M.M. Obertino^{a,c}, G. Ortona^{a,b}, N. Pastrone^a, M. Pelliccioni^a, A. Potenza^{a,b}, A. Romero^{a,b}, M. Ruspa^{a,c}, R. Sacchi^{a,b}, A. Solano^{a,b}, A. Staiano^a, U. Tamponi^a

INFN Sezione di Trieste ^a, Università di Trieste ^b, Trieste, Italy

S. Belforte^a, V. Candelise^{a,b}, M. Casarsa^a, F. Cossutti^{a,2}, G. Della Ricca^{a,b}, B. Gobbo^a, C. La Licata^{a,b}, M. Marone^{a,b,2}, D. Montanino^{a,b}, A. Penzo^a, A. Schizzi^{a,b}, A. Zanetti^a

Kangwon National University, Chunchon, Korea

T.Y. Kim, S.K. Nam

Kyungpook National University, Daegu, Korea

S. Chang, D.H. Kim, G.N. Kim, J.E. Kim, D.J. Kong, Y.D. Oh, H. Park, D.C. Son

Chonnam National University, Institute for Universe and Elementary Particles, Kwangju, Korea

J.Y. Kim, Zero J. Kim, S. Song

Korea University, Seoul, Korea

S. Choi, D. Gyun, B. Hong, M. Jo, H. Kim, T.J. Kim, K.S. Lee, D.H. Moon, S.K. Park, Y. Roh

University of Seoul, Seoul, Korea

M. Choi, J.H. Kim, C. Park, I.C. Park, S. Park, G. Ryu

Sungkyunkwan University, Suwon, Korea

Y. Choi, Y.K. Choi, J. Goh, M.S. Kim, E. Kwon, B. Lee, J. Lee, S. Lee, H. Seo, I. Yu

Vilnius University, Vilnius, Lithuania

I. Grigelionis, A. Juodagalvis

Centro de Investigacion y de Estudios Avanzados del IPN, Mexico City, Mexico

H. Castilla-Valdez, E. De La Cruz-Burelo, I. Heredia-de La Cruz, R. Lopez-Fernandez, J. Martínez-Ortega, A. Sanchez-Hernandez, L.M. Villasenor-Cendejas

Universidad Iberoamericana, Mexico City, Mexico

S. Carrillo Moreno, F. Vazquez Valencia

Benemerita Universidad Autonoma de Puebla, Puebla, Mexico

H.A. Salazar Ibarguen

Universidad Autónoma de San Luis Potosí, San Luis Potosí, Mexico

E. Casimiro Linares, A. Morelos Pineda, M.A. Reyes-Santos

University of Auckland, Auckland, New Zealand

D. Krofcheck

University of Canterbury, Christchurch, New Zealand

A.J. Bell, P.H. Butler, R. Doesburg, S. Reucroft, H. Silverwood

National Centre for Physics, Quaid-I-Azam University, Islamabad, Pakistan

M. Ahmad, M.I. Asghar, J. Butt, H.R. Hoorani, S. Khalid, W.A. Khan, T. Khurshid, S. Qazi, M.A. Shah, M. Shoaib

National Centre for Nuclear Research, Swierk, Poland

H. Bialkowska, B. Boimska, T. Frueboes, M. Górski, M. Kazana, K. Nawrocki, K. Romanowska-Rybinska, M. Szleper, G. Wrochna, P. Zalewski

Institute of Experimental Physics, Faculty of Physics, University of Warsaw, Warsaw, Poland

G. Brona, K. Bunkowski, M. Cwiok, W. Dominik, K. Doroba, A. Kalinowski, M. Konecki, J. Krolikowski, M. Misiura, W. Wolszczak

Laboratório de Instrumentação e Física Experimental de Partículas, Lisboa, Portugal

N. Almeida, P. Bargassa, A. David, P. Faccioli, P.G. Ferreira Parracho, M. Gallinaro, J. Seixas², J. Varela, P. Vischia

Joint Institute for Nuclear Research, Dubna, Russia

P. Bunin, I. Golutvin, I. Gorbunov, A. Kamenev, V. Karjavin, V. Konoplyanikov, G. Kozlov, A. Lanev, A. Malakhov, P. Moisenz, V. Palichik, V. Perelygin, M. Savina, S. Shmatov, N. Skatchkov, V. Smirnov, A. Zarubin

Petersburg Nuclear Physics Institute, Gatchina (St. Petersburg), Russia

S. Evstyukhin, V. Golovtsov, Y. Ivanov, V. Kim, P. Levchenko, V. Murzin, V. Oreshkin, I. Smirnov, V. Sulimov, L. Uvarov, S. Vavilov, A. Vorobyev, An. Vorobyev

Institute for Nuclear Research, Moscow, Russia

Yu. Andreev, A. Dermenev, S. Gninenko, N. Golubev, M. Kirsanov, N. Krasnikov, V. Matveev, A. Pashenkov, D. Tlisov, A. Toropin

Institute for Theoretical and Experimental Physics, Moscow, Russia

V. Epshteyn, M. Erofeeva, V. Gavrilov, N. Lychkovskaya, V. Popov, G. Safronov, S. Semenov, A. Spiridonov, V. Stolin, E. Vlasov, A. Zhokin

P.N. Lebedev Physical Institute, Moscow, Russia

V. Andreev, M. Azarkin, I. Dremin, M. Kirakosyan, A. Leonidov, G. Mesyats, S.V. Rusakov, A. Vinogradov

Skobeltsyn Institute of Nuclear Physics, Lomonosov Moscow State University, Moscow, Russia

A. Belyaev, E. Boos, M. Dubinin⁶, L. Dudko, A. Ershov, A. Gribushin, V. Klyukhin, O. Kodolova, I. Lokhtin, A. Markina, S. Obraztsov, S. Petrushanko, V. Savrin, A. Snigirev

State Research Center of Russian Federation, Institute for High Energy Physics, Protvino, Russia

I. Azhgirey, I. Bayshev, S. Bitioukov, V. Kachanov, A. Kalinin, D. Konstantinov, V. Krychkine, V. Petrov, R. Ryutin, A. Sobol, L. Tourtchanovitch, S. Troshin, N. Tyurin, A. Uzunian, A. Volkov

University of Belgrade, Faculty of Physics and Vinca Institute of Nuclear Sciences, Belgrade, Serbia

P. Adzic²⁸, M. Ekmedzic, D. Krpic²⁸, J. Milosevic

Centro de Investigaciones Energéticas Medioambientales y Tecnológicas (CIEMAT), Madrid, Spain

M. Aguilar-Benitez, J. Alcaraz Maestre, C. Battilana, E. Calvo, M. Cerrada, M. Chamizo Llatas², N. Colino, B. De La Cruz, A. Delgado Peris, D. Domínguez Vázquez, C. Fernandez Bedoya, J.P. Fernández Ramos, A. Ferrando, J. Flix, M.C. Fouz, P. Garcia-Abia, O. Gonzalez Lopez, S. Goy Lopez, J.M. Hernandez, M.I. Josa, G. Merino, E. Navarro De Martino, J. Puerta Pelayo, A. Quintario Olmeda, I. Redondo, L. Romero, J. Santaolalla, M.S. Soares, C. Willmott

Universidad Autónoma de Madrid, Madrid, Spain

C. Albajar, J.F. de Trocóniz

Universidad de Oviedo, Oviedo, Spain

H. Brun, J. Cuevas, J. Fernandez Menendez, S. Folgueras, I. Gonzalez Caballero, L. Lloret Iglesias, J. Piedra Gomez

Instituto de Física de Cantabria (IFCA), CSIC-Universidad de Cantabria, Santander, Spain

J.A. Brochero Cifuentes, I.J. Cabrillo, A. Calderon, S.H. Chuang, J. Duarte Campderros, M. Fernandez, G. Gomez, J. Gonzalez Sanchez, A. Graziano, C. Jorda, A. Lopez Virto, J. Marco, R. Marco, C. Martinez Rivero, F. Matorras, F.J. Munoz Sanchez, T. Rodrigo, A.Y. Rodríguez-Marrero, A. Ruiz-Jimeno, L. Scodellaro, I. Vila, R. Vilar Cortabitarte

CERN, European Organization for Nuclear Research, Geneva, Switzerland

D. Abbaneo, E. Auffray, G. Auzinger, M. Bachtis, P. Baillon, A.H. Ball, D. Barney, J. Bendavid, J.F. Benitez, C. Bernet⁷, G. Bianchi, P. Bloch, A. Bocci, A. Bonato, O. Bondu, C. Botta, H. Breuker, T. Camporesi, G. Cerminara, T. Christiansen, J.A. Coarasa Perez, S. Colafranceschi²⁹, D. d'Enterria, A. Dabrowski, A. De Roeck, S. De Visscher, S. Di Guida, M. Dobson, N. Dupont-Sagorin, A. Elliott-Peisert, J. Eugster, W. Funk, G. Georgiou, M. Giffels, D. Gigi, K. Gill, D. Giordano, M. Girone, M. Giunta, F. Glege, R. Gomez-Reino Garrido, S. Gowdy, R. Guida, J. Hammer, M. Hansen, P. Harris, C. Hartl, B. Hegner, A. Hinzmann, V. Innocente, P. Janot, K. KAADZE, E. Karavakis, K. Kousouris, K. Krajczar, P. Lecoq, Y.-J. Lee, C. Lourenço, N. Magini, M. Malberti, L. Malgeri, M. Mannelli, L. Masetti, F. Meijers, S. Mersi, E. Meschi, R. Moser, M. Mulders, P. Musella, E. Nesvold, L. Orsini, E. Palencia Cortezon, E. Perez, L. Perrozzi, A. Petrilli, A. Pfeiffer, M. Pierini, M. Pimiä, D. Piparo, G. Polese, L. Quertenmont, A. Racz, W. Reece, J. Rodrigues Antunes, G. Rolandi³⁰, C. Rovelli³¹, M. Rovere, H. Sakulin, F. Santanastasio, C. Schäfer, C. Schwick, I. Segoni, S. Sekmen, A. Sharma, P. Siegrist, P. Silva, M. Simon, P. Sphicas³², D. Spiga, M. Stoye, A. Tsiros, G.I. Veres²⁰, J.R. Vlimant, H.K. Wöhri, S.D. Worm³³, W.D. Zeuner

Paul Scherrer Institut, Villigen, Switzerland

W. Bertl, K. Deiters, W. Erdmann, K. Gabathuler, R. Horisberger, Q. Ingram, H.C. Kaestli, S. König, D. Kotlinski, U. Langenegger, F. Meier, D. Renker, T. Rohe

Institute for Particle Physics, ETH Zurich, Zurich, Switzerland

F. Bachmair, L. Bäni, P. Bortignon, M.A. Buchmann, B. Casal, N. Chanon, A. Deisher, G. Dissertori, M. Dittmar, M. Donegà, M. Dünser, P. Eller, C. Grab, D. Hits, P. Lecomte, W. Lustermann, A.C. Marini, P. Martinez Ruiz del Arbol, N. Mohr, F. Moortgat, C. Nägeli³⁴, P. Nef, F. Nessi-Tedaldi, F. Pandolfi, L. Pape, F. Pauss, M. Peruzzi, F.J. Ronga, M. Rossini, L. Sala, A.K. Sanchez, A. Starodumov³⁵, B. Stieger, M. Takahashi, L. Tauscher[†], A. Thea, K. Theofilatos, D. Treille, C. Urscheler, R. Wallny, H.A. Weber

Universität Zürich, Zurich, Switzerland

C. AMSLER³⁶, V. Chiochia, C. Favaro, M. Ivova Rikova, B. Kilminster, B. Millan Mejias, P. Otiougova, P. Robmann, H. Snoek, S. Taroni, S. Tupputi, M. Verzetti

National Central University, Chung-Li, Taiwan

M. Cardaci, K.H. Chen, C. Ferro, C.M. Kuo, S.W. Li, W. Lin, Y.J. Lu, R. Volpe, S.S. Yu

National Taiwan University (NTU), Taipei, Taiwan

P. Bartalini, P. Chang, Y.H. Chang, Y.W. Chang, Y. Chao, K.F. Chen, C. Dietz, U. Grundler, W.-S. Hou, Y. Hsiung, K.Y. Kao, Y.J. Lei, R.-S. Lu, D. Majumder, E. Petrakou, X. Shi, J.G. Shiu, Y.M. Tzeng, M. Wang

Chulalongkorn University, Bangkok, Thailand

B. Asavapibhop, N. Suwonjandee

Cukurova University, Adana, Turkey

A. Adiguzel, M.N. Bakirci³⁷, S. Cerci³⁸, C. Dozen, I. Dumanoglu, E. Eskut, S. Girgis, G. Gokbulut, E. Gurpinar, I. Hos, E.E. Kangal, A. Kayis Topaksu, G. Onengut, K. Ozdemir, S. Ozturk³⁹, A. Polatoz, K. Sogut⁴⁰, D. Sunar Cerci³⁸, B. Tali³⁸, H. Topakli³⁷, M. Vergili

Middle East Technical University, Physics Department, Ankara, Turkey

I.V. Akin, T. Aliev, B. Bilin, S. Bilmis, M. Deniz, H. Gamsizkan, A.M. Guler, G. Karapinar⁴¹, K. Ocalan, A. Ozpineci, M. Serin, R. Sever, U.E. Surat, M. Yalvac, M. Zeyrek

Bogazici University, Istanbul, Turkey

E. Gülmez, B. Isildak⁴², M. Kaya⁴³, O. Kaya⁴³, S. Ozkorucuklu⁴⁴, N. Sonmez⁴⁵

Istanbul Technical University, Istanbul, Turkey

H. Bahtiyar⁴⁶, E. Barlas, K. Cankocak, Y.O. Günaydin⁴⁷, F.I. Vardarli, M. Yücel

National Scientific Center, Kharkov Institute of Physics and Technology, Kharkov, Ukraine

L. Levchuk, P. Sorokin

University of Bristol, Bristol, United Kingdom

J.J. Brooke, E. Clement, D. Cussans, H. Flacher, R. Frazier, J. Goldstein, M. Grimes, G.P. Heath, H.F. Heath, L. Kreczko, S. Metson, D.M. Newbold³³, K. Nirunpong, A. Poll, S. Senkin, V.J. Smith, T. Williams

Rutherford Appleton Laboratory, Didcot, United Kingdom

L. Basso⁴⁸, K.W. Bell, A. Belyaev⁴⁸, C. Brew, R.M. Brown, D.J.A. Cockerill, J.A. Coughlan, K. Harder, S. Harper, J. Jackson, E. Olaiya, D. Petyt, B.C. Radburn-Smith, C.H. Shepherd-Themistocleous, I.R. Tomalin, W.J. Womersley

Imperial College, London, United Kingdom

R. Bainbridge, O. Buchmuller, D. Burton, D. Colling, N. Cripps, M. Cutajar, P. Dauncey, G. Davies, M. Della Negra, W. Ferguson, J. Fulcher, A. Gilbert, A. Guneratne Bryer, G. Hall, Z. Hatherell, J. Hays, G. Iles, M. Jarvis, G. Karapostoli, M. Kenzie, R. Lane, R. Lucas, L. Lyons, A.-M. Magnan, J. Marrouche, B. Mathias, R. Nandi, J. Nash, A. Nikitenko³⁵, J. Pela, M. Pesaresi, K. Petridis, M. Pioppi⁴⁹, D.M. Raymond, S. Rogerson, A. Rose, C. Seez, P. Sharp[†], A. Sparrow, A. Tapper, M. Vazquez Acosta, T. Virdee, S. Wakefield, N. Wardle, T. Whyntie

Brunel University, Uxbridge, United Kingdom

M. Chadwick, J.E. Cole, P.R. Hobson, A. Khan, P. Kyberd, D. Leggat, D. Leslie, W. Martin, I.D. Reid, P. Symonds, L. Teodorescu, M. Turner

Baylor University, Waco, USA

J. Dittmann, K. Hatakeyama, A. Kasmi, H. Liu, T. Scarborough

The University of Alabama, Tuscaloosa, USA

O. Charaf, S.I. Cooper, C. Henderson, P. Rumerio

Boston University, Boston, USA

A. Avetisyan, T. Bose, C. Fantasia, A. Heister, P. Lawson, D. Lazic, J. Rohlf, D. Sperka, J. St. John, L. Sulak

Brown University, Providence, USA

J. Alimena, S. Bhattacharya, G. Christopher, D. Cutts, Z. Demiragli, A. Ferapontov, A. Garabedian, U. Heintz, G. Kukartsev, E. Laird, G. Landsberg, M. Luk, M. Narain, M. Segala, T. Sinthuprasith, T. Speer

University of California, Davis, Davis, USA

R. Breedon, G. Breto, M. Calderon De La Barca Sanchez, S. Chauhan, M. Chertok, J. Conway, R. Conway, P.T. Cox, R. Erbacher, M. Gardner, R. Houtz, W. Ko, A. Kopecky, R. Lander, O. Mall, T. Miceli, R. Nelson, D. Pellett, F. Ricci-Tam, B. Rutherford, M. Searle, J. Smith, M. Squires, M. Tripathi, R. Yohay

University of California, Los Angeles, Los Angeles, USA

V. Andreev, D. Cline, R. Cousins, S. Erhan, P. Everaerts, C. Farrell, M. Felcini, J. Hauser, M. Ignatenko, C. Jarvis, G. Rakness, P. Schlein[†], E. Takasugi, P. Traczyk, V. Valuev, M. Weber

University of California, Riverside, Riverside, USA

J. Babb, R. Clare, M.E. Dinardo, J. Ellison, J.W. Gary, F. Giordano, G. Hanson, H. Liu, O.R. Long, A. Luthra, H. Nguyen, S. Paramesvaran, J. Sturdy, S. Sumowidagdo, R. Wilken, S. Wimpenny

University of California, San Diego, La Jolla, USA

W. Andrews, J.G. Branson, G.B. Cerati, S. Cittolin, D. Evans, A. Holzner, R. Kelley, M. Lebourgeois, J. Letts, I. Macneill, B. Mangano, S. Padhi, C. Palmer, G. Petrucciani, M. Pieri, M. Sani, V. Sharma, S. Simon, E. Sudano, M. Tadel, Y. Tu, A. Vartak, S. Wasserbaech⁵⁰, F. Würthwein, A. Yagil, J. Yoo

University of California, Santa Barbara, Santa Barbara, USA

D. Barge, R. Bellan, C. Campagnari, M. D'Alfonso, T. Danielson, K. Flowers, P. Geffert, C. George, F. Golf, J. Incandela, C. Justus, P. Kalavase, D. Kovalskyi, V. Krutelyov, S. Lowette, R. Magaña Villalba, N. Mccoll, V. Pavlunin, J. Ribnik, J. Richman, R. Rossin, D. Stuart, W. To, C. West

California Institute of Technology, Pasadena, USA

A. Apresyan, A. Bornheim, J. Bunn, Y. Chen, E. Di Marco, J. Duarte, D. Kcira, Y. Ma, A. Mott, H.B. Newman, C. Rogan, M. Spiropulu, V. Timciuc, J. Veverka, R. Wilkinson, S. Xie, Y. Yang, R.Y. Zhu

Carnegie Mellon University, Pittsburgh, USA

V. Azzolini, A. Calamba, R. Carroll, T. Ferguson, Y. Iiyama, D.W. Jang, Y.F. Liu, M. Paulini, J. Russ, H. Vogel, I. Vorobiev

University of Colorado at Boulder, Boulder, USA

J.P. Cumalat, B.R. Drell, W.T. Ford, A. Gaz, E. Luiggi Lopez, U. Nauenberg, J.G. Smith, K. Stenson, K.A. Ulmer, S.R. Wagner

Cornell University, Ithaca, USA

J. Alexander, A. Chatterjee, N. Eggert, L.K. Gibbons, W. Hopkins, A. Khukhunaishvili, B. Kreis, N. Mirman, G. Nicolas Kaufman, J.R. Patterson, A. Ryd, E. Salvati, W. Sun, W.D. Teo, J. Thom, J. Thompson, J. Tucker, Y. Weng, L. Winstrom, P. Wittich

Fairfield University, Fairfield, USA

D. Winn

Fermi National Accelerator Laboratory, Batavia, USA

S. Abdullin, M. Albrow, J. Anderson, G. Apollinari, L.A.T. Bauerdick, A. Beretvas, J. Berryhill, P.C. Bhat, K. Burkett, J.N. Butler, V. Chetluru, H.W.K. Cheung, F. Chlebana, S. Cihangir, V.D. Elvira, I. Fisk, J. Freeman, Y. Gao, E. Gottschalk, L. Gray, D. Green, O. Gutsche, R.M. Harris, J. Hirschauer, B. Hooberman, S. Jindariani, M. Johnson, U. Joshi, B. Klima, S. Kunori, S. Kwan, J. Linacre, D. Lincoln, R. Lipton, J. Lykken, K. Maeshima, J.M. Marraffino, V.I. Martinez Outschoorn, S. Maruyama, D. Mason, P. McBride, K. Mishra, S. Mrenna, Y. Musienko⁵¹, C. Newman-Holmes, V. O'Dell, O. Prokofyev, E. Sexton-Kennedy, S. Sharma, W.J. Spalding, L. Spiegel, L. Taylor, S. Tkaczyk, N.V. Tran, L. Uplegger, E.W. Vaandering, R. Vidal, J. Whitmore, W. Wu, F. Yang, J.C. Yun

University of Florida, Gainesville, USA

D. Acosta, P. Avery, D. Bourilkov, M. Chen, T. Cheng, S. Das, M. De Gruttola, G.P. Di Giovanni, D. Dobur, A. Drozdetskiy, R.D. Field, M. Fisher, Y. Fu, I.K. Furic, J. Hugon, B. Kim, J. Konigsberg, A. Korytov, A. Kropivnitskaya, T. Kypreos, J.F. Low, K. Matchev, P. Milenovic⁵², G. Mitselmakher, L. Muniz, R. Remington, A. Rinkevicius, N. Skhirtladze, M. Snowball, J. Yelton, M. Zakaria

Florida International University, Miami, USA

V. Gaultney, S. Hewamanage, L.M. Lebolo, S. Linn, P. Markowitz, G. Martinez, J.L. Rodriguez

Florida State University, Tallahassee, USA

T. Adams, A. Askew, J. Bochenek, J. Chen, B. Diamond, J. Haas, S. Hagopian, V. Hagopian, K.F. Johnson, H. Prosper, V. Veeraraghavan, M. Weinberg

Florida Institute of Technology, Melbourne, USA

M.M. Baarmand, B. Dorney, M. Hohlmann, H. Kalakhety, F. Yumiceva

University of Illinois at Chicago (UIC), Chicago, USA

M.R. Adams, L. Apanasevich, V.E. Bazterra, R.R. Betts, I. Bucinskaite, J. Callner, R. Cavanaugh, O. Evdokimov, L. Gauthier, C.E. Gerber, D.J. Hofman, S. Khalatyan, P. Kurt, F. Lacroix, C. O'Brien, C. Silkworth, D. Strom, P. Turner, N. Varelas

The University of Iowa, Iowa City, USA

U. Akgun, E.A. Albayrak, B. Bilki⁵³, W. Clarida, K. Dilsiz, F. Duru, S. Griffiths, J.-P. Merlo, H. Mermerkaya⁵⁴, A. Mestvirishvili, A. Moeller, J. Nachtman, C.R. Newsom, H. Ogul, Y. Onel, F. Ozok⁴⁶, S. Sen, P. Tan, E. Tiras, J. Wetzel, T. Yetkin⁵⁵, K. Yi

Johns Hopkins University, Baltimore, USA

B.A. Barnett, B. Blumenfeld, S. Bolognesi, D. Fehling, G. Giurgiu, A.V. Gritsan, G. Hu, P. Maksimovic, M. Swartz, A. Whitbeck

The University of Kansas, Lawrence, USA

P. Baringer, A. Bean, G. Benelli, R.P. Kenny III, M. Murray, D. Noonan, S. Sanders, R. Stringer, J.S. Wood

Kansas State University, Manhattan, USA

A.F. Barfuss, I. Chakaberia, A. Ivanov, S. Khalil, M. Makouski, Y. Maravin, S. Shrestha, I. Svintradze

Lawrence Livermore National Laboratory, Livermore, USA

J. Gronberg, D. Lange, F. Rebassoo, D. Wright

University of Maryland, College Park, USA

A. Baden, B. Calvert, S.C. Eno, J.A. Gomez, N.J. Hadley, R.G. Kellogg, T. Kolberg, Y. Lu,

M. Marionneau, A.C. Mignerey, K. Pedro, A. Peterman, A. Skuja, J. Temple, M.B. Tonjes, S.C. Tonwar

Massachusetts Institute of Technology, Cambridge, USA

A. Apyan, G. Bauer, W. Busza, E. Butz, I.A. Cali, M. Chan, V. Dutta, G. Gomez Ceballos, M. Goncharov, Y. Kim, M. Klute, Y.S. Lai, A. Levin, P.D. Luckey, T. Ma, S. Nahn, C. Paus, D. Ralph, C. Roland, G. Roland, G.S.F. Stephans, F. Stöckli, K. Sumorok, K. Sung, D. Velicanu, R. Wolf, B. Wyslouch, M. Yang, Y. Yilmaz, A.S. Yoon, M. Zanetti, V. Zhukova

University of Minnesota, Minneapolis, USA

B. Dahmes, A. De Benedetti, G. Franzoni, A. Gude, J. Haupt, S.C. Kao, K. Klapoetke, Y. Kubota, J. Mans, N. Pastika, R. Rusack, A. Singovsky, N. Tambe, J. Turkewitz

University of Mississippi, Oxford, USA

L.M. Cremaldi, R. Kroeger, L. Perera, R. Rahmat, D.A. Sanders, D. Summers

University of Nebraska-Lincoln, Lincoln, USA

E. Avdeeva, K. Bloom, S. Bose, D.R. Claes, A. Dominguez, M. Eads, R. Gonzalez Suarez, J. Keller, I. Kravchenko, J. Lazo-Flores, S. Malik, G.R. Snow

State University of New York at Buffalo, Buffalo, USA

J. Dolen, A. Godshalk, I. Iashvili, S. Jain, A. Kharchilava, A. Kumar, S. Rappoccio, Z. Wan

Northeastern University, Boston, USA

G. Alverson, E. Barberis, D. Baumgartel, M. Chasco, J. Haley, D. Nash, T. Orimoto, D. Trocino, D. Wood, J. Zhang

Northwestern University, Evanston, USA

A. Anastasov, K.A. Hahn, A. Kubik, L. Lusito, N. Mucia, N. Odell, B. Pollack, A. Pozdnyakov, M. Schmitt, S. Stoynev, M. Velasco, S. Won

University of Notre Dame, Notre Dame, USA

D. Berry, A. Brinkerhoff, K.M. Chan, M. Hildreth, C. Jessop, D.J. Karmgard, J. Kolb, K. Lannon, W. Luo, S. Lynch, N. Marinelli, D.M. Morse, T. Pearson, M. Planer, R. Ruchti, J. Slaunwhite, N. Valls, M. Wayne, M. Wolf

The Ohio State University, Columbus, USA

L. Antonelli, B. Bylsma, L.S. Durkin, C. Hill, R. Hughes, K. Kotov, T.Y. Ling, D. Puigh, M. Rodenburg, G. Smith, C. Vuosalo, G. Williams, B.L. Winer, H. Wolfe

Princeton University, Princeton, USA

E. Berry, P. Elmer, V. Halyo, P. Hebda, J. Hegeman, A. Hunt, P. Jindal, S.A. Koay, D. Lopes Pegna, P. Lujan, D. Marlow, T. Medvedeva, M. Mooney, J. Olsen, P. Piroué, X. Quan, A. Raval, H. Saka, D. Stickland, C. Tully, J.S. Werner, S.C. Zenz, A. Zuranski

University of Puerto Rico, Mayaguez, USA

E. Brownson, A. Lopez, H. Mendez, J.E. Ramirez Vargas

Purdue University, West Lafayette, USA

E. Alagoz, D. Benedetti, G. Bolla, D. Bortoletto, M. De Mattia, A. Everett, Z. Hu, M. Jones, O. Koybasi, M. Kress, N. Leonardo, V. Maroussov, P. Merkel, D.H. Miller, N. Neumeister, I. Shipsey, D. Silvers, A. Svyatkovskiy, M. Vidal Marono, H.D. Yoo, J. Zablocki, Y. Zheng

Purdue University Calumet, Hammond, USA

S. Guragain, N. Parashar

Rice University, Houston, USA

A. Adair, B. Akgun, K.M. Ecklund, F.J.M. Geurts, W. Li, B.P. Padley, R. Redjimi, J. Roberts, J. Zabel

University of Rochester, Rochester, USA

B. Betchart, A. Bodek, R. Covarelli, P. de Barbaro, R. Demina, Y. Eshaq, T. Ferbel, A. Garcia-Bellido, P. Goldenzweig, J. Han, A. Harel, D.C. Miner, G. Petrillo, D. Vishnevskiy, M. Zielinski

The Rockefeller University, New York, USA

A. Bhatti, R. Ciesielski, L. Demortier, K. Goulios, G. Lungu, S. Malik, C. Mesropian

Rutgers, The State University of New Jersey, Piscataway, USA

S. Arora, A. Barker, J.P. Chou, C. Contreras-Campana, E. Contreras-Campana, D. Duggan, D. Ferencek, Y. Gershtein, R. Gray, E. Halkiadakis, D. Hidas, A. Lath, S. Panwalkar, M. Park, R. Patel, V. Rekovic, J. Robles, K. Rose, S. Salur, S. Schnetzer, C. Seitz, S. Somalwar, R. Stone, M. Walker

University of Tennessee, Knoxville, USA

G. Cerizza, M. Hollingsworth, S. Spanier, Z.C. Yang, A. York

Texas A&M University, College Station, USA

R. Eusebi, W. Flanagan, J. Gilmore, T. Kamon⁵⁶, V. Khotilovich, R. Montalvo, I. Osipenkov, Y. Pakhotin, A. Perloff, J. Roe, A. Safonov, T. Sakuma, I. Suarez, A. Tatarinov, D. Toback

Texas Tech University, Lubbock, USA

N. Akchurin, J. Damgov, C. Dragoiu, P.R. Duder, C. Jeong, K. Kovitanggoon, S.W. Lee, T. Libeiro, I. Volobouev

Vanderbilt University, Nashville, USA

E. Appelt, A.G. Delannoy, S. Greene, A. Gurrola, W. Johns, C. Maguire, Y. Mao, A. Melo, M. Sharma, P. Sheldon, B. Snook, S. Tuo, J. Velkovska

University of Virginia, Charlottesville, USA

M.W. Arenton, M. Balazs, S. Boutle, B. Cox, B. Francis, J. Goodell, R. Hirosky, A. Ledovskoy, C. Lin, C. Neu, J. Wood

Wayne State University, Detroit, USA

S. Gollapinni, R. Harr, P.E. Karchin, C. Kottachchi Kankanamge Don, P. Lamichhane, A. Sakharov

University of Wisconsin, Madison, USA

M. Anderson, D.A. Belknap, L. Borrello, D. Carlsmith, M. Cepeda, S. Dasu, E. Friis, K.S. Grogg, M. Grothe, R. Hall-Wilton, M. Herndon, A. Hervé, P. Klabbers, J. Klukas, A. Lanaro, C. Lazaridis, R. Loveless, A. Mohapatra, M.U. Mozer, I. Ojalvo, G.A. Pierro, I. Ross, A. Savin, W.H. Smith, J. Swanson

†: Deceased

1: Also at Vienna University of Technology, Vienna, Austria

2: Also at CERN, European Organization for Nuclear Research, Geneva, Switzerland

3: Also at National Institute of Chemical Physics and Biophysics, Tallinn, Estonia

4: Also at Skobeltsyn Institute of Nuclear Physics, Lomonosov Moscow State University, Moscow, Russia

5: Also at Universidade Estadual de Campinas, Campinas, Brazil

6: Also at California Institute of Technology, Pasadena, USA

7: Also at Laboratoire Leprince-Ringuet, Ecole Polytechnique, IN2P3-CNRS, Palaiseau, France

- 8: Also at Suez Canal University, Suez, Egypt
- 9: Also at Cairo University, Cairo, Egypt
- 10: Also at Fayoum University, El-Fayoum, Egypt
- 11: Also at Helwan University, Cairo, Egypt
- 12: Also at British University in Egypt, Cairo, Egypt
- 13: Now at Ain Shams University, Cairo, Egypt
- 14: Also at National Centre for Nuclear Research, Swierk, Poland
- 15: Also at Université de Haute Alsace, Mulhouse, France
- 16: Also at Joint Institute for Nuclear Research, Dubna, Russia
- 17: Also at Brandenburg University of Technology, Cottbus, Germany
- 18: Also at The University of Kansas, Lawrence, USA
- 19: Also at Institute of Nuclear Research ATOMKI, Debrecen, Hungary
- 20: Also at Eötvös Loránd University, Budapest, Hungary
- 21: Also at Tata Institute of Fundamental Research - HECR, Mumbai, India
- 22: Now at King Abdulaziz University, Jeddah, Saudi Arabia
- 23: Also at University of Visva-Bharati, Santiniketan, India
- 24: Also at Sharif University of Technology, Tehran, Iran
- 25: Also at Isfahan University of Technology, Isfahan, Iran
- 26: Also at Plasma Physics Research Center, Science and Research Branch, Islamic Azad University, Tehran, Iran
- 27: Also at Università degli Studi di Siena, Siena, Italy
- 28: Also at Faculty of Physics, University of Belgrade, Belgrade, Serbia
- 29: Also at Facoltà Ingegneria, Università di Roma, Roma, Italy
- 30: Also at Scuola Normale e Sezione dell'INFN, Pisa, Italy
- 31: Also at INFN Sezione di Roma, Roma, Italy
- 32: Also at University of Athens, Athens, Greece
- 33: Also at Rutherford Appleton Laboratory, Didcot, United Kingdom
- 34: Also at Paul Scherrer Institut, Villigen, Switzerland
- 35: Also at Institute for Theoretical and Experimental Physics, Moscow, Russia
- 36: Also at Albert Einstein Center for Fundamental Physics, Bern, Switzerland
- 37: Also at Gaziosmanpasa University, Tokat, Turkey
- 38: Also at Adiyaman University, Adiyaman, Turkey
- 39: Also at The University of Iowa, Iowa City, USA
- 40: Also at Mersin University, Mersin, Turkey
- 41: Also at Izmir Institute of Technology, Izmir, Turkey
- 42: Also at Ozyegin University, Istanbul, Turkey
- 43: Also at Kafkas University, Kars, Turkey
- 44: Also at Suleyman Demirel University, Isparta, Turkey
- 45: Also at Ege University, Izmir, Turkey
- 46: Also at Mimar Sinan University, Istanbul, Istanbul, Turkey
- 47: Also at Kahramanmaras Sütcü Imam University, Kahramanmaras, Turkey
- 48: Also at School of Physics and Astronomy, University of Southampton, Southampton, United Kingdom
- 49: Also at INFN Sezione di Perugia; Università di Perugia, Perugia, Italy
- 50: Also at Utah Valley University, Orem, USA
- 51: Also at Institute for Nuclear Research, Moscow, Russia
- 52: Also at University of Belgrade, Faculty of Physics and Vinca Institute of Nuclear Sciences, Belgrade, Serbia
- 53: Also at Argonne National Laboratory, Argonne, USA

54: Also at Erzincan University, Erzincan, Turkey

55: Also at Yildiz Technical University, Istanbul, Turkey

56: Also at Kyungpook National University, Daegu, Korea